

<sup>1</sup> Observation of the Higgs boson in the  $WW^*$   
<sup>2</sup> channel and search for Higgs boson pair  
<sup>3</sup> production in the  $b\bar{b}b\bar{b}$  channel with the  
<sup>4</sup> ATLAS detector

<sup>5</sup> A DISSERTATION PRESENTED  
<sup>6</sup> BY  
<sup>7</sup> TOMO LAZOVICH  
<sup>8</sup> TO  
<sup>9</sup> THE DEPARTMENT OF PHYSICS

<sup>10</sup> IN PARTIAL FULFILLMENT OF THE REQUIREMENTS  
<sup>11</sup> FOR THE DEGREE OF  
<sup>12</sup> DOCTOR OF PHILOSOPHY  
<sup>13</sup> IN THE SUBJECT OF  
<sup>14</sup> PHYSICS

<sup>15</sup> HARVARD UNIVERSITY  
<sup>16</sup> CAMBRIDGE, MASSACHUSETTS  
<sup>17</sup> MAY 2016

<sup>18</sup> ©2016 – TOMO LAZOVICH

<sup>19</sup> ALL RIGHTS RESERVED.

20     **Observation of the Higgs boson in the  $WW^*$  channel and search  
21     for Higgs boson pair production in the  $b\bar{b}b\bar{b}$  channel with the  
22     ATLAS detector**

23     ABSTRACT

24     This dissertation presents two studies: the observation and measurement of the Higgs boson in the  
25      $H \rightarrow WW^* \rightarrow \ell\nu\ell\nu$  channel at  $\sqrt{s} = 7$  TeV and  $\sqrt{s} = 8$  TeV and a search for Higgs pair pro-  
26     duction in the  $HH \rightarrow b\bar{b}b\bar{b}$  channel at  $\sqrt{s} = 13$  TeV with the ATLAS detector in  $pp$  collisions at the  
27     Large Hadron Collider.

28     First, the discovery of a particle consistent with the Higgs in  $4.8 \text{ fb}^{-1}$  at  $\sqrt{s} = 7$  TeV and  $5.8 \text{ fb}^{-1}$  at  
29      $\sqrt{s} = 8$  TeV is discussed. Then, the measurement of the Higgs boson signal strength and cross section  
30     in both the gluon fusion and vector boson fusion (VBF) production modes using  $20.3 \text{ fb}^{-1}$  of  $\sqrt{s} =$   
31      $8$  TeV data combined with  $4.8 \text{ fb}^{-1}$  of  $7$  TeV data is shown. The combined signal strength is measured  
32     to be  $\mu = 1.09^{+0.23}_{-0.21}$ . The total observed significance of the  $H \rightarrow WW^*$  process is observed to be  
33      $6.1\sigma$  (with  $5.8\sigma$  expected). Advanced methods for background reduction and estimation, particularly in  
34     same-flavor lepton final states, are shown. The VBF signal strength is measured to be  $\mu_{\text{VBF}} = 1.27^{+0.53}_{-0.45}$   
35     with an observed significance of  $3.2\sigma$  (with  $2.7\sigma$  expected). In the VBF channel, a selection requirement  
36     based method, the precursor to the final multivariate technique used for the result, is detailed.

37     Finally, a search for Higgs pair production in the  $b\bar{b}b\bar{b}$  final state with  $3.2 \text{ fb}^{-1}$  at  $\sqrt{s} = 13$  TeV  
38     is presented. A particular focus is placed on a tailored signal region for resonant production of Higgs  
39     pairs at high masses, utilizing novel techniques in object reconstruction to increase signal acceptance in  
40     boosted final state topologies. No significant excesses are observed, and upper limits on cross sections are  
41     placed for spin-2 Randall Sundrum gravitons (RSG) and narrow spin-0 resonances. The cross section of  
42      $\sigma(pp \rightarrow G_{\text{KK}}^* \rightarrow hh \rightarrow b\bar{b}b\bar{b})$  with  $k/\bar{M}_{\text{Pl}} = 1$  is constrained to be less than  $70 \text{ fb}$  for masses in the  
43     range  $600 < m_{G_{\text{KK}}^*} < 3000 \text{ GeV}$ . For the RSG model with  $k/\bar{M}_{\text{Pl}} = 2$ , cross sections limits between  
44      $40 \text{ fb}$  and  $200 \text{ fb}$  are set for the mass range of  $500 < m_{G_{\text{KK}}^*} < 3000 \text{ GeV}$ . The cross section upper  
45     limits for  $\sigma(pp \rightarrow H \rightarrow hh \rightarrow b\bar{b}b\bar{b})$  ranges from  $30$  to  $300 \text{ fb}$  in the mass range of  $500 < m_H <$   
46      $3000 \text{ GeV}$ .

# Contents

47

48	o INTRODUCTION	I
49	I Theoretical and Experimental Background	5
50	I.1 THE PHYSICS OF THE HIGGS BOSON	6
51	I.1.1 The Standard Model of Particle Physics	6
52	I.1.2 Electroweak Symmetry Breaking and the Higgs	8
53	I.1.3 Higgs Boson Production and Decay	II
54	I.1.4 Higgs Pair Production in the Standard Model	15
55	I.1.5 Higgs Pair Production in Theories Beyond the Standard Model	16
56	I.1.6 Conclusion	21
57	2 THE ATLAS DETECTOR AND THE LARGE HADRON COLLIDER	22
58	2.1 The Large Hadron Collider	23
59	2.2 The ATLAS Detector	25
60	2.3 The ATLAS Muon New Small Wheel Upgrade	36
61	2.4 Object Reconstruction in ATLAS	40
62	II Observation and measurement of Higgs boson decays to $WW^*$ in LHC	
63	Run I at $\sqrt{s} = 7$ and 8 TeV	49
64	3 $H \rightarrow WW^* \rightarrow \ell\nu\ell\nu$ ANALYSIS STRATEGY	50
65	3.1 Introduction	50
66	3.2 The $H \rightarrow WW^* \rightarrow \ell\nu\ell\nu$ signal in ATLAS	51
67	3.3 Background processes	52
68	3.4 Shared signal region selection requirements	56
69	3.5 Background reduction in same-flavor final states	58
70	3.6 Parameters of interest and statistical treatment	64
71	4 THE DISCOVERY OF THE HIGGS BOSON AND THE ROLE OF THE $H \rightarrow WW^* \rightarrow \ell\nu\ell\nu$ CHANNEL	69
72	4.1 Introduction	69

74	4.2	Data and simulation samples . . . . .	70
75	4.3	$H \rightarrow WW \rightarrow e\nu\mu\nu$ search . . . . .	70
76	4.4	$H \rightarrow \gamma\gamma$ search . . . . .	75
77	4.5	$H \rightarrow ZZ \rightarrow 4\ell$ search . . . . .	76
78	4.6	Combined results . . . . .	77
79	4.7	Conclusion . . . . .	79
80	5	OBSERVATION OF VECTOR BOSON FUSION PRODUCTION OF $H \rightarrow WW^* \rightarrow \ell\nu\ell\nu$ . . . . .	82
81	5.1	Introduction . . . . .	82
82	5.2	Data and simulation samples . . . . .	83
83	5.3	Object selection . . . . .	87
84	5.4	Analysis selection . . . . .	90
85	5.5	Background estimation . . . . .	99
86	5.6	Systematic uncertainties . . . . .	109
87	5.7	Results . . . . .	113
88	6	COMBINED RUN I $H \rightarrow WW^* \rightarrow \ell\nu\ell\nu$ RESULTS . . . . .	118
89	6.1	Introduction . . . . .	118
90	6.2	Results of dedicated gluon fusion $H \rightarrow WW^* \rightarrow \ell\nu\ell\nu$ search . . . . .	119
91	6.3	Signal strength measurements in ggF and VBF production . . . . .	121
92	6.4	Measurement of Higgs couplings to vector bosons and fermions . . . . .	124
93	6.5	Higgs production cross section measurement . . . . .	125
94	6.6	Conclusion . . . . .	126
95	III	Search for Higgs pair production in the $HH \rightarrow b\bar{b}b\bar{b}$ channel in LHC Run 2 at $\sqrt{s} = 13$ TeV . . . . .	128
97	7	SEARCH FOR HIGGS PAIR PRODUCTION IN BOOSTED $b\bar{b}b\bar{b}$ FINAL STATES . . . . .	129
98	7.1	Introduction . . . . .	129
99	7.2	Motivation . . . . .	130
100	7.3	Data and simulation samples . . . . .	132
101	7.4	Event reconstruction and object selection . . . . .	134
102	7.5	Event selection . . . . .	137
103	7.6	Data-driven background estimation . . . . .	140
104	7.7	Systematic uncertainties . . . . .	146
105	7.8	Results . . . . .	149

106	<b>8 COMBINED LIMITS FROM BOOSTED AND RESOLVED SEARCHES</b>	151
107	8.1 Introduction . . . . .	151
108	8.2 Resolved results . . . . .	152
109	8.3 Search technique and results . . . . .	152
110	8.4 Limit setting . . . . .	153
111	<b>IV Looking ahead</b>	157
112	<b>9 CONCLUSION</b>	158
113	<b>APPENDIX A OPTIMIZATION OF <math>b</math>-TAGGING WORKING POINT IN <math>X \rightarrow HH \rightarrow b\bar{b}b\bar{b}</math></b>	
114	SEARCH	160
115	<b>APPENDIX B <math>b</math>-TAGGING PERFORMANCE AT HIGH <math>p_T</math></b>	162
116	B.1 MV2 algorithm overview . . . . .	162
117	B.2 Changes in MV2 score at high $p_T$ . . . . .	163
118	B.3 Tagging efficiency by individual jet . . . . .	166
119	B.4 Effect of multiple $b$ -quarks inside one jet . . . . .	167
120	B.5 Changes in track quality at high $p_T$ . . . . .	168
121	<b>REFERENCES</b>	170

# Listing of figures

122

123	I.1	The particles of the Standard Model and their properties [6]. . . . .	7
124	I.2	The four most common Higgs boson production modes at the LHC: (a) gluon-gluon fu- 125 sion, (b) vector boson fusion, (c) $W/Z + H$ production, (d) $t\bar{t}H$ production . . . . .	II
126	I.3	Higgs production cross sections as a function of center of mass energy ( $\sqrt{s}$ ) at a $pp$ collider [18]. .	12
127	I.4	Higgs boson branching ratios as a function of $m_H$ [18]. . . . .	14
128	I.5	The two leading diagrams for Standard Model di-Higgs production at the LHC: (a) box di- 129 agram, (b) Higgs self coupling . . . . .	16
130	I.6	Diagrams with new vertices for non-resonant Higgs pair production arising in composite 131 Higgs models . . . . .	17
132	I.7	Generic Feynman diagram for resonant Higgs pair production in BSM theories . . . . .	18
133	I.8	Branching ratios for a spin-2 Randall-Sundrum graviton as a function of mass computed in 134 MadGraph with the CP3-Origins implementation [24, 30] . . . . .	18
135	I.9	$\sigma \times BR(HH)$ for RSG as a function of mass computed in MadGraph with the CP3-Origins 136 implementation [24, 30] . . . . .	19
137	I.10	RSG width as a function of mass computed in MadGraph with the CP3-Origins implemen- 138 tation [24, 30] . . . . .	20
139	I.11	Branching ratios for heavy Higgs $H$ in Type I (left) and Type II (right) 2HDM models with 140 $\tan \beta = 1.5$ and $\cos(\beta - \alpha) = 0.1(0.01)$ for Type I (Type II). [28] . . . . .	21
141	2.1	A schematic view of the LHC ring [36] . . . . .	23
142	2.2	A full diagram of the ATLAS detector [32] . . . . .	26
143	2.3	The ATLAS coordinate system . . . . .	27
144	2.4	Layout of the ATLAS Inner Detector system [40] . . . . .	28
145	2.5	Layout of the ATLAS calorimeter system [32] . . . . .	30
146	2.6	Layout of the ATLAS muon system [32] . . . . .	32
147	2.7	Predicted field integral as a function of $ \eta $ for the ATLAS magnet system [32] . . . . .	34
148	2.8	ATLAS trigger rates for Level-1 triggers as a function of instantaneous luminosity in 2012 149 and 2015 operation. These are single object triggers for electromagnetic clusters (EM), muons 150 (MU), jets (J), missing energy (XE), and $\tau$ leptons (TAU). The threshold of the trigger is given 151 in the name in GeV. [42] . . . . .	35
152	2.9	Instantaneous luminosity as a function of time for data recorded by ATLAS at different cen- 153 ter of mass energies [43, 44] . . . . .	36

154	2.10	MDT tube hit (solid) and segment (dashed) efficiency as a function of hit rate per tube [45]	37
155	2.11	Trigger rate as a function of $p_T$ threshold with and without the NSW upgrade [45]	38
156	2.12	Illustrations of the geometry (left) and operating principle (right) of the micromegas detector [45]	39
157	2.13	Geometry of the sTGC detector [45]	40
158	2.14	Illustration of particle interactions in ATLAS [48]	41
159	2.15	Electron performance: (a) reconstruction efficiency as a function of electron $E_T$ [50] (b) energy resolution in simulation as a function of $ \eta $ for different energy electrons [51]	42
160	2.16	Muon performance: (a) reconstruction efficiency as a function of muon $p_T$ (b) dimuon mass resolution as a function of average $p_T$ [52]	44
161	2.17	Jet energy response after calibration as a function of true $p_T$ in simulation [56]	45
162	2.18	Light jet rejection (1/efficiency) vs. $b$ -jet efficiency for MV1 and its input algorithms (a) [57] and MV2 (b) [58] in simulated $t\bar{t}$ events. The numbers in the algorithm names in (b) refer to the fraction of charm events used in the MV2 training.	46
163	2.19	Resolution of $E_T^{\text{miss}}$ components as a function of $\sum E_T$ before pileup suppression with different pileup techniques [60]	48
164	3.1	Branching ratios for a $WW$ system. $q$ refers to quarks. $\ell$ can be either an electron or muon, and the leptonic branching ratios of the $\tau$ are included. For example, the $\ell\nu qq$ final state includes one $W$ decaying to $e\nu$ , $\mu\nu$ , or $\tau\nu$ . $\tau_h$ refer to hadronic decays of the $\tau$ .	52
165	3.2	Feynman diagram for Standard Model $WW$ production	53
166	3.3	Feynman diagrams for top pair production (left) and $Wt$ production (right)	54
167	3.4	An example Feynman diagram of $W + \text{jets}$ production	54
168	3.5	An example Feynman diagram of $Z + \text{jets}$ production	55
169	3.6	An illustration of the unique analysis signal regions [61]	56
170	3.7	A graphical illustration of the $E_{T,\text{rel}}^{\text{miss}}$ calculation	58
171	3.8	Predicted backgrounds (compared with data) as a function of $n_j$ (a and b) and $n_b$ (c)	59
172	3.9	An event display of a $Z/\gamma^* + \text{jets}$ event illustrating the effect of pileup interactions	60
173	3.10	The RMS of different missing transverse momentum definitions as a function of the average number of interactions per bunch crossing	61
174	3.11	The difference between the true and reconstructed values of the missing transverse momentum (a) and $m_T$ (b) in a gluon fusion signal sample	62
175	3.12	Comparison of $f_{\text{recoil}}$ distributions for $Z/\gamma^* + \text{jets}$ , $H \rightarrow WW^*$ , and other backgrounds with real neutrinos.	63
176	3.13	Signal significance as a function of required value for $f_{\text{recoil}}$ and $p_{T,\text{rel}}^{\text{miss}(\text{trk})}$ in the ggF $H \rightarrow WW^*$ with $n_j = 0$	64

189	4.1	Jet multiplicity distribution in data and MC after applying lepton, jet, and $E_{\mathrm{T},\mathrm{rel}}^{\mathrm{miss}}$ selections. The $WW$ and top backgrounds have been normalized using control samples, and the hashed band indicates the total uncertainty on the prediction. [1] . . . . .	71
190			
191	4.2	Comparison of $m_{\mathrm{T}}$ between data and simulation in the $n_j = 0$ $WW$ (a) and $n_j = 1$ top (b) control samples [1] . . . . .	73
192			
193	4.3	$m_{\mathrm{T}}$ distribution in the $H \rightarrow WW \rightarrow e\nu\mu\nu$ $n_j \leq 1$ channels for 8 TeV data [1]. . . . .	75
194			
195	4.4	Diphoton mass spectrum in 7 and 8 TeV data. Panel a) shows the unweighted data distri- bution superimposed on the background fit, while panel c) shows the data where each event category is weighted by its signal to background ratio. Panels b) and d) show the respective distributions with background subtracted [1]. . . . .	76
196			
197	4.5	Four lepton invariant mass spectrum ( $m_{4\ell}$ ) in 7 and 8 TeV data compared to background estimate. A 125 GeV SM Higgs signal is shown in blue [1]. . . . .	77
198			
199	4.6	Local $p_0$ distribution as a function of hypothesized Higgs mass for the $H \rightarrow ZZ^* \rightarrow 4\ell$ (a), $H \rightarrow \gamma\gamma$ (b), and $H \rightarrow WW^* \rightarrow \ell\nu\ell\nu$ (c) channels. Dashed curves show expected results, while solid curves show observed. Red curves are from 7 TeV data, blue curves from 8 TeV, and black curved combined [1]. . . . .	79
200			
201	4.7	Combined 95% CL limits (a), local $p_0$ values (b), and signal strength measurement (c) as a function of Higgs mass [1]. . . . .	80
202			
203	4.8	Comparison of measured signal strength $\mu$ for a 126 GeV Higgs in the 7 and 8 TeV datasets [1].	81
204			
205	4.9	Two dimensional likelihood as a function of signal strength $\mu$ and Higgs mass $m_H$ [1]. . .	81
206			
207	5.1	A comparison of the subleading lepton $p_{\mathrm{T}}$ spectrum between VBF $H \rightarrow WW^*$ production and $t\bar{t}$ background . . . . .	84
208			
209	5.2	Leading jet $\eta$ in VBF $H \rightarrow WW^*$ (red) and $t\bar{t}$ (black) . . . . .	92
210			
211	5.3	Distributions of (a) $m_{jj}$ , (b) $\Delta y_{jj}$ , (c) $C_{\ell 1}$ , and (d) $\sum m_{\ell j}$ , for the VBF analysis. The top panels compare simulation and data, while the bottom panels show normalized distributions for all background processes and signal [61]. . . . .	94
212			
213	5.4	A cartoon of the $WW$ final state. Momenta are represented with thin arrows, spins with thick arrows. [61] . . . . .	95
214			
215	5.5	Event display of a VBF candidate event [61]. . . . .	97
216			
217	5.6	Distributions of $m_{\ell\ell}$ (top left), $\Delta\phi_{\ell\ell}$ (top right), and $m_{\mathrm{T}}$ (bottom), Higgs topology vari- ables used in the selection requirements of the cut-based signal region and as inputs to the BDT result. These are plotted after all of the BDT pre-training selection cuts [61]. . . . .	98
218			
219	5.7	Distributions of $m_{jj}$ (top left), $\Delta y_{jj}$ (top right), $\sum C_{\ell}$ (bottom), VBF topology variables used in the selection requirements of the cut-based signal region and as inputs to the BDT result. These are plotted after all of the BDT pre-training selection cuts [61]. . . . .	99
220			
221	5.8	Distributions of $m_{jj}$ (a) and $O_{\mathrm{BDT}}$ (b) in the VBF $n_b = 1$ top CR [61]. . . . .	102
222			
223			
224			

225	5.9	Comparison of $m_{jj}$ shape in a same flavor $Z \rightarrow \ell\ell$ control region and the VBF cut-based signal region. . . . .	103
226	5.10	General illustration of the ABCD region definitions for $Z/\gamma^* \rightarrow \ell\ell$ background estimation. . . . .	104
227	5.11	Distribution of $m_{T2}$ in the $WW$ validation region of the VBF analysis [61]. . . . .	106
228	5.12	Extrapolation factors for the $W + \text{jets}$ estimate derived for muons (a) and electrons (b) as a function of lepton $p_T$ [61]. . . . .	108
229	5.13	Background composition in final VBF signal region [61]. . . . .	109
230	5.14	Variations in the top background extrapolation factor in the cut-based analysis due to PDF uncertainties, binned in $m_T$ . . . . .	III
231	5.15	Variations in the top background extrapolation factor in the cut-based analysis due to QCD scale uncertainties, binned in $m_T$ . . . . .	II2
232	5.16	Post-fit distributions in the cut-based VBF analysis. Panel (a) shows the one-dimensional $m_T$ distribution, while (b) shows the data candidates split into the bins of $m_T$ and $m_{jj}$ used in the final fit [61]. . . . .	II5
233	5.17	Postfit distributions in the BDT VBF analysis [61]. . . . .	II6
234	5.18	Overlap between cut-based and BDT VBF signal region candidates in the $m_{jj}$ - $m_T$ plane. .	II6
241	6.1	Post-fit $m_T$ distribution in the $n_j \leq 1$ regions [61]. . . . .	120
242	6.2	Best fit signal strength $\hat{\mu}$ as a function of hypothesized $m_H$ [61]. . . . .	122
243	6.3	Local $p_0$ as a function of $m_H$ [61]. . . . .	122
244	6.4	Likelihood as a function of $\mu_{\text{VBF}}/\mu_{\text{ggF}}$ [61]. . . . .	123
245	6.5	Likelihood scan as a function of $\mu_{\text{VBF}}$ and $\mu_{\text{ggF}}$ [61]. . . . .	124
246	6.6	Likelihood scan as a function of $\kappa_F$ and $\kappa_V$ [61]. . . . .	125
247	6.7	Comparison of signal strength measurements in different Higgs decay channels on ATLAS [85].	127
249	7.1	Parton luminosity ratios as a function of resonance mass $M_X$ for 13/8 TeV and 7/8 TeV [86].	130
250	7.2	Summary of $HH$ branching ratios [87]. . . . .	131
251	7.3	Minimum $\Delta R$ between $B$ decay vertices for different RSG masses in a $G_{\text{KK}}^* \rightarrow HH \rightarrow 4b$ sample with $c = 1$ . . . . .	132
252	7.4	Trigger efficiency for events passing all signal region selections as a function of mass in $G_{\text{KK}}^* \rightarrow HH \rightarrow 4b$ samples with $c = 1$ [96]. In the trigger names, “j” refers to a jet or jets. “ht” refers to $H_T$ , the scalar sum of transverse momenta in the event. “bloose” refers to a loose $b$ -tagging requirement applied to the jet. “aior” refers to anti- $k_T$ jets with $R = 1.0$ . The numbers at the end are the thresholds on the given quantity in GeV. . . . .	134
258	7.5	Comparison of untrimmed and trimmed jet masses for large radius jets in a RSG sample with $m_{G_{\text{KK}}^*} = 1$ TeV. JES (JMS) refers to the standard jet energy (mass) scale calibration for ATLAS [56].	135
259			

260	7.6	Efficiency of finding two $b$ -jets from each Higgs in an RSG event using calorimeter jets with $R = 0.3$ or different track jet radii [100] . . . . .	136
261	7.7	Illustration of the boosted selection requirements on Higgs candidates. Each large-radius calorime- ter jet (Higgs candidate) must contain two track jets . . . . .	138
262	7.8	Acceptance $\times$ efficiency as a function of mass for (a) RSG and (b) narrow heavy scalar sig- nal models [102]. . . . .	139
263	7.9	Efficiency of requiring 3 or 4 $b$ -tagged track jets vs. RSG mass. The efficiency quoted is rel- ative to the previous selection requirements (rather than an absolute efficiency). . . . .	140
264	7.10	$M_J^{\text{sublead}}$ vs. $M_J^{\text{lead}}$ in a 2 $b$ -tag data sample. The signal region is defined by the inner black contour ( $X_{hh} < 1.6$ ) and the sideband region is defined by the outer contour ( $R_{hh} >$ 35.8 GeV). The region between the black contours is the control region. The mass region which is enriched in $t\bar{t}$ background is also shown for illustration. [102] . . . . .	142
265	7.11	An illustration of the data-driven background estimation technique for the boosted anal- ysis . . . . .	143
266	7.12	Leading large-R jet mass in the 3 $b$ (a) and 4 $b$ (b) sideband regions. The multijet and $t\bar{t}$ back- grounds are estimated using the data-driven methods described above. Because their normal- izations are derived in the sideband region, the total background normalization is constrained by default to match the normalization of the data [102]. . . . .	144
267	7.13	Di-jet invariant mass ( $M_{2,J}$ ) in the 3 $b$ (a) and 4 $b$ (b) control regions. The multijet and $t\bar{t}$ back- grounds are estimated using the data-driven methods described above [102]. . . . .	145
268	7.14	Di-jet invariant mass ( $M_{2,J}$ ) in the 3 $b$ (a) and 4 $b$ (b) signal regions. The multijet and $t\bar{t}$ back- grounds are estimated using the data-driven methods described above. In the 3 $b$ region, a graviton signal with $m_{G_{KK}^*} = 1.8$ TeV and $c = 1$ is overlaid, with the cross section mul- tiplied by a factor of 50 so that the signal is visible. In the 4 $b$ region, signals with $m_{G_{KK}^*} =$ 1.0 TeV and $m_{G_{KK}^*} = 1.5$ TeV are overlaid, both with $c = 1$ and the yields multiplied by factors of 2 and 5 respectively [102]. . . . .	150
269	8.1	Di-jet invariant mass ( $M_{2,J}$ ) in the resolved signal region. A graviton signal with $m_{G_{KK}^*} =$ 800 GeV and $c = 1$ is overlaid. [102]. . . . .	153
270	8.2	Expected and observed upper limit as a function of mass for $G_{KK}^*$ in the RSG model with (a) $c = 1$ and (b) $c = 2$ , as well as (c) $H$ with fixed $\Gamma_H = 1$ GeV, at the 95% confidence level in the $CL_s$ method. [102] . . . . .	156
271	A.1	Estimated significance as a function of signal mass for RSG $c = 1$ models in the 3 $b$ (a) and 4 $b$ (b) regions for different $b$ -tagging efficiency working points . . . . .	161
272	B.1	Summary of the inputs to the MV2 $b$ -tagging algorithm . . . . .	163
273	B.2	$p_T$ of the leading track jet in the leading calorimeter jet for different signal masses in RSG $c =$ 1 models . . . . .	164

296	B.3	MV <sub>2c2o</sub> score for the leading track jet (a) and subleading track jet (b) of the leading calorimeter jet for different signal masses in RSG $c = 1$ models . . . . .	164
297	B.4	IP <sub>3D</sub> log-likelihood ratio ( $\log(p_b/p_u)$ ) of the leading track jet in the leading calorimeter jet for different signal masses in RSG $c = 1$ models . . . . .	165
298	B.5	Mass (a) and number of tracks (b) for the secondary vertices computed with the SV <sub>1</sub> algorithm. When no secondary vertex is found, the quantities are assigned to default negative values. . . . .	165
299	B.6	Mass (a) and number of tracks (b) for vertices computed with the JetFitter algorithm. When no vertices are found, the quantities are assigned to default negative values. . . . .	166
300	B.7	MV <sub>2c2o</sub> $b$ -tagging efficiency for each of the four track jets in the boosted $4b$ selection as a function of RSG mass for $c = 1$ models. . . . .	167
301	B.8	MV <sub>2c2o</sub> score (a) and SV <sub>1</sub> mass (b) for leading track jets with two truth $b$ quarks ( $n_{tb,lead} = 2$ ) compared to those with only one truth $b$ ( $n_{tb,lead} = 1$ ). . . . .	168
302	B.9	Track fit $\chi^2/n_{DOF}$ (a) and number of pixel detector hits (b) for the leading track of the leading track jet in different mass RSG $c = 1$ samples . . . . .	169
303	B.10	MV <sub>2c2o</sub> score (a) and SV <sub>1</sub> mass (b) for leading track jets whose leading track jet has at least four pixel hits ( $N_{pix} \geq 4$ ) compared to those which do not ( $N_{pix} < 4$ ). . . . .	169
312			

# Listing of tables

313

314	1.1 Production cross sections for a 125 GeV Higgs boson at $\sqrt{s} = 8$ TeV with scale and PDF uncertainties [18]. . . . .	13
315		
316	1.2 Branching ratios for a 125 GeV Higgs boson [18]. . . . .	15
317		
318	1.3 Possible channels for Higgs searches. Checkmarks denote the most sensitive production modes [5]. . . . .	15
319		
320	1.4 Production cross sections for pair production of a 125 GeV Higgs boson at $\sqrt{s} = 14$ TeV with total uncertainty [19]. The uncertainties include QCD scale and PDF variations as well as uncertainties on $\alpha_S$ . . . . .	16
321		
322	2.1 Evolution of LHC machine conditions [38, 39] . . . . .	25
323		
324	2.2 Performance requirements for the ATLAS detector [32]. . . . .	37
325		
326	2.3 Signal efficiencies for $WH$ production with $H \rightarrow b\bar{b}$ and $H \rightarrow WW^* \rightarrow \mu\nu qq$ under different trigger configurations [45]. . . . .	40
327		
328	3.1 A summary of backgrounds to the $H \rightarrow WW^* \rightarrow \ell\nu\ell\nu$ signal . . . . .	55
329		
330	4.1 Monte carlo generators used to model signal and background for the Higgs search [1]. . . . .	70
331		
332	4.2 Normalization factors (ratio of data and MC yields in a control sample) for the Standard Model $WW$ and top backgrounds in the $H \rightarrow WW^* \rightarrow \ell\nu\ell\nu$ analysis [1]. Only statistical uncertainties are shown. . . . .	73
333		
334	4.3 Data and expected yields for signal and background in the final $H \rightarrow WW^* \rightarrow \ell\nu\ell\nu$ signal region. Uncertainties shown are both statistical and systematic. [1] . . . . .	74
335		
336	4.4 Summary of the expected and observed significance and measured signal strengths in the combined 7 and 8 TeV datasets for the Higgs discovery analysis [1]. . . . .	78
337		
338	5.1 Single lepton triggers used for electrons and muons. A logical “or” of the triggers listed for each lepton type is taken. Units are in GeV, and the $i$ denotes an isolation requirement in the trigger. . . . .	84
339		
340	5.2 Di-lepton triggers used for different flavor combinations. The two thresholds listed refer to leading and sub-leading leptons, respectively. The di-muon trigger only requires a single lepton at level-i. . . . .	84

341	5.3	Trigger efficiency for signal events and relative gain of adding a dilepton trigger on top of the single lepton trigger selection. The first lepton is the leading, while the second is the sub-leading. Efficiencies shown here are for the ggF signal in the $n_j = 0$ category but are comparable for the VBF signal. . . . .	85
342			
343	5.4	Monte Carlo samples used to model the signal and background processes [61]. . . . .	86
344			
345	5.5	$p_T$ dependent isolation requirements for muons. Muons are required to have the amount of calorimeter or track based cone sums be less than this fraction of their $p_T$ . . . . .	88
346			
347	5.6	$p_T$ dependent requirements for electrons. Electrons are required to have the amount of calorimeter or track based cone sums be less than this fraction of their $E_T$ . . . . .	89
348			
349	5.7	Event selection for the $n_j \geq 2$ VBF analysis in the 8 TeV cut-based analysis [61]. . . . .	96
350			
351	5.8	Top normalization factors computed at each stage of the cut-based selection. Uncertainties are statistical only. . . . .	101
352			
353	5.9	Top normalization factors computed for each bin of $O_{\text{BDT}}$ . Uncertainties are statistical only. . . . .	101
354			
355	5.10	$Z/\gamma^* \rightarrow \tau\tau$ correction factors for the VBF cut-based analysis. Uncertainties are statistical only. . . . .	104
356			
357	5.11	$Z/\gamma^* \rightarrow \ell\ell$ normalization factors for cut-based and BDT analyses. Uncertainties are statistical only. . . . .	106
358			
359	5.12	Systematic uncertainties for various processes in the cut-based VBF analysis, given in units of % change in yield. Values are given for the low $m_{jj}$ signal region. . . . .	110
360			
361	5.13	Composition of the post-fit uncertainties (in %) on the total signal ( $N_{\text{sig}}$ ), total background ( $N_{\text{bkg}}$ ), and individual background yields in the VBF analysis [61]. . . . .	113
362			
363	5.14	Event selection for the VBF BDT analysis. The event yields in (a) are shown after the pre-selection and the additional requirements applied before the BDT classification (see text). The event yields in (b) are given in bins in $O_{\text{BDT}}$ after the classification [61]. . . . .	114
364			
365	6.1	All signal regions definitions input into final statistical fit [61]. . . . .	119
366	6.2	Post-fit yields in the different ggF and VBF dedicated signal regions [61]. . . . .	120
367	7.1	Summary of requirements on objects used in the $X \rightarrow HH \rightarrow b\bar{b}b\bar{b}$ search . . . . .	137
368	7.2	Effect of boosted selection on data, RSG signal models, $t\bar{t}$ , and $Z+\text{jets}$ . The numbers from simulation are normalized with the MC generator cross section and do not take into account the data driven estimates described in section 7.6 [103]. . . . .	141
369			
370	7.3	Mass region definitions used for background estimation . . . . .	142
371			
372	7.4	Parameters derived for exponential fit to background $M_{2J}$ shape in the 3 $b$ and 4 $b$ signal regions [103] . . . . .	145
373			
374	7.5	The number of events in data and predicted background events in the boosted 3-tag and 4-tag sideband and control regions. The uncertainties shown are statistical only. [102] . . . . .	146
375			

376	7.6	Summary of systematic uncertainties in the total background and signal event yields (expressed in %) in the boosted 3-tag and 4-tag signal regions. Systematic uncertainties on the signal normalization are shown for models with $m_{G_{\text{KK}}^*} = 1.5 \text{ TeV}$ and both $c = 1$ and $c = 2$ as well as a narrow width heavy scalar. . . . .	148
377			
378	7.7	Alternate fit functions used to model the $M_{JJ}$ distribution in the QCD multijet background. In the equations, $x = M_{JJ}/\sqrt{s}$ . . . . .	149
379			
380	7.8	Observed yields in the 3-tag and 4-tag signal regions for the boosted analysis compared to the predicted number of background events Errors correspond to the total uncertainties in the predicted event yields. The yields for a graviton with $m_{G_{\text{KK}}^*} = 1 \text{ TeV}$ and $c = 1$ are also shown. [102] . . . . .	150
381			
382	8.1	Observed yields in the resolve selection 4-tag signal region compared to the predicted num- ber of background events Errors correspond to the total uncertainties in the predicted event yields. The yields for a graviton with $m_{G_{\text{KK}}^*} = 800 \text{ GeV}$ and $c = 1$ are also shown. [102] . .	152
383			
384			
385			
386			
387			
388			



# Acknowledgments

391 I have been a member of the Harvard ATLAS group for many years now, first as an undergraduate  
 392 and then as a graduate student. As a result, I have had the privilege of interacting with many amazing  
 393 people there over the years and have accumulated a large list of folks to thank.

394 First and foremost, I must thank the two people who have effectively been my academic parents since  
 395 I started in the Harvard group: João Guimarães da Costa and Melissa Franklin. Melissa Franklin and  
 396 João Guimarães da Costa. They have both been so important to both my academic and personal devel-  
 397 opment that I can't even put one before the other. João has been an excellent PhD advisor, showing me  
 398 how to look at the big picture and helping me navigate the sometimes complicated politics of ATLAS.  
 399 He got me started on my first projects with ATLAS as a young college sophomore before there was even  
 400 beam in the LHC (go cosmic ray muons!). He has also been a constant source of advice and support,  
 401 even when we have been on different continents. Melissa gave me my start in HEP as a summer student  
 402 on CDF and has been an unbelievable mentor throughout my time at Harvard. I still remember our  
 403 weekly chalkboard particle physics lessons after that first summer. She also graciously took me on as a  
 404 co-advisee after João moved on to his new position at IHEP. I am incredibly lucky to have had both of  
 405 them as advisors.

406 Another mentor who was essential to my development as a graduate student is Paolo Giromini. His  
 407 uncanny knowledge and intuition about detectors is unmatched and I am very grateful to have had  
 408 the chance to work with him on the micromegas for the ATLAS New Small Wheel upgrade project. I  
 409 owe essentially all my practical knowledge about detectors (and building things in general) to him. I also  
 410 appreciated his unique sense of humor which made sometimes difficult tasks much easier to get through.

411 I am grateful to John Huth and Masahiro Morii for their helpful advice as the other professors in the  
 412 Harvard ATLAS group as well. I especially thank John for helping me get started on the micromegas  
 413 trigger project and being a great professor to TF particle physics for. Additionally I thank Howard  
 414 Georgi for serving as my third committee member and offering me feedback throughout my graduate  
 415 career.

416 I also owe enormous thanks to Hugh Skottowe, the postdoc that I worked most closely with in my  
 417 early years as a graduate student. He was always able to help me through complicated tasks in everything  
 418 from writing code to understanding difficult physics concepts. I particularly enjoyed walking down to  
 419 his office in Palfrey at random times and talking through whatever problem I was tackling on that day.

420 Alex Tuna, the second postdoc that I worked closely with at Harvard, deserves great thanks as well.  
 421 He helped me push through to the end of my graduate career and offered great advice along the way.

422 Being at Harvard, I have seen an incredible array of graduate students graduate before me: Ben Smith,

423 Verena Martinez Outschoorn, Srivas Prasad, Michael Kagan, Giovanni Zevi Della Porta, Laura Jeanty,  
424 Kevin Mercurio, William Spearman, and Andy Yen. I want to thank them all for showing me what a  
425 good physicist looks like and for patiently answering my questions and offering insightful advice about  
426 physics and life.

427 Getting through graduate school would not have been possible without the support and friendship  
428 of the other students in our group. Thanks to Emma Tolley for geeking out with me about cool com-  
429 puting stuff, going to taste delicious beers with me, and helping start the Palfrey tradition of Taco Tues-  
430 days. Thanks to Brian Clark for being a great friend and housing companion both in Kirkland House  
431 and in our tiny summer apartment in Geneva (and thanks to his partner Allison Goff for the same rea-  
432 sons!). Thanks to Siyuan Sun for giving me my first aikido lesson and always being there for great con-  
433 versations, big and small. Tony (Baojia) Tong deserves special recognition for working with me on the  
434  $4b$  analysis and putting up with my sometimes strange requests (and giving me rides to the Val Thoiry  
435 Migros so I wouldn't have to pay exorbitant Geneva grocery prices!). Stephen Chan is probably the only  
436 student in the group who both understands my references to the Sopranos and makes some of his own.  
437 To the younger graduate students - Karri Di Petrillo, Jennifer Roloff, Julia Gonski, and Ann Wang - I  
438 want to say thank you for making the group a fun and lively place to be and giving all of us energy that  
439 the older graduate students like myself can sometimes lack.

440 I'd like to thank Annie Wei and Gray Putnam, the two undergraduates I have worked with as a gradu-  
441 ate student. Their unbelievable intuition and quickness in picking up difficult particle physics concepts  
442 is inspiring.

443 I would also like to thank all of the postdocs that I have interacted with in my time in the Harvard  
444 group: Kevin Black, Alberto Belloni (who would always ask me "Do you have it?"...I can now say that  
445 I do!), Shulamit Moed, Corrinne Mills, Geraldine Conti, David Lopez Mateos, Chris Rogan, Valerio  
446 Ippolito, and Stefano Zambito.

447 There are many people on ATLAS who have helped me get to this point as well. In the  $WW$  group,  
448 I have to thank Jonathan Long, Joana Machado Miguens, Ben Cerio, Philip Chang, Bonnie Chow,  
449 Richard Polifka, Heberth Torres, Tae Min Hong, and Jennifer Hsu for being wonderful colleagues and  
450 making the entire analysis run smoothly. In the  $4b$  group, I have to thank Qi Zeng, Tony Tong, Alex  
451 Tuna, Michael Kagan, Max Bellomo, John Alison, and Patrick Bryant.

452 Kirkland House was my home for the last three years of graduate school and was an wonderful envi-  
453 ronment and support system. I want to thank my fellow tutors, especially Brian Clark and Allison Goff  
454 (again), Zach Abel, Kelly Bodwin, Alex Lupsasca, John and Pam Park, Luke and Erin Walczewski, and  
455 Philip Gant for their friendship and support. I also want to thank Kate Drizos Cavell, Bob Butler, and  
456 the Faculty Deans Tom and Verena Conley.

457 There are still a few friends that haven't been covered yet and deserve great thanks. Jake Connors and  
458 Meredith MacGregor have been absolutely wonderful friends and I thank them in particular for the  
459 many home-cooked meals and great conversations we've had in their apartment. Nihar Shah has been

460 my friend and confidant since we were both wee freshmen in Harvard Yard. Gareth Kafka, though he  
461 sits on the “neutrino” side of Palfrey House, has made days there more fun and has also been an enthusiastic  
462 participant in the Palfrey Taco Tuesdays.

463 Being at Harvard necessarily means having to navigate through bureaucracy at some point or another.  
464 I thank Lisa Cacciabaudo, Carol Davis, and Jacob Barandes for always having open doors and being the  
465 most kind, helpful people in the Physics department.

466 I thank Venky Narayananamurti for putting on a great SPU course that I was proud to be a part of and  
467 TF for. I'd also like to thank Jim Waldo for offering me much advice about working in Computer Science  
468 and giving me a fun data project to be a part of in my free time.

469 I grew up in a very tight knit Serbian community on the south side of Chicago which helped make  
470 me the person I am today. I would like to thank all of the people at St. Simeon Mirotochivi Serbian  
471 Orthodox Church who have always been sources of enthusiasm and support in my life.

472 I would not be here without the unconditional love and constant support and encouragement of my  
473 family. To my pokojni Dendas Branko and Miloje, my pokojni Baba Milka, and my Baba Desa, I want to  
474 say thank you for instilling in me at an early age the love of curiosity and storytelling that I have carried  
475 throughout my life. To my sister Angelina, I want to say thank you for always loving me and being my  
476 partner in crime throughout our childhoods. To my parents, Miroljub and Nada, Tata and Mama, I  
477 really cannot express how grateful I am to you and how much I owe you. As I look back now I see how  
478 I am a combination of both of your best qualities and every day I am in situations where I understand  
479 more and more the lessons you made sure to teach me and the sacrifices you made to make sure I got the  
480 best possible education. I love you all.

481 Finally, I have to thank my soul mate, the one person in my life who understands me more than anyone  
482 else, my fiancee Kelly Brock. You are my sounding board, my support system, my cheerleader (fig-  
483 uratively and literally!), my best friend, my role model, and my everything. I would not have gotten  
484 through graduate school without you and my life would not be the same without you. I cannot wait to  
485 start our new lives together as the married doctors, tackling whatever comes our way with the same zeal  
486 with which we tackled graduate school. I love you with all my heart and soul.

# 0

487

488

## Introduction

489 The Higgs boson is often described as one of the cornerstones of the Standard Model. Since the con-  
490 ception of the Higgs mechanism as the source of electroweak symmetry breaking in the early 1960s,  
491 countless collider experiments have searched for this elusive particle. This dissertation presents multi-  
492 ple studies of the Higgs boson with the ATLAS detector at the Large Hadron Collider (LHC).

493 One of the first priorities of the early LHC was the search for the Higgs boson. This search was first  
494 tackled in three main channels:  $H \rightarrow \gamma\gamma$ ,  $H \rightarrow ZZ^*$ , and  $H \rightarrow WW^*$ . Each channel has its own  
495 merits, but the  $WW^*$  is particularly suited to searching over a wide range of masses. The  $H \rightarrow WW$   
496 branching ratio is large and it is the primary decay channel above the  $2m_W$  mass threshold.

497 While the rate of events produced in  $H \rightarrow WW^*$  is large, the channel poses some challenges. First,  
498 the most common mode of study for this channel is  $H \rightarrow WW^* \rightarrow \ell\nu\ell\nu$ . With neutrinos in the  
499 final state, it is not possible to fully reconstruct the invariant mass of the parent Higgs like the  $\gamma\gamma$  and  
500  $ZZ \rightarrow 4\ell$  channels. Second, the final state topology is mimicked by a wide variety of backgrounds that

501 need to be properly estimated. This means tailored selection requirements for background reduction  
502 and robust background estimation techniques must both be developed.

503 In 2012, the ATLAS and CMS experiments announced the discovery of a new particle consistent with  
504 the Higgs boson [1, 2]. In ATLAS, this discovery was made with  $4.8 \text{ fb}^{-1}$  collected at  $\sqrt{s} = 7 \text{ TeV}$  and  
505  $5.8 \text{ fb}^{-1}$  at  $\sqrt{s} = 8 \text{ TeV}$ . The  $H \rightarrow WW^* \rightarrow \ell\nu\ell\nu$  analysis played an important role in this discovery.  
506 After the discovery, measurement of the properties of the newly discovered particle and confirmation  
507 of its consistency with the Standard Model Higgs were the main priorities. The  $WW^*$  channel is also  
508 uniquely suited to these types of measurements. Because of its good rate, it offers some of the best cross  
509 section measurements available among the various Higgs decay modes. It is also suited for measurement  
510 of multiple Higgs production modes, like the vector boson fusion (VBF) mode, where incoming quarks  
511 radiate  $W/Z$  bosons which fuse to make a Higgs. In VBF production with the  $WW^*$  decay channel,  
512 the coupling of the Higgs to the  $W$  boson is present in both the production and decay which allows for  
513 more precise measurements of this coupling than other channels which rely on gluon fusion production  
514 (where gluons couple to the Higgs through a top loop in the production). The measurement of VBF  
515 carries the additional challenge that its cross section is an order of magnitude smaller than that of gluon  
516 fusion, meaning that the large branching ratio to  $WW^*$  offers an additional advantage in isolating this  
517 production mode. In the final ATLAS Run 1 results, combining  $20.3 \text{ fb}^{-1}$  taken at  $\sqrt{s} = 8 \text{ TeV}$  with  
518 the  $4.8 \text{ fb}^{-1}$  collected at  $\sqrt{s} = 7 \text{ TeV}$ , the  $WW^*$  channel achieved its first observation of VBF produc-  
519 tion of the Higgs.

520 After Run 1 of the LHC, with the existence of the Higgs now firmly established, the focus shifted to  
521 searches for physics beyond the Standard Model. In particular, searches for high mass resonances benefit  
522 from the LHC's increase to  $\sqrt{s} = 13 \text{ TeV}$  in Run 2. The newly discovered Higgs can be used as a tool  
523 in these searches. Higgs pair production in the Standard Model has a low cross section that requires large  
524 datasets (on the order of the LHC's lifetime) for full measurement. However, new physics can modify  
525 this cross section, especially new resonances which decay to two Higgs bosons. A search for Higgs pair  
526 production in the  $HH \rightarrow b\bar{b}b\bar{b}$  final state was performed with  $3.2 \text{ fb}^{-1}$  collected with ATLAS at  $\sqrt{s} =$   
527  $13 \text{ TeV}$  in 2015.

528 This dissertation begins by discussing the discovery of the Higgs and the role of the  $H \rightarrow WW^* \rightarrow$   
529  $\ell\nu\ell\nu$  channel. It then discusses the first observation of the VBF production mode in  $H \rightarrow WW^* \rightarrow$   
530  $\ell\nu\ell\nu$  with the full ATLAS Run 1 dataset, as well as the final combined Run 1 measurements from this  
531 channel. Finally, it presents a search for Higgs pair production in the  $HH \rightarrow b\bar{b}b\bar{b}$  channel. It is orga-  
532 nized into four parts.

533 Part 1 presents the theoretical and experimental background required for the subsequent parts. Chap-  
534 ter 1 gives an overview of Higgs physics, particularly single and double Higgs production in the Standard  
535 Model and beyond. Chapter 2 presents details regarding the Large Hadron Collider and the ATLAS  
536 experiment. The evolution of machine conditions, descriptions of the ATLAS sub-detectors, and an  
537 overview of object reconstruction in ATLAS are all shown. A brief interlude on the ATLAS Muon New  
538 Small Wheel upgrade is also given, as this upgrade has been a focus of my graduate work and will have  
539 important impact on ATLAS' ability to study the Higgs at the High Luminosity LHC.

540 Part 2 discusses the observation and measurement of the Higgs in the  $H \rightarrow WW^* \rightarrow \ell\nu\ell\nu$   
541 channel in the ATLAS Run 1 dataset at  $\sqrt{s} = 7$  and 8 TeV. Because I worked in this channel from  
542 before the discovery through to the final analysis of the Run 1 dataset, Part 2 is organized in such a way  
543 to allow easy presentation of multiple analyses on different subsets of the full Run 1 dataset. Chapter 3  
544 presents a general overview of the  $H \rightarrow WW^*$  analysis strategy and defines many of the variables and  
545 common elements used in the rest of Part 2. Chapter 4 presents the discovery of the Higgs boson, fo-  
546 cusing on the role of the  $WW^*$  channel in this discovery. Chapter 5 presents the first observation of the  
547 VBF production mode of the Higgs in the  $WW^*$  channel, a study which was done on the full Run 1  
548 ATLAS dataset. In this chapter, the focus is mainly on the selection cut-based VBF analysis. The cut-  
549 based analysis was an important first step to the final VBF result which used a Boosted Decision Tree  
550 (BDT). Where appropriate, connections between the cut-based and BDT analyses are shown and their  
551 compatibility is discussed. Finally, the VBF analysis was an important input into the combined Run 1  
552  $H \rightarrow WW^* \rightarrow \ell\nu\ell\nu$  result, which used both the gluon fusion and VBF channels in a combined  
553 fit to infer properties of the Higgs, including its couplings to the gauge bosons and its production cross  
554 section. This is the topic of Chapter 6.

555        Part 3 presents a search for Higgs pair production in the  $HH \rightarrow b\bar{b}b\bar{b}$  channel. Chapter 7 presents  
556        an overview of this search in the boosted regime, where the Higgs pairs are the result of the decay of a  
557        heavy resonance. Chapter 8 shows the combined results between the boosted regime and the resolved  
558        regime, which is sensitive to lower mass resonances and non-resonant Higgs pair production. Finally,  
559        Part 4 presents a conclusion and brief outlook of future Higgs physics with ATLAS.

<sup>560</sup>

## Part I

<sup>561</sup>

## Theoretical and Experimental Background

*In modern physics, there is no such thing as “nothing.”*

Richard Morris

# 1

562

563

## The Physics of the Higgs Boson

564 This chapter presents an overview of the Standard Model of Particle Physics and in particular the physics  
565 of the Higgs boson. First, a brief overview of the Standard Model and its history are presented. Then, a  
566 description of the Higgs mechanism of electroweak symmetry breaking is given. Next, the physics of sin-  
567 ggle Higgs boson production and decay is described. The Standard Model also allows for production of  
568 two Higgs bosons and this is detailed as well. Finally, di-Higgs production in two beyond the Standard  
569 Model (BSM) theories - Randall-Sundrum gravitons (RSG) and Two Higgs Doublet Models (2HDM) -  
570 is shown.

571 1.1 THE STANDARD MODEL OF PARTICLE PHYSICS

572 The Standard Model (SM) of Particle Physics is a quantum field theory describing the fundamental  
573 particles of nature and the forces that govern their interactions. Several comprehensive treatments of  
574 the SM already exist in the literature [3–8] and this section will not rehash those. Rather, this section

575 presents a brief overview of the SM particles and forces in order to define them for subsequent discussions.  
 576

577 The Standard Model consists of two primary categories of fundamental particles: fermions (spin 1/2  
 578 particles) and bosons (integer spin particles). The SM also describes three forces: electromagnetism, the  
 579 weak nuclear force, and the strong nuclear force. Gravity is not included in the theory and is largely irrele-  
 580 vant at the scales currently probed by collider experiments. Within the fermions, there are both quarks  
 581 (which interact via all three forces) and the leptons. The charged leptons interact via electromagnetic and  
 582 weak interactions, while neutrinos (neutral leptons) interact only via the weak force. Within the bosons,  
 583 there are the  $W^\pm$  and  $Z$  bosons (the mediators of the weak force), the gluon ( $g$ , the mediator of the  
 584 strong force), and the photon ( $\gamma$ ), the mediator of the electromagnetic force. Finally, there is the Higgs  
 585 boson, a fundamental spin-0 particle resulting from the Higgs mechanism of electroweak symmetry  
 586 breaking. Figure 1.1 summarizes the fermions and bosons of the SM.

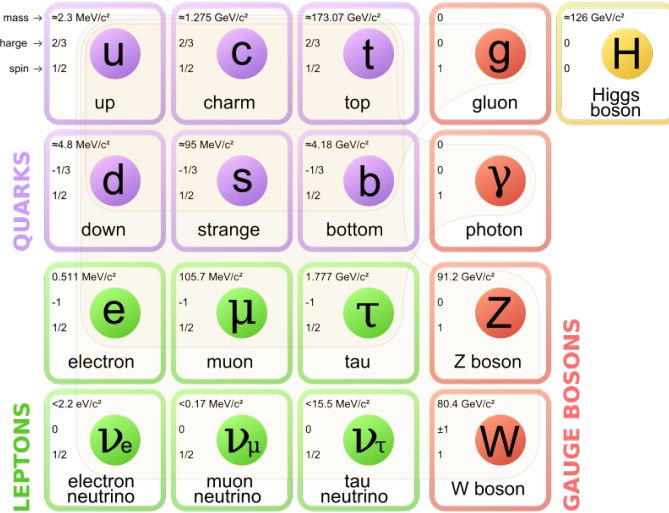


Figure 1.1: The particles of the Standard Model and their properties [6].

587 The Standard Model coalesced into a unified theoretical framework in the 1960s through the work  
 588 of Glashow, Weinberg, Salam, and others on the theory of electroweak interactions [9–12]. This theory  
 589 characterized both the electromagnetic and weak interactions as unified under a single gauge symmetry  
 590 group, namely  $SU(2) \times U(1)$ . At low enough energy scales (on the order of the  $W$  and  $Z$  masses,  
 591 the electroweak symmetry is broken, as evidenced by the fact that the weak bosons have mass while the

592 photon does not. The discovery of the Higgs boson in 2012 confirmed the Higgs mechanism as the most  
 593 likely candidate for this electroweak symmetry breaking [1, 2]. The electroweak theory is then combined  
 594 with the theory of quantum chromodynamics (which models the strong sector as a non-Abelian  $SU(3)$   
 595 gauge group) to form the complete SM [13].

## 596 1.2 ELECTROWEAK SYMMETRY BREAKING AND THE HIGGS

597 In the Standard Model Lagrangian, it is difficult to include mass terms for the  $W$  and  $Z$  bosons without  
 598 breaking the fundamental gauge symmetry of the Lagrangian. A traditional mass term does not preserve  
 599 the  $SU(2) \times U(1)$  symmetry. Additionally, scattering of massive  $W$  and  $Z$  bosons violate unitarity  
 600 and these diagrams diverge at high energy scales. In the 1960s, Higgs, Brout, Englert, Guralnik, Kibble,  
 601 and Hagen developed a mechanism for spontaneous symmetry breaking via the addition of a complex  
 602 scalar doublet to the SM. Three of the four real degrees of freedom of this complex field would go to the  
 603 longitudinal modes of the  $W^\pm$  and  $Z$ , thus allowing them to have mass [14–17]. The remaining degree  
 604 of freedom would manifest as an additional scalar, known now as the Higgs boson.

605 The mechanism works by introducing a Lagrangian for the newly introduced field that still respects  
 606 the symmetry of the Standard Model inherently, but with a minimum at a non-zero vacuum expectation  
 607 value for the field. In this minimum of the potential, the electroweak symmetry is broken. Specifically,  
 608 consider a complex scalar doublet  $\Phi$  with four degrees of freedom, as shown in equation 1.1.

$$\Phi = \begin{pmatrix} \phi^+ \\ \phi^0 \end{pmatrix} = \frac{1}{\sqrt{2}} \begin{pmatrix} \phi_1^+ + i\phi_2^+ \\ \phi_1^0 + i\phi_2^0 \end{pmatrix} \quad (1.1)$$

609 The minimal potential of a self-interacting Higgs that still respects the SM symmetry is given in equa-  
 610 tion 1.2.

$$V(\Phi) = \mu^2 \Phi^\dagger \Phi + \lambda (\Phi^\dagger \Phi)^2 \quad (1.2)$$

611 If the  $\mu^2$  term of this potential is positive, then the potential has a minimum at  $\Phi = 0$  and the SM

<sup>612</sup> symmetry is preserved. However, if instead  $\mu^2 < 0$ , then the minimum is at a finite value of  $\Phi$ , namely

$$\Phi_{\min} = \frac{1}{\sqrt{2}} \begin{pmatrix} 0 \\ v \end{pmatrix} \quad (1.3)$$

<sup>613</sup> where  $v = \sqrt{\mu^2/\lambda}$ . Because this is the location of the minimum, it corresponds to the vacuum expecta-  
<sup>614</sup> tion value for the field ( $\langle \Phi \rangle = \Phi_{\min}$ ). The excitations of the Higgs can then be parameterized as

$$\Phi = \frac{1}{\sqrt{2}} \begin{pmatrix} 0 \\ v + H \end{pmatrix} \quad (1.4)$$

<sup>615</sup> The full scalar Lagrangian, including the kinetic term, is then given as

$$\mathcal{L}_s = (D^\mu \Phi)^\dagger (D_\mu \Phi) - V(\Phi) \quad (1.5)$$

<sup>616</sup> where the covariant derivative is defined as

$$D_\mu = \partial_\mu + \frac{ig}{2} \tau^a W_\mu^a + ig' Y B_\mu \quad (1.6)$$

<sup>617</sup> and  $W^1, W^2, W^3$  and  $B$  are the  $SU(2)$  and  $U(1)$  gauge fields of the electroweak theory, respectively.  $g$   
<sup>618</sup> and  $g'$  are the corresponding coupling constants. With the scalar Lagrangian in place, the physical gauge  
<sup>619</sup> fields can then be written as

$$W_\mu^\pm = \frac{1}{\sqrt{2}} (W_\mu^1 \mp i W_\mu^2) \quad (1.7)$$

<sup>620</sup>

$$Z_\mu = \frac{-g'B_\mu + gW_\mu^3}{\sqrt{g^2 + g'^2}} \quad (1.8)$$

<sup>621</sup>

$$A_\mu = \frac{gB_\mu + g'W_\mu^3}{\sqrt{g^2 + g'^2}} \quad (1.9)$$

<sup>622</sup> Equation 1.7 corresponds to the charged  $W^+$  and  $W^-$  bosons, equation 1.8 corresponds to the neutral

623  $Z$  boson, and equation 1.9 corresponds to the neutral photon. The masses of the particles also arise from  
 624 the Lagrangian. The photon has zero mass, while the masses of the  $W$  and  $Z$  bosons are given in equa-  
 625 tion 1.10.

$$\begin{aligned} M_W^2 &= \frac{1}{4}g^2v^2 \\ M_Z^2 &= \frac{1}{4}(g^2 + g'^2)v^2 \end{aligned} \quad (1.10)$$

626 The fermion masses also arise through a coupling with the Higgs via the Yukawa interaction (for a de-  
 627 tailed description, see [8]). In this case the coupling between the Higgs and the fermions goes as

$$g_{Hf\bar{f}} = \frac{m_f}{v} \quad (1.11)$$

628 The full Lagrangian of Higgs interactions can be written as

$$\mathcal{L}_{\text{Higgs}} = -g_{Hf\bar{f}}\bar{f}fH + \frac{g_{HHH}}{6}H^3 + \frac{g_{HHHH}}{24}H^4 + \delta_V V_\mu V^\mu \left( g_{HVV}H + \frac{g_{HHVV}}{2}H^2 \right) \quad (1.12)$$

629 with

$$\begin{aligned} g_{HVV} &= \frac{2m_V^2}{v} & g_{HHVV} &= \frac{2m_V^2}{v^2} \\ g_{HHH} &= \frac{3m_H^2}{v} & g_{HHHH} &= \frac{3m_H^2}{v^2} \end{aligned} \quad (1.13)$$

630 Here,  $V$  refers to the  $W^\pm$  and  $Z$ , and  $\delta_W = 1$  while  $\delta_Z = 1/2$ . Phenomenologically, there are a few  
 631 features of this Lagrangian that are useful to note. First, note that the Higgs mass is a free parameter  
 632 of the theory that must be determined experimentally. Second, note that the coupling of the Higgs to  
 633 the vector bosons and fermions scales with the masses of these particles, a fact that is important when  
 634 considering both the production and decays of the particle. Also note that the branching ratio of the  
 635 Higgs to  $W$  bosons will be twice that of the branching ratio to  $Z$  if the Higgs mass is large enough to  
 636 produce the particles on shell because of the extra symmetry factor associated with the  $W$  coupling.  
 637 Finally, note the presence of the cubic and quartic Higgs self interaction terms, which can lead to final  
 638 states with multiple Higgs bosons produced.

639 1.3 HIGGS BOSON PRODUCTION AND DECAY

640 This section discusses the properties of Higgs production and decay mechanisms. The details presented  
641 here will focus on the properties of a 125 GeV Higgs boson, as this is the mass closest to that of the  
642 newly discovered Higgs.

643 1.3.1 HIGGS PRODUCTION

644 The Higgs is produced by four main production modes at the Large Hadron Collider - gluon-gluon  
645 fusion (ggF), vector boson fusion (VBF), associated production with a  $W$  or  $Z$  boson, or associated  
646 production with top quarks ( $t\bar{t}H$ ). Figure 1.2 shows the Feynman diagrams for these four modes.

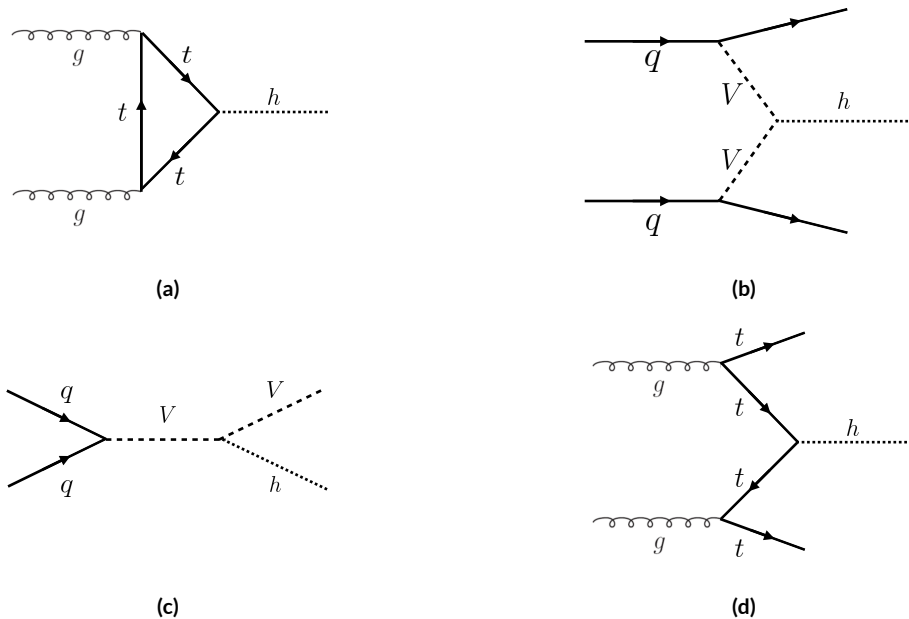
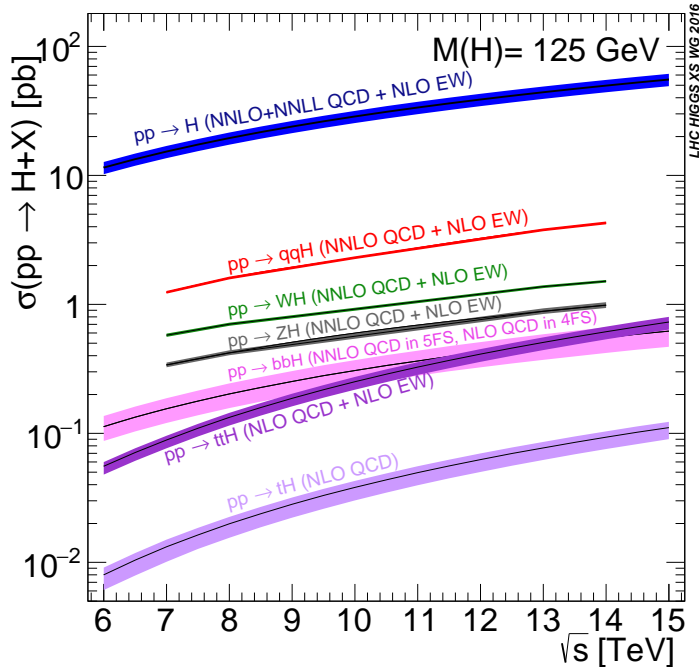


Figure 1.2: The four most common Higgs boson production modes at the LHC: (a) gluon-gluon fusion, (b) vector boson fusion, (c)  $W/Z + H$  production, (d)  $t\bar{t}H$  production

647 In gluon-gluon fusion, gluons from the incoming protons fuse via a top-quark loop to produce a  
648 Higgs. The top quark is the dominant contribution in the loop due to its heavy mass and the fact that  
649 the Higgs-fermion coupling constant scales with fermion mass. In vector boson fusion, the incoming  
650 quarks each radiate a  $W$  or  $Z$  boson which fuse to produce the Higgs. This production mode results in  
651 a final state with a Higgs boson and two additional jets which tend to be forward because they carry the

652 longitudinal momentum of the incoming partons. The Higgs can also be produced in association with a  
 653  $W$  or  $Z$  boson. The  $W/Z$  is produced normally and then radiates a Higgs (this mode is also sometimes  
 654 known as “Higgs-strahlung”). Finally, the Higgs can be produced in association with two top quarks.  
 655 Each incoming gluon splits into a  $t\bar{t}$  pair, and one of the top pairs combines to create a Higgs. Figure 1.3  
 656 shows the production cross section for a 125 GeV Higgs boson in each of these modes at a  $pp$  collider as  
 657 a function of center of mass energy.



**Figure 1.3:** Higgs production cross sections as a function of center of mass energy ( $\sqrt{s}$ ) at a  $pp$  collider [18].

658 In figure 1.3, note that gluon fusion has the largest cross section, while VBF is the second largest at  
 659 approximately a factor of 10 smaller. The figure also includes the less commonly studied  $b\bar{b}H$  and  $tH$   
 660 modes. The  $b\bar{b}H$  and  $tH$  modes are not studied as commonly as  $t\bar{t}H$  due to the larger background con-  
 661 tributions and lower cross sections, respectively. At  $\sqrt{s} = 8$  TeV, ggF production of a 125 GeV Higgs  
 662 has a cross section of 19.47 pb, while VBF has a cross section of 1.601 pb [18]. The cross sections of all  
 663 of the main Higgs production modes at this center of mass energy, as well as their uncertainties from  
 664 varying the renormalization and factorization scales and PDFs, are summarized in table 1.1 for a 125 GeV  
 665 Higgs.

Production mode	$\sigma$ ( pb)	QCD scale uncert. (%)	PDF + $\alpha_s$ uncert. (%)
Gluon fusion	19.47	+7.3 / - 8.0	3.1
Vector boson fusion	1.601	+0.3 / - 0.2	2.2
$WH$	0.7026	+0.6 / - 0.9	2.0
$ZH$	0.4208	+2.9 / - 2.4	1.7
$t\bar{t}H$	0.1330	+4.1 / - 9.2	4.3
$b\bar{b}H$	0.2021	+20.7 / - 22.3	
$tH$ ( $t$ -channel)	0.01869	+7.3 / - 16.5	4.6
$tH$ ( $s$ -channel)	$1.214 \times 10^{-3}$	+2.8 / - 2.4	2.8

**Table 1.1:** Production cross sections for a 125 GeV Higgs boson at  $\sqrt{s} = 8$  TeV with scale and PDF uncertainties [18].

### 666 1.3.2 HIGGS BRANCHING RATIOS

667 The fact that the Higgs couples more strongly to more massive particles is crucial for understanding its  
 668 branching ratios. The width for Higgs decays to fermions is given in equation 1.14 [5].

$$\Gamma(H \rightarrow f\bar{f}) = \frac{N_c \sqrt{2} G_F m_f^2 m_H}{8\pi} \quad (1.14)$$

669 In this case,  $N_c$  is the number of colors,  $G_F$  is the Fermi constant,  $m_f$  is the mass of the fermion, and  
 670  $m_H$  is the mass of the Higgs. Note that the width scales with the square of the fermion mass. (This also  
 671 assumes that the Higgs mass is large enough to decay with both the fermions on shell.)

672 The decay width to  $WW$  is given in equation 1.15 [5].

$$\Gamma(H \rightarrow W^+W^-) = \frac{\sqrt{2} G_F M_W^2 m_H}{16\pi} \frac{\sqrt{1-x_W}}{x_W} (3x_W^2 - 4x_W + 4) \quad (1.15)$$

673 where  $m_W$  is the mass of the  $W$  and  $x_W = 4M_W^2/m_H^2$ . To get the branching ratio to  $ZZ$ , the equa-  
 674 tion is divided by 2 to account for identical particles in the final state, and  $x_W$  is replaced with  $x_Z =$   
 675  $4M_Z^2/m_H^2$ . This is shown in equation 1.16 [5].

$$\Gamma(H \rightarrow ZZ) = \frac{\sqrt{2} G_F M_Z^2 m_H}{32\pi} \frac{\sqrt{1-x_Z}}{x_Z} (3x_Z^2 - 4x_Z + 4) \quad (1.16)$$

676 These formulas can also be visualized as a function of Higgs mass. Figure 1.4 shows the branching ratios  
 as a function of the Higgs mass. There are a few interesting features to note in this figure. First, note that

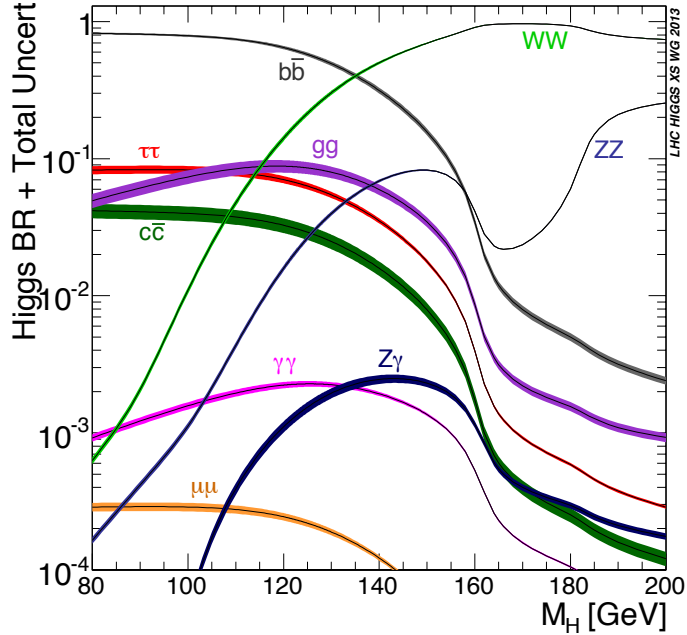


Figure 1.4: Higgs boson branching ratios as a function of  $m_H$  [18].

677  
 678 at high Higgs masses, once on-shell production of both  $W$  and  $Z$  bosons is possible, these two decays  
 679 are the dominant ones due to the large masses of the  $W/Z$ . Also note that the branching ratio to  $W$ s  
 680 is twice that of  $Z$ s at these large masses due to the  $\delta_V$  symmetry factor noted previously. At 125 GeV,  
 681 the Higgs is accessible through many different decay modes. The largest branching ratio is the decay  
 682  $H \rightarrow b\bar{b}$  at 58.24% [18]. This branching is larger than the  $WW/ZZ$  decays because one of the two  
 683 bosons must be produced off-shell for  $m_H = 125$  GeV. The second largest branching ratio is to  $WW^*$   
 684 at 21.37 % (before taking into account the branching ratios of the  $W$ ). Table 1.2 summarizes the branch-  
 685 ing ratios for a 125 GeV Higgs. Note that there is in fact a Higgs branching ratio to  $\gamma\gamma$  even though  
 686 photons are massless. This decay happens through a loop (the largest contributions to the loop are top  
 687 and  $W$ ) which suppresses the branching ratio.

688 Note that the branching ratios alone do not tell the full story of which Higgs channels are the most  
 689 sensitive. For example, a  $H \rightarrow b\bar{b}$  search in gluon fusion production is incredibly difficult due to the

Decay	Branching ratio (%)
$b\bar{b}$	58.24
$WW^*$	21.37
$gg$	8.187
$\tau\tau$	6.272
$c\bar{c}$	2.891
$ZZ^*$	2.619
$\gamma\gamma$	0.2270
$Z\gamma$	0.1533
$\mu\mu$	0.02176

Table 1.2: Branching ratios for a 125 GeV Higgs boson [18].

large QCD dijet background at the LHC. However, in associated production of the Higgs, where a  $W$  or  $Z$  gives additional final state particles that can be used to reduce background, a search for  $H \rightarrow b\bar{b}$  can be sensitive. The combinations of production and decay modes that are most commonly studied are summarized in table 1.3 [5].

Decay	Inclusive (incl. ggF)	VBF	$WH/ZH$	$t\bar{t}H$
$H \rightarrow \gamma\gamma$	✓	✓	✓	✓
$H \rightarrow b\bar{b}$			✓	✓
$H \rightarrow \tau^+\tau^-$		✓		
$H \rightarrow WW^* \rightarrow \ell\nu\ell\nu$	✓	✓	✓	
$H \rightarrow ZZ \rightarrow 4\ell$	✓			
$H \rightarrow Z\gamma \rightarrow \ell\ell\gamma$	very low			

Table 1.3: Possible channels for Higgs searches. Checkmarks denote the most sensitive production modes [5].

#### 1.4 HIGGS PAIR PRODUCTION IN THE STANDARD MODEL

The Standard Model also allows for processes that produce two Higgs bosons in the final state, known as Higgs pair production or di-Higgs production. The two main production mechanisms are shown in figure 1.5. The two diagrams in figure 1.5 interfere destructively with one another, resulting in a low overall cross section for di-Higgs production at the LHC. Nevertheless, Higgs pair production is quite interesting to study because it gives direct access to the  $\lambda$  parameter of the Higgs potential, also known as the Higgs self coupling. The diagram in figure 1.5(b) is sensitive to this coupling through the triple Higgs

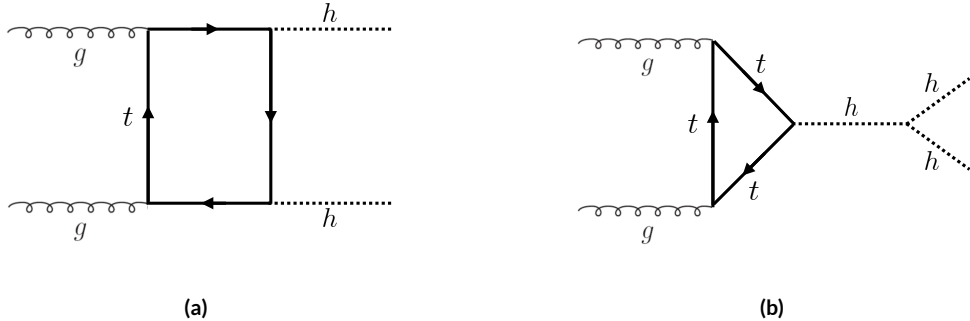


**Figure 1.5:** The two leading diagrams for Standard Model di-Higgs production at the LHC: (a) box diagram, (b) Higgs self coupling

701 vertex.

702 One can substitute the gluon fusion production of diagram 1.5(b) with any of the other production  
 703 modes previously discussed. These other modes do not suffer from interference with the box diagram  
 704 in figure 1.5(a) due to the presence of additional particles in the final state. They still have a lower cross  
 705 section than the gluon fusion mode, however. The cross sections for di-Higgs production in the differ-  
 706 ent modes, as well as their uncertainties, are shown in table 1.4 [19]. These are shown for  $\sqrt{s} = 14$  TeV  
 707 as the higher center of mass energy is more sensitive to this process. Note that the scale of cross section  
 quoted is now in fb rather than pb.

Production mode	$\sigma$ (fb)	Total uncert. (%)
Gluon fusion	33.89	+37.2 / - 27.8
Vector boson fusion	2.01	+7.6 / - 5.1
$W H H$	0.57	+3.7 / - 3.3
$Z H H$	0.42	+7.0 / - 5.5
$t\bar{t}H$	1.02	-

**Table 1.4:** Production cross sections for pair production of a 125 GeV Higgs boson at  $\sqrt{s} = 14$  TeV with total uncertainty [19]. The uncertainties include QCD scale and PDF variations as well as uncertainties on  $\alpha_S$ .

708

## 709 1.5 HIGGS PAIR PRODUCTION IN THEORIES BEYOND THE STANDARD MODEL

710 The Standard Model Higgs pair production cross section is rather small, and datasets on the scale of the  
 711 full lifetime of the LHC will be required to obtain sensitive measurements of the Higgs self-coupling.

712 However, the discovery of the Higgs also gives particle physicists a new tool that can be exploited in the  
 713 search for new physics beyond the Standard Model. In particular, Higgs pair production is a promising  
 714 channel in the search for new physics. The cross section for di-Higgs production can be altered through  
 715 both resonant and non-resonant production of Higgs pairs. In non-resonant production, di-Higgs pro-  
 716 duction vertices can arise from the presence of a new strong sector and additional colored particles [20–  
 717 22]. Figure 1.6 shows examples of the types of vertices that can arise. In the resonant case, new heavy par-  
 718 ticle can decay to Higgs pairs. Such new particles can include heavy Higgs bosons arising in two Higgs  
 719 doublet models (2HDM) or Higgs portal models as well as heavy gravitons in Randall-Sundrum theo-  
 720 ries [20, 23–29]. Figure 1.7 shows a generic diagram for a heavy resonance decaying to two Higgs bosons.  
 721 In the 2HDM,  $X$  corresponds to the heavy CP-even scalar  $H$ . In the Randall-Sundrum model,  $X$  cor-  
 722 responds to a heavy spin-2 graviton  $G$ . The next sections provide more detail on the phenomenology of

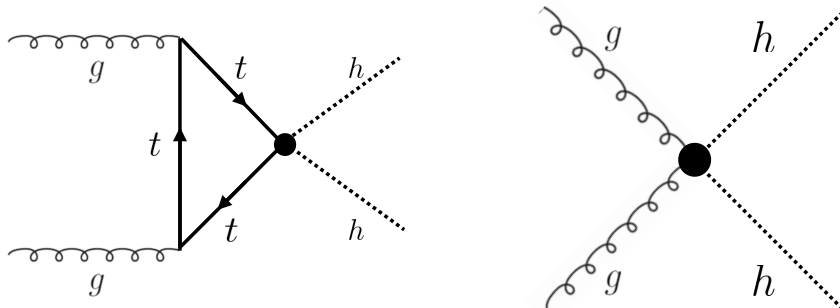


**Figure 1.6:** Diagrams with new vertices for non-resonant Higgs pair production arising in composite Higgs models

722  
 723 resonant Higgs production in Randall-Sundrum and 2HDM models, as these models will later be tested  
 724 in a dedicated search for resonant production of boosted Higgs pairs.

### 725 1.5.1 RANDALL-SUNDRUM GRAVITONS

726 The Randall-Sundrum model is a proposed solution to the hierarchy problem that posits a five-dimensional  
 727 warped spacetime that contains two branes: one where the force of gravity is very strong and a second  
 728 brane at the TeV scale corresponding to the known Standard Model sector [23]. In the theory, the  
 729 branes are weakly coupled and the graviton probability function drops exponentially going from the  
 730 gravity brane to the SM brane, rendering gravity weak on the SM brane. The experimental consequence

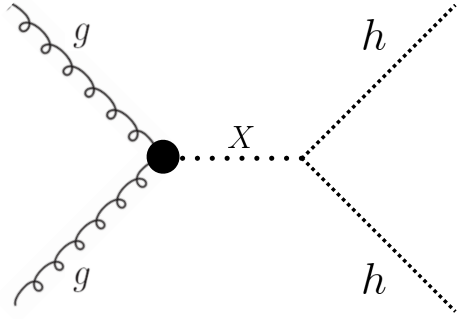


**Figure 1.7:** Generic Feynman diagram for resonant Higgs pair production in BSM theories

of this theory is a tower of widely spaced (in mass) Kaluza-Klein graviton resonances. In theories where the fermions are localized to the SM brane, production of gravitons from fermion pairs is suppressed and the primary mode of production is gluon fusion [24]. These gravitons have a substantial branching fraction to Higgs pairs, ranging from 6.43% for gravitons with a mass of 500 GeV to 7.66% at 3 TeV. Figure 1.8 shows the branching ratios of the spin-2 Randall Sundrum graviton (RSG) as a function of its mass. The predominant decays are to  $t\bar{t}$  above the mass threshold for that channel.

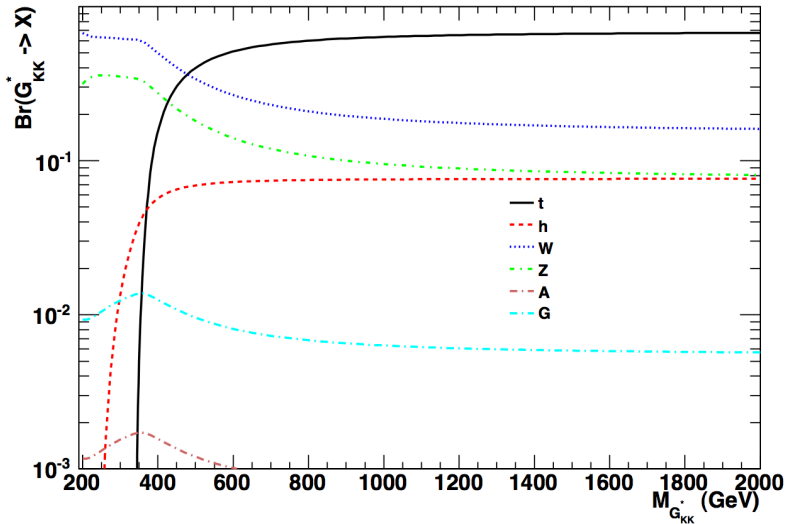


**Figure 1.8:** Branching ratios for a spin-2 Randall-Sundrum graviton as a function of mass computed in MadGraph with the CP3-Origins implementation [24, 30]

These models have two free parameters - the mass of the graviton and a curvature parameter  $k$ . Typically, rather than  $k$ , the theory is parameterized using  $c \equiv k/\bar{M}_{\text{pl}}$ , where  $\bar{M}_{\text{pl}}$  is the reduced Planck

739 mass. The cross section for production of the RSG decreases as a function of mass and is strongly depen-  
 740 dent on the gluon PDF. The increase in center of mass energy from 8 to 13 TeV in LHC Run 2 greatly  
 741 increases the cross section at higher mass. Figure 1.9 shows the cross section as a function of graviton  
 742 mass at  $\sqrt{s} = 13$  TeV for RSG models with  $c = 1.0$  and  $c = 2.0$ .

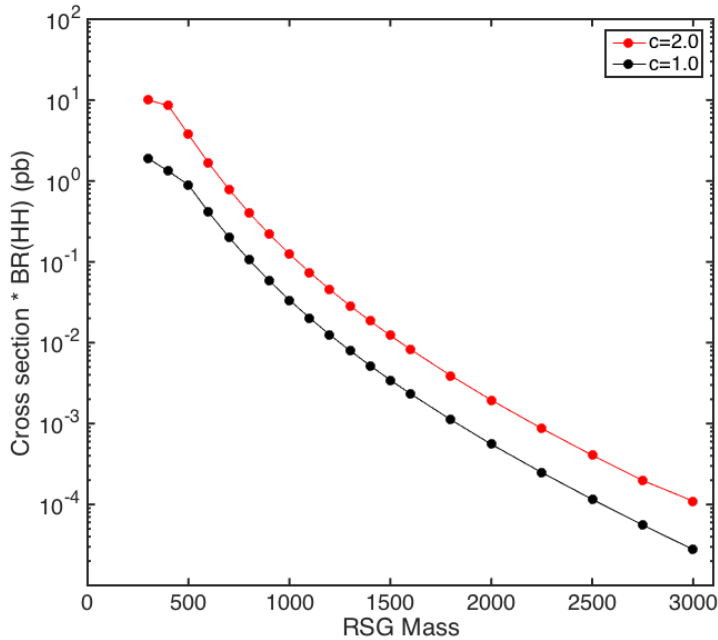


**Figure 1.9:**  $\sigma \times \text{BR}(HH)$  for RSG as a function of mass computed in MadGraph with the CP3-Origins implementation [24, 30]

743 Another interesting feature of the theory is that the width of the graviton increases with both  $c$  and  
 744  $m_G$ . Figure 1.10 shows the graviton width for both  $c = 1.0$  and  $c = 2.0$  as a function of mass. In  
 745  $c = 1.0$ , the width starts at 8.365 GeV for a mass of 300 GeV and increases to 187.2 GeV at a mass of  
 746 3 TeV. Similarly, with  $c = 2.0$ , the width starts at 33.46 GeV for  $m_G = 300$  GeV and increases to  
 747 748.8 GeV at a mass of 3 TeV.

### 748 1.5.2 TWO HIGGS DOUBLET MODELS

749 In Two Higgs Doublet Models (2HDM), a second complex scalar doublet is added to SM [26–28]. In  
 750 this case, all four degrees of freedom in the second doublet correspond to new particles, meaning that

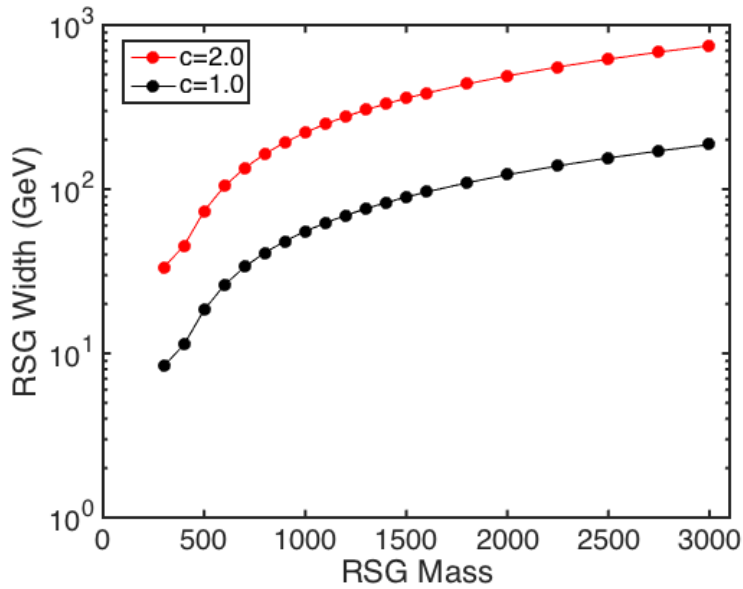


**Figure 1.10:** RSG width as a function of mass computed in MadGraph with the CP3-Origins implementation [24, 30]

there are five total scalars from the two Higgs doublets -  $h$  (light CP-even Higgs),  $H$  (heavy CP-even Higgs),  $A$  (heavy CP-odd Higgs), and  $H^\pm$  (charged Higgs). The model is parameterized by two main parameters. The first,  $\tan \beta \equiv \frac{v_2}{v_1}$ , is the ratio of the vacuum expectation values of the two Higgs doublets (where  $v_1$  corresponds to the  $v$  in the SM Higgs model described above). The second parameter is  $\alpha$ , a mixing angle between the heavy and light Higgs fields. Models are also often parameterized with  $\cos(\beta - \alpha)$  rather than  $\alpha$  directly. The limit where  $\cos(\beta - \alpha) = 0$  is called the alignment limit, and it is in this limit that the light Higgs  $h$  has the same couplings as a Standard Model Higgs.

2HDM models are usually separated into two main types - Type I and Type II. In Type I models, the charged fermions only couple to the second Higgs doublet, leading to a fermiophobic light Higgs. In Type II models, up-type quarks couple to the first doublet while down-type quarks couple to the second doublet. One specific realization of a Type II 2HDM is the Minimal Supersymmetric Standard Model (MSSM).

Resonant di-Higgs production in this model can proceed through decays of the heavy CP-even Higgs  $H \rightarrow hh$ . The branching ratio for  $H \rightarrow hh$  depends on the model type as well as the values of  $\tan \beta$  and  $\cos \beta - \alpha$ . Figure 1.11 shows the branching ratios as a function of the mass of the heavy scalar  $H$  for

766 both Type I and Type II models. Depending on the type of model  $hh$  can be a substantial fraction of the  
 767 decays of  $H$ .

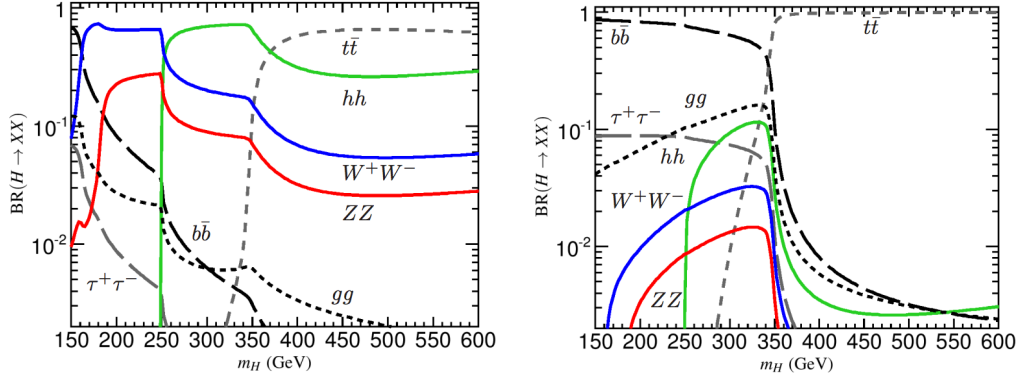


**Figure 1.11:** Branching ratios for heavy Higgs  $H$  in Type I (left) and Type II (right) 2HDM models with  $\tan \beta = 1.5$  and  $\cos(\beta - \alpha) = 0.1(0.01)$  for Type I (Type II). [28]

## 768 1.6 CONCLUSION

769 Studying the Higgs sector is essential for understanding the details of how mass arises in the Standard  
 770 Model and how the electroweak symmetry is broken. The discovery of the Higgs boson also opens the  
 771 door for its use as a tool to search for new physics, and Higgs pair production is an ideal candidate for  
 772 this study. Even if no BSM physics is found in Higgs pair production, searches for Higgs pairs will put  
 773 constraints on the Higgs self coupling and thus further knowledge of the Standard Model and the details  
 774 of the Higgs potential.

*The enthusiasm and motivation to explore particle physics at the high-energy frontier knows no borders between the nations and regions of the planet.*

Peter Jenni

# 2

775

776

777

## The ATLAS detector and the Large Hadron Collider

778 This chapter presents an overview of the experimental systems used to conduct the measurements pre-  
779 sented in this thesis. First, a brief overview of the accelerator, the Large Hadron Collider, will be given.  
780 In this section, the accelerator conditions relevant to data-taking are presented as well. Next, an overview  
781 of the ATLAS experiment is given. The basics of each sub-detector's role are summarized, as well as the  
782 details of the datasets accumulated. Then, a brief interlude on the ATLAS Muon New Small Wheel up-  
783 grade is presented. While this new detector does not have a direct impact on any of the datasets taken  
784 so far, it will have an impact on future analyses and the work done on it is briefly summarized here. Fi-  
785 nally, an overview of object reconstruction in ATLAS is given. While the details of all of the algorithms  
786 will not be presented in detail, aspects of the reconstruction performance such as object resolutions are  
787 shown as these are relevant to the two studies presented later in this thesis.

788 2.1 THE LARGE HADRON COLLIDER

789 The Large Hadron Collider (LHC) is a proton-proton collider at the CERN laboratory in Geneva,  
790 Switzerland [31]. It is designed for a maximum collision center of mass energy of  $\sqrt{s} = 14 \text{ TeV}$  and  
791 has a circumference of 26.7 kilometers. Four main experiments are located at the interaction points (IP)  
792 of the accelerator: ATLAS (A Toroidal LHC ApparatuS), CMS (the Compact Muon Solenoid), AL-  
793 ICE (A Large Ion Collider Experiment), and LHCb [32–35]. The studies performed in this thesis were  
794 all completed with the ATLAS detector. Figure 2.1 shows a schematic of the LHC ring and the various  
795 experiments.

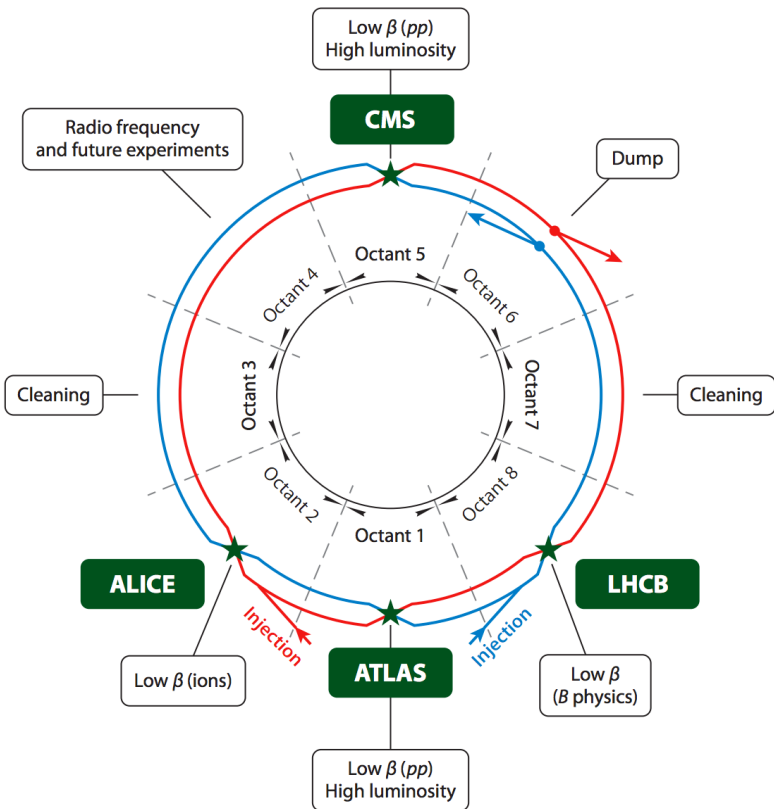


Figure 2.1: A schematic view of the LHC ring [36]

796 One of the most interesting features of the LHC is in its magnet design. Because the tunnel does not  
797 have room for separate superconducting magnets for each of the beam pipes, the LHC employs a twin-  
798 bore magnet design. Each magnet must hold an 8.3 Tesla magnetic field in order to bend the proton

799 beams at  $\sqrt{s} = 14$  TeV. The superconducting magnets are cooled to a temperature of 1.9 Kelvin with  
800 superfluid helium.

801 2.1.1 INSTANTANEOUS LUMINOSITY

802 The rate of physics events expected from the accelerator is dependent on the instantaneous luminosity  
803 of the machine and the cross section of the physics process,  $R_{\text{events}} = L\sigma$ . Here,  $R_{\text{events}}$  is the number  
804 of events per second,  $L$  is the instantaneous luminosity of the machine, and  $\sigma$  is the cross section for the  
805 physics process being measured. The instantaneous luminosity of the LHC is determined by numerous  
806 factors related to machine conditions. Equation 2.1 gives the equation for instantaneous luminosity of  
807 Gaussian beam profile [36].

$$L = \frac{N_b^2 n_b f_{\text{rev}} \gamma_r}{4\pi \epsilon_n \beta^*} F \quad (2.1)$$

808 The LHC collides protons in bunches, and in the above equation  $N_b$  is the number of protons per  
809 bunch while  $n_b$  is the number of bunches per beam. Nominally, the LHC can hold up to 2808 pro-  
810 ton bunches.  $f_{\text{rev}}$  is the revolution frequency.  $\epsilon_n$  is the normalized transverse beam emittance, a mea-  
811 surement of the average spread of the particles position-momentum space which has the dimension of  
812 length.  $\beta^*$  is the value of the *beta* function for the beam at the interaction point. It relates the emittance  
813 to the Gaussian width of the beam with  $\sigma_{\text{beam}} = \sqrt{\epsilon \cdot \beta}$ .  $F$  is a reduction factor that corrects for the  
814 fact that the beams are colliding at an angle at the IP.

815 Another way of writing the instantaneous luminosity is shown in equation 2.2. In this case, the in-  
816 stantaneous luminosity is written as the ratio of the rate of inelastic collisions with the inelastic cross  
817 section [37].

$$L = \frac{R_{\text{inel}}}{\sigma_{\text{inel}}} = \frac{\mu n_b f_{\text{rev}}}{\sigma_{\text{inel}}} \quad (2.2)$$

818 In this case,  $\mu$  is the average number of interactions per bunch crossing in the accelerator.  $\mu$  is a useful  
819 parameter for characterizing the amount of activity recorded in an experiment. As the instantaneous  
820 luminosity and thus  $\mu$  increase, there are more interactions per bunch crossing and more activity in the  
821 detector. This is often characterized with  $\langle \mu \rangle$ , the measured per bunch crossing  $\mu$  value averaged over

822 all bunch crossings. The interactions inside each bunch crossing that are not the main physics process of  
 823 interest are often referred to as “pileup” interactions, and  $\langle \mu \rangle$  is a measurement of the level of pileup in  
 824 the detector.

825 **2.1.2 EVOLUTION OF MACHINE CONDITIONS**

826 This thesis uses datasets taken at three different center of mass energies:  $\sqrt{s} = 7\text{ TeV}$  data taken in  
 827 the year 2011,  $\sqrt{s} = 8\text{ TeV}$  data taken in the year 2012, and  $\sqrt{s} = 13\text{ TeV}$  data taken in the year  
 828 2015. In addition to increasing center of mass energy, the instantaneous luminosity and parameters that  
 829 determine it were evolving. Table 2.1 summarizes that machine conditions in each of these datasets.

	2011	2012	2015	Design
$\sqrt{s} [\text{TeV}]$	7	8	13	14
Number of bunches	1380	1380	1825	2808
Max. protons per bunch	$1.45 \times 10^{11}$	$1.7 \times 10^{11}$		$1.15 \times 10^{11}$
Bunch spacing [ns]	50	50	25	25
Max. instantaneous luminosity [ $\text{cm}^{-2}\text{s}^{-1}$ ]	$3.7 \times 10^{33}$	$7.7 \times 10^{33}$	$5 \times 10^{33}$	$10^{34}$
$\beta^* [\text{m}]$	1.0	0.6	0.8	0.55
$\langle \mu \rangle$	11.6	20.7	13.7	-

Table 2.1: Evolution of LHC machine conditions [38, 39]

830 **2.2 THE ATLAS DETECTOR**

831 The ATLAS detector is a multi-purpose particle detector experiment at the LHC’s Point 1 [32]. It has  
 832 nearly  $4\pi$  coverage in solid angle around the interaction point. It consists of an inner detector for mea-  
 833 suring charged particles, electromagnetic and hadronic calorimeters, and a muon spectrometer. Fig-  
 834 ure 2.2 gives an overview of the detector.

835 **2.2.1 COORDINATE SYSTEM**

836 Before defining the properties of the individual detectors, it is important to establish the coordinate  
 837 system used. Figure 2.3 shows a schematic of the coordinate system. The azimuthal plane (perpendicular

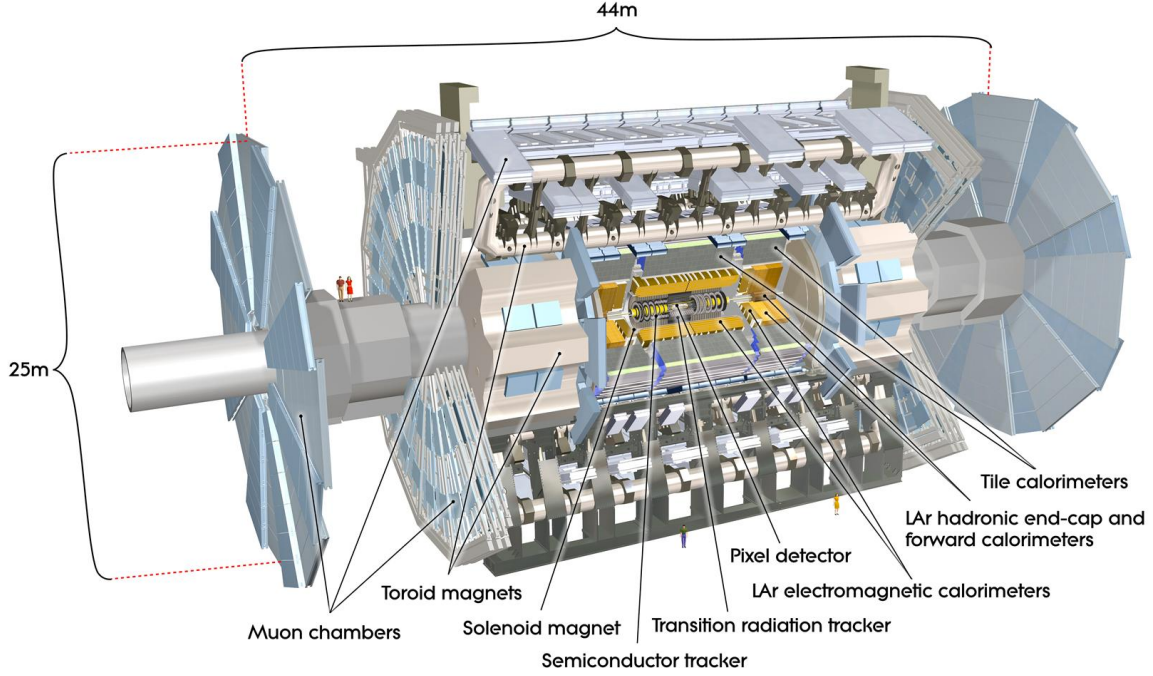
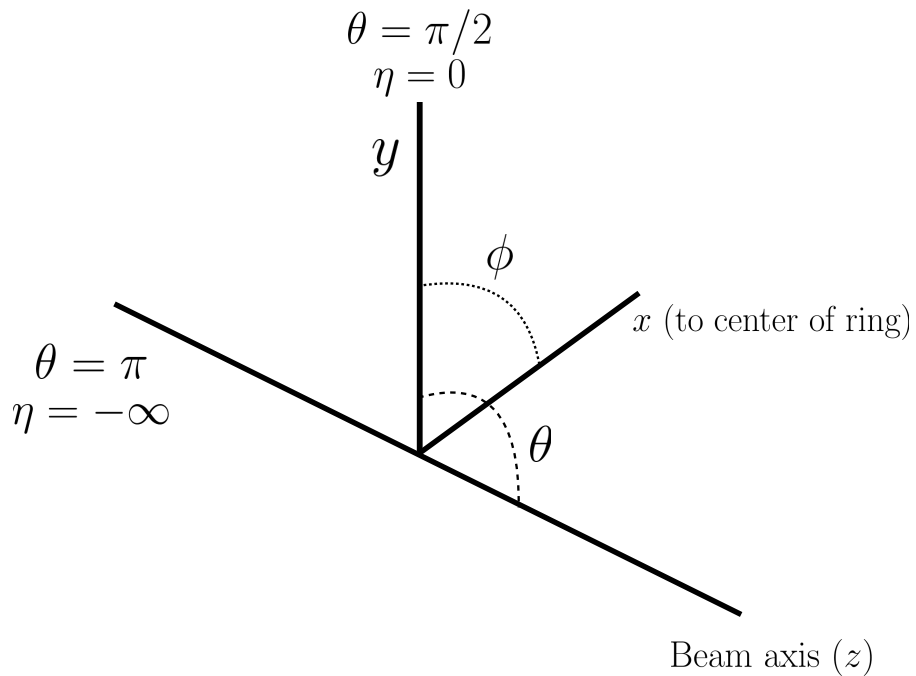


Figure 2.2: A full diagram of the ATLAS detector [32]

838 to the beam line) is defined as the  $x$ - $y$  plane. The angle in this plane is referred to as  $\phi$ . The angle relative  
 839 to the beam axis is referred to as  $\theta$ . Rather than using  $\theta$  directly as a coordinate, the experiment often  
 840 uses the pseudorapidity  $\eta$ .  $\eta$  is defined in equation 2.3.

$$\eta = \ln \left( \tan \left( \frac{\theta}{2} \right) \right) \quad (2.3)$$

841 Pseudorapidity is the massless approximation of rapidity, the angle used to parameterize boosts in  
 842 special relativity. This is important for two reasons. First, it means that differences in  $\eta$  are Lorentz in-  
 843 variant. Second, particle production is roughly constant in pseudorapidity. Particles with  $\eta$  close to zero  
 844 are referred to as “central”, while those at high  $|\eta|$  are called “forward”. In general, two main detector  
 845 topologies can be seen in figure 2.2. There are “barrel” elements, which surround the beam line cylin-  
 846 drically and are in the central region of the detector. In the forward region, there are “endcap” regions  
 847 which are arranged as disks perpendicular to the beam line.



**Figure 2.3:** The ATLAS coordinate system

#### 848    2.2.2    INNER DETECTOR

849    The ATLAS Inner Detector (ID) system is built for precision tracking of charged particles. It covers the  
 850    range  $|\eta| < 2.5$ . In this range, approximately 1000 particles are generated every bunch crossing in the  
 851    detector. This requires having fine granularity to achieve the resolutions required for good momentum  
 852    measurement and vertex reconstruction.

853    The ID consists of three sub-components: the pixel detector, semiconductor tracker (SCT), and trans-  
 854    sition radiation tracker (TRT). It is surrounded by a solenoid providing a 2 T axial magnetic field which  
 855    bends particles in the transverse plane to allow for momentum measurement. Figure 2.4 shows the layout  
 856    of each of these components.

#### 857    PIXEL DETECTOR

858    The pixel detector is the first detector particles traverse after being generated in proton collisions and is  
 859    the most granular detector. Its operation is crucial for precision tracking and vertex reconstruction as

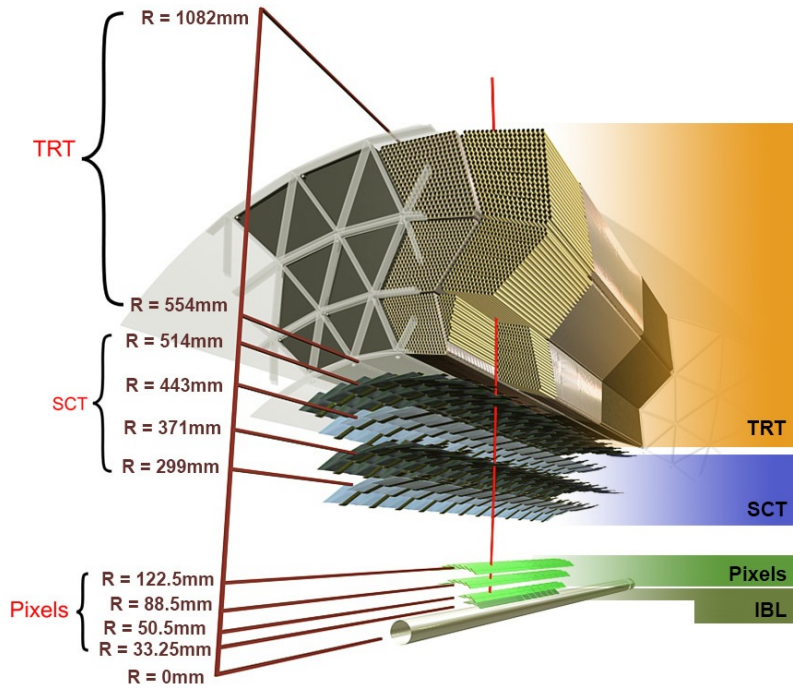


Figure 2.4: Layout of the ATLAS Inner Detector system [40]

well as higher level object reconstruction like tagging of jets from  $b$ -quarks. The basic sensing element in this subdetector is a silicon pixel detector. The operating principle for the silicon pixels is that of a  $p-n$  junction. When a charged particle passes through, it creates electron-hole pairs that are then separated by the electric field. The sensors are  $250 \mu\text{m}$  thick and use oxygenated  $n$ -type wafers with readout pixels on the  $n^+$  side of the detector [32]. Overall, the pixel detector has 1744 sensors and 80.4 million readout channels.

In the barrel region, the pixel detector has three concentric layers of sensors surrounding the beam-line. In the endcap region, it consists of disks perpendicular to the beam axis. The detector is segmented in the  $R-\phi$  plane and in  $z$ . Usually, three pixel layers are crossed by a charged particle track. The intrinsic accuracies of the sensors are  $10 \mu\text{m}$  in  $R-\phi$  and  $115 \mu\text{m}$  in  $z$  (or  $R$  for the endcap).

#### 870 INSERTABLE B-LAYER

871 In Run 2, a new innermost pixel layer, known as the insertable B-layer (IBL), was added to the Inner  
 872 Detector [41]. This layer was added to cope with the higher luminosities planned in LHC Run 2 and

873 at the high luminosity HL-LHC. Additionally it improves tracking position resolution which in turn  
874 improves the vertexing and  $b$ -tagging capabilities in ATLAS. The detector sits directly on a new beam  
875 pipe, only 33.25 mm away from the collision points in the azimuthal plane.

876 **SEMICONDUCTOR TRACKER (SCT)**

877 The semiconductor tracker (SCT) consists of silicon microstrips and comprises the next four layers of  
878 the ID. This sub-detector has 6.4cm long sensors that are daisy-chained into strips with a strip pitch  
879 of  $80\ \mu\text{m}$  [32]. Some of the strips have a small stereo angle to allow for measurement of both angular  
880 coordinates. In total there are 6.3 million readout channels. The intrinsic accuracies are  $17\ \mu\text{m}$  in  $R\phi$   
881 and  $580\ \mu\text{m}$  in  $z$  (or  $R$  in the endcap).

882 **TRANSITION RADIATION TRACKER (TRT)**

883 The transition radiation tracker (TRT) serves two purposes. First, it consists of 4mm diameter straw  
884 tubes filled with a 70/27/3% gas mixture of xenon, carbon dioxide, and oxygen to provide tracking of  
885 charged particles. Particles typically have 36 TRT straw tube hits per track. The material in between  
886 the straws is designed to induce transition radiation which can be useful for particle identification. As  
887 particles pass between media with different dielectric constants, they emit transition radiation that can  
888 cause additional showers in the TRT. In particular it is useful for discrimination between electrons and  
889 pions or other charged hadrons, as the amount of transition radiation is proportional to the Lorentz  
890 factor of the particle.

891 **2.2.3 CALORIMETERS**

892 The calorimeter system consists of two main sub-components: a fine granularity electromagnetic calorime-  
893 ter tailored for the measurement of photons and electrons and multiple coarser hadronic calorimeters  
894 dedicated to the measurement of hadronic showers [32]. The calorimeter system has broader cover-  
895 age than the inner detector, covering the region out to  $|\eta| < 4.9$ . It is also designed to deliver good  
896 containment of showers so as to limit leakage into the muon system. Figure 2.5 shows the layout of the  
897 calorimeter system.

898 Both the electromagnetic and hadronic calorimeters are sampling calorimeters. They alternate active  
 899 material for energy measurement with passive material for energy absorption. The materials used for  
 900 each purpose vary based on the type of calorimeter and its location in the detector.

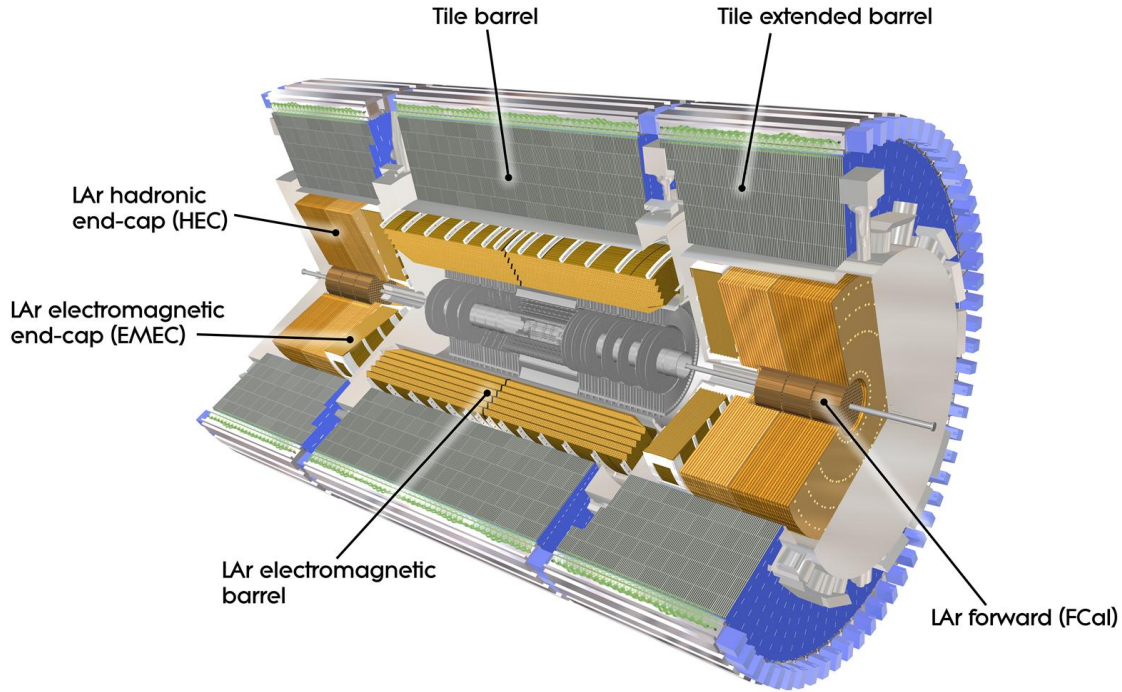


**Figure 2.5:** Layout of the ATLAS calorimeter system [32]

## 901 ELECTROMAGNETIC CALORIMETER

902 The electromagnetic calorimeter (EM calorimeter) use liquid Argon (LAr) as its active material and lead  
 903 as its passive material. It is arrange in an accordion geometry to increase the absorption area while still  
 904 allowing it to have no azimuthal cracks (complete symmetry in  $\phi$ ). The EM calorimeter is divided into a  
 905 barrel portion that extends to  $|\eta| < 1.475$  and an endcap portion going from  $1.375 < |\eta| < 3.2$ . The  
 906 region where these two units overlap is called the “transition region”.

907 In order to provide good containment the calorimeter depth must be optimized. Typically, for elec-  
 908 tromagnetic calorimeters the depth is measured in radiation lengths. In general, the intensity of a par-  
 909 ticle beam attenuates exponentially in distance with a constant equal to the radiation length. That is,

910  $I(x) = I_0 e^{-x/X_0}$ , where  $I$  is the intensity,  $x$  is the distance traveled, and  $X_0$  is the radiation length.

911 The ATLAS EM calorimeter is designed to have  $> 22$  radiation lengths in the barrel and  $> 24$  in the  
912 endcap [32].

913 **HADRONIC CALORIMETERS**

914 There are three types of hadronic calorimeters present in ATLAS: the tile calorimeter (TileCal), hadronic  
915 endcap (HEC), and forward calorimeter (FCal). Each one is optimized for stopping of hadronic showers  
916 and the materials chosen are specific to their placement in the detector.

917 The TileCal is a scintillating tile calorimeter placed directly outside the EM calorimeter. It uses steel as  
918 the absorber and plastic scintillator tiles as the active material. It has coverage in the barrel at  $|\eta| < 1.0$   
919 and in the “extended barrel” region of  $0.8 < |\eta| < 1.7$ .

920 The HEC had two wheels perpendicular to the beam line per endcap and is located directly behind  
921 the EM calorimeter endcap modules. The HEC covers the region from  $1.5 < |\eta| < 3.2$ , overlapping  
922 slightly with both the tile calorimeter and the forward calorimeter. Like the EM calorimeter, it uses liq-  
923 uid Argon as the active material, but it uses copper as the absorber.

924 The FCal covers the most forward regions of the calorimeter system, extending to the region of  $3.1 <$   
925  $|\eta| < 4.9$ . It again uses liquid argon as its active material. For absorber, it consists of an innermost  
926 module made of copper followed by a module made of tungsten.

927 The hadronic equivalent of radiation length is called the interaction length and is denoted as  $\lambda$ . In the  
928 barrel, the hadronic calorimeter depth is approximately  $9.7\lambda$ , while in the endcap is is  $10\lambda$ . The outer  
929 supports contribute an additional  $1.3\lambda$ . This is been shown to be sufficient to limit punch-through of  
930 showers to the muon system [32].

931 **2.2.4 MUON SPECTROMETER**

932 The muon spectrometer is dedicated to measuring the momentum and position of muons. It consists  
933 of tracking and trigger chambers which are unique in the barrel and endcap regions. The magnetic field  
934 for bending of muons is provided by a system of three large air-core toroid magnets (from which ATLAS

935 derives its name.) These magnets provide 1.5 to 5.5 Tm of bending power at  $0 < |\eta| < 1.4$  and approx-  
 936 imately 1 to 7.5 Tm in the endcap region of  $1.6 < |\eta| < 2.7$ . The entire muon system covers the range  
 937  $0 < |\eta| < 2.7$ . Monitored drift tubes (MDTs) are used for tracking in the barrel and the two outer  
 938 layers of the endcap, while cathode strip chambers (CSCs) are used to provide tracking in the innermost  
 939 endcap wheel. In the barrel, resistive plate chambers (RPCs) are used as trigger chambers while thin gap  
 940 chambers (TGCs) are used in the endcap. Figure 2.6 shows the layout of the ATLAS muon system. The  
 941 entire muon system is designed with the specification of providing a 10% momentum resolution for a  
 942 1 TeV muon.

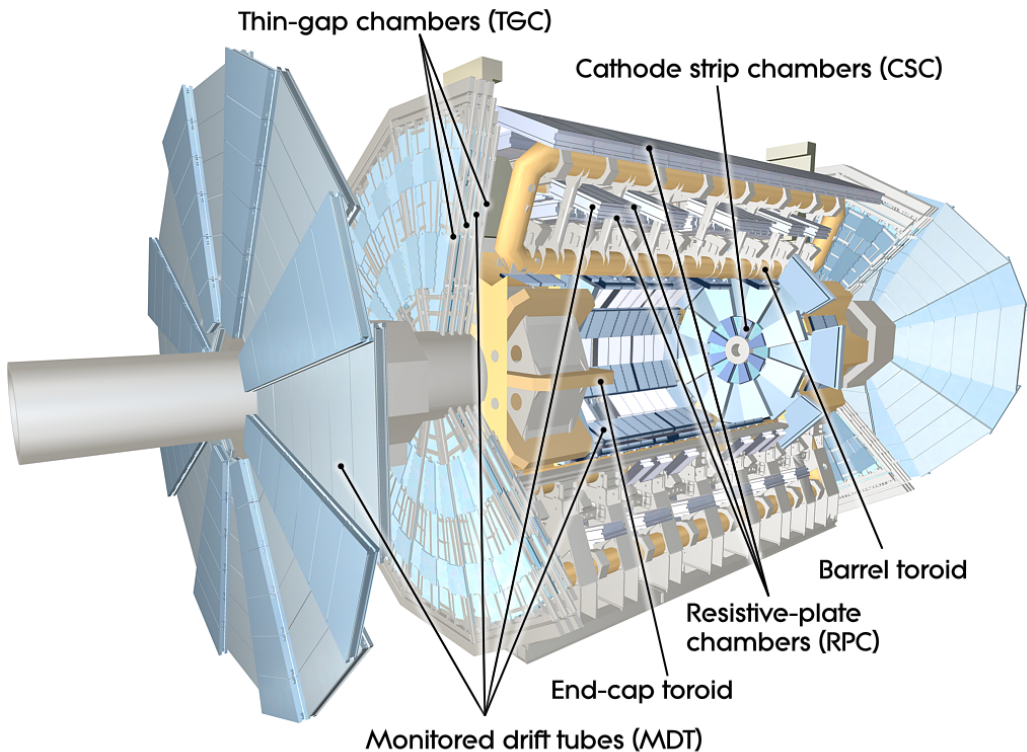


Figure 2.6: Layout of the ATLAS muon system [32]

#### 943 MONITORED DRIFT TUBES (MDTs)

944 The monitored drift tubes (MDTs) are aluminum 3cm diameter tubes filled with a 93/7 % mixture of  
 945 Argon and CO<sub>2</sub>, with trace amounts of water. As a charged particle traverses the tube, it ionizes the gas

946 and the ions drift to a wire at the center of the tube. The radial distance of traversal of the particle in the  
947 tube is determined by the drift time of the electrons, allowing for fine position resolution. The tubes  
948 have an average resolution of  $80 \mu\text{m}$  per tube and a maximum drift time of approximately 700ns. The  
949 tubes are oriented so that they give precision measurement in  $\eta$  and run along  $\phi$ . They cover  $|\eta| < 2.7$ ,  
950 except in the innermost layer of the endcap where they only go to  $|\eta| < 2.0$  [32].

### 951 CATHODE STRIP CHAMBERS (CSCs)

952 The cathode strip chambers cover a narrow window of the innermost endcap region at  $2.0 < |\eta| <$   
953 2.7. In this region the background rates in the cavern are particularly high and the CSCs are designed  
954 to handle these higher rates. The CSCs are multiwire proportional chambers with wires pointing in  
955 the radial direction (away from the beam pipe). The wire serves as an anode and there are two types of  
956 segmented cathode strip, one perpendicular to the wires which gives the precision measurement and one  
957 parallel which provides the transverse coordinate. It has an 80/20 gas mixture of Argon and CO<sub>2</sub> [32].

### 958 RESISTIVE PLATE CHAMBERS (RPCs)

959 The resistive plate chambers (RPCs) are gaseous electrode-plate detectors covering the region  $|\eta| <$   
960 1.05. They consist of two resistive plates separated by a distance of 2 mm. The gas mixture used is a  
961 94.7/5/0.3% mixture of C<sub>2</sub>H<sub>2</sub>F<sub>4</sub>, Iso-C<sub>4</sub>H<sub>10</sub>, and SF<sub>6</sub>. It has readout strips with a pitch of 23-35 mm  
962 for both  $\eta$  and  $\phi$  measurement and thus provides measurement of the azimuthal coordinate in the barrel  
963 that the MDTs do not. The thin gas gap allows for a quick response time which makes it ideal for use in  
964 the trigger. There are three layers of RPCs which are referred to as the three trigger stations. They allow  
965 for both a low  $p_T$  and high  $p_T$  trigger. The coincidence of hits in the innermost chambers allows for  
966 triggering of muons between 6 and 9 GeV, while the outermost layer allows the trigger to select high  
967 momentum tracks in the range of 9 to 35 GeV [32].

### 968 THIN GAP CHAMBERS (TGCs)

969 The thin gap chambers (TGCs) are multiwire proportional chambers where the wire to cathode distance  
970 (1.4mm) is smaller than the wire-to-wire distance (1.8 mm). They contain a gas mixture of CO<sub>2</sub> and

971 *n*-pentane and use a high electric field to gain good time resolution. They serve two functions in the  
 972 end-cap system. First, they serve as the trigger chambers. Second, they also provide azimuthal coordi-  
 973 nate measurement which the MDTs do not. They sit on the inner and middle layers of the endcap. The  
 974 outermost layer's azimuthal coordinate is determined by extrapolation [32].

### 975 2.2.5 MAGNET SYSTEM

976 As mentioned previously, there are two independent magnet systems in ATLAS. The first is a 2 T solenoid  
 977 field in the inner detector which provides bending in the azimuthal plane. The second is an approxi-  
 978 mately 0.5 T toroidal field in the muon system which provides bending in  $\eta$ . Figure 2.7 shows the pre-  
 979 dicted field integral as a function of  $|\eta|$  [32].

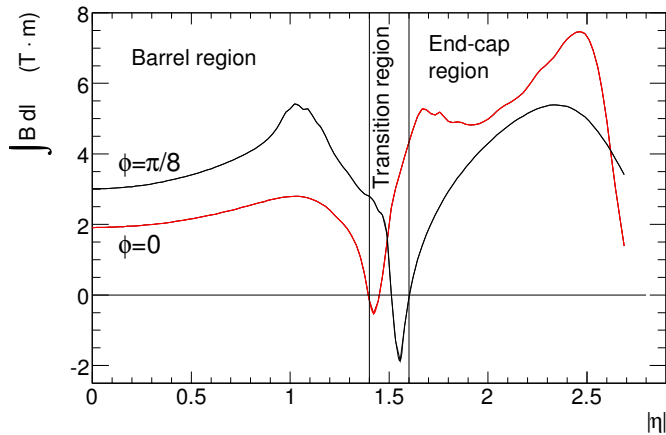


Figure 2.7: Predicted field integral as a function of  $|\eta|$  for the ATLAS magnet system [32]

### 980 2.2.6 TRIGGER SYSTEM

981 The ATLAS trigger system searches for signatures of muons, electrons, photons, hadronically decay-  
 982 ing  $\tau$  leptons, and jets in order to save these events for further analysis. The trigger system in ATLAS  
 983 is designed to reduce the maximum LHC event rate of 40 MHz to a more reasonable rate that can be  
 984 recorded. The trigger first consists of a fast, hardware based system called the Level-1 (L1) trigger. The  
 985 L1 trigger consists of independent dedicated detector sub-components that can seed regions of inter-  
 986 est (RoIs) for further analysis downstream. For muons, the RPCs and TGCs are used, while in the

987 calorimeter coarsely grained sections of calorimeter cells called towers are used. Once regions of inter-  
 988 est are seeded, a software based system called the High Level Trigger (HLT) is used to reconstruct objects  
 989 and integrate information from different parts of the detector. In Run 1 of ATLAS, the HLT consisted  
 990 of two separate stages: the level 2 (L2) trigger and the event filter (EF).

991 The maximum trigger rate that the L1 trigger can handle is 75 kHz. In the HLT, the rate of events  
 992 written to disk is approximately 200 Hz. Figure 2.8 shows the trigger rates for different L1 triggers in  
 993 2012 and 2015 for ATLAS [42].

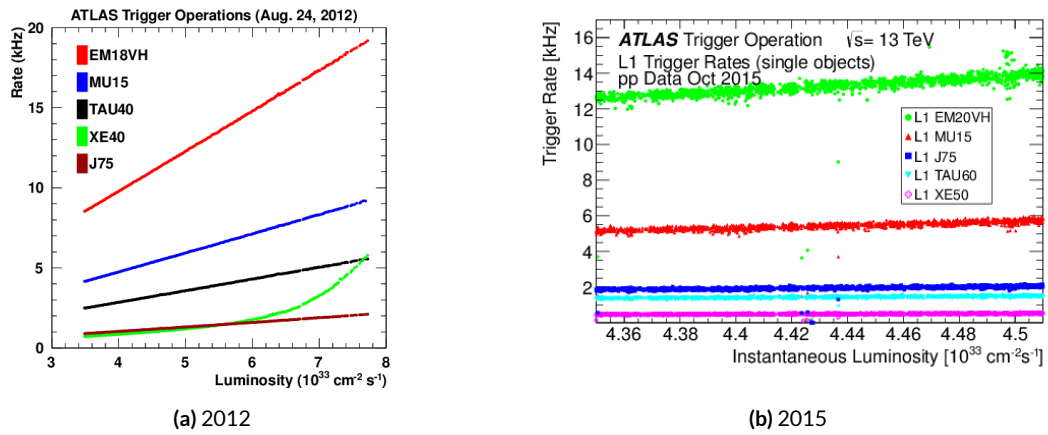


**Figure 2.8:** ATLAS trigger rates for Level-1 triggers as a function of instantaneous luminosity in 2012 and 2015 operation. These are single object triggers for electromagnetic clusters (EM), muons (MU), jets (J), missing energy (XE), and  $\tau$  leptons (TAU). The threshold of the trigger is given in the name in GeV. [42]

### 994 2.2.7 ATLAS DATASETS

995 ATLAS has collected data at center of mass energies of 7, 8, and 13 TeV. Figure 2.9 shows the integrated  
 996 luminosity as a function of time for each of the three collected datasets. At  $\sqrt{s} = 7$  TeV, ATLAS  
 997 recorded  $5.08 \text{ fb}^{-1}$ . Increased instantaneous luminosity in 2012 led to a larger dataset of  $21.3 \text{ fb}^{-1}$   
 998 recorded at  $\sqrt{s} = 8$  TeV. After Long Shutdown 1 (LS1) of the LHC and a restart in 2015, ATLAS  
 999 recorded  $3.9 \text{ fb}^{-1}$  of data at  $\sqrt{s} = 13$  TeV. [43, 44]

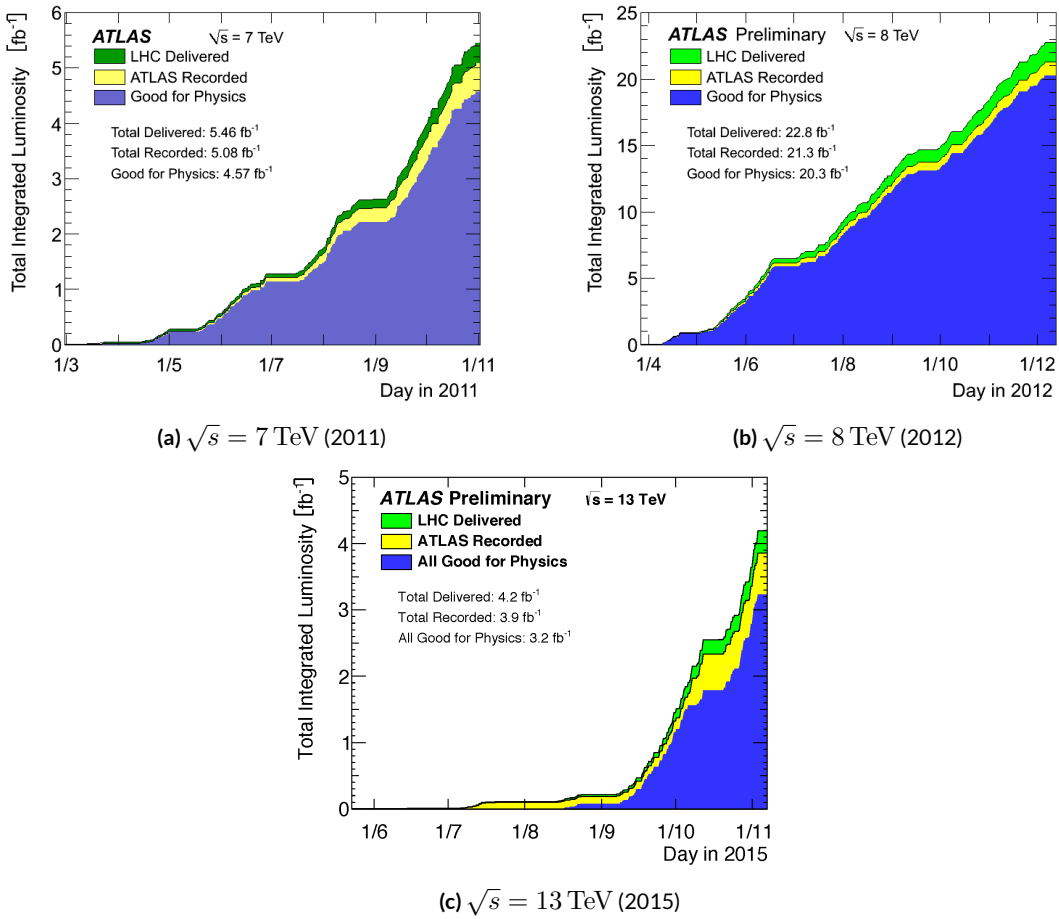


**Figure 2.9:** Instantaneous luminosity as a function of time for data recorded by ATLAS at different center of mass energies [43, 44]

### 1000 2.2.8 DETECTOR PERFORMANCE

1001 Table 2.2 summarizes the design requirements for each of the different sub-detectors. This table shows  
 1002 the energy and momentum resolution of each tracking, calorimetry, and muon measurements.

### 1003 2.3 THE ATLAS MUON NEW SMALL WHEEL UPGRADE

1004 As the LHC continues operation, it is scheduled to be upgraded in several phases to allow it to reach  
 1005 higher instantaneous luminosities and thus collect larger datasets. These conditions will open new doors  
 1006 for study of rare physics processes but will also present interesting challenges that must be faced. ATLAS  
 1007 will require new detector technologies to cope with the increased background rates in the cavern in these

	Required resolution
Tracking	$\sigma_{p_T}/p_T = 0.05\% p_T \oplus 1\%$
EM calorimetry	$\sigma_E/E = 10\%/\sqrt{E} \oplus 0.7\%$
Hadronic calorimetry	
Barrel and end-cap	$\sigma_E/E = 50\%/\sqrt{E} \oplus 3\%$
Forward	$\sigma_E/E = 100\%/\sqrt{E} \oplus 10\%$
Muon spectrometer	$\sigma_{p_T}/p_T$ at $p_T = 1$ TeV

Table 2.2: Performance requirements for the ATLAS detector [32].

1008 high luminosity conditions. One such upgrade, scheduled to be installed during Long Shutdown 2  
 1009 (LS2) of the LHC in 2018, is the ATLAS Muon New Small Wheel (NSW) upgrade [45]. The NSW will  
 1010 replace the innermost end-cap wheel of the muon system with new technologies, as this is the part of the  
 1011 muon detector closest to the beam and thus suffers from the highest rates.

1012 **2.3.1 MOTIVATION**

1013 The motivation of the NSW is two-fold. First, the objective is to alleviate the decreased tracking effi-  
 1014 ciency that comes in a high rate environment. As figure 2.10, at the LHC design luminosity both the  
 1015 efficiency of recording hits and reconstructing track segments in the MDTs decreases at the LHC design  
 1016 luminosity.

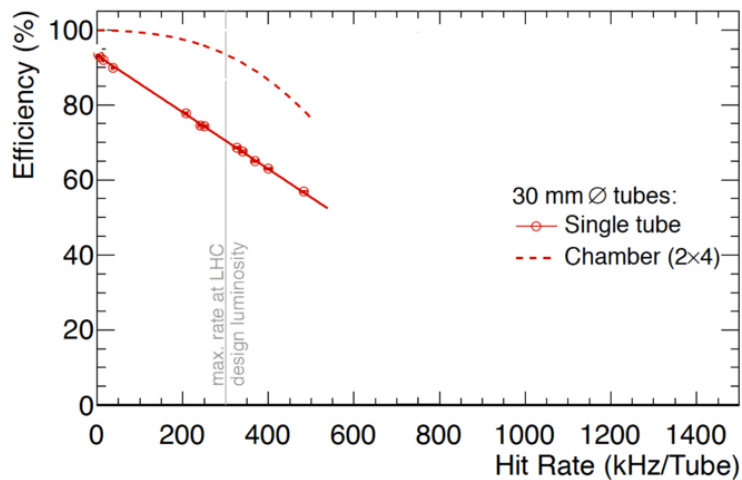


Figure 2.10: MDT tube hit (solid) and segment (dashed) efficiency as a function of hit rate per tube [45]

1017 Second, the NSW will work to alleviate the rate of fake triggers arising in the endcap. Figure 2.11  
 1018 shows the extrapolated trigger rates as a function of the  $p_T$  threshold with and without the NSW up-  
 1019 grade. As the figure shows, the NSW upgrade will reduce the trigger rate by an order of magnitude com-  
 1020 pared to the current endcap trigger system.

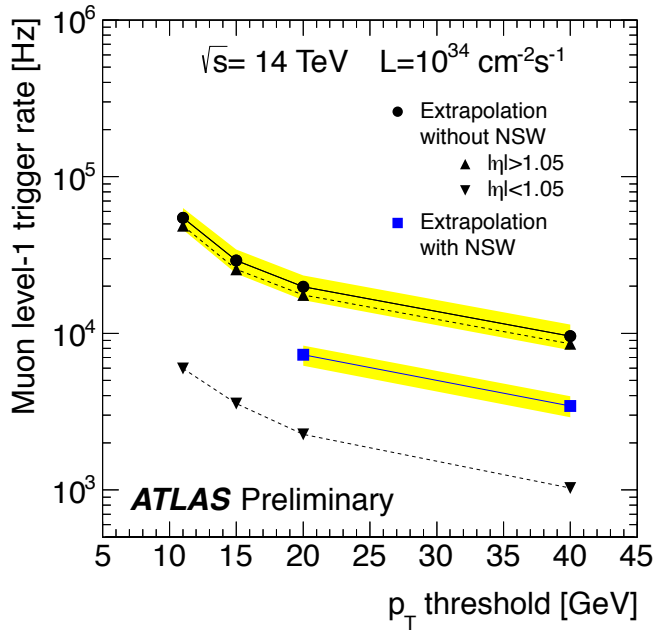


Figure 2.11: Trigger rate as a function of  $p_T$  threshold with and without the NSW upgrade [45]

### 1021 2.3.2 NSW DETECTOR TECHNOLOGIES

1022 The NSW will use two new detector technologies - micromesh gaseous structure detectors (micromegas)  
 1023 and small-strip thin gap chambers (sTGCs) [45, 46]. Unlike the previous detectors, both of these detec-  
 1024 tor technologies can be used for tracking or trigger. However, the micromegas is more suited to tracking  
 1025 because of its good spatial resolution, while the sTGCs have better time resolution and are more suited  
 1026 for the trigger. To maintain a fully redundant system, both technologies are used for both purposes.

1027 **MICROMEGAS**

1028 Micromegas detectors operate using a thin metallic mesh that sits approximately  $100 \mu\text{m}$  away from  
1029 the readout electrodes to create the amplification region. Above this mesh, there is a drift region on the  
1030 order of a few mm in length capped by a drift electrode. As a charged particle traverses the detector, it  
1031 ionizes gas and the electrons drift down towards readout strips. The timing of the drift can be used to  
1032 reconstruct the angle of traversal of the particle. This is illustrated in figure 2.12. The micromegas used in  
1033 ATLAS will be resistive micromegas, where the readout electrodes are topped with resistive strips [47].  
1034 This alleviates the risk of sparking in the large area detectors that ATLAS will use.

1035 In ATLAS, the micromegas drift gap will be 5 mm and the amplification gap will be  $128 \mu\text{m}$ . They  
1036 are filled with the same gas mixture as the MDTs. They will be stacked in an octuplet in an XXUV-  
1037 UVXX geometry, where X refers to straight strips and U and V refer to stereo strips at an angle of  $\pm 1.5^\circ$ .  
1038 This arrangement allows for measurement of the azimuthal coordinate and gives a large lever arm be-  
1039 tween the straight strips for triggering purposes. Figure 2.12 shows the geometry of a single micromegas  
1040 detector as well as its operating principle [45].

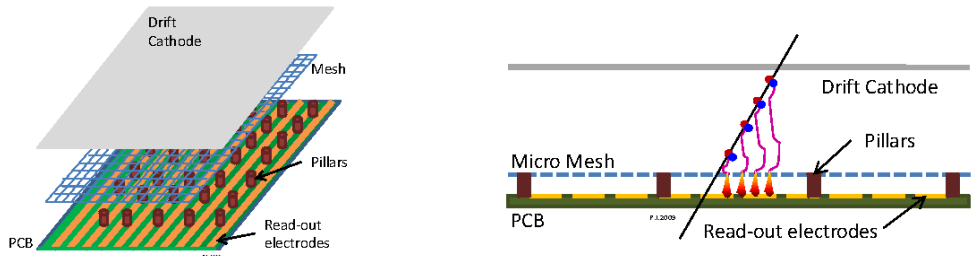
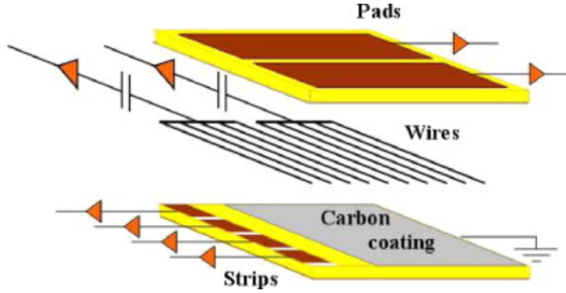


Figure 2.12: Illustrations of the geometry (left) and operating principle (right) of the micromegas detector [45]

1041 **sTGCs**

1042 The sTGCs are similar to the TGCs already described. They consist of gold-plated tungsten wires with  
1043 a 1.8 mm pitch between two cathode planes 1.4 mm away from the wire plane. One cathode plane  
1044 consists of strips with a 3.2 mm pitch (much smaller pitch than the TGCs), while the other consists  
1045 of coarser pads that are used for defining regions of interest in the sTGC trigger algorithm. Figure 2.13  
1046 shows the basic detector geometry.



**Figure 2.13:** Geometry of the sTGC detector [45]

### 1047 2.3.3 PHYSICS IMPACT

1048 Maintaining low  $p_T$  thresholds for muons while still staying within the trigger rate budget at Level 1  
 1049 (20 kHz) for the muon system is crucial for physics analyses to be successful in high luminosity condi-  
 1050 tions. One realm where the lepton trigger threshold is especially important is in Higgs physics. In the  
 1051  $H \rightarrow WW^*$  analysis, one of the  $W$  bosons is off shell and tends to decay to soft leptons. In associated  
 1052 production of a Higgs with a  $W$ , the lepton is also important because the lepton provides the main han-  
 1053 dle which allows the event to be triggered. Table 2.3 shows the impact of increasing the trigger thresholds  
 1054 on these analyses. It shows that either raising the threshold or using only the barrel both have signifi-  
 1055 cant impacts on the signal efficiency. With the NSW, the signal efficiency is largely maintained and the  
 1056 triggers can be unprescaled.

Threshold	$H \rightarrow b\bar{b}$ (%)	$H \rightarrow WW^*$ (%)
$p_T > 20$ GeV	93	94
$p_T > 40$ GeV	61	75
$p_T > 20$ GeV (barrel only)	43	72
$p_T > 20$ GeV (with NSW)	90	92

**Table 2.3:** Signal efficiencies for  $WH$  production with  $H \rightarrow b\bar{b}$  and  $H \rightarrow WW^* \rightarrow \mu\nu qq$  under different trigger configurations [45].

### 1057 2.4 OBJECT RECONSTRUCTION IN ATLAS

1058 ATLAS analyses first start by requiring the presence of certain reconstructed physics objects in the event.  
 1059 This section will present a brief overview of the algorithms used to reconstruct electrons, muons, jets

1060 (including  $b$ -jets), and missing energy<sup>\*</sup>. The performance of object reconstruction and measurement will  
 1061 also be discussed as these are relevant to the analyses presented later. Figure 2.14 gives an overview of the  
 1062 different sub-detectors that each type of particle will interact with in ATLAS.

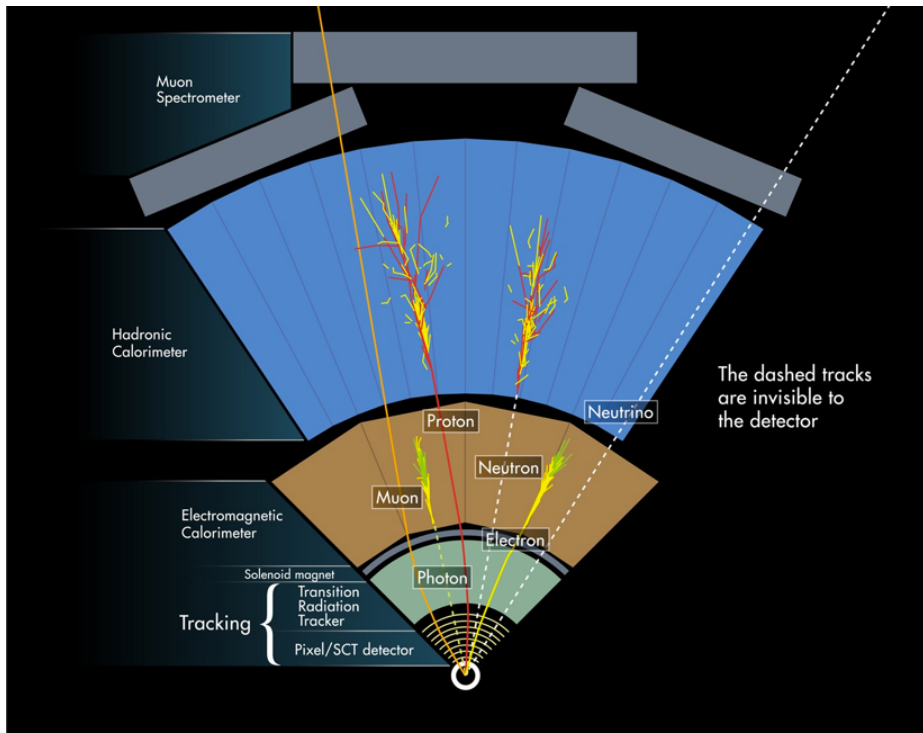


Figure 2.14: Illustration of particle interactions in ATLAS [48]

#### 1063 2.4.I ELECTRONS

1064 Electrons in ATLAS will leave tracks in the inner detector and energy deposits in the electromagnetic  
 1065 calorimeter. The algorithm for recognizing the signature of electrons proceeds in two steps: reconstruc-  
 1066 tion and identification.

1067 In reconstruction, an electron candidate is formed by matching EM calorimeter deposits with ID  
 1068 tracks. The algorithm first chooses seed clusters in the EM calorimeter by using a sliding window algo-  
 1069 rithm that searches for towers with transverse energy larger than 2.5 GeV. In addition to seed clusters,  
 1070 track candidates must be identified in the ID. The algorithm selects seed tracks with  $p_T > 1$  GeV that

---

\*Reconstruction algorithms for other objects, such as photons and  $\tau$  leptons, are not detailed here as these objects are not used in the presented studies.

1071 do not fit well with a pion hypothesis. Once candidate tracks are selected, they are re-fit with a Gaussian Sum Filter (GSF) algorithm to estimate electron parameters [49]. Finally, an electron candidate is  
 1072 formed if at least one track matches to a seed cluster in the calorimeter. The full details of the reconstruction  
 1073 algorithm can be found in reference [50].

1075 Once an electron candidate is present, identification criteria must be applied in order to reject fake  
 1076 electrons from background. Many different variables are used for this identification, most of them re-  
 1077 lated to the shower shape in the EM calorimeter and the amount of leakage into the hadronic calorime-  
 1078 ter, as well as information from the ID and in particular the TRT. There are both cut-based and likelihood-  
 1079 based criteria that range from “loose” to “very tight”. For details, see reference [50].

1080 Figure 2.15 shows the algorithm’s reconstruction efficiency of true electrons for different identification  
 1081 criteria as well as the electron energy resolution in simulation [50, 51]. The reconstruction efficiency is  
 1082 measured using both  $Z$  and  $J/\psi$  tag and probe techniques.

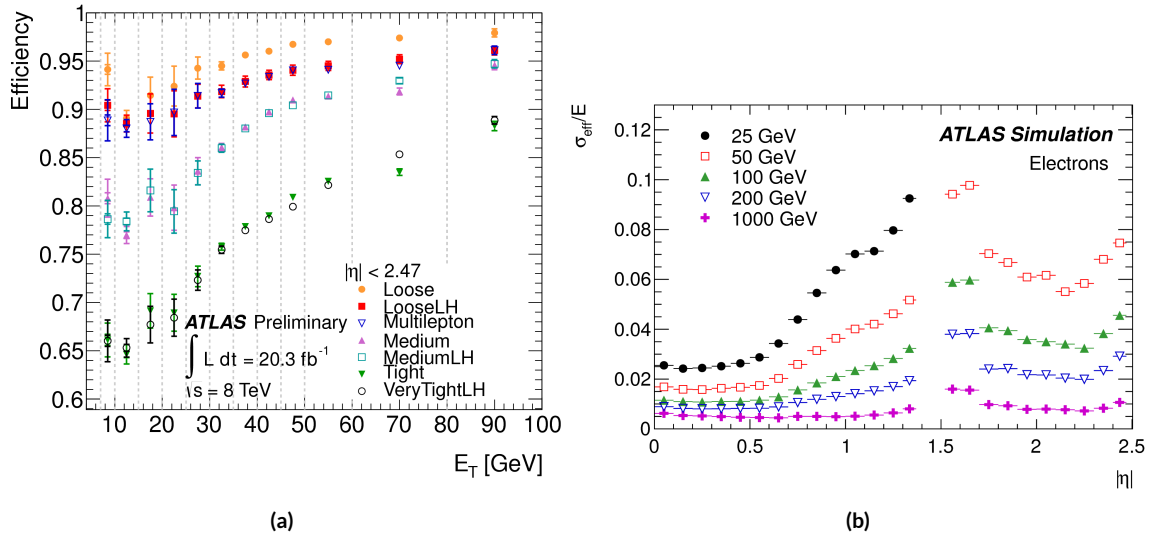


Figure 2.15: Electron performance: (a) reconstruction efficiency as a function of electron  $E_T$  [50] (b) energy resolution in simulation as a function of  $|\eta|$  for different energy electrons [51]

#### 1083 2.4.2 MUONS

1084 The ATLAS detector is designed to stop most particles before they reach the muon spectrometer. Muons,  
 1085 however, are minimum ionizing particles, meaning that they will not lose a significant amount of energy

1086 through interactions with the detector and will thus pass through. Therefore, the muon reconstruction  
1087 works to match tracks in the muon spectrometer with tracks in the inner detector.

1088 The first step of reconstruction is to reconstruct local straight line tracks, called segments, in each  
1089 muon chamber. Segments are then fit to larger tracks that traverse the entire muon spectrometer. Such  
1090 muon tracks are referred to as “standalone” tracks (SA) as they only use information from the muon  
1091 spectrometer. The standalone tracks are then matched to tracks in the inner detector to form “com-  
1092 bined” (CB) muons, where the combined ID and MS fit are used to determine the momentum and di-  
1093 rection of the muon. To improve acceptance, segment-tagged and calorimeter-tagged muons are also  
1094 reconstructed. In these cases, ID tracks are matched to segments in the MS and calorimeter deposits con-  
1095 sistent with a minimum ionizing particle, respectively. The details of the reconstruction can be found in  
1096 reference [52].

1097 As with electrons, once muon candidates are reconstructed they have identification criteria applied to  
1098 reduce background. These criteria include the  $\chi^2$  match between the ID and MS tracks, the number of  
1099 hits in the ID, overall ID and MS track fit quality, and additional variables [52]. The criteria range from  
1100 “loose” to “tight” as with electrons.

1101 Figure 2.16 shows the muon reconstruction efficiency (measured with  $Z$  and  $J/\psi$  tag and probe) and  
1102 invariant mass resolution [52].

### 1103 2.4.3 JETS

1104 When a quark or gluon is produced in collisions, it is not measured directly in ATLAS. Rather, due to  
1105 QCD effects, it produces a collimated spray of hadrons in the direction of the original parton, which is  
1106 known as a jet. Jets are reconstructed in ATLAS using energy deposits in the hadronic calorimeter. The  
1107 first step is build “topological clusters” out of energy deposits in calorimeter cells [53, 54]. This is done  
1108 using strategy where seed cells are chosen by picking cells whose energy measurements are four times the  
1109 amount of noise expected for that cell. Adjacent cells with at least  $2\sigma$  energy measurements are added  
1110 to the cluster, then a final layer of clusters with energy above  $0\sigma$  are added. Once calorimeter clusters  
1111 are formed, they are clustered further into jet candidates using the anti- $k_T$  jet clustering algorithm [55].

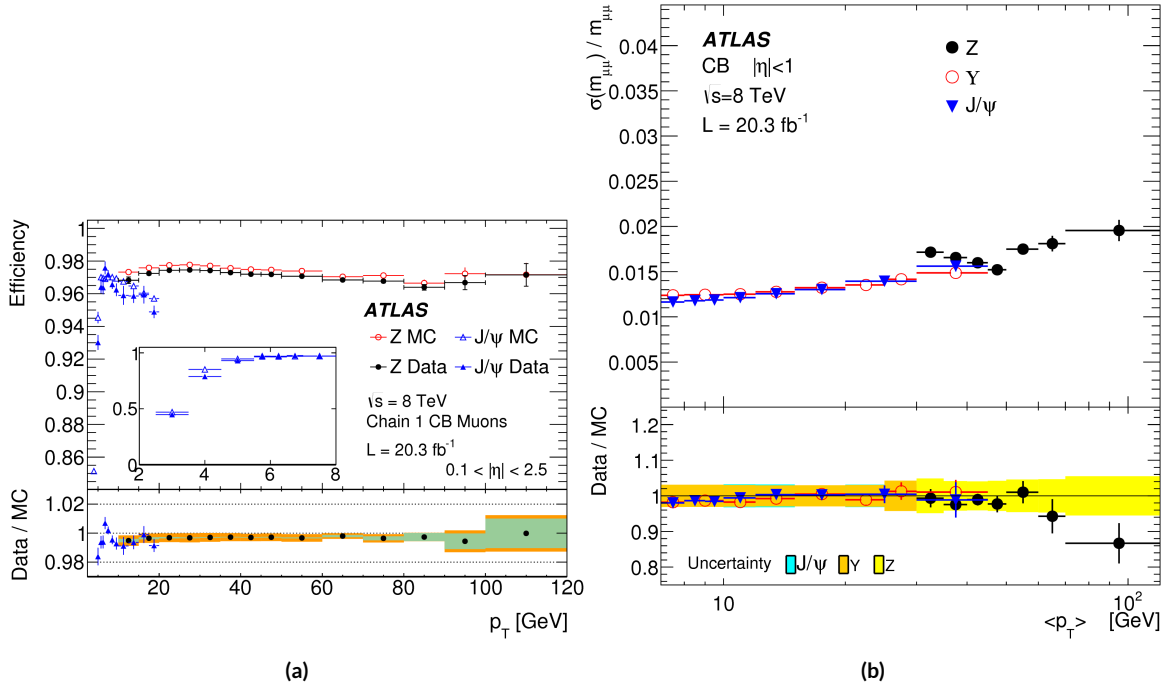


**Figure 2.16:** Muon performance: (a) reconstruction efficiency as a function of muon  $p_T$  (b) dimuon mass resolution as a function of average  $p_T$  [52]

This algorithm uses a parameter  $R$  that appears in the denominator of the clustering distance metric and defines the radial size of the jet in  $\eta\phi$  space.

The energy response of the calorimeter must be properly characterized in order to reconstruct jet energy. Calorimeter clusters can be calibrated either with the EM calibration, where each cluster is assumed to have come from the energy deposit of an electron or photon, or the LCW calibration, where local cluster weights are computed to allow for local calibration of clusters as hadronic or electromagnetic. The details of the jet energy calibration are not detailed here and are discussed in reference [56].

Figure 2.17 shows the jet energy response after calibration in Monte Carlo as a function of the true  $p_T$  of the jet [56].

#### 2.4.4 $b$ -TAGGING

One important aspect of jet physics is the task of identifying the flavor of parton that produced the measured jet. While in general this is very difficult, jets from  $b$ -quarks offer an interesting case where such identification is possible.  $B$  mesons have a lifetime on the order of  $10^{-12}$  seconds, which makes a  $c\tau$

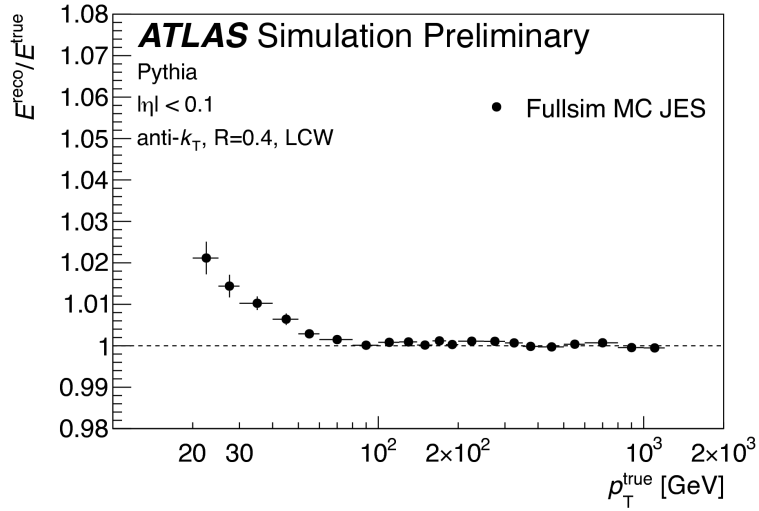


**Figure 2.17:** Jet energy response after calibration as a function of true  $p_T$  in simulation [56]

on the order of millimeters [6]. This type of displaced decay vertex can be identified in detectors like ATLAS and allows  $b$ -jets to be distinguished from other flavors of jets<sup>†</sup>.

ATLAS uses a multivariate machine learning algorithm to identify jets from  $b$ -quarks. The inputs to this algorithm are determined from lower level reconstruction algorithms. There are three distinct algorithms that reconstruct variables which are used as input to the multivariate technique.

The first family is referred to as IPxD (where the x can either be 2 or 3). These algorithms use the transverse and longitudinal impact parameters  $d_0$  and  $z_0$  of the tracks inside a jet to determine their consistency with the primary vertex. They two or three dimensional (hence the x) templates for light flavor, charm, and bottom jets and then evaluate the likelihood of the jet coming from each of these types. The likelihood ratios are used as inputs to the multivariate algorithm.

The next two algorithms used as input are referred to as the secondary vertex (SV) and JetFitter (JF) algorithms. The SV algorithm uses tracks inside the jet to fit for vertices that are displaced from the primary vertex. The JF algorithm attempts to reconstruct the full flight path of the  $b$  by looking for multiple displaced vertices along the same line (as  $B$  decays often result in subsequent  $c$  decays).

In Run 1, the multivariate  $b$ -tagging algorithm used a neural network and was referred to as MV1.

---

<sup>†</sup>Jets from charm quarks can also be detected in this way but they do not live quite as long so the displacement of the vertex is harder to distinguish

1140 The details of this algorithm and its inputs are given in reference [57]. In Run 2, the number of inputs  
 1141 was simplified and a boosted decision tree with 24 input variables was used, referred to as MV2. The  
 1142 details of this algorithm are in reference [58]. Figure 2.18 shows the performance of each of these algo-  
 1143 rithms.

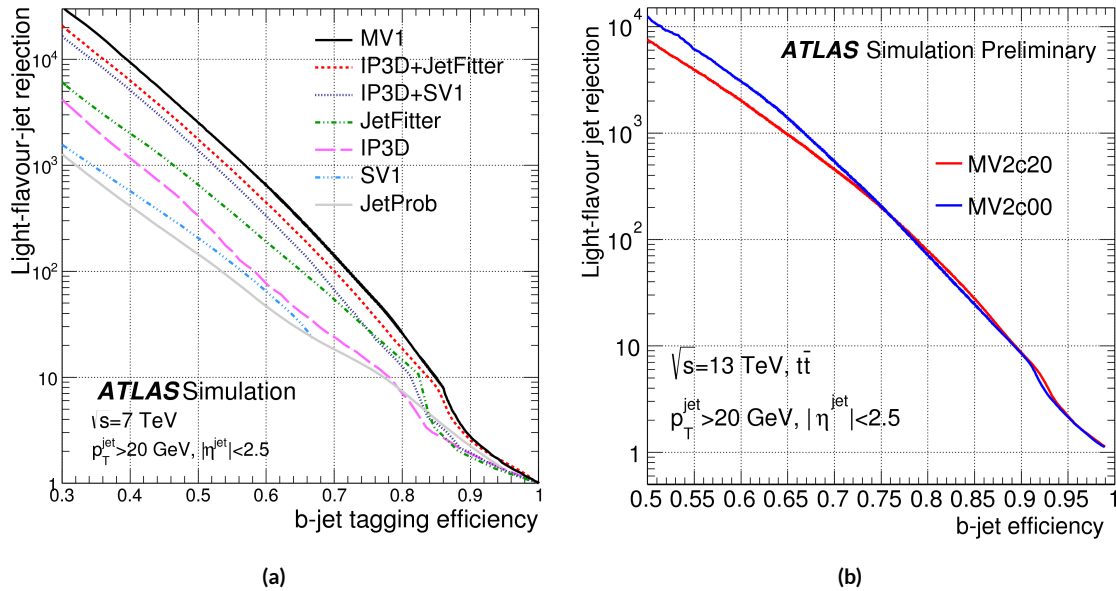


**Figure 2.18:** Light jet rejection ( $1/\text{efficiency}$ ) vs.  $b$ -jet efficiency for MV1 and its input algorithms (a) [57] and MV2 (b) [58] in simulated  $t\bar{t}$  events. The numbers in the algorithm names in (b) refer to the fraction of charm events used in the MV2 training.

#### 1144 2.4.5 MISSING TRANSVERSE ENERGY

1145 As noted in figure 2.14, neutrinos produced in ATLAS will pass through the detector without inter-  
 1146 acting. The only way of detecting the presence of particles like neutrinos (or BSM particles that are  
 1147 long-lived) is to use missing transverse momentum. The basic principle of missing transverse energy is  
 1148 to use the momentum balance of the incoming protons to infer the presence of missing particles. The  
 1149 net longitudinal momentum of the incoming partons that collide is not known (since each carries an un-  
 1150 known fraction of the proton's momentum). However, the protons (and thus incoming partons) have  
 1151 no net momentum in the plane transverse to the beam line (the  $x$ - $y$ ) plane. Therefore, if there are no  
 1152 un-measured particles in the final state, the transverse momenta of all of the final state particles should

balance. The magnitude of this imbalance is known as missing transverse momentum ( $E_T^{\text{miss}}$ ).

The basic calculation of missing transverse momentum from calorimeter cells is given in equation 2.4 [59].

1155

$$\begin{aligned} E_x^{\text{miss}} &= -\sum_{i=1}^{N_{\text{cell}}} E_i \sin \theta_i \cos \phi_i \\ E_y^{\text{miss}} &= -\sum_{i=1}^{N_{\text{cell}}} E_i \sin \theta_i \sin \phi_i \end{aligned} \quad (2.4)$$

1156 The  $E_T^{\text{miss}}$  calculation is separated into different terms based on the objects that the calorimeter clusters

1157 are associated with. This way, each cell's contribution is calibrated appropriately according to the object.

1158 This separation of terms is shown in equation 2.5 [59].

$$\begin{aligned} E_{x(y)}^{\text{miss,calo}} &= E_{x(y)}^{\text{miss},e} + E_{x(y)}^{\text{miss},\gamma} + E_{x(y)}^{\text{miss},\tau} + E_{x(y)}^{\text{miss,jets}} \\ &\quad + E_{x(y)}^{\text{miss,softjets}} + E_{x(y)}^{\text{miss},\mu} + E_{x(y)}^{\text{miss,CellOut}} \end{aligned} \quad (2.5)$$

1159 The CellOut term of the above equation corresponds to calorimeter cells with energy deposits that are

1160 not associated with other objects. The soft jets term comes from cells associated to jets with  $p_T$  between

1161 7 and 20 GeV, while the jets term comes from jets with  $p_T > 20$  GeV. Because muons do not deposit

1162 significant energy in the calorimeter, the muon momentum is used for the muon term [59]. The final

1163  $E_T^{\text{miss}}$  is calculated using equation 2.6.

$$E_T^{\text{miss}} = \sqrt{(E_x^{\text{miss}})^2 + (E_y^{\text{miss}})^2} \quad (2.6)$$

1164 Figure 2.19 shows the resolution of the components of the  $E_T^{\text{miss}}$  under different pileup suppression

1165 techniques [60].

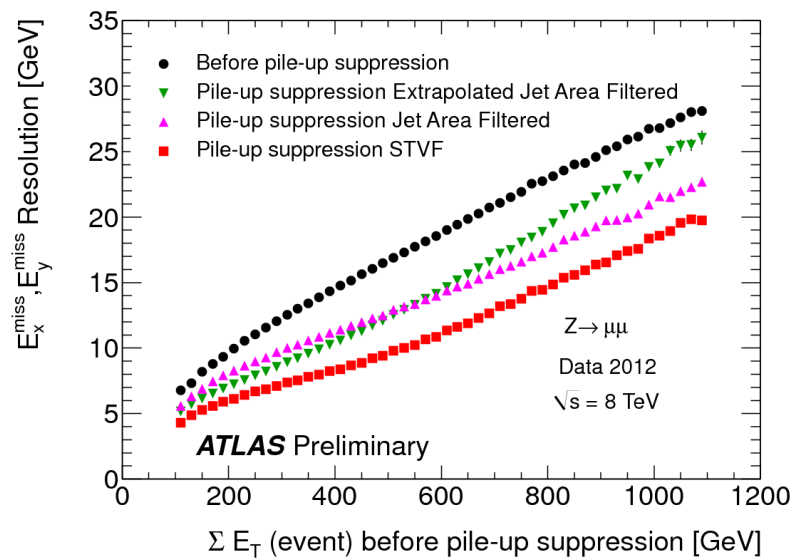


**Figure 2.19:** Resolution of  $E_T^{\text{miss}}$  components as a function of  $\sum E_T$  before pileup suppression with different pileup techniques [60]

1166

## Part II

1167

Observation and measurement of Higgs

1168

boson decays to  $WW^*$  in LHC Run I at

1169

$\sqrt{s} = 7$  and 8 TeV

*Basic research is what I am doing when I don't know  
what I am doing.*

Wernher von Braun

# 3

1170

## 1171 $H \rightarrow WW^* \rightarrow \ell\nu\ell\nu$ Analysis Strategy

### 1172 3.1 INTRODUCTION

1173 This chapter presents an overview of the strategy for searching for a Higgs boson in the  $H \rightarrow WW^* \rightarrow$   
1174  $\ell\nu\ell\nu$  decay topology. Its purpose is to define in broad terms how the search and measurement are un-  
1175 dertaken, before going into details on the specific sub-categories within the larger analysis. First, the  
1176 properties of the Higgs signal are discussed and the associated backgrounds are presented. Next, the ob-  
1177 servables used to enhance the signal to background ratio are defined. Finally, the parameters of interest  
1178 in the search and measurement will be shown, along with a brief overview of the statistical treatment of  
1179 the final Higgs candidates.

1180 Following this chapter, the results of three different studies within the  $H \rightarrow WW^* \rightarrow \ell\nu\ell\nu$  channel  
1181 are shown. Chapter 4 presents a search for Higgs boson production in gluon fusion mode and the role  
1182 of the  $H \rightarrow WW^*$  channel in its discovery. Chapter 5 shows the search and first observation in ATLAS  
1183 of the Vector Boson Fusion (VBF) production mode of the Higgs in the  $H \rightarrow WW^*$  decay channel.

1184 Finally, chapter 6 shows the combined Run 1  $H \rightarrow WW^*$  results for the measurement of the Higgs  
1185 cross section and relative coupling strengths to other SM particles.

### 1186 3.2 THE $H \rightarrow WW^* \rightarrow \ell\nu\ell\nu$ SIGNAL IN ATLAS

1187 The signal studied in this and subsequent chapters is the Higgs boson in the  $WW^*$  final state, where  
1188 each  $W$  boson subsequently decays into a charged lepton and a neutrino. In its simplest decay path, the  
1189 final state consists of two neutrinos and two charged leptons, each of which can be either an electron or  
1190 a muon. If one or both of the  $W$ s decay to  $\tau$  leptons, only leptonic decays of the  $\tau$  are considered. This  
1191 decay path produces additional neutrinos in the final state but still gives two charged leptons as before.  
1192 Neutrinos are not detected in ATLAS, so the final state ultimately consists of two reconstructed leptons  
1193 and missing transverse momentum (denoted as  $E_T^{\text{miss}}$ ). Final states where both of the charged leptons  
1194 are electrons or muons are referred to as the “same flavor” ( $ee/\mu\mu$ ) final states, while those with one  
1195 electron and one muon are referred to as “different flavor” ( $e\mu$  or  $\mu e$ ).

1196 While the basic final state consists of two leptons and  $E_T^{\text{miss}}$ , there can be additional objects depend-  
1197 ing on the production mode of the Higgs. As described in detail in Chapter 1, if the Higgs is produced  
1198 via vector boson fusion production, there will be two additional forward jets in the event. Even in gluon  
1199 fusion, one or more jets can be produced through initial state radiation from the incoming gluons. Be-  
1200 cause of the varying background composition as a function of jet multiplicity, each bin in this variable  
1201 has its own dedicated requirements applied in the search and measurement. The  $n_j = 0$  and  $n_j = 1$   
1202 bins are dedicated to gluon fusion production, while the  $n_j \geq 2$  bin has separate dedicated searches for  
1203 ggF and VBF production.

1204 Figure 3.1 shows the relative branching fractions for the  $H \rightarrow WW^*$  process, calculated from the  
1205 Particle Data Group values for the  $W$  and  $\tau$  branching ratios [? ]. The largest branching ratio is both  
1206  $W$  bosons decaying to quark pairs at 45.44%. The next largest is one  $W$  decaying leptonically and the  
1207 other decaying to quarks, a branching ratio of 34.18%. In all cases,  $\ell$  denotes either an electron or muon,  
1208 and the leptonic branching ratios of the  $\tau$  are included. For example, the  $\ell\nu qq$  final state includes one  $W$   
1209 decaying to  $e\nu$ ,  $\mu\nu$ , or  $\tau\nu$ . In the case of the  $W \rightarrow \tau\nu$  decay, the  $\tau$  lepton then decays to an electron or

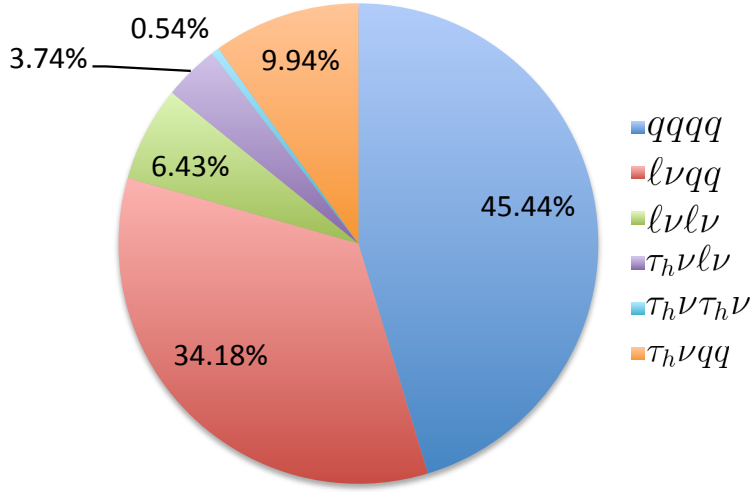


**Figure 3.1:** Branching ratios for a  $WW$  system.  $q$  refers to quarks.  $\ell$  can be either an electron or muon, and the leptonic branching ratios of the  $\tau$  are included. For example, the  $\ell\nu qq$  final state includes one  $W$  decaying to  $e\nu$ ,  $\mu\nu$ , or  $\tau\nu$ .  $\tau_h$  refer to hadronic decays of the  $\tau$ .

1210 muon via  $\tau \rightarrow \nu_\tau \ell \nu_\ell$ . Final states with a  $\tau_h$  refer to hadronic decays of the  $\tau$ . The branching ratio to the  
1211  $\ell\nu \ell\nu$  final state is 6.43%.

1212 While the  $\ell\nu \ell\nu$  final state is not a large fraction of the branching ratio, there are significant advantages  
1213 in this channel. First, both the  $qqqq$  and  $\ell\nu qq$  channels suffer from a large QCD multijet background,  
1214 which is often difficult to model. Second, events in the the  $\ell\nu \ell\nu$  channel in data can be triggered more  
1215 efficiently due to the presence of two leptons.

### 1216 3.3 BACKGROUND PROCESSES

1217 Many processes from the Standard Model can also produce a final state with two leptons and missing  
1218 transverse momentum . This section lists the dominant backgrounds to Higgs production. It gives gen-  
1219 eral descriptions of how the backgrounds mimic Higgs production and how they can be reduced. Ta-  
1220 ble3.1 summarizes the different processes.

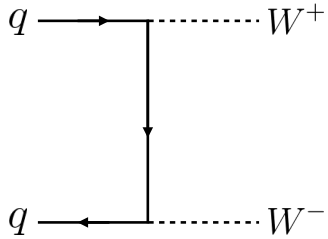


**Figure 3.2:** Feynman diagram for Standard Model WW production

### 1221 3.3.1 STANDARD MODEL WW PRODUCTION

1222 Non-resonant Standard Model diboson production, as shown in figure 3.2, is an irreducible background  
 1223 to Higgs boson production in the WW final state. It produces the same exact final state objects, namely  
 1224 leptonically decaying W bosons. There are no additional objects in the final state that allow for back-  
 1225 ground reduction. Therefore the analysis solely relies on the correlations between the leptons to reduce  
 1226 this background.

### 1227 3.3.2 TOP QUARK PRODUCTION

1228 Production of top quarks, either in pairs ( $t\bar{t}$  production) or singly (e.g.  $Wt$  production), can also mimic  
 1229 Higgs production. Because top quarks decay via  $t \rightarrow Wb$ , top pair production can produce a final state  
 1230 with two W bosons that then decay leptonically. In this case, however, there are two additional jets from  
 1231 the bottom quarks in the final state. This allows the analysis to veto on the presence of jets identified as  
 1232 originating from a  $b$  in order to reduce the size of the background.

1233 Single top production can occur via  $s$ -channel,  $t$ -channel, or associated production ( $Wt$ ). The mode  
 1234 which most closely resembles the Higgs final state is  $Wt$ . In this case, there are two real W bosons pro-  
 1235 duced, as with  $t\bar{t}$ . However, the decay of the single top quark will still also produce one  $b$ -jet, meaning  
 1236 a  $b$  veto will reduce this background as well. Figure 3.3 shows the Feynman diagrams for  $t\bar{t}$  and  $Wt$  pro-  
 1237 duction.

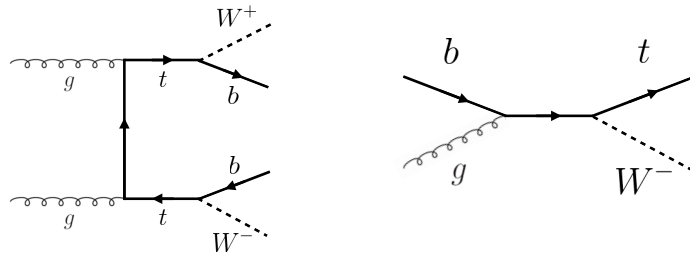


**Figure 3.3:** Feynman diagrams for top pair production (left) and  $Wt$  production (right)

### 1238 3.3.3 $W$ +JETS BACKGROUND

1239 Single  $W$  boson production, in association with jets, is a unique background. The other background  
 1240 considered so far have all included real leptons in the final state. In this case, however, only one real lep-  
 1241 ton from the decay of a  $W$  exists in the final state. The second reconstructed lepton can arise from two  
 1242 different cases. First, the lepton may truly be an algorithm “fake”, or a jet misidentified as a lepton by  
 1243 either the electron or muon reconstruction algorithms. Second, the lepton may be a real lepton but  
 1244 coming from semi-leptonic decays of particles inside the shower of the jet. This background can be re-  
 1245 duced by requiring that the reconstructed lepton have little activity surrounding it in the calorimeter  
 1246 (also known as an “isolated” lepton). Figure 3.4 shows the Feynman diagram for  $W$ +jets production.

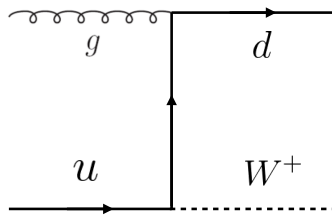


**Figure 3.4:** An example Feynman diagram of  $W$ +jets production

### 1247 3.3.4 $Z/\gamma^*$ +JETS BACKGROUND

1248 Production of a  $Z/\gamma^*$  in association with jets (also known as Drell-Yan) is also a background to Higgs  
 1249 production. In particular, the same flavor final states have a large  $Z$ +jets background, as the  $Z$  decays  
 1250 into two leptons of the same flavor. (This background also enters the different flavor final state through

the leptonic decays of  $Z \rightarrow \tau\tau$ ). Figure 3.5 shows the production of a  $Z$  in association with one jet. Because there are no neutrinos in this final state, variables like  $E_T^{\text{miss}}$  can be used to reduce the background.

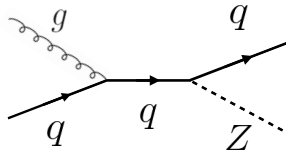


**Figure 3.5:** An example Feynman diagram of  $Z + \text{jets}$  production

### 3.3.5 OTHER (SUBDOMINANT) BACKGROUNDS

There are additional processes which contribute to the background composition but are not produced as frequently as those listed already. The first of these are referred to as  $VV$  or “Other diboson” processes and include multiple Standard Model diboson processes, including  $WZ$ ,  $ZZ$ ,  $W\gamma$ ,  $W\gamma^*$ , and  $Z\gamma$  production. Additionally, there is background from QCD multijet production, where two jets are misidentified as leptons.

Category	Process	Description
SM $WW$	$WW \rightarrow \ell\nu\ell\nu$	Real leptons and neutrinos
Top quark production	$t\bar{t} \rightarrow WbWb \rightarrow \ell\nu b\bar{\nu} b$ $tW \rightarrow WbW \rightarrow \ell\nu\ell\nu b$ $t\bar{b}, t\bar{q}\bar{b}$	Real leptons, untagged $b$ s Real leptons, untagged $b$ Untagged $b$ , jet misidentified as lepton
Drell-Yan	$Z/\gamma^* \rightarrow ee, \mu\mu$ $Z/\gamma^* \rightarrow \tau\tau \rightarrow \ell\nu\ell\nu$	“Fake” $E_T^{\text{miss}}$ Real leptons and neutrinos
Other dibosons	$ZZ \rightarrow \ell\ell\nu\nu$ $W\gamma^*, WZ \rightarrow \ell\nu\ell\ell, ZZ \rightarrow \ell\ell\ell\ell$ $W\gamma, Z\gamma$	Real leptons and neutrinos Unreconstructed leptons $\gamma$ reconstructed as $e$ , unreconstructed lepton
$W + \text{jets}$	$Wj \rightarrow \ell\nu j$	Jet reconstructed as lepton
QCD multijet	$jj$	Jets reconstructed as leptons

**Table 3.1:** A summary of backgrounds to the  $H \rightarrow WW^* \rightarrow \ell\nu\ell\nu$  signal

1259 **3.4 SHARED SIGNAL REGION SELECTION REQUIREMENTS**

1260 As presented in section 3.2, there are many different combinations of objects that can define a  $H \rightarrow$   
 1261  $WW^* \rightarrow \ell\nu\ell\nu$  final state. The multiplicity of jets and the flavor combinations of the leptons both lead  
 1262 to many potential signal regions. Additionally, signal regions can be optimized separately to be sensi-  
 1263 tive to the distinct production modes of the Higgs. Gluon fusion, vector boson fusion, and associated  
 1264 production of a Higgs all lead to unique final state topologies. Figure 3.6 delineates the different signal  
 1265 regions used in the gluon fusion and vector boson fusion  $H \rightarrow WW^*$  analyses. While there are different  
 1266 optimizations possible in each signal region, there are also some commonly shared selections that will be  
 1267 described here.

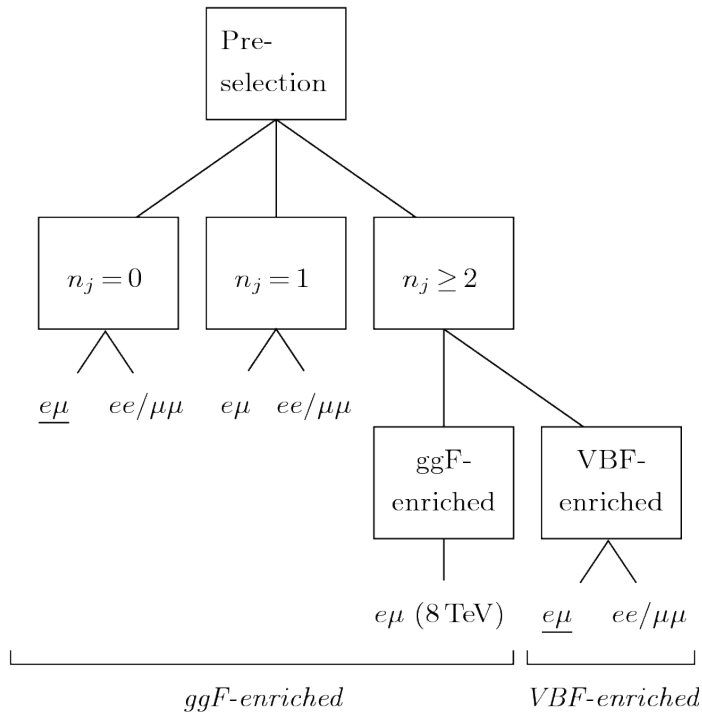


Figure 3.6: An illustration of the unique analysis signal regions [61]

1268 **3.4.1 EVENT PRE-SELECTION**

1269 Before being sorted into the distinct signal regions, basic requirements are applied on the reconstructed  
 1270 objects in the event to select Higgs-like event candidates. First, two oppositely charged leptons are re-

1271 quired.

1272 Once the leptons are selected, the last requirement for event pre-selection is the presence of neutrinos.  
1273 As neutrinos cannot be detected directly in ATLAS,  $E_T^{\text{miss}}$  can be used as a proxy for the combined neu-  
1274 trino momentum in the transverse plane. In general, it is expected that the signal should have a harder  
1275  $E_T^{\text{miss}}$  spectrum than backgrounds, especially if those backgrounds did not contain neutrinos. One ad-  
1276 ditional consideration when using  $E_T^{\text{miss}}$  is the fact that mis-measurements of objects in the detector  
1277 can lead to imbalances in the transverse plane that are not due to real particles escaping the detector.  
1278 One indicator that this is the case is that the  $E_T^{\text{miss}}$  vector in the transverse plane will be pointing in the  
1279 same direction as the mis-measured object. Therefore, a new variable,  $E_{T,\text{rel}}^{\text{miss}}$ , is used in the pre-selection.  
1280  $E_{T,\text{rel}}^{\text{miss}}$  is defined in equation 3.1.

$$E_{T,\text{rel}}^{\text{miss}} = \begin{cases} E_T^{\text{miss}} \sin \Delta\phi_{\text{near}} & \text{if } \Delta\phi_{\text{near}} < \pi/2 \\ E_T^{\text{miss}} & \text{otherwise,} \end{cases} \quad (3.1)$$

1281 If the closest object to the  $E_T^{\text{miss}}$  vector is within  $\pi/2$  radians in the transverse plane, the  $E_T^{\text{miss}}$  is pro-  
1282 jected away from this object. Otherwise, the normal  $E_T^{\text{miss}}$  vector is used. Figure 3.7 shows a graphical  
1283 illustration of this concept.

1284 Once both the lepton and  $E_T^{\text{miss}}$  pre-selections are made, the analysis can be divided into different  
1285 regions according to jet multiplicity.

### 1286 3.4.2 JET MULTIPLICITY

1287 Jet multiplicity, denoted as  $n_j$ , is used to sub-divide the analysis into its distinct signal regions. The rea-  
1288 son for this is twofold. First, different jet multiplicity bins will be more or less sensitive to different Higgs  
1289 production modes. For example, the  $n_j \geq 2$  region is more sensitive to VBF production because of  
1290 the two high momentum jets produced at matrix element level. For gluon fusion production to enter  
1291 this bin, two initial state radiation jets must be emitted. Second, background composition varies greatly  
1292 in different bins of  $n_j$ . Figure 3.8 shows the jet multiplicity in both the different flavor and same flavor  
1293 regions. It also shows the background composition in the bins of  $n_b$ . There are a few clear trends from

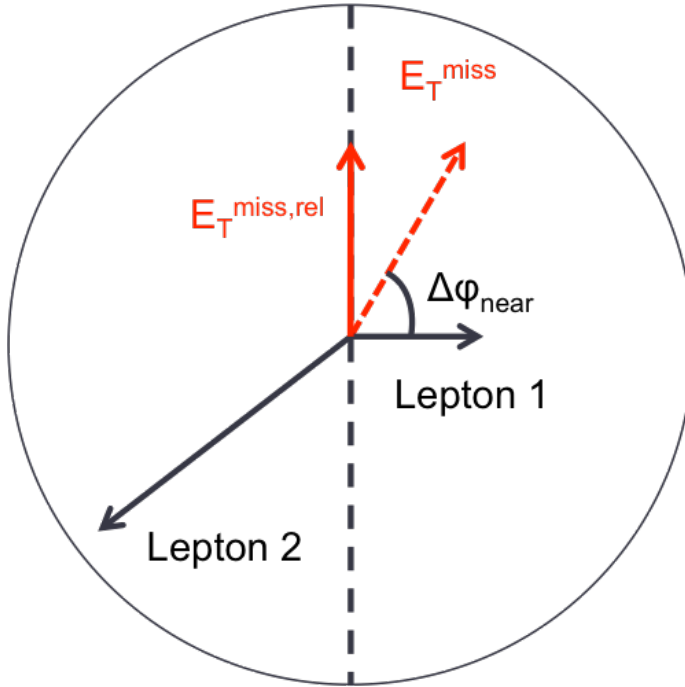


Figure 3.7: A graphical illustration of the  $E_{T,\text{rel}}^{\text{miss}}$  calculation

1294 this distribution. The first is that the Drell-Yan background dominates in the same flavor channels for  
 1295  $n_j \leq 1$ . Second, the top background becomes a clear contributor to the total background for  $n_j \geq 1$ .  
 1296 Lastly, the SM WW production dominates in the  $n_j = 0$  bin, as it is an irreducible background to  
 1297  $H \rightarrow WW^*$  production. Because of these distinct features, each jet multiplicity bin is treated separately.

### 1298 3.5 BACKGROUND REDUCTION IN SAME-FLAVOR FINAL STATES

1299 As described in section 3.4.2, the background composition of the same flavor final states is unique to that  
 1300 of the different flavor states. In particular, Drell Yan processes play a much larger role because the  $Z/\gamma^*$   
 1301 decays to same flavor leptons. Because real neutrinos are absent in the  $Z/\gamma^*$  decays to  $ee$  and  $\mu\mu$ , a re-  
 1302 quirement on  $E_T^{\text{miss}}$  should largely reduce the background. However, as this section will demonstrate,  
 1303 with increasing pileup conditions the resolution of the calorimeter-based  $E_T^{\text{miss}}$  degrades greatly. There-  
 1304 fore, two new variables for  $Z/\gamma^*$  background reduction are constructed and described in this section.

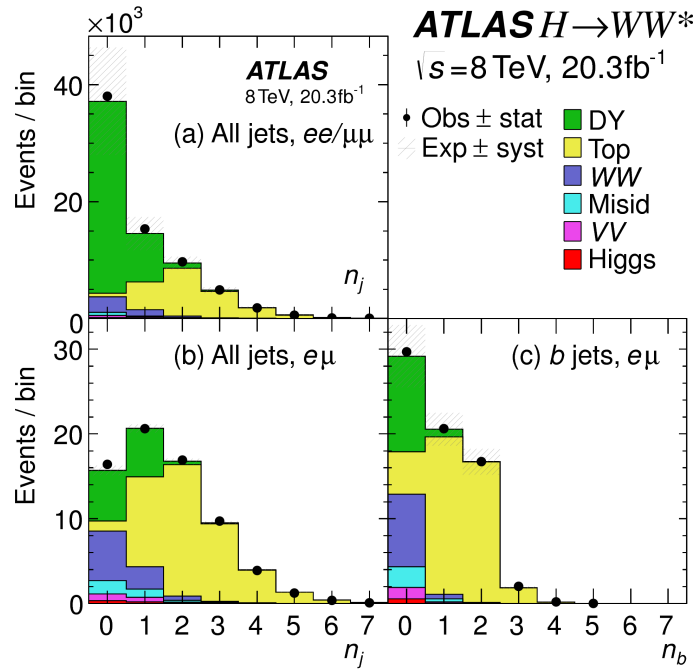


Figure 3.8: Predicted backgrounds (compared with data) as a function of  $n_j$  (a and b) and  $n_b$  (c)

### 3.5.1 PILEUP AND $E_T^{\text{miss}}$ RESOLUTION

Secondary interactions of protons in the colliding bunches of the LHC (known as pileup interactions, described in detail in Chapter 2) deposit energy into the ATLAS calorimeter on top of the energy that comes from the hard scatter process that is being searched for or analyzed. The calculation of  $E_T^{\text{miss}}$  is fundamentally Poissonian, as summing up all of the energy deposits in individual calorimeter cells or clusters is similar to a counting experiment. Thus, the energy resolution scales as  $\sqrt{E}$ , just as the error on a mean of  $N$  in a Poisson distribution is  $\sqrt{N}$ . As more energy is deposited in the calorimeter, the  $E_T^{\text{miss}}$  resolution degrades, meaning that the  $E_T^{\text{miss}}$  resolution is particularly sensitive to LHC instantaneous luminosity conditions.

Figure 3.9 shows an event display of a  $Z/\gamma^* + \text{jets}$  event candidate with the twenty-five reconstructed primary vertices. This display illustrates that while the interaction of interest only has tracks coming from the hardest primary vertex, all of the secondary interactions will deposit energy in the calorimeter as well.

Figure 3.10 shows the RMS of the  $E_T^{\text{miss}}$  distribution in  $Z \rightarrow \mu\mu$  events (where there are no real neu-

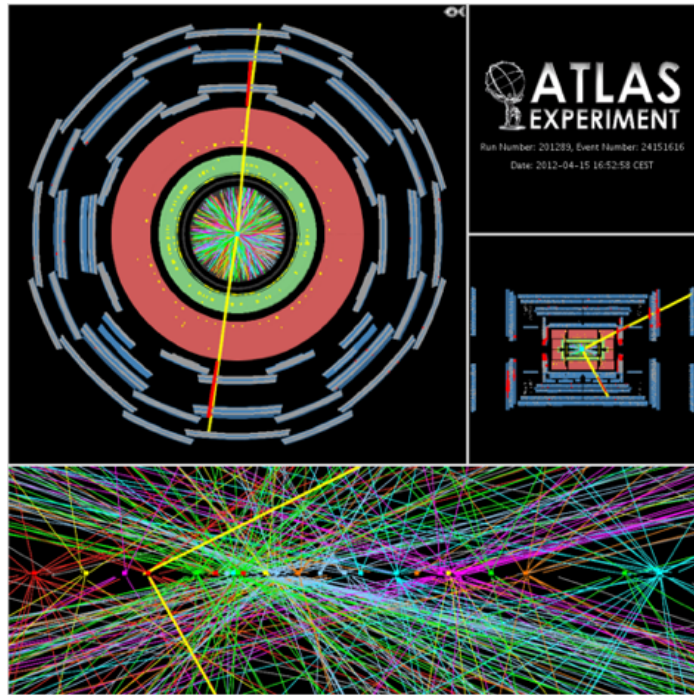


**Figure 3.9:** An event display of a  $Z/\gamma^*$  + jets event illustrating the effect of pileup interactions

trinos) as a function of the number of the average number of interactions. Under 2011 LHC conditions, this RMS was approximately 9 GeV, while under 2012 running conditions the resolution worsened to 12 GeV. This worsening dilutes the  $E_T^{\text{miss}}$  variable's ability to reduce the  $Z/\gamma^*$  background.

### 3.5.2 TRACK-BASED DEFINITIONS OF MISSING TRANSVERSE MOMENTUM

Because the increasing number of secondary proton-proton interactions degrades calorimeter-based  $E_T^{\text{miss}}$  resolution, a new variable using only contributions from the primary interaction vertex is necessary to further reduce the  $Z/\gamma^*$  background. While it is not possible to associate calorimeter energy deposits with a particular vertex, individual charged particle tracks in the Inner Detector are associated to unique vertices. Thus, two track-based definitions of missing transverse momentum , using only tracks coming from the primary vertex in the event, are used in the analysis. The simplest variable,  $p_T^{\text{miss}(\text{trk})}$ , is the vectorial sum of the  $p_T$  of all of the tracks from the primary vertex and the selected leptons (excluding the tracks associated with the selected leptons to avoid double counting). This is defined in equa-

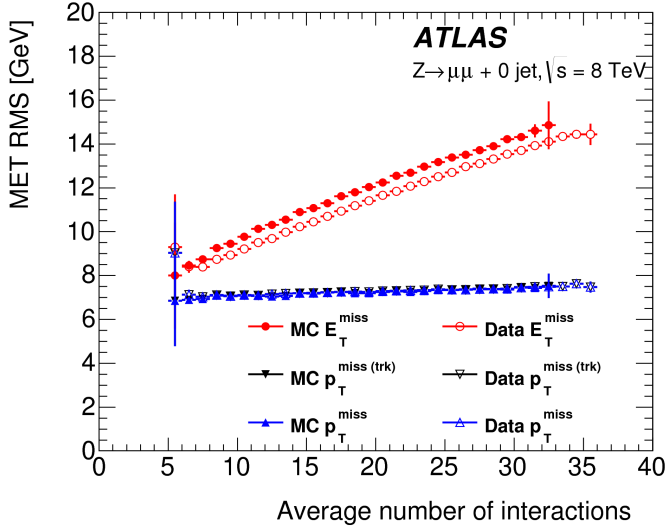


**Figure 3.10:** The RMS of different missing transverse momentum definitions as a function of the average number of interactions per bunch crossing

1331      tion 3.2.

$$p_T^{\text{miss}(\text{trk})} = - \left( \sum_{\text{selected leptons}} p_T + \sum_{\text{other tracks}} p_T \right), \quad (3.2)$$

1332      In events with hard jets, a better resolution on the missing transverse momentum is obtained by includ-  
 1333      ing the calorimeter based measurement of the hard jets rather than the track based measurements. Thus,  
 1334      another variable,  $p_T^{\text{miss}}$ , is defined, using the nominal measurements of  $p_T$  for the selected leptons and  
 1335      jets and using tracks rather than calorimeter clusters for the soft component of the missing transverse  
 1336      momentum . This is defined in equation 3.3.

$$p_T^{\text{miss}} = - \left( \sum_{\text{selected leptons}} p_T + \sum_{\text{selected jets}} p_T + \sum_{\text{other tracks}} p_T \right), \quad (3.3)$$

1337      Figure 3.10 illustrates that these two new variables accomplish their intended purpose. The resolution  
 1338      as a function of mean number of interactions for both  $p_T^{\text{miss}(\text{trk})}$  and  $p_T^{\text{miss}}$  is much flatter compared to  
 1339      the dependence for  $E_T^{\text{miss}}$ . Figure 3.11a shows the difference between the true and reconstructed values of  
 1340      missing transverse momentum using both the track-based  $p_T^{\text{miss}}$  and calorimeter based  $E_T^{\text{miss}}$ . The RMS  
 1341      of the distribution improves by 3.5 GeV when using  $p_T^{\text{miss}}$ .

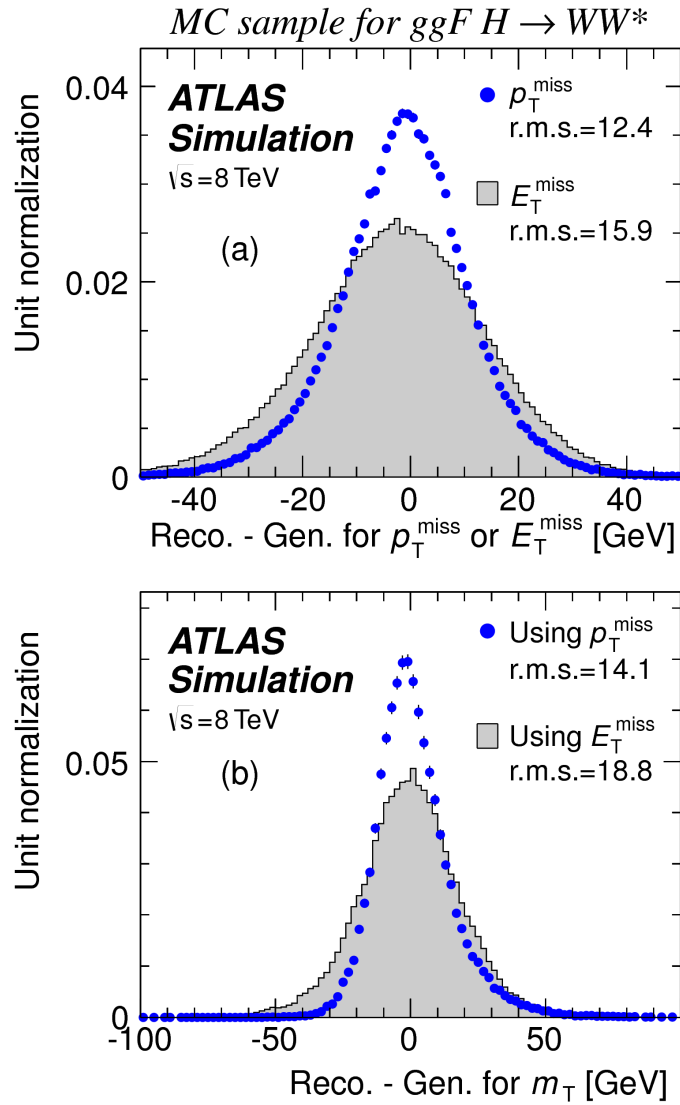


**Figure 3.11:** The difference between the true and reconstructed values of the missing transverse momentum (a) and  $m_T$  (b) in a gluon fusion signal sample

### 1342 3.5.3 DISTINGUISHING $Z/\gamma^*$ +JETS AND $H \rightarrow WW^*$ TOPOLOGIES

1343 The track-based definitions of missing transverse momentum were constructed to mitigate degrading  
 1344 performance as a function of pileup. However, an additional variable can be constructed to exploit kine-  
 1345 matic and topological differences between the  $Z/\gamma^*$  background and  $H \rightarrow WW^*$  signal. Because there  
 1346 are no real neutrinos in the final state (in the case of  $Z/\gamma^* \rightarrow ee, \mu\mu$  decays), the dilepton system of a  
 1347  $Z/\gamma^*$  will be balanced with the jets produced in the hard scatter. A new variable,  $f_{\text{recoil}}$ , is constructed

1348 to estimate the balance between the dilepton system and the jets in the quadrant opposite the dilepton  
 1349 vector in the transverse plane. It is defined in equation 3.4. The numerator of  $f_{\text{recoil}}$  is the magnitude of  
 1350 the vectorial sum of the  $p_T$  of jets in the quadrant opposite the dilepton system, weighted by each jet's Jet  
 1351 Vertex Fraction (JVF, described in chapter 2). The denominator is the magnitude of the dilepton  $p_T$ .

$$f_{\text{recoil}} = \left| \sum_{\text{jets } j \text{ in } \wedge} \text{JVF}_j \cdot \mathbf{p}_T^j \right| / p_T^{\ell\ell}. \quad (3.4)$$

1352 Figure 3.12 shows a shape comparison of the distribution of  $f_{\text{recoil}}$  in a simulated  $Z/\gamma^* + \text{jets}$  sample, a  
 1353  $H \rightarrow WW^*$  signal sample, and other backgrounds that contain real neutrinos. The  $Z/\gamma^* + \text{jets}$  events  
 1354 tend to be more balanced between the dilepton system and recoiling jets, while the processes containing  
 1355 real neutrinos are less balanced in the transverse plane. Thus, a requirement on  $f_{\text{recoil}}$  will also reduce  
 1356 the  $Z/\gamma^* + \text{jets}$  background while maintaining a good signal efficiency.

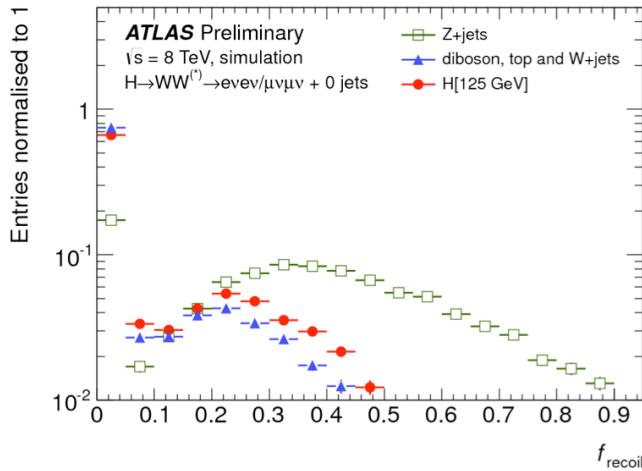


**Figure 3.12:** Comparison of  $f_{\text{recoil}}$  distributions for  $Z/\gamma^* + \text{jets}$ ,  $H \rightarrow WW^*$ , and other backgrounds with real neutrinos.

### 1357 3.5.4 OPTIMIZING BACKGROUND REDUCTION SELECTION REQUIREMENTS

1358 The requirements on  $p_T^{\text{miss(trk)}}$  and  $f_{\text{recoil}}$  used to reduce the  $Z + \text{jets}$  background must be optimized  
 1359 to maximize their efficacy. Figure 3.13 shows an early attempt to optimize the combination of the two  
 1360 requirements in the gluon fusion zero jet bin. Each bin shows the expected signal significance if the

1361  $p_{T,\text{rel}}^{\text{miss}(\text{trk})}$  is required to be greater than the left edge of the bin and the  $f_{\text{recoil}}$  is required to be less than  
 1362 the top edge of the bin. The figure shows that the best signal significance comes from requiring low val-  
 1363 ues of  $f_{\text{recoil}}$  ( $< 0.05$ ) and  $p_{T,\text{rel}}^{\text{miss}(\text{trk})}$  values greater than 45 GeV.

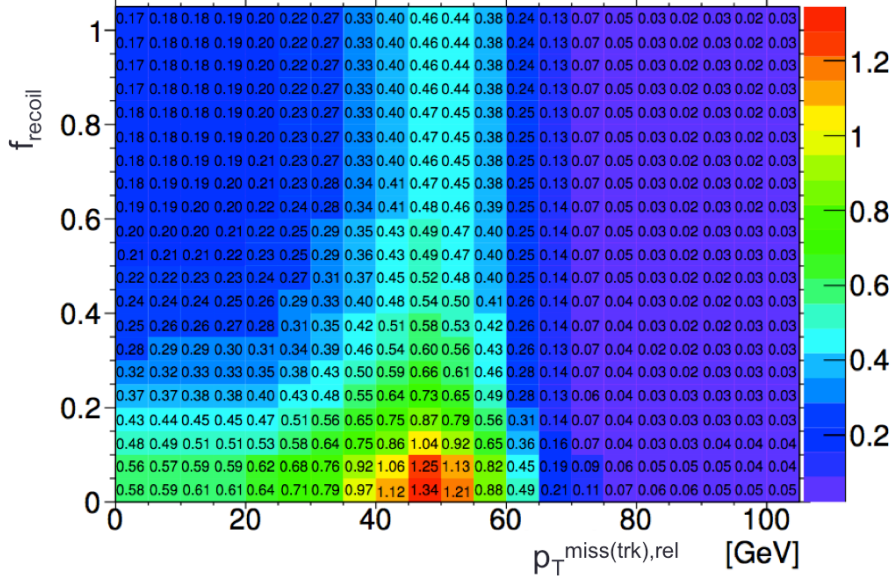


**Figure 3.13:** Signal significance as a function of required value for  $f_{\text{recoil}}$  and  $p_{T,\text{rel}}^{\text{miss}(\text{trk})}$  in the ggF  $H \rightarrow WW^*$  with  
 $n_j = 0$

### 1364 3.6 PARAMETERS OF INTEREST AND STATISTICAL TREATMENT

1365 As with any search or measurement, there are particular parameters of the Higgs that the  $H \rightarrow WW^*$   
 1366 analysis is interested in measuring. In this case, the parameters of interest are the mass of the Higgs bo-  
 1367 son and its production cross section. Because the  $H \rightarrow WW^* \rightarrow \ell\nu\ell\nu$  process does not have a closed  
 1368 final state, it is not possible to measure the full invariant mass of the particle that may have produced  
 1369 the final state. However, a proxy for the invariant mass using transverse plane information can be de-  
 1370 fined. This is described in more detail in section 3.6.1. The second parameter of interest is the ratio of the  
 1371 measured cross section to that expected from the Standard Model Higgs, which is denoted a  $\mu$ . This is  
 1372 defined in equation 3.5.

$$\mu = \frac{\sigma}{\sigma_{\text{SM}}} \quad (3.5)$$

1373 All of the likelihoods used in the statistical analysis of the final signal region events are parameterized as a  
 1374 function of  $\mu$ .  $\mu$  is a natural variable for hypothesis testing, as  $\mu = 0$  corresponds to a background only  
 1375 hypothesis and  $\mu = 1$  corresponds exactly to a Standard Model Higgs.

1376 **3.6.1 TRANSVERSE MASS**

1377 Because the longitudinal information about the neutrinos is not attainable, the  $H \rightarrow WW^* \rightarrow \ell\nu\ell\nu$   
 1378 analysis uses a mass variable, the transverse mass, that exploits information in the transverse plane as a  
 1379 proxy for the full invariant mass. The transverse mass is defined in equation 3.6.

$$m_T = \sqrt{(E_T^{\ell\ell} + p_T^{\text{miss}})^2 - |\vec{p}_T^{\ell\ell} + \vec{p}_T^{\text{miss}}|^2}, \quad (3.6)$$

1380 Here the  $E_T^{\ell\ell}$  and  $p_T^{\ell\ell}$  are the transverse energy and momentum of the dilepton system, while  $p_T^{\text{miss}}$  is a  
 1381 proxy for the transverse momentum of the di-neutrino system. The track-based  $p_T^{\text{miss}}$  is used in the  $m_T$   
 1382 rather than the calorimeter based  $E_T^{\text{miss}}$  because it has a better resolution on the true transverse mass.  
 1383 Figure 3.11b shows the improvement in the RMS of the difference between the true and reconstructed  
 1384 transverse mass in a ggF signal sample. The RMS improves by 4.7 GeV using  $p_T^{\text{miss}}$  in the  $m_T$  calcula-  
 1385 tion.

1386 **3.6.2 STATISTICAL TREATMENT<sup>\*</sup>**

1387 **LIKELIHOOD FUNCTION**

1388 The statistical analysis of final event candidates is framed as a hypothesis test, where the null hypothe-  
 1389 sis is background-only (no Standard Model Higgs). The first step in the analysis is to form a likelihood  
 1390 function for the data. In its simplest form, this likelihood is the probability of observing the number  
 1391 of events seen in the final signal region given knowledge of the signal strength. Because observation of  
 1392 events is fundamentally a Poisson counting experiment, this simple likelihood can be expressed as a Pois-  
 1393 son probability of observing  $N$  events given a total number of predicted signal and background events.

---

\*Many thanks to Aaron Armbruster, whose thesis [62] inspired parts of this section.

1394 This basic likelihood is shown in equation 3.7.

$$\mathcal{L}(\mu) = P(N|\mu S + B) \quad (3.7)$$

1395 Here,  $P$  is the Poisson probability density function,  $N$  is the total number of observed events,  $\mu$  is the  
1396 signal strength,  $S$  is the predicted number of signal events, and  $B$  is the predicted number of back-  
1397 ground events.

1398 In particle physics, certain background estimates are commonly normalized in so-called “control” re-  
1399 gions and those predictions are scaled by the same normalization factor in the signal region. This leads  
1400 to a slightly more complicated likelihood, which is a function of both the signal strength and the back-  
1401 ground normalization. This is shown in equation 3.8.

$$\mathcal{L}(\mu, \theta) = P(N|\mu S + \theta B) P(N_{\text{CR}}|\theta B_{\text{CR}}) \quad (3.8)$$

1402 Here,  $\theta$  is a so-called “nuisance parameter”, a parameter that is not a primary parameter of interest but  
1403 still enters the likelihood. The second Poisson term adds an extra term to the likelihood, enforcing the  
1404 fact that the background normalization must be consistent with the number of observed events in data  
1405 in the control region,  $N_{\text{CR}}$ .

1406 So far, these two formulations of likelihoods have assumed a single signal region and do not take into  
1407 account any shape information of potential discriminating variables. The  $H \rightarrow WW^*$  analysis is di-  
1408 vided into many different categories, and we can perform the same counting experiment described above  
1409 in each individual category. As mentioned in section 3.6.1, the transverse mass is used as the primary dis-  
1410 criminating variable in many of the  $H \rightarrow WW^*$  sub-analyses, so additionally we can perform the same  
1411 counting experiment in each bin of the  $m_T$  distribution to incorporate some shape information. Thus,  
1412 the total likelihood becomes a product over signal regions and bins of the  $m_T$  distribution. Finally, there  
1413 are usually many backgrounds that are normalized in control regions, so the new formulation of the like-  
1414 lihood takes this into account as well by including a product over control regions in the second Poisson

<sup>1415</sup> term. All of these modifications are shown in equation 3.9.

$$\mathcal{L}(\mu, \theta) = \prod_{\substack{\text{SRs i} \\ \text{bins b}}} P\left(N_{ib} \middle| \mu S_{ib} + \sum_{\text{bkg k}} \theta_k B_{kib}\right) \prod_{\text{CRs l}} P\left(N_l \middle| \sum_{\text{bkg k}} \theta_k B_{kl}\right) \quad (3.9)$$

<sup>1416</sup> The final step to get the full likelihood used in the analysis is to add nuisance parameters for the sys-  
<sup>1417</sup> tematic uncertainties. In cases where the uncertainty does not affect the shape of  $m_T$  bin-by-bin, each  
<sup>1418</sup> systematic uncertainty  $\epsilon$  is allowed to affect the expected event yields through a linear response function  
<sup>1419</sup> of the nuisance parameter, namely  $\nu(\theta) = (1 + \epsilon)\theta$ . If instead the uncertainty does affect the shape,  
<sup>1420</sup> the effect is instead parameterized by  $\nu_b(\theta) = 1 + \epsilon_b\theta$ . The value of the nuisance parameters for the  
<sup>1421</sup> systematic uncertainty are constrained with a Gaussian term that is added to the likelihood as well. This  
<sup>1422</sup> is of the form  $g(\delta|\theta) = e^{-(\delta-\theta)^2/2}/\sqrt{2\pi}$ , where  $\delta$  is the central value and  $\theta$  is a nuisance parameter.  
<sup>1423</sup> Finally, a last term is added to account for the statistical uncertainty in the Monte Carlo samples used,  
<sup>1424</sup> which adds an additional poisson term. The full likelihood used in the final statistical analysis is defined  
<sup>1425</sup> in equation 3.10.

$$\begin{aligned} \mathcal{L}(\mu, \theta) = & \prod_{\substack{\text{SRs i} \\ \text{bins b}}} P\left(N_{ib} \middle| \mu S_{ib} \cdot \prod_{\substack{\text{sig.} \\ r}} \nu_{br}(\theta_r) + \sum_{\text{bkg k}} \theta_k B_{kib} \cdot \prod_{\substack{\text{bkg.} \\ s}} \nu_{bs}(\theta_s)\right) \\ & \cdot \prod_{\text{CRs l}} P\left(N_l \middle| \sum_{\text{bkg k}} \theta_k B_{kl}\right) \\ & \cdot \prod_{\substack{\text{syst} \\ t}} g(\delta_t|\theta_t) \cdot \prod_{\text{bkg k}} P(\xi_k|\zeta_k \theta_k) \end{aligned} \quad (3.10)$$

<sup>1426</sup> In the fourth term of the equation, quantifying uncertainty due to finite Monte Carlo sample size,  $\xi$   
<sup>1427</sup> represents the central value of the background prediction,  $\theta$  is the associated nuisance parameter,  $\zeta =$   
<sup>1428</sup>  $(B/\delta B)^2$ , where  $\delta B$  is the statistical uncertainty of  $B$ .

<sup>1429</sup> The best fit value of the signal strength  $\mu$  is determined by finding the values of  $\mu$  and  $\theta$  that maxi-  
<sup>1430</sup> mize the likelihood, while setting  $\delta = 0$  and  $\xi = \zeta$ . Once the likelihood is defined, a test statistic must

1431 be built for use in hypothesis testing.

1432 TEST STATISTIC

1433 To distinguish whether the data match a background only or background and signal hypothesis, a test  
1434 statistic must be used. The  $H \rightarrow WW^*$  analysis used the profile likelihood technique [63]. The first  
1435 step in formulating this test statistic is to define the profile likelihood ratio, shown in equation 3.n.

$$\lambda(\mu) = \frac{\mathcal{L}(\mu, \hat{\theta}_\mu)}{\mathcal{L}(\hat{\mu}, \hat{\theta})} \quad (3.n)$$

1436 Here  $\hat{\theta}_\mu$  is the value of  $\theta$  that maximizes the likelihood for the choice of  $\mu$  being tested. Additionally,  $\hat{\theta}$   
1437 and  $\hat{\mu}$  represent the values of  $\theta$  and  $\mu$  that gives the overall maximum value of the likelihood.

1438 Once this is defined, a test statistic  $q_\mu$  is constructed. This is shown in equation 3.12.

$$q_\mu = -2 \ln \lambda(\mu) \quad (3.12)$$

1439 A higher value of  $q_\mu$  means that the data are more incompatible with the hypothesized value of  $\mu$ , and  
1440  $q_0$  then corresponds to the value of the test statistic for the background only hypothesis. A  $p_0$  value is  
1441 then defined to quantify the compatibility between the data and the null hypothesis. The  $p_0$  value is the  
1442 probability of obtaining a value of  $q_0$  larger than the observed value, and this is shown in equation 3.13.

$$p_0 = \int_{q_0^{\text{obs}}}^{\infty} f(q_\mu | \mu = 0) dq_\mu \quad (3.13)$$

1443 Here  $f(q_\mu)$  is the probability distribution function of the test statistic. Finally, the  $p_0$  value can be con-  
1444 verted into a signal significance, using the formula in equation 3.14, or the one-sided tail of the Gaussian  
1445 distribution.

$$Z_0 = \sqrt{2} \operatorname{erf}^{-1}(1 - 2p_0) \quad (3.14)$$

1446 The threshold for discovery used in particle physics is  $Z_0 \geq 5$ , more commonly known as a value of  $5\sigma$ .

*The real voyage of discovery consists not in seeking new landscapes, but in having new eyes.*

Marcel Proust

# 4

1447

1448

## The discovery of the Higgs boson and the role of the $H \rightarrow WW^* \rightarrow \ell\nu\ell\nu$ channel

1449

### 1450 4.1 INTRODUCTION

1451 This chapter presents the results of the search for the Higgs boson in  $4.8 \text{ fb}^{-1}$  collected at  $\sqrt{s} = 7 \text{ TeV}$   
1452 and  $5.8 \text{ fb}^{-1}$  at  $\sqrt{s} = 8 \text{ TeV}$ . The results of three searches at  $\sqrt{s} = 8 \text{ TeV}$  in the  $H \rightarrow WW^* \rightarrow \ell\nu\ell\nu$   
1453 ,  $H \rightarrow \gamma\gamma$ , and  $H \rightarrow ZZ \rightarrow 4\ell$  channels are combined with results of searches at  $\sqrt{s} = 7 \text{ TeV}$   
1454 in the same search channels (as well as the  $H \rightarrow \tau\tau$  production and associated production searches for  
1455  $H \rightarrow b\bar{b}$ ). The results of this combination are a  $5.9\sigma$  detection of a new particle consistent with a Higgs  
1456 boson. Rather than going into detail for all of the different Higgs decay searches, this chapter will discuss  
1457 the three most sensitive channels and in particular focus on  $H \rightarrow WW^* \rightarrow \ell\nu\ell\nu$ . While the focus is  
1458 on  $WW^*$ , some of the  $ZZ^*$  and  $\gamma\gamma$  results are shown for completeness. The results not discussed here

1459 can be found in the ATLAS Higgs discovery publication [1].

1460 **4.2 DATA AND SIMULATION SAMPLES**

1461 The data sample used for the following results was taken in 2011 and 2012 at center of mass energies of 7  
1462 and 8 TeV, respectively, with  $4.8 \text{ fb}^{-1}$  collected at 7 TeV and  $5.8 \text{ fb}^{-1}$  collected at 8 TeV. Higgs pro-  
1463 duction in the gluon fusion and vector boson fusion modes is modeled with **POWHEG** for the hard scat-  
1464 tering event and **PYTHIA** for the showing and hadronization. Associated production of a Higgs with a  
1465 vector boson or top quarks is modeled via **PYTHIA**. Table 4.1 shows the Monte Carlo generators used for  
1466 modeling the signal and background processes relevant for the three analyses to be discussed.

Process	Generator
$ggF, VBF H$	<b>POWHEG + PYTHIA</b>
$WH, ZH, t\bar{t}H$	<b>PYTHIA</b>
$W + \text{jets}, Z/\gamma^* + \text{jets}$	<b>ALPGEN + HERWIG</b>
$t\bar{t}, tW, tb$	<b>MC@NLO + HERWIG</b>
$tqb$	<b>ACERMC + PYTHIA</b>
$q\bar{q} \rightarrow WW$	<b>MC@NLO + HERWIG</b>
$gg \rightarrow WW$	<b>GG2WW+ HERWIG</b>
$q\bar{q} \rightarrow ZZ$	<b>POWHEG + PYTHIA</b>
$gg \rightarrow ZZ$	<b>GG2ZZ+ HERWIG</b>
$WZ$	<b>MADGRAPH+ PYTHIA , HERWIG</b>
$W\gamma + \text{jets}$	<b>ALPGEN + HERWIG</b>
$W\gamma^*$	<b>MADGRAPH+ PYTHIA</b>
$q\bar{q}/gg \rightarrow \gamma\gamma$	<b>SHERPA</b>

**Table 4.1:** Monte carlo generators used to model signal and background for the Higgs search [1].

1467 **4.3  $H \rightarrow WW \rightarrow e\nu\mu\nu$  SEARCH**

1468 The  $H \rightarrow WW \rightarrow e\nu\mu\nu$  search is unique compared to the  $ZZ$  and  $\gamma\gamma$  channels. The Higgs mass can-  
1469 not be fully reconstructed due to the presence of neutrinos in the final state, so the transverse mass  $m_T$   
1470 is used as the final discriminating variable. Compared to the other channels, there are more backgrounds  
1471 here as well, as discussed in chapter 3. The same flavor final states are excluded from this search due to  
1472 high pileup in the 8 TeV dataset.

1473 4.3.1 EVENT SELECTION

1474 The analysis requires two opposite charge isolated leptons, with the leading (sub-leading) lepton required  
 1475 to have  $p_T > 25(15)$  GeV. The events are separated into different signal regions depending on which  
 1476 flavor of lepton is leading ( $e\mu$  for leading electron,  $\mu e$  for leading muon). Strict lepton quality cuts are  
 1477 applied to the sample to reduce backgrounds from fake leptons.

1478 Jets are reconstructed with the anti- $k_T$  algorithm with a radius parameter  $R = 0.4$ . The jets are  
 1479 required to have  $p_T > 25$  GeV and  $|eta| < 4.5$ , with jets in the tracking volume required to have a  
 1480 jet vertex fraction of 0.5 and jets in the forward region required to have  $p_T > 30$  GeV. The analysis is  
 1481 separated into three different signal regions based on jet multiplicity:  $n_j = 0, 1, \geq 2$ .

1482 To indicate the presence of neutrinos in the event, a requirement of  $E_{T,\text{rel}}^{\text{miss}} > 25$  GeV is made\*. This  
 1483 requirement significantly reduces the QCD multijet and  $Z/\gamma^* + \text{jets}$  backgrounds. Figure 4.1 shows the  
 1484 distribution of  $n_j$  in data and simulation after applying these “pre-selection” requirements.

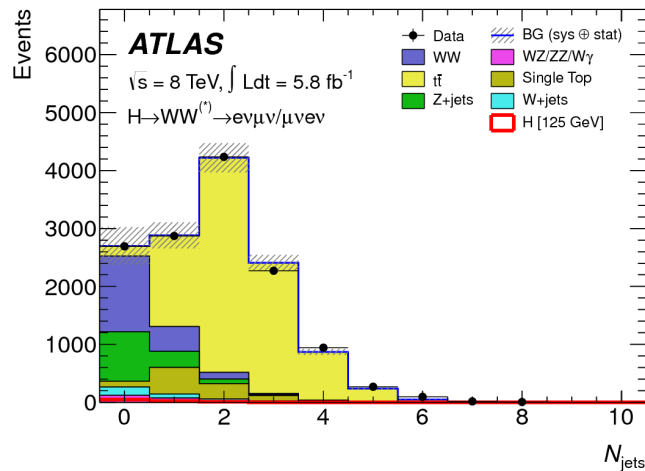


**Figure 4.1:** Jet multiplicity distribution in data and MC after applying lepton, jet, and  $E_{T,\text{rel}}^{\text{miss}}$  selections. The  $WW$  and top backgrounds have been normalized using control samples, and the hashed band indicates the total uncertainty on the prediction. [1]

1485 Additional selections are applied to require the dilepton topology to correspond to that of a SM  
 1486 Higgs. The requirements are presented here - more detailed discussion on the motivation for each re-  
 1487 quirement is saved for Chapter 5. In all of the jet multiplicity channels, the dilepton system is required to

\*For the definition of  $E_{T,\text{rel}}^{\text{miss}}$ , see chapter 3

1488 have a small gap in azimuthal angle,  $\Delta\phi_{\ell\ell} < 1.8$ . Similarly, the  $m_{\ell\ell}$  is required to be less than 50 GeV  
1489 in the lower jet multiplicity channels and less than 80 GeV in the  $n_j \geq 2$  channel. In the  $n_j = 0$  chan-  
1490 nel, the magnitude of the dilepton  $p_T$ ,  $p_T^{\ell\ell}$ , is required to be greater than 30 GeV.

1491 In the higher jet multiplicity channels ( $n_j \geq 1$ ), the top background is a more important component  
1492 and must be reduced. The total transverse momentum  $p_T^{\text{sum}}$  is thus required to be less than 30 GeV.  
1493 Additionally, the di- $\tau$  invariant mass  $m_{\tau\tau}$  (dilepton mass computed under the assumption that the neu-  
1494 trinos from the  $\tau$  decay are emitted collinear to the charged leptons) is used to reject  $Z \rightarrow \tau\tau$  events by  
1495 requiring  $|m_{\tau\tau} - m_Z| > 25$  GeV. These variables are also discussed in more detail in Chapter 5.

1496 In the  $n_j \geq 2$  channel, requirements are made to isolate the VBF contribution to Higgs production.  
1497 The kinematics of the two leading jets are used to make these requirements. In particular, the event must  
1498 have  $\Delta y_{jj} > 3.8$  and  $m_{jj} > 500$  GeV, along with a veto on having any additional jets with rapidity  
1499 between the two leading jets.

#### 1500 4.3.2 BACKGROUND ESTIMATION

1501 The details of the background estimation techniques used in the  $H \rightarrow WW^* \rightarrow \ell\nu\ell\nu$  analysis are dis-  
1502 cussed in section 5.5. As that section refers to a later iteration of the analysis, a general discussion is given  
1503 here for completeness. The dominant backgrounds are SM  $WW$  production and top (both pair and  
1504 single) production, and these backgrounds have their normalizations estimated from dedicated control  
1505 regions while their shapes are taken from simulation.

1506 The control sample for the Standard Model  $WW$  background is defined by making the same require-  
1507 ments as the signal region with the  $m_{\ell\ell}$  requirement inverted (now requiring  $m_{\ell\ell} > 80$  GeV) and  
1508 removing the  $\Delta\phi_{\ell\ell}$  requirement. This creates a control sample that is 70% (40%) pure in the 0(1)-jet  
1509 region. The correction to the pure MC-based background estimate is quantified by defining a normal-  
1510 ization factor  $\beta$  which is the ratio of the data yield to the MC yield ( $N_{\text{data}}/N_{\text{MC}}$ ) in this control sample.  
1511 Table 4.2 shows the  $WW$  normalization factors in the  $n_j = 0$  and  $n_j = 1$  bins (the  $n_j \geq 2$  estimate is  
1512 taken directly from MC).

1513 The top background estimate is also computed separately in each jet multiplicity bin. In the  $n_j = 0$

$n_j$	$\beta_{WW}$	$\beta_t$
= 0	$1.06 \pm 0.06$	$1.11 \pm 0.06$
= 1	$0.99 \pm 0.15$	$1.11 \pm 0.05$
$\geq 2$	-	$1.01 \pm 0.26$

**Table 4.2:** Normalization factors (ratio of data and MC yields in a control sample) for the Standard Model  $WW$  and top backgrounds in the  $H \rightarrow WW^* \rightarrow \ell\nu\ell\nu$  analysis [1]. Only statistical uncertainties are shown.

channel, the background is first normalized using data after pre-selection requirements with no selection on  $n_j$ . Then, a dedicated  $b$ -tagged control sample is used to evaluate the ratio of one-jet to two-jet events in data. The details of this technique are shown in reference [64]. In the  $n_j = 1$  and the  $n_j \geq 2$  regions, the top background is normalized in a control sample where the signal region selections are applied, but the  $b$ -jet veto is reversed and the Higgs topology requirements on  $m_{\ell\ell}$  and  $\Delta\phi_{\ell\ell}$  are removed. The resulting normalization factors for these techniques are shown in table 4.2.

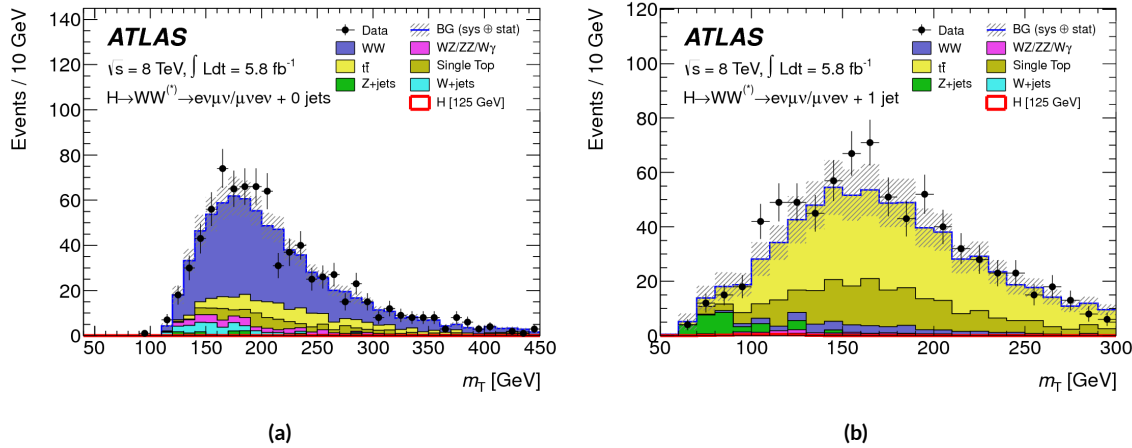


**Figure 4.2:** Comparison of  $m_T$  between data and simulation in the  $n_j = 0$   $WW$  (a) and  $n_j = 1$  top (b) control samples [1]

The control samples which are used for background normalization can also be used to validate the modeling of the  $m_T$  distribution for each background. Figure 4.2 shows the comparison between data and MC for the  $m_T$  distribution after correcting the normalization of the backgrounds in the  $WW$  and top control regions. Good agreement between data and simulation is seen in both cases.

The  $W+jets$  background estimate is taken entirely from data using a control sample with one well reconstructed lepton and one anti-identified lepton. All other backgrounds are taken purely from simu-

1526 lation.

1527 **4.3.3 SYSTEMATIC UNCERTAINTIES**

1528 The systematic uncertainties that have the largest impact on the analysis are the theoretical uncertainties  
1529 associated with the signal cross section, and these are shared with the  $ZZ^*$  and  $\gamma\gamma$  channels. The un-  
1530 certainties resulting from variations of the QCD scale are  $+7\% / -8\%$  on the final singal yield. Those  
1531 coming from variations of the parton distribution function (PDF) used in the simulation add a  $\pm 8\%$   
1532 uncertainty on the yield. The uncertainties on the branching ratios of the Higgs are  $\pm 5\%$ .

1533 The main experimental uncertainties come from variations of the jet energy scale (JES), jet energy  
1534 resolution, pile-up,  $E_T^{\text{miss}}$ ,  $b$ -tagging efficiency,  $W + \text{jets}$  background estimate, and integrated luminosity.  
1535 For more details, see reference [1].

1536 **4.3.4 RESULTS**

1537 Table 4.3 shows the signal and background yields in the final signal region after normalizing the back-  
1538 grounds according to the methods described above.

	$n_j = 0$	$n_j = 1$	$n_j \geq 2$
Signal	$20 \pm 4$	$5 \pm 2$	$0.34 \pm 0.07$
$WW$	$101 \pm 13$	$12 \pm 5$	$0.10 \pm 0.14$
Other dibosons	$12 \pm 3$	$1.9 \pm 1.1$	$0.10 \pm 0.10$
$t\bar{t}$	$8 \pm 2$	$6 \pm 2$	$0.15 \pm 0.10$
Single top	$3.4 \pm 1.5$	$3.7 \pm 1.6$	-
$Z/\gamma^* + \text{jets}$	$1.9 \pm 1.3$	$0.10 \pm 0.10$	-
$W + \text{jets}$	$15 \pm 7$	$2 \pm 1$	-
Total background	$142 \pm 16$	$26 \pm 6$	$0.35 \pm 0.18$
Observed in data	185	38	0

**Table 4.3:** Data and expected yields for signal and background in the final  $H \rightarrow WW^* \rightarrow \ell\nu\ell\nu$  signal region.  
Uncertainties shown are both statistical and systematic. [1]

1539 Figure 4.3 shows the  $m_T$  distribution in the  $n_j \leq 1$  channels for 8 TeV data. (No events are observed  
1540 in data in the  $n_j \geq 2$  channels in this dataset). The excess shown here relatively flat as a function of  
1541 hypothesized Higgs mass. The combined 7 and 8 TeV data gives an excess with local significance of  $2.8\sigma$   
1542 with an expected significance of  $2.3\sigma$ , corresponding to a  $\mu$  measurement of  $1.3 \pm 0.5$ .

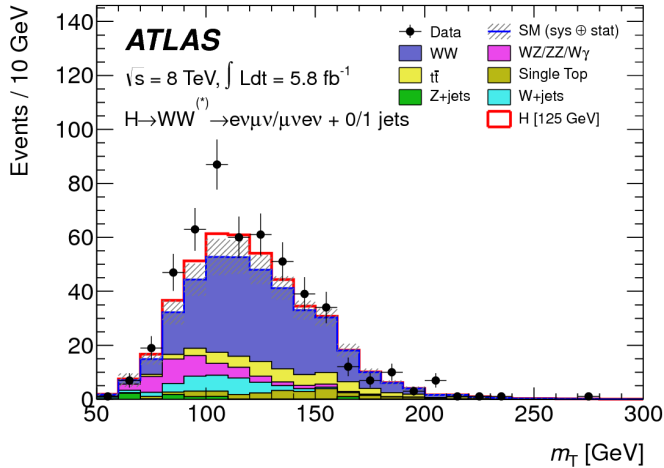


**Figure 4.3:**  $m_T$  distribution in the  $H \rightarrow WW \rightarrow e\nu\mu\nu n_j \leq 1$  channels for 8 TeV data [1].

#### 1543 4.4 $H \rightarrow \gamma\gamma$ SEARCH

1544 The  $H \rightarrow \gamma\gamma$  search is in essence a search for a peaked excess above the falling SM diphoton mass spec-  
 1545 trum, with  $m_{\gamma\gamma}$  as the ultimate discriminating variable. Events are selected by requiring two isolated  
 1546 photons, with the leading (sub-leading) photon required to have  $E_T > 40(30)$  GeV. In the 8 TeV  
 1547 data, the photons are required to pass cut-based identification criteria consistent with a photon in the  
 1548 electromagnetic calorimeter and little leakage in the hadronic calorimeter.

1549 The main challenges for this analysis are accurate mass reconstruction and background estimation.  
 1550 In order to accurately reconstruct the invariant mass of the di-photon system, both the energy and di-  
 1551 rection of the photons must be measured well. Therefore, the identification of the primary vertex of the  
 1552 hard interaction is particularly important, and is done using a multivariate likelihood which combines  
 1553 information about the photon direction and vertex position. The background is modeled with a falling  
 1554 spectrum in  $m_{\gamma\gamma}$  that is parameterized by different functions depending on the category of the event.

##### 1555 4.4.1 RESULTS

1556 The resulting diphoton mass spectrum is shown in figure 4.4. The best fit mass value in the  $\gamma\gamma$  channel  
 1557 alone in the combined 7 and 8 TeV data is 126.5 GeV. The local significance at this point is  $4.5\sigma$ , with  
 1558 an expected significance of  $2.5\sigma$ . Therefore, the measured signal strength  $\mu$  is  $1.8 \pm 0.5$  in this channel.

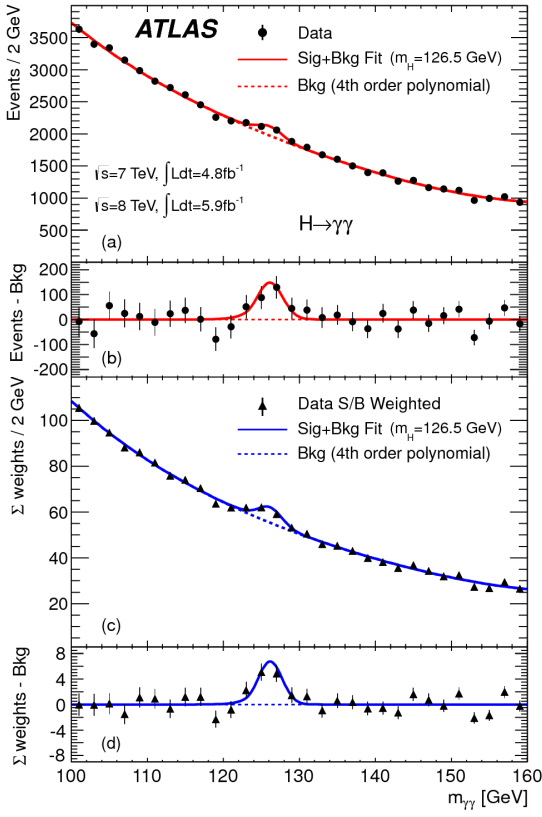


**Figure 4.4:** Diphoton mass spectrum in 7 and 8 TeV data. Panel a) shows the unweighted data distribution superimposed on the background fit, while panel c) shows the data where each event category is weighted by its signal to background ratio. Panels b) and d) show the respective distributions with background subtracted [1].

#### 1559 4.5 $H \rightarrow ZZ \rightarrow 4\ell$ SEARCH

1560 The  $H \rightarrow ZZ \rightarrow 4\ell$  analysis searches for a Standard Model Higgs boson decaying to two  $Z$  bosons,  
 1561 each of which decays to a pair of same flavor, opposite charge isolated leptons. The ultimate discriminat-  
 1562 ing variable is  $m_{4\ell}$ , or the invariant mass of the four selected leptons. The  $\ell$  denotes an  $e$  or  $\mu$  as with the  
 1563  $H \rightarrow WW^* \rightarrow \ell\nu\ell\nu$  analysis.

1564 Four distinct signal regions are constructed depending on the flavors of the final state, additionally  
 1565 separated by the flavor of the leading lepton pair. These are referred to as  $4e$ ,  $2e2\mu$ ,  $2\mu2e$ ,  $4\mu$ .

1566 The main backgrounds in the  $H \rightarrow ZZ \rightarrow 4\ell$  search are continuum  $ZZ^*$  production,  $Z +$  jets pro-  
 1567 duction, and  $t\bar{t}$ . The  $m_{4\ell}$  distribution for background is estimated from simulation. The normalization  
 1568 of the SM  $ZZ^*$  background is also taken from MC simulation, while the  $Z +$  jets and  $t\bar{t}$  normalizations

1569 are taken from data-driven methods.

1570 **4.5.1 RESULTS**

1571 Figure 4.5 shows the  $m_{4\ell}$  spectrum measured in the 7 and 8 TeV datasets. The total number of events  
1572 observed in the window between 120 and 130 GeV is 13, with 6 events in the  $4\mu$  channel, 2 events in  
1573 the  $4e$  channel, and 5 events in the  $2e2\mu/2\mu2e$ . The best fit  $\mu$  value in the combined 7 and 8 TeV data  
1574 occurs at 125 GeV and is measured to be  $1.2 \pm 0.6$ . The observed significance at this mass is  $3.6\sigma$ , with  
1575 an expected significance of  $2.7\sigma$ .

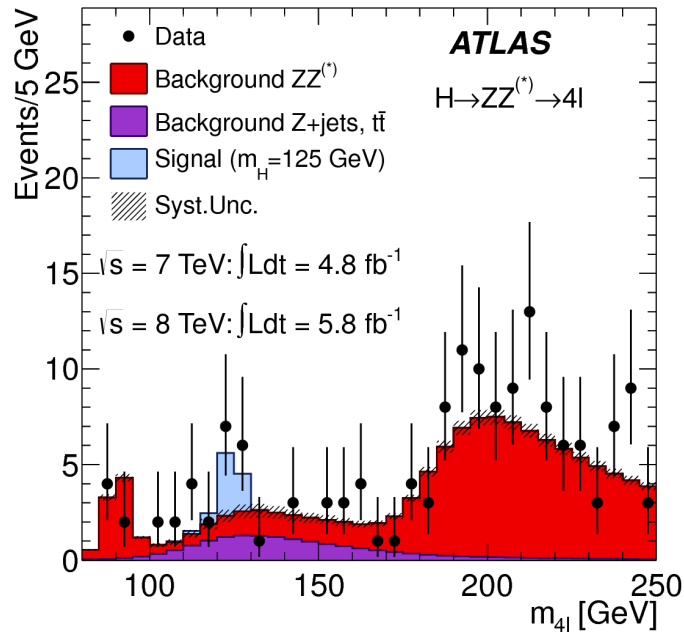


Figure 4.5: Four lepton invariant mass spectrum ( $m_{4\ell}$ ) in 7 and 8 TeV data compared to background estimate. A 125 GeV SM Higgs signal is shown in blue [1].

1576 **4.6 COMBINED RESULTS**

1577 The statistical interpretation of the combined results is undertaken as described in section 3.6.2, with a  
1578 hypothesis test based on a likelihood ratio parameterized by the Higgs signal strength  $\mu$ . The null hy-  
1579 pothesis corresponds to  $\mu = 0$ , while the SM Higgs corresponds to  $\mu = 1$ .

1580 Table 4.4 summarizes the properties of the individual channels as well as the significances of the ex-  
 1581 cesses seen. The most significant observed local excess comes from the  $\gamma\gamma$  channel. Figure 4.6 shows a  
 1582 comparison of the observed local  $p_0$  values as a function of hypothesized mass for the three different  
 1583 search channels. Both the  $ZZ^*$  and  $\gamma\gamma$  channels have very peaked excesses, while the  $WW^*$  excess can  
 1584 be seen as very broad because the  $m_T$  distribution does not provide detailed information about the true  
 1585 Higgs mass.

Channel	Fit var.	Observed $Z_l$	Expected $Z_l$	$\hat{\mu}$
$H \rightarrow ZZ^* \rightarrow 4\ell$	$m_{4\ell}$	3.6	2.7	$1.2 \pm 0.6$
$H \rightarrow \gamma\gamma$	$m_{\gamma\gamma}$	4.5	2.5	$1.8 \pm 0.5$
$H \rightarrow WW^* \rightarrow e\nu\mu\nu$	$m_T$	2.8	2.3	$1.3 \pm 0.5$
Combined	-	6.0	4.9	$1.4 \pm 0.3$

**Table 4.4:** Summary of the expected and observed significance and measured signal strengths in the combined 7 and 8 TeV datasets for the Higgs discovery analysis [1].

1586 Figure 4.7 shows the combined exclusion limit,  $p_0$ , and signal strength. The highest local excess comes  
 1587 at a value of 126.5 GeV and corresponds to a  $6.0\sigma$  observed excess.

1588 Figure 4.8 shows a comparison of the measured signal strengths between the different Higgs search  
 1589 channels. All measured  $\mu$  are consistent with unity within their uncertainty, and the combined  $\mu$  mea-  
 1590 surement is  $1.4 \pm 0.3$ .

1591 The likelihood can also be computed in a two-dimensional plane of  $m_H$  and  $\mu$ , and this is shown in  
 1592 figure 4.9. The figure shows that while the  $\gamma\gamma$  and  $ZZ^*$  channels have very good mass resolution, the  
 1593 excess in  $WW^*$  covers a broad mass range. The banana shape of the  $WW^*$  result is due to the fact that  
 1594 the excess in this channel can either be explained by increasing the signal strength or by changing the  
 1595 mass (and thus the cross section). The two parameters are correlated due to the lack of mass sensitivity in  
 1596 this channel.

1597 Because multiple Higgs mass points are searched for, the local significance must be corrected for a  
 1598 look-elsewhere effect to compute a true global significance. The global significance for finding a Higgs  
 1599 anywhere in the mass range of 110 GeV to 600 GeV is  $5.1\sigma$ . This increases slightly to  $5.3\sigma$  if only mass  
 1600 range from 110 to 150 GeV.

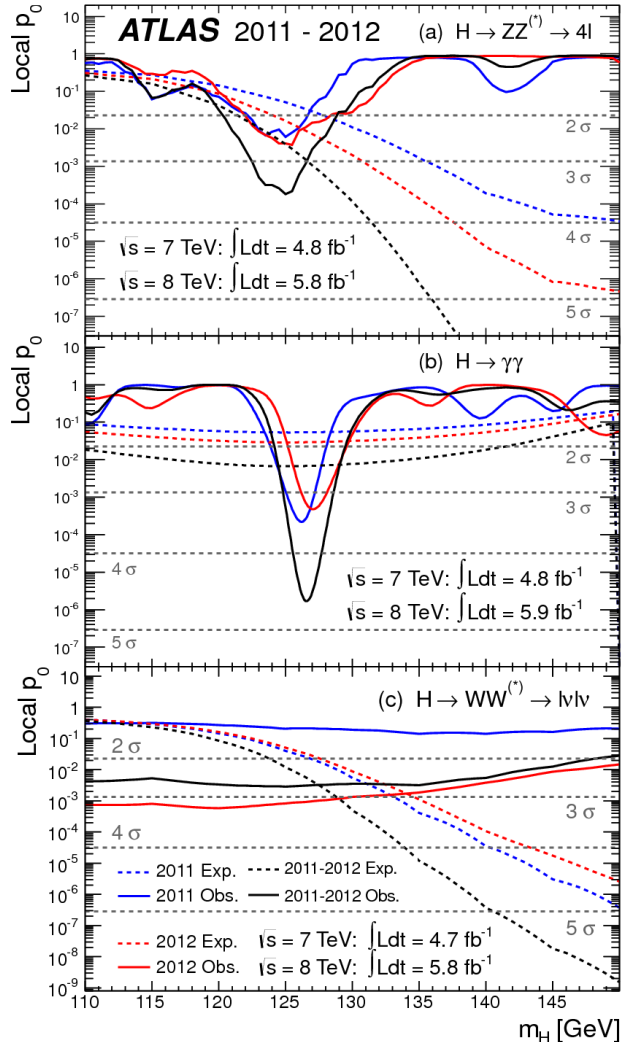


**Figure 4.6:** Local  $p_0$  distribution as a function of hypothesized Higgs mass for the  $H \rightarrow ZZ^* \rightarrow 4\ell$  (a),  $H \rightarrow \gamma\gamma$  (b), and  $H \rightarrow WW^* \rightarrow \ell\nu\ell\nu$  (c) channels. Dashed curves show expected results, while solid curves show observed. Red curves are from 7 TeV data, blue curves from 8 TeV, and black curved combined [1].

## 1601 4.7 CONCLUSION

1602 A search for the production of a Standard Model Higgs boson was conducted in  $4.8 \text{ fb}^{-1}$  collected at  
 1603  $\sqrt{s} = 7 \text{ TeV}$  and  $5.8 \text{ fb}^{-1}$  at  $\sqrt{s} = 8 \text{ TeV}$ . A new particle consistent with the Higgs boson was  
 1604 observed, with a mass of  $126.5 \text{ GeV}$  and a global (local) significance of  $5.1(6.0)\sigma$ . This is the first dis-  
 1605covery level observation of a particle consistent with the Higgs.

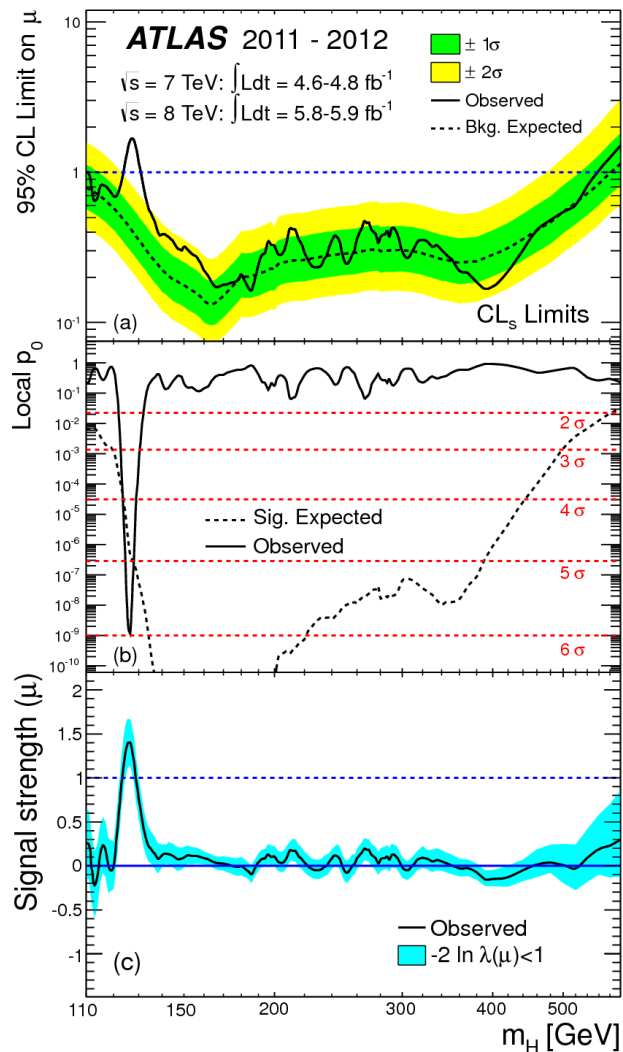


**Figure 4.7:** Combined 95% CL limits (a), local  $p_0$  values (b), and signal strength measurement (c) as a function of Higgs mass [1].

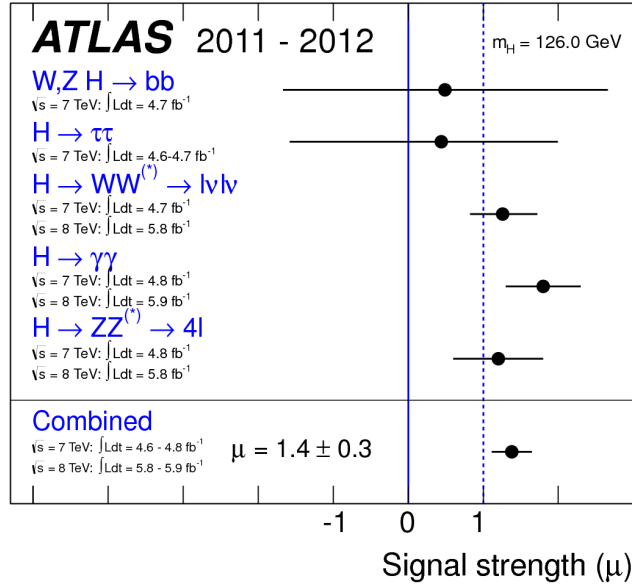


Figure 4.8: Comparison of measured signal strength  $\mu$  for a 126 GeV Higgs in the 7 and 8 TeV datasets [1].

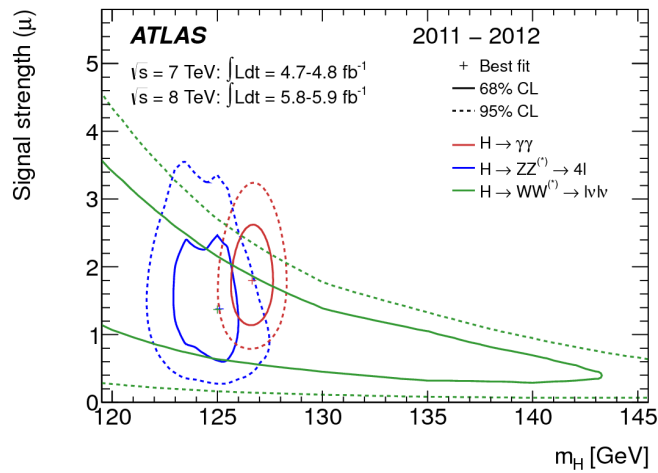


Figure 4.9: Two dimensional likelihood as a function of signal strength  $\mu$  and Higgs mass  $m_H$  [1].

*The imagination of nature is far, far greater than the  
imagination of man.*

Richard Feynman

# 5

1606

1607

## Observation of Vector Boson Fusion

1608

production of  $H \rightarrow WW^* \rightarrow \ell\nu\ell\nu$

1609 **5.1 INTRODUCTION**

1610 After the discovery of a particle consistent with the Higgs boson, the  $H \rightarrow WW^*$  analysis had two main  
1611 goals. The first goal was to increase the sensitivity of the analysis to fully confirm that the  $H \rightarrow WW^*$   
1612 process did indeed exist. The second goal was to characterize the particle as much as possible, including  
1613 searching for the lower cross-section production modes, in order to confirm that it was indeed a Higgs  
1614 boson. This chapter presents a dedicated search for Vector Boson Fusion (VBF) production of a Higgs  
1615 boson decaying via the  $H \rightarrow WW^* \rightarrow \ell\nu\ell\nu$  mode. First, basics of the topology of VBF production  
1616 are presented. Then, the details of the analysis are shown, including signal region definition, background  
1617 estimation techniques, and systematic uncertainties. Finally, the results of the analysis are presented. As

1618 will be shown, this analysis is the first and most sensitive observation of the VBF production mode of the  
1619 Higgs on ATLAS.

1620 In the VBF channel, there are both a selection requirement based signal region analysis (known as the  
1621 “cut-based”) and a multivariate analysis which uses a boosted decision tree (known as the BDT analysis).  
1622 The focus of this chapter will be on the cut-based signal region, as this is an important component of the  
1623 VBF analysis and in particular acts as strong validation for the final BDT result. Connections between  
1624 the cut-based and BDT analyses will be discussed where appropriate.

## 1625 5.2 DATA AND SIMULATION SAMPLES

1626 The results presented here are with  $20.3 \text{ fb}^{-1}$  taken at  $\sqrt{s} = 8 \text{ TeV}$  and  $4.5 \text{ fb}^{-1}$  taken at  $\sqrt{s} = 7 \text{ TeV}$ .  
1627 The details of the LHC and detector conditions during this period are given in Chapter 2. The trigger  
1628 selection defining the dataset is discussed in section 5.2.1. The simulation samples used for signal and  
1629 background modeling are given in section 5.2.2.

### 1630 5.2.1 TRIGGERS

1631 The analysis uses a combination of single lepton and dilepton triggers to allow lowering of the  $p_T$  thresh-  
1632 olds and increased signal acceptance. The  $p_T$  threshold on the leptons is a particularly important consid-  
1633 eration for this signal. Because the second  $W$  produced in the decay can be off-shell, it tends to pro-  
1634 duce lower momentum leptons. Thus, being able to lower the  $p_T$  threshold while still maintaining  
1635 a low background rate is critical. Figure 5.1 shows an example of the subleading lepton  $p_T$  for a VBF  
1636  $H \rightarrow WW^*$  signal compared to the corresponding  $t\bar{t}$  background. Note that the lepton  $p_T$  spectrum is  
1637 considerably softer in the signal sample.

1638 As discussed in Chapter 2, there are multiple levels in the ATLAS trigger system, and there are differ-  
1639 ent  $p_T$  thresholds imposed for the leptons at each level. Additionally, some triggers have a loose selection  
1640 on the isolation of the lepton (looser than that applied offline in the analysis object selection). Table 5.1  
1641 shows the thresholds used for single lepton triggers, while table 5.2 shows the thresholds coming from  
1642 di-lepton triggers. The single lepton trigger efficiency for muons that pass the analysis object selection is

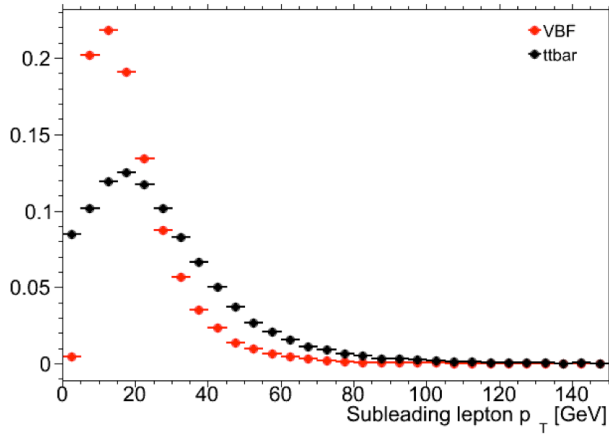


**Figure 5.1:** A comparison of the subleading lepton  $p_T$  spectrum between VBF  $H \rightarrow WW^*$  production and  $t\bar{t}$  background

1643 70% for muons in the barrel region ( $|\eta| < 1.05$ ) and 90% in the endcap region. The electron trigger ef-  
1644 ficiency increases with electron  $p_T$  but the average is approximately 90%. These efficiencies are measured  
1645 by combined performance and trigger signature groups [65, 66].

	Level-1 threshold	High-level threshold
Electron	18	$24i$
	30	60
Muon	15	$24i$
		36

**Table 5.1:** Single lepton triggers used for electrons and muons. A logical “or” of the triggers listed for each lepton type is taken. Units are in GeV, and the  $i$  denotes an isolation requirement in the trigger.

	Level-1 threshold	High-level threshold
$ee$	10 and 10	12 and 12
$\mu\mu$	15	18 and 8
$e\mu$	10 and 6	12 and 8

**Table 5.2:** Di-lepton triggers used for different flavor combinations. The two thresholds listed refer to leading and sub-leading leptons, respectively. The di-muon trigger only requires a single lepton at level-1.

1646 The combination of all triggers shown gives good efficiency for signal events. This efficiency is sum-  
1647 marized in table 5.3. The relative improvement in efficiency by adding the dilepton triggers is also shown  
1648 in the same table. The largest gain comes in the  $\mu\mu$  channel. Overall the trigger selection shows a good  
1649 efficiency for  $H \rightarrow WW^*$  signal events.

Channel	Trigger efficiency	Gain from $2\ell$ trigger
$ee$	97%	9.1%
$\mu\mu$	89%	18.5%
$e\mu$	95%	8.3%
$\mu e$	81%	8.2%

**Table 5.3:** Trigger efficiency for signal events and relative gain of adding a dilepton trigger on top of the single lepton trigger selection. The first lepton is the leading, while the second is the sub-leading. Efficiencies shown here are for the ggF signal in the  $n_j = 0$  category but are comparable for the VBF signal.

### 1650 5.2.2 MONTE CARLO SAMPLES

1651 Modeling of signal and background processes in the signal region, in particular for the  $m_T$  distribution,  
 1652 is an important consideration for the final interpretation of the analysis. Therefore, careful consideration  
 1653 must be paid to which Monte Carlo (MC) generators are used for specific processes. With the exception  
 1654 of the  $W + \text{jet}$  and multijet backgrounds, the  $m_T$  shape used as the final discriminant is taken from simu-  
 1655 lation. (Many backgrounds are normalized from data, as described in section 5.5).

1656 Table 5.4 shows the MC generators used for the signal and background processes, as well as their cross  
 1657 sections. In order to include corrections up to next-to-leading order (NLO) in the QCD coupling con-  
 1658 stant  $\alpha_s$ , the `POWHEG` [67] generator is often used. In some cases, only leading order generators like  
 1659 `ACERMC` [68] and `GG2VV` [69] are available for the process in question. If the process requires good  
 1660 modeling for very high parton multiplicities, the `SHERPA` [70] and `ALPGEN` [71] generators are used  
 1661 to provide merged calculations for five or fewer additional partons. These matrix element level calcula-  
 1662 tions must then be additionally matched to models of the underlying event, hadronization, and parton  
 1663 shower. There are four possible generators for this: `SHERPA`, `PYTHIA 6` [72], `PYTHIA 8` [73], or `HERWIG`  
 1664 [74] + `JIMMY` [75]. The simulation additionally requires an input parton distribution function (PDF).  
 1665 The `CT10` [76] PDFs are used for `SHERPA` and `POWHEG` simulated samples, while `CTEQ6L1` [77] is used  
 1666 for `ALPGEN + HERWIG` and `ACERMC` simulations. The Drell-Yan samples are reweighted to the `MRST`  
 1667 [78] PDFs, as these are found to give the best agreement between data and simulation.

1668 Once the basic hard scattering process is simulated, it must be passed through a detector simulation  
 1669 and additional pile-up events must be overlaid. The pile-up events are modeled with `PYTHIA 8`, and the

Process	MC generator	$\sigma \cdot \mathcal{B}$ (pb)
<b>Signal</b>		
ggF	$H \rightarrow WW^*$ POWHEG +PYTHIA 8	0.435
VBF	$H \rightarrow WW^*$ POWHEG +PYTHIA 8	0.0356
VH	$H \rightarrow WW^*$ PYTHIA 8	0.0253
<b><math>WW</math></b>		
$q\bar{q} \rightarrow WW$ and $qg \rightarrow WW$	POWHEG +PYTHIA 6	5.68
$gg \rightarrow WW$	GG2VV +HERWIG	0.196
$(q\bar{q} \rightarrow W) + (q\bar{q} \rightarrow W)$	PYTHIA 8	0.480
$q\bar{q} \rightarrow WW$	SHERPA	5.68
VBS $WW + 2$ jets	SHERPA	0.0397
<b>Top quarks</b>		
$t\bar{t}$	POWHEG +PYTHIA 6	26.6
$Wt$	POWHEG +PYTHIA 6	2.35
$tq\bar{b}$	ACERMC +PYTHIA 6	28.4
$t\bar{b}$	POWHEG +PYTHIA 6	1.82
<b>Other dibosons (<math>VV</math>)</b>		
$W\gamma$ ( $p_T^\gamma > 8$ GeV)	ALPGEN +HERWIG	369
$W\gamma^*$ ( $m_{\ell\ell} \leq 7$ GeV)	SHERPA	12.2
$WZ$ ( $m_{\ell\ell} > 7$ GeV)	POWHEG +PYTHIA 8	12.7
VBS $WZ + 2$ jets	SHERPA	0.0126
( $m_{\ell\ell} > 7$ GeV)		
$Z\gamma$ ( $p_T^\gamma > 8$ GeV)	SHERPA	163
$Z\gamma^*$ (min. $m_{\ell\ell} \leq 4$ GeV)	SHERPA	7.31
$ZZ$ ( $m_{\ell\ell} > 4$ GeV)	POWHEG +PYTHIA 8	0.733
$ZZ \rightarrow \ell\ell\nu\nu$ ( $m_{\ell\ell} > 4$ GeV)	POWHEG +PYTHIA 8	0.504
<b>Drell-Yan</b>		
$Z$ ( $m_{\ell\ell} > 10$ GeV)	ALPGEN +HERWIG	16500
VBF $Z + 2$ jets	SHERPA	5.36
( $m_{\ell\ell} > 7$ GeV)		

**Table 5.4:** Monte Carlo samples used to model the signal and background processes [61].

ATLAS detector is simulated with GEANT4 [79]. Because of the unique phase space of the  $H \rightarrow WW^*$  analysis, events are sometimes filtered at generator level to allow for more efficient generation of relevant events. The efficiency of the trigger in MC simulation does not always match the measured efficiency in

1673 data, so trigger scale factors are applied to correct the MC efficiency to the data. These are derived by the  
1674 combined performance groups [65, 66].

1675 **5.3 OBJECT SELECTION**

1676 In order to define the signal region, the analysis must first select the objects to be considered. The de-  
1677 tails of the object reconstruction algorithms are discussed in Chapter 2, while this section gives specific  
1678 selection cuts used in the  $H \rightarrow WW^*$  analysis.

1679 The first step in this process is to select a primary vertex candidates. The event’s primary vertex is the  
1680 vertex with the largest sum of  $p_T^2$  for associated tracks and is required to have at least three tracks with  
1681  $p_T > 450$  MeV. Many of the object selection cuts are then made relative to this chosen primary vertex.

1682 **5.3.1 MUONS**

1683 The analysis uses combined muon candidates, where a track in the Inner Detector has been matched  
1684 to a standalone track in the Muon Spectrometer. The track parameters are combined statistically in the  
1685 muon reconstruction algorithm [52]. The muons are required to be within  $|\eta| < 2.5$  and have a  $p_T >$   
1686 10 GeV. To reduce backgrounds coming from mis-reconstructed leptons, there are requirements on  
1687 the impact parameter of the muon relative to the primary vertex. The transverse impact parameter  $d_0$   
1688 is required to be small relative to its estimated uncertainty, the exact cut value being  $d_0/\sigma_{d_0} < 3$ . The  
1689 longitudinal impact parameter  $z_0$  must satisfy  $|z_0 \sin \theta| < 1$  mm.

1690 As discussed previously, the muons must also be isolated. There are two types of lepton isolations  
1691 that are calculated: track-based and calorimeter-based. For muons, the track-based isolation is defined  
1692 using the scalar sum  $\sum p_T$  for tracks with  $p_T > 1$  GeV (excluding the muon’s track) within a cone of  
1693  $\Delta R = 0.3$  ( $0.4$ ) for muon with  $p_T > 15$  GeV ( $10 < p_T < 15$  GeV). The final isolation requirement  
1694 is made my requiring that this scalar sum be no more than a certain fraction of the muon’s  $p_T$ . This re-  
1695 quirement varies with muon  $p_T$  and the exact cuts are defined in table 5.5.

1696 The calorimeter-based muon isolation is defined using as a  $\sum E_T$  calculated from calorimeter cells  
1697 using the same cone size as the track-based isolation but excluding cells with  $\Delta R < 0.05$  around the

1698 muon. This requirement is also defined as a cut on the ratio of the sum to the muon  $p_T$  and varies with  
1699 muon  $p_T$ . The cut values are also given in table 5.5.

1700 The isolation requirements loosen as a function of  $p_T$  to allow for larger signal acceptance. At low  $p_T$ ,  
1701 the isolation is tightened to reduce the  $W + \text{jets}$  background which arises from a misidentified lepton.

$p_T$ range (GeV)	Calorimeter isolation	Track isolation
10 – 15	0.06	0.06
15 – 20	0.12	0.08
20 – 25	0.18	0.12
> 25	0.30	0.12

**Table 5.5:**  $p_T$  dependent isolation requirements for muons. Muons are required to have the amount of calorimeter or track based cone sums be less than this fraction of their  $p_T$ .

### 1702 5.3.2 ELECTRONS

1703 Electrons are identified by matching reconstructed clusters in the electromagnetic calorimeter with tracks  
1704 in the inner detector. The electrons are identified using a likelihood based method [49, 50] which takes  
1705 into account the shower shapes in the calorimeter, the matching of tracks to clusters, and the amount of  
1706 transition radiation in the TRT. The electrons are required to have  $|\eta| < 2.47$ , and candidates in the  
1707 transition region between the barrel and endcap ( $1.37 < |\eta| < 1.52$ ) are excluded. As the muons, the  
1708 electrons are required to have transverse impact parameter significance  $< 3$ , while in the longitudinal  
1709 direction they must have  $|z_0 \sin \theta| < 0.4$  mm. Some electron requirements also vary with electron  $E_T$ ,  
1710 and these requirements are summarized in table 5.6.

1711 The isolation for electrons are defined similarly to the muons but with unique cuts on the objects in-  
1712 cluded. The track-based isolation is defined using tracks with  $p_T > 400$  MeV with cone sizes as defined  
1713 previously. The calorimeter-based isolation also uses the same cone size as the muon, but here the cells  
1714 within a  $0.125 \times 0.175$  area in  $\eta \times \phi$  around the electron cluster's barycenter are excluded. The other  
1715 difference with respect to muons is that the denominator of the isolation ratio is the electron's  $E_T$  rather  
1716 than  $p_T$ . The isolation cuts very with electron  $E_T$  and are defined in table 5.6.

1717 The electron is also required to not be consistent with a vertex coming from a photon conversion.

$p_T$ range (GeV)	Quality cut	Calorimeter isolation	Track isolation
10 – 15	Very tight LH	0.20	0.06
15 – 20	Very tight LH	0.24	0.08
20 – 25	Very tight LH	0.28	0.10
> 25	Medium	0.28	0.10

**Table 5.6:**  $p_T$  dependent requirements for electrons. Electrons are required to have the amount of calorimeter or track based cone sums be less than this fraction of their  $E_T$ .

### 1718 5.3.3 JETS

1719 Jets are clustered with the anti- $k_T$  reconstruction algorithm using a radius parameter of  $R = 0.4$ . They  
 1720 are required to have a jet vertex fraction (JVF) of at least 50%, meaning that half of the tracks associated  
 1721 with the jet originated from the primary vertex. Jets with no tracks associated (i.e. those outside the ac-  
 1722 ceptance of the ID) do not have this requirement applied. Jets are required to have  $p_T > 25$  GeV if  
 1723 they are within the tracking acceptance ( $|\eta| < 2.4$ ). Jets with  $2.4 < |\eta| < 4.5$  are required to have  
 1724  $p_T > 30$  GeV. This tighter requirement reduces jets from pileup in the region where JVF requirements  
 1725 cannot be applied. The two highest  $p_T$  jets in the event are referred to as the “VBF” jets and used to com-  
 1726 pute various analysis selections later.

1727 Identification of  $b$ -jets is done using the MV1 algorithm and is limited to the acceptance of the ID  
 1728 ( $|\eta| < 2.5$ ). The operating point of MV1 that is used is the one that is 85% efficient for identifying true  
 1729  $b$ -jets. This operating point has a 10.3% of mis-tagging a light quark jet as a  $b$ -jet. In order to improve  
 1730 the rejection of  $b$ -jets, a lower threshold than the nominal  $p_T$  threshold described above is used. For the  
 1731 purposes of counting the number of  $b$ -jets, jets with  $p_T$  down to 20 GeV are used.

### 1732 5.3.4 OVERLAP REMOVAL

1733 There are some cases where certain reconstructed objects will overlap and one will have to be chosen  
 1734 (for example, an electron and a jet in the calorimeter). First, the case of lepton overlap is dealt with. If  
 1735 an electron candidate extends into the muon spectrometer, it is removed. If a muon or electron have a  
 1736  $\Delta R < 0.1$ , the electron is removed and the muon is kept. If two electron candidates overlap within  
 1737 the same radius, then the higher  $E_T$  electron is kept. Next, the overlap between leptons and jets is con-

1738 sidered. If an electron and jet are within  $\Delta R < 0.3$  of one another, the electron is kept and the jet is  
1739 removed. However, if a muon and jet overlap within  $\Delta R < 0.3$ , the jet is kept (as it is likely that the  
1740 muon is the result of a semileptonic decay inside the jet).

1741 Once the overlap removal is complete, the final set of objects used in the analysis is defined.

#### 1742 5.4 ANALYSIS SELECTION

1743 The VBF analysis uses two distinct selections. The first is a more standard selection, referred to as “cut-  
1744 based”, that applies requirements on the VBF variables and uses  $m_T$  as the final discriminating variable.  
1745 The second is a looser selection that uses a Boosted Decision Tree (BDT) score as the final discriminator  
1746 in order to take advantage of the detailed correlations between the VBF variables. While the BDT analy-  
1747 sis is ultimately more sensitive, the cut-based serves as an important component of the analysis. First, the  
1748 cut-based allows for confirming the modeling and validity of many variables used as input to the BDT.  
1749 Second, because this is the first use of such an MVA technique in the  $H \rightarrow WW^*$  analysis, the cut-based  
1750 selection allows confirmation of the final BDT result with a more traditional analysis. The cut-based  
1751 techniques are the focus of this chapter, but connections to the BDT result will be illustrated when ap-  
1752 propriate.

1753 One important note is that because this analysis is dedicated to the measurement of the VBF pro-  
1754 duction mode of the Higgs, events coming from gluon fusion production with the Higgs decaying via  
1755  $H \rightarrow WW^* \rightarrow \ell\nu\ell\nu$  are treated as background events. This will be seen throughout the various  
1756 predictions shown.

##### 1757 5.4.1 COMMON PRE-SELECTION

1758 Both the cut-based and BDT analyses have a common pre-selection that is applied before the main signal  
1759 region requirements. The requirements on leptons are common to all  $n_j$  bins. The analysis requires two  
1760 oppositely charged leptons, with the leading lepton required to have  $p_T > 22$  GeV while the subleading  
1761 lepton must have  $p_T > 10$  GeV. Next, to remove low mass  $Z/\gamma^*$  events, a cut on the dilepton mass  
1762  $m_{\ell\ell} > 10$  (12) GeV is applied in the different (same) flavor channel. In the same flavor channels, there is

1763 an additional veto placed on the region around the Z peak, requiring that  $|m_{\ell\ell} - m_Z| > 15$  GeV.

1764 There are also requirements on the amount of missing transverse momentum in the event. These  
1765 are only applied in the same flavor channels, as in the different flavor channels  $t\bar{t}$  is the dominant back-  
1766 ground in  $n_j \geq 2$ . The BDT analysis requires  $p_T^{\text{miss}} > 40$  GeV and  $E_T^{\text{miss}} > 45$  GeV. The cut-  
1767 based analysis must select more tightly on these variables to have maximal sensitivity and thus requires  
1768  $p_T^{\text{miss}} > 50$  GeV and  $E_T^{\text{miss}} > 55$  GeV.

1769 Finally, because this analysis is focused on VBF, a requirement on the jet multiplicity is placed, with  
1770  $n_j \geq 2$ . Additionally, the analysis requires that there are no jets identified as b-quarks in the event, or  
1771  $n_b = 0$ .

#### 1772 5.4.2 CUT-BASED SELECTION

1773 The cut-based selection places sequential requirements on variables reconstructed from the VBF jets in  
1774 order to increase the signal to background ratio.

#### 1775 GENERAL BACKGROUND REDUCTION

1776 Top pair production is the primary background in the  $n_j \geq 2$  bin. Even though  $n_b = 0$  is required,  
1777 an additional variable is constructed to further suppress the top background. There is often additional  
1778 QCD radiation that accompanies the  $t\bar{t}$  system when it is produced. Therefore, a variable which tests for  
1779 the presence of this additional radiation,  $p_T^{\text{sum}}$ , is constructed. It is defined in equation 5.1.

$$p_T^{\text{sum}} = p_T^{\ell\ell} + p_T^{\text{miss}} + \sum p_T^j \quad (5.1)$$

1780 The first cut after pre-selection in the cut-based analysis requires  $p_T^{\text{sum}} < 15$  GeV to further suppress  $t\bar{t}$   
1781 production.

1782 In the different flavor channels, a cut is made to reduce the contamination from  $Z \rightarrow \tau\tau$  decays.  
1783 The di- $\tau$  invariant mass,  $m_{\tau\tau}$ , is constructed by assuming that the neutrinos from the  $\tau$  decays were  
1784 collinear with the leptons [? ]. The analysis requires that this mass not be consistent with a  $Z$  by requir-  
1785 ing  $m_{\tau\tau} < m_Z - 25$  GeV.

1786 VBF TOPOLOGICAL CUTS

1787 The characteristic feature of VBF production of the Higgs is the presence of two additional forward jets  
1788 coming from the incoming partons which radiate the vector bosons that make the Higgs. These jets are  
1789 forward because the outgoing partons still carry the longitudinal momentum of the incoming partons.  
1790 Figure 5.2 shows the distribution of the  $\eta$  for the leading jet in a VBF event compared to a background  
1791 top pair production event. As can be seen, the VBF jets tend to be more forward in  $\eta$ , while the  $t\bar{t}$  jets are  
1792 more central.

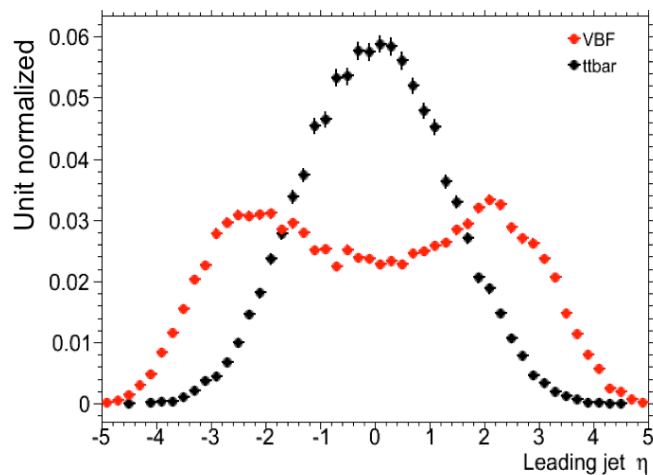


Figure 5.2: Leading jet  $\eta$  in VBF  $H \rightarrow WW^*$  (red) and  $t\bar{t}$  (black)

1793 Because the cross section for VBF production is an order of magnitude smaller than gluon fusion pro-  
1794 duction, these forward jets must be used in order to better reduce background and achieve a good signal  
1795 to background ratio. The dedicated VBF search selection requirements are constructed to maximally  
1796 exploit the features of the unique VBF topology.

1797 Requirements on the VBF jets are collectively referred to as the “VBF topological cuts”. First, a re-  
1798 quirement on the dijet invariant mass of the VBF jets,  $m_{jj}$ , is placed, requiring  $m_{jj} > 600$  GeV. Next,  
1799 the event is required to have a large gap in rapidity between the two VBF jets, or  $\Delta y_{jj} > 3.6$ . Both  
1800 of these cuts put tight requirements on the presence of two forward, high  $p_T$  jets moving in opposite

1801 directions in the longitudinal plane.

1802 Beyond requiring the presence of the two forward VBF jets, the analysis also vetoes on the presence  
1803 of any additional jets that fall between the two VBF jets. This cut is referred to as the central jet veto, or  
1804 CJV. Any events with a third jet with  $p_T > 20$  GeV whose rapidity is between the region defined by the  
1805 two VBF jets are vetoed. This can be expressed in terms of a variable called the jet centrality, defined in  
1806 equation 5.2.

$$C_{j3} = \left| \eta_{j3} - \frac{\eta_{j1} + \eta_{j2}}{2} \right| / \frac{|\eta_{j1} - \eta_{j2}|}{2}, \quad (5.2)$$

1807 Here,  $\eta_{j1}$  and  $\eta_{j2}$  are the pseudorapidities of the leading and subleading jets, respectively, while  $\eta_{j3}$  is  
1808 the pseudorapidity of the extra jet in the event (if one exists). Intuitively,  $C_{j3}$  is zero when  $\eta_{j3}$  is directly  
1809 centered between the two jets and unity when  $\eta_{j3}$  is aligned with either of the VBF jets. Thus, the CJV  
1810 can be expressed as a requirement that  $C_{j3} > 1$ .

1811 The decay products of the Higgs tend to be central as well. Thus, the analysis also requires that both  
1812 leptons in the analysis fall within the rapidity gap defined by the jets. This cut is referred to as the outside  
1813 lepton veto, or OLV. A quantitative way to define the cut is to require that the centrality of each lepton  
1814 (defined analogously to that of the third jet in equation 5.2) correspond to the lepton being within the jet  
1815 rapidity gap, or  $C_\ell < 1$  for both leptons.

1816 Figure 5.3a-c shows the  $m_{jj}$ ,  $\Delta y_{jj}$ , and  $C_\ell$  variables at the stage where all previous cuts in the se-  
1817 quence have been made. The agreement between data and Monte Carlo is good, and the bottom panels  
1818 show their power in discriminating the VBF signal from the background processes.

1819 The final signal region is also split into two bins of  $m_{jj}$ , with the first bin corresponding to  $600 \text{ GeV} <$   
1820  $m_{jj} < 1 \text{ TeV}$  and the second bin corresponding to  $m_{jj} > 1 \text{ TeV}$ . The first bin has more statistics but  
1821 also a larger contribution from background, while the second bin has lower statistics but a 1:1 signal to  
1822 background ratio.

## 1823 HIGGS TOPOLOGICAL CUTS

1824 The final state leptons will exhibit unique correlations due to the fact that they are arising from the decay  
1825 of a spin zero resonance. In particular, the spins of the final state leptons and neutrinos must all cancel,

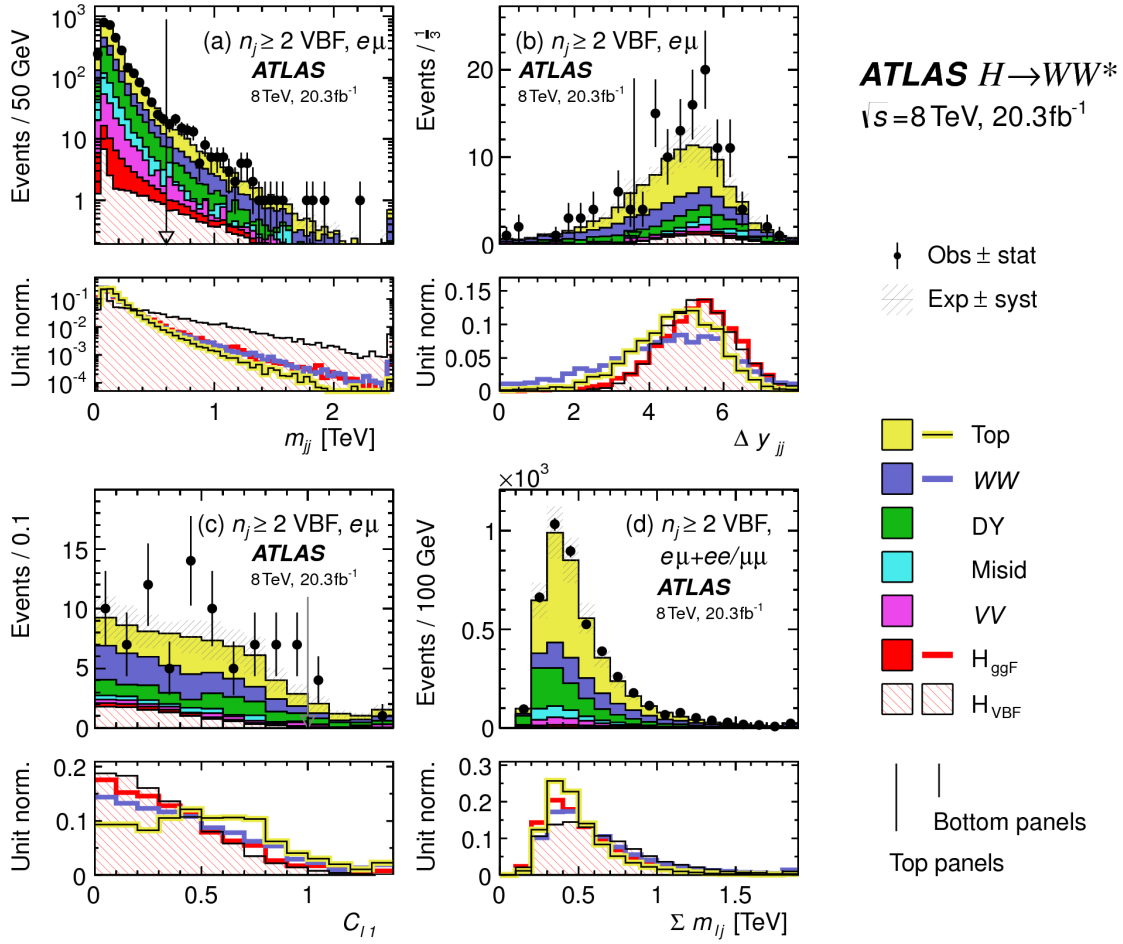


**Figure 5.3:** Distributions of (a)  $m_{jj}$ , (b)  $\Delta y_{jj}$ , (c)  $C_{\ell 1}$ , and (d)  $\sum m_{ij}$ , for the VBF analysis. The top panels compare simulation and data, while the bottom panels show normalized distributions for all background processes and signal [61].

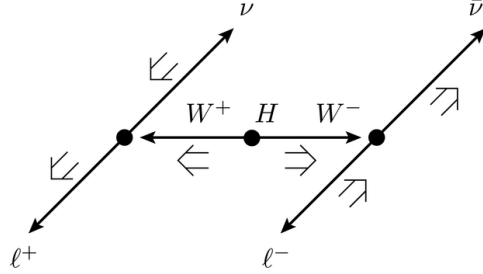


**Figure 5.4:** A cartoon of the WW final state. Momenta are represented with thin arrows, spins with thick arrows. [61]

as shown in figure 5.4. Because the neutrino has a left handed chirality and the anti-neutrino has a right handed chirality (in the massless neutrino approximation), the spin and momentum of the particles will be anti-aligned and aligned, respectively. In the transverse plane, the momenta of all four final state objects must cancel as well. With the constraint of having both the momenta and the spin alignments cancel, the final state kinematics strongly prefer having a small angle between the leptons in the transverse plane (low  $\Delta\phi_{\ell\ell}$ ). This angular correlation will also lead to low values of the di-lepton invariant mass  $m_{\ell\ell}$ . These unique signal final state kinematic correlations will be exploited to define the ultimate signal region.

The analysis places additional requirements on the final state leptons. Two requirements on dilepton kinematics are made that are common with lower multiplicity jet bins as well. The angle between leptons in the transverse plane,  $\Delta\phi_{\ell\ell}$ , is required to be less than 1.8 radians. Additionally, the dilepton mass  $m_{\ell\ell}$  is required to be less than 50 GeV.

The cut-based analysis uses  $m_T$  as the final discriminating variable as in the ggF focused analysis. The optimal number of bins in  $m_T$  was found to be three bins, with the bin boundaries at 80 and 130 GeV.

Table 5.7 shows the data and estimated signal and background yields from simulation as each cut described above is made. The table shows how each cut reduces specific backgrounds and how the overall signal to background ratio grows through the various selection requirements.

Figure 5.5 shows an ATLAS event display of a candidate event in the final signal region.

**Table 5.7:** Event selection for the  $n_j \geq 2$  VBF analysis in the 8 TeV cut-based analysis [61].

Selection	Summary										Composition of $N_{\text{bkg}}$							
	$N_{\text{obs}}/N_{\text{bkg}}$	$N_{\text{obs}}$	$N_{\text{bkg}}$	$N_{\text{signal}}$	$N_{\text{ggF}}$	$N_{\text{VBF}}$	$N_{\text{VH}}$	$N_{WW}^{\text{QCD}}$	$N_{WW}^{\text{EW}}$	$N_{t\bar{t}}$	$N_t$	$N_{\text{top}}$	$N_{Wj}$	$N_{jj}$	$N_{VV}$	$N_{\text{misid}}$	$N_{\text{Drell-Yan}}$	$N_{ee/\mu\mu} N_{\tau\tau}^{\text{QCD}}$
$e\mu$ sample	1.00 ± 0.00	61434	61180	85	32	26	1350	68	51810	2970	847	308	380	51	3260	46		
$n_b = 0$	1.02 ± 0.01	7818	7700	63	26	16	993	43	3000	367	313	193	273	35	2400	29		
$p_T^{\text{sum}} < 15$	1.03 ± 0.01	5787	5630	46	23	13	781	38	1910	270	216	107	201	27	2010	23		
$m_{\tau\tau} < m_Z - 25$	1.05 ± 0.02	3129	2970	40	20	9.9	484	22	1270	177	141	66	132	7.6	627	5.8		
$m_{jj} > 600$	1.31 ± 0.12	131	100	2.3	8.2	—	18	8.9	40	5.3	1.8	2.4	5.1	0.1	15	1.0		
$\Delta y_{jj} > 3.6$	1.33 ± 0.13	107	80	2.1	7.9	—	11.7	6.9	35	5.0	1.6	2.3	3.3	—	11.6	0.8		
$C_{j3} > 1$	1.36 ± 0.18	58	43	1.3	6.6	—	6.9	5.6	14	3.0	1.3	1.3	2.0	—	6.8	0.6		
$C_{\ell 1} < 1, C_{\ell 2} < 1$	1.42 ± 0.20	51	36	1.2	6.4	—	5.9	5.2	10.8	2.5	1.3	1.3	1.6	—	5.7	0.6		
$m_{\ell\ell}, \Delta\phi_{\ell\ell}, m_\tau$	2.53 ± 0.71	14	5.5	0.8	4.7	—	1.0	0.5	1.1	0.3	0.3	0.3	0.6	—	0.5	0.2		
<hr/>																		
$ee/\mu\mu$ sample	0.99 ± 0.01	26949	27190	31	14	10.1	594	37	23440	1320	230	8.6	137	690	679	16		
$n_b, p_T^{\text{sum}}, m_{\tau\tau}$	1.03 ± 0.03	1344	1310	13	8.0	4.0	229	12.0	633	86	26	0.9	45	187	76	1.5		
$m_{jj}, \Delta y_{jj}, C_{j3}, C_\ell$	1.39 ± 0.28	26	19	0.4	2.9	0.0	3.1	3.1	5.5	1.0	0.2	0.0	0.7	3.8	0.7	0.1		
$m_{\ell\ell}, \Delta\phi_{\ell\ell}, m_\tau$	1.63 ± 0.69	6	3.7	0.3	2.2	0.0	0.4	0.2	0.6	0.2	0.2	0.0	0.1	1.5	0.3	0.1		

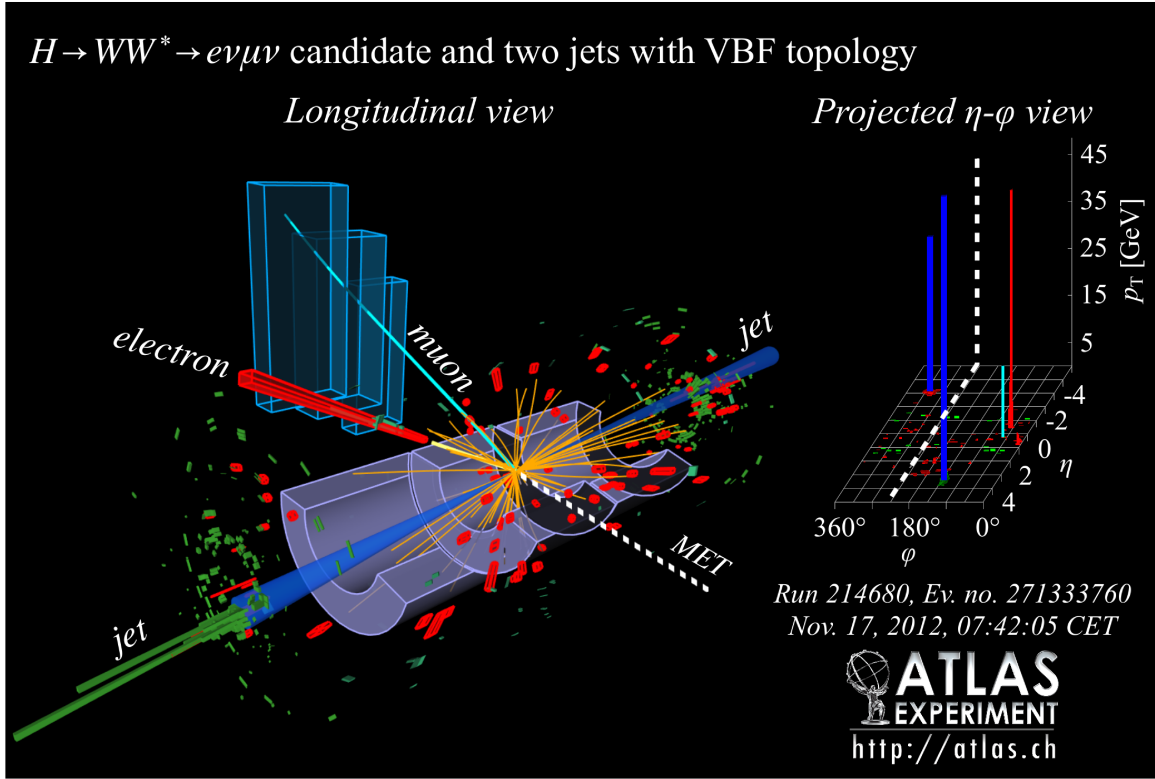


Figure 5.5: Event display of a VBF candidate event [61].

#### 1844 5.4.3 BDT-BASED SELECTION

1845 The boosted decision tree based analysis takes a different philosophy compared to the cut-based. Rather  
 1846 than cutting sequentially on many variables, the BDT analysis uses many of these variables as inputs  
 1847 to the BDT and the output BDT score ( $O_{\text{BDT}}$ ) as the final discriminant. The BDT is trained with the  
 1848 VBF  $H \rightarrow WW^*$  simulation as the signal samples and all other processes as background, including ggF  
 1849  $H \rightarrow WW^*$  production. While the BDT based analysis is treated as a separate result, it has significant  
 1850 overlap with the cut-based selection.

#### 1851 PRE-TRAINING SELECTION AND BDT INPUTS

1852 Before training, the common pre-selection cuts described in section 5.4.1 are applied. Additionally, the  
 1853 central jet veto and outside lepton veto described in section 5.4.2 are applied. The BDT has eight input  
 1854 variables, six of which are also variables that are used in the cut-based analysis. The six shared variables

1855 are  $p_T^{\text{sum}}$ ,  $m_{jj}$ ,  $\Delta y_{jj}$ ,  $m_{\ell\ell}$ ,  $\Delta\phi_{\ell\ell}$ , and  $m_T$ . The seventh variable input in the BDT is a combination of  
 1856 the variables used to do the OLV in the cut-based analysis. The BDT uses as input the sum of lepton  
 1857 centralities, or  $\sum C_\ell = C_{\ell 1} + C_{\ell 2}$ . The final BDT input variable,  $\Sigma m_{\ell j}$ , is constructed to account for  
 1858 the correlations between the jets and leptons in the event. It is the sum of the invariant masses of all four  
 1859 possible lepton-jet combinations.

1860 Figure 5.3d shows the agreement between data and simulation for the  $\Sigma m_{\ell j}$  variable, as well as show-  
 1861 ing its discriminating power. Figure 5.6 shows the distributions of the Higgs topological variables that  
 1862 are shared between the cut-based and BDT analyses. Figure 5.7 shows the distributions of the VBF topo-  
 1863 logical variables shared between the cut-based and BDT analyses. In both cases, the VBF yield has been  
 1864 scaled by a factor of 50 to better show the shape difference compared to the backgrounds.

1865 Table ?? summarizes the cuts applied for the cut-based and analyses, as well as which variables are used  
 1866 as input to the BDT.

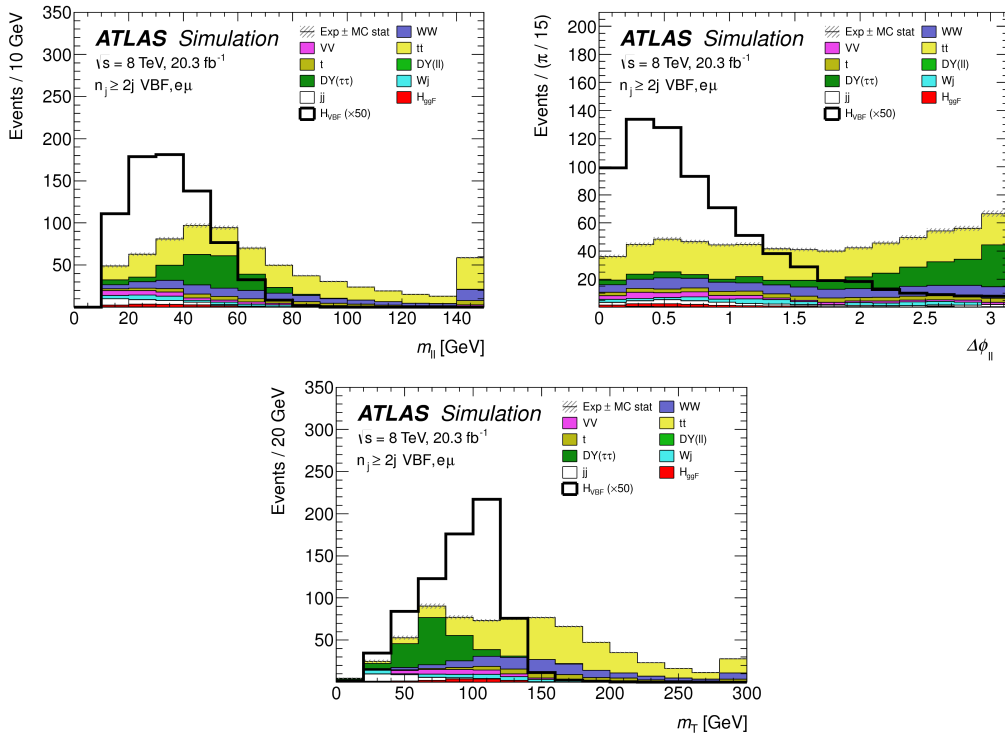


**Figure 5.6:** Distributions of  $m_{ll}$  (top left),  $\Delta\phi_{ll}$  (top right), and  $m_T$  (bottom), Higgs topology variables used in the selection requirements of the cut-based signal region and as inputs to the BDT result. These are plotted after all of the BDT pre-training selection cuts [61].

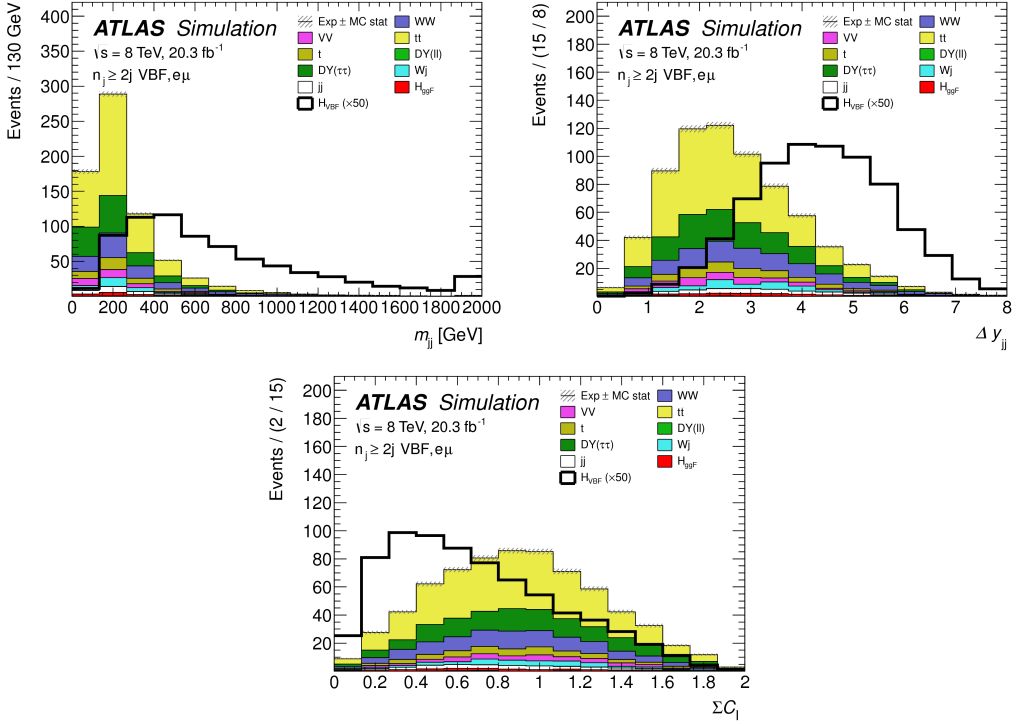


**Figure 5.7:** Distributions of  $m_{jj}$  (top left),  $\Delta y_{jj}$  (top right),  $\sum C_\ell$  (bottom), VBF topology variables used in the selection requirements of the cut-based signal region and as inputs to the BDT result. These are plotted after all of the BDT pre-training selection cuts [61].

## 1867 5.5 BACKGROUND ESTIMATION

1868 This section describes the procedures used to estimate backgrounds for the VBF analysis in both the  
 1869 cut-based and BDT analyses.

### 1870 5.5.1 GENERAL STRATEGY

1871 Most of the backgrounds in the VBF analysis have shapes estimated from Monte Carlo simulation but  
 1872 normalizations derived from control regions in data. In essence, a normalization factor (denoted with  
 1873  $\beta$  or abbreviated as NF) is derived by scaling the MC yield in the control region to the corresponding  
 1874 yield in data. Once this factor is derived, it can be used to scale the MC estimate of the background in the

1875 signal region. This is illustrated in equation 5.3.

$$B_{\text{SR}}^{\text{est}} = B_{\text{SR}} \times \frac{N_{\text{CR}}}{B_{\text{CR}}} \equiv B_{\text{SR}} \times \beta \quad (5.3)$$

1876 Here,  $B$  denotes the MC yield prediction in the denoted region, while  $N$  denotes the observed number  
1877 of events in data in the denoted region.

1878 Another way of writing the same equation, in terms of an extrapolation factor  $\alpha$  rather than a nor-  
1879 malization factor  $\beta$ . The overall calculation is exactly the same. However, when phrased in this way, it  
1880 shows how the uncertainty on the background estimation can be reduced. This is shown in equation 5.4.

1881

$$B_{\text{SR}}^{\text{est}} = N_{\text{CR}} \times \frac{B_{\text{SR}}}{B_{\text{CR}}} \equiv N_{\text{CR}} \times \alpha \quad (5.4)$$

1882 Phrased this way, the equation shows that with enough statistics in the control region, a large theoretical  
1883 uncertainty on the overall background yield in the signal region can be replaced by a small statistical  
1884 uncertainty coming from the number of data events in the CR and a smaller theoretical uncertainty on  
1885 the extrapolation from the control region to the signal region.

### 1886 5.5.2 TOP BACKGROUND

1887 The normalization factor  $\beta_t$  for the top background in the VBF analysis is derived in a region required  
1888 to have one b-tagged jet, or  $n_b = 1$ . In the cut-based analysis, normalization factors are computed at  
1889 every stage of the cutflow by applying the appropriate cuts in the CR. These NF are then applied to the  
1890  $t\bar{t}$  and single top event yields in the SR. In the BDT analysis, a single normalization factor is computed  
1891 for each bin of  $O_{\text{BDT}}$  after applying the BDT pre-training cuts described previously. The computed  
1892 normalization factors are derived with all flavor combinations combined in order to decrease statistical  
1893 uncertainty. Additionally, in the BDT analysis, BDT bins 2 and 3 are merged for the same reason.

1894 Table 5.8 shows the evolution of the  $\beta_t$  through the cut-based selection. Table 5.9 shows the value  
1895 of the  $\beta_t$  in each bin of  $O_{\text{BDT}}$ . In all cases, the computed factors are relatively consistent with unity,  
1896 with the largest discrepancy coming in bin 1 of  $O_{\text{BDT}}$ . The normalization factors in the bins of  $O_{\text{BDT}}$

1897 are also consistent with those derived in teh cut-based sisignal region, increasing confidence in the BDT  
 1898 estimation.

Cut	$\beta_t$
$p_T^{\text{sum}} < 15 \text{ GeV}$	$1.03 \pm 0.01$
$m_{\tau\tau} < m_Z - 25$	$1.05 \pm 0.01$
$m_{jj} > 600 \text{ GeV}$	$0.96 \pm 0.06$
$\Delta y_{jj} > 3.6$	$1.02 \pm 0.08$
CJV	$1.13 \pm 0.16$
OLV	$1.01 \pm 0.19$
$m_{jj} < 1 \text{ TeV}$	$0.94 \pm 0.19$
$m_{jj} > 1 \text{ TeV}$	$1.48 \pm 0.66$

**Table 5.8:** Top normalization factors computed at each stage of the cut-based selection. Uncertainties are statistical only.

$O_{\text{BDT}}$	$\beta_t$
Bin0	$1.09 \pm 0.02$
Bin1	$1.58 \pm 0.15$
Bin2	$0.95 \pm 0.31$
Bin3	$0.95 \pm 0.31$

**Table 5.9:** Top normalization factors computed for each bin of  $O_{\text{BDT}}$ . Uncertainties are statistical only.

1899 Figure 5.8 shows the  $m_{jj}$  and  $O_{\text{BDT}}$  distributions in the top control region. Overall the modeling  
 1900 looks consistent with the data.

1901 While these normalization factors can be computed and applied to the expected background yields  
 1902 listed in tables like table 5.7, in the end the normalization of the top background is profiled (meaning  
 1903 there is a dedicated Poisson constraint) and allowed to float in the final statistical fit.

### 1904 5.5.3 $Z/\gamma^* \rightarrow \tau\tau$ BACKGROUND

1905 In the different flavor channels, the  $Z/\gamma^* \rightarrow \tau\tau$  background is an important one. Di-tau production  
 1906 can produce an  $e\mu$  final state if each  $\tau$  lepton decays to a different flavor lepton.

1907 In the BDT analysis, a single normalization factor for the background is derived. A control region is  
 1908 defined using the pre-training selection cuts, except requiring that  $|m_{\tau\tau} - m_Z| < 25 \text{ GeV}$  so that  
 1909 the region is enriched in  $Z/\gamma^* \rightarrow \tau\tau$  background. Additional requirements of  $m_{\ell\ell} < 80(75) \text{ GeV}$

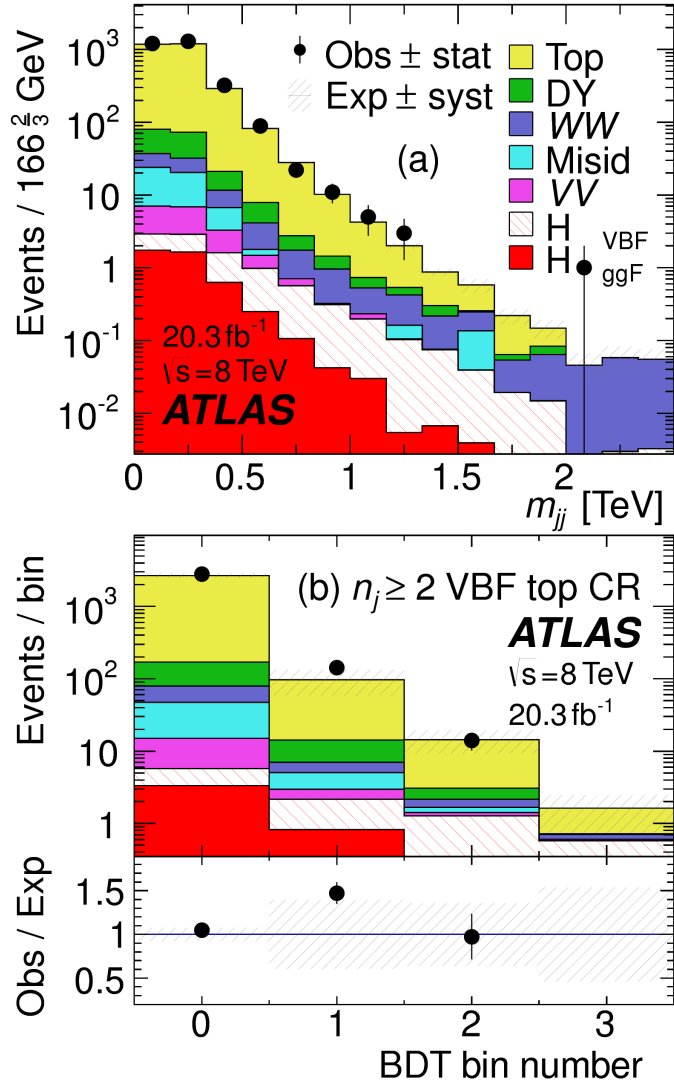


**Figure 5.8:** Distributions of  $m_{jj}$  (a) and  $O_{\text{BDT}}$  (b) in the VBF  $n_b = 1$  top CR [61].

in the different (same) flavor channel, as well as  $O_{\text{BDT}} > -0.48$  are applied to increase the purity of  
 the region. The final  $\beta_{Z/\gamma^* \rightarrow \tau\tau}$  is calculated to be  $0.9 \pm 0.3$  (statistical uncertainty only). Because of  
 the small contribution of this background in the BDT analysis and the large statistical uncertainty, no  
 additional systematics are calculated. The final SR estimate is scaled by this  $\beta$  and not allowed to float in  
 the fit.

The cut-based corrections are a bit more involved because they need to be applied selection by selec-  
 tion, as well as in the final signal region for the fit. The region is defined including all SR cuts up to the

1917  $Z/\gamma^* \rightarrow \tau\tau$  veto, which is instead made into a  $Z$  mass peak requirement as for the BDT region. The  
 1918  $m_{\ell\ell}$  cut from the BDT region is included as well. The cut-based approach aims to correct the normal-  
 1919 ization of the  $Z/\gamma^* \rightarrow \tau\tau$  background in two ways. First, an overall normalization factor is computed  
 1920 from the control region. However, the VBF topological cuts are not included in this region, and apply-  
 1921 ing them as is done in the top CR is not feasible due to limited statistics. So, instead, correction factors  
 1922 (CF) to the cut efficiencies of the VBF cuts are derived in a same flavor  $Z \rightarrow \ell\ell$  control region, which has  
 1923 significantly more statistics. The CF is simply the ratio of the cut efficiencies in data and MC derived in  
 1924 this region. In the end, the overall background estimate is given by equation 5.5.

$$N_{Z/\gamma^* \rightarrow \tau\tau}^{\text{est}} = B_{Z/\gamma^* \rightarrow \tau\tau}^{\text{SR}} \times \beta_{\tau\tau} \times \frac{\epsilon_{\text{VBF cuts}}^{\text{data}}}{\epsilon_{\text{VBF cuts}}^{\text{MC}}} \quad (5.5)$$

1925 The hypothesis is that while the normalization correction must be derived in a dedicated region, the  
 1926 efficiency of the VBF cuts should not be sensitive to the type of  $Z/\gamma^*$  process and thus the larger control  
 1927 region can be exploited to derive the CF. Figure 5.9 shows a shape comparison for the  $m_{jj}$  variable in  
 1928  $Z \rightarrow \tau\tau$  events in the signal region and  $Z \rightarrow \ell\ell$  events in the control region. The figure shows that the  
 1929 shapes are indeed comparable and thus any CF derived in the same flavor control region can reliably be  
 1930 applied in the signal region.

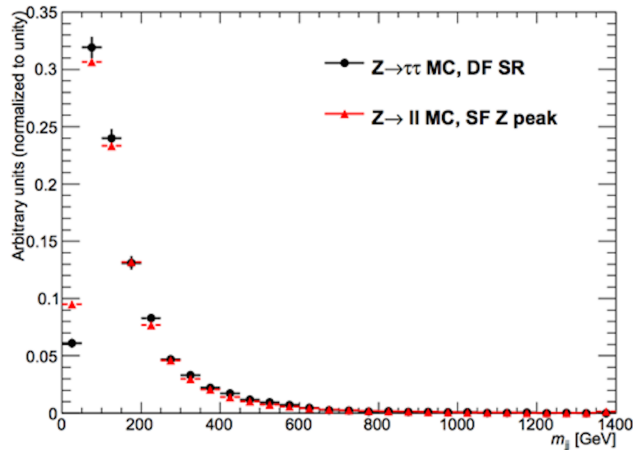


Figure 5.9: Comparison of  $m_{jj}$  shape in a same flavor  $Z \rightarrow \ell\ell$  control region and the VBF cut-based signal region.

1931 Table 5.10 shows the overall normalization factor  $\beta_{\tau\tau}$  and the efficiency correction factors for the var-

<sup>1932</sup> ious VBF topological cuts. In general, the statistical uncertainties on the cut efficiency corrections are  
<sup>1933</sup> quite good, and the MC tends to underestimate the efficiency of the VBF cuts for the  $Z/\gamma^* \rightarrow \tau\tau$  back-  
<sup>1934</sup> ground. The overall normalization factor is also consistent with that calculated for the BDT analysis.

$\beta_{\tau\tau}$	$0.97 \pm 0.04$
Cut	Correction factors
$m_{jj} > 600 \text{ GeV}$	$1.09 \pm 0.01$
$\Delta y_{jj} > 3.6$	$1.14 \pm 0.02$
CJV	$1.20 \pm 0.02$
OLV	$1.17 \pm 0.03$
$m_{jj} < 1 \text{ TeV}$	$1.17 \pm 0.06$
$m_{jj} > 1 \text{ TeV}$	$1.18 \pm 0.13$

**Table 5.10:**  $Z/\gamma^* \rightarrow \tau\tau$  correction factors for the VBF cut-based analysis. Uncertainties are statistical only.

#### <sup>1935</sup> 5.5.4 $Z/\gamma^* \rightarrow \ell\ell$ BACKGROUND

<sup>1936</sup> In the same flavor channels, the  $Z/\gamma^* \rightarrow \ell\ell$  background is dominant and thus must be estimated  
<sup>1937</sup> correctly. In both the BDT and cut-based analyses, the background is estimated using the so-called  
<sup>1938</sup> “ABCD” method. The ABCD method creates four different regions by defining cuts on two variables.  
<sup>1939</sup> One of the regions (A) is the signal region, while the other regions are defined by inverting one of both  
<sup>1940</sup> of the cuts. in this case, the two variables used are  $m_{\ell\ell}$  and  $E_T^{\text{miss}}$ , because inverting either of the SR cuts  
<sup>1941</sup> on these variables will give regions rich in the  $Z/\gamma^* \rightarrow \ell\ell$  background. Figure 5.10 illustrates the general  
<sup>1942</sup> strategy for each region.

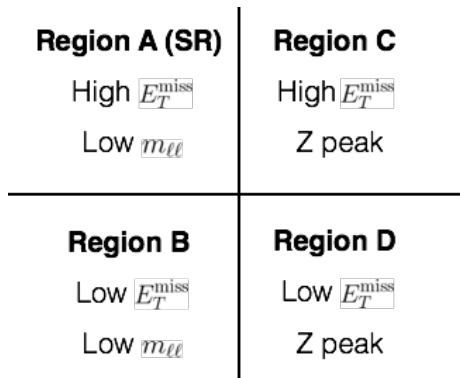


**Figure 5.10:** General illustration of the ABCD region definitions for  $Z/\gamma^* \rightarrow \ell\ell$  background estimation.

1943 In both of the cut-based and BDT analyses, the  $Z$  peak region is defined with  $|m_{\ell\ell} - m_Z| < 15$  GeV.  
 1944 In the cut-based analysis, low  $m_{\ell\ell}$  corresponds to  $m_{\ell\ell} < 50$  GeV (this defines the cut-based SR) while  
 1945 in the BDT it is  $m_{\ell\ell} < 75$  GeV. In the cut-based, high and low  $E_T^{\text{miss}}$  are defined as opposite ends of  
 1946 the 55 GeV cut applied for the signal region definition. The BDT low  $E_T^{\text{miss}}$  region is between 25 and  
 1947 45 GeV, while the high  $E_T^{\text{miss}}$  region is  $E_T^{\text{miss}} > 45$  GeV.

1948 Once the regions are defined, the final signal region background estimate is done by taking the esti-  
 1949 mate in region B and extrapolating it to the signal region (A) by multiplying it by the ratio of regions  
 1950 C and D. Effectively, the  $Z$  peak region is used to estimate the efficiency of the  $E_T^{\text{miss}}$  cut in data, and  
 1951 then this efficiency is applied in the low  $m_{\ell\ell}$  region. An additional correction is also applied for the non-  
 1952 closure of the method in MC. This is summarized in equations 5.6 and 5.7.

$$N_{Z/\gamma^* \rightarrow \ell\ell}^{\text{SR}} = N_{Z/\gamma^* \rightarrow \ell\ell}^B \times \frac{N_{Z/\gamma^* \rightarrow \ell\ell}^C}{N_{Z/\gamma^* \rightarrow \ell\ell}^D} \times f_{\text{corr}} \quad (5.6)$$

$$f_{\text{corr}} = \frac{B_{\text{MC}}^A / B_{\text{MC}}^B}{B_{\text{MC}}^C / B_{\text{MC}}^D} \quad (5.7)$$

1953 Here, the  $N$  refer to data yields in each region with the non  $Z/\gamma^*$  backgrounds subtracted, while  $B$   
 1954 refer to the  $Z/\gamma^*$  yields in MC in each region.

1955 A normalization factor  $\beta_{\ell\ell}$  is computed for each analysis as the ratio of the predicted data yield to  
 1956 the MC yield in the SR. The shape of the BDT distribution is taken from data region B, while the shape  
 1957 of the  $m_T$  distribution in the cut-based analysis is taken from  $Z/\gamma^*$  MC in the SR. The values of the  
 1958  $\beta_{\ell\ell}$  in the cut-based and BDT analyses from this method are summarized in table 5.11. They are quite  
 1959 consistent with one another within the statistical uncertainties. In the cut-based analysis, the same cut  
 1960 efficiency correction factors shown in table 5.10 are also applied (in product with the  $\beta_{\ell\ell}$ ) in the same  
 1961 flavor channels to this background, as they were derived in the  $Z$  peak region.

	$\beta_t$
BDT Bin 1	$1.01 \pm 0.15$
BDT Bin 2	$0.89 \pm 0.28$
Cut-based	$0.81 \pm 0.21$

**Table 5.11:**  $Z/\gamma^* \rightarrow \ell\ell$  normalization factors for cut-based and BDT analyses. Uncertainties are statistical only.

### 1962 5.5.5 $WW$ AND OTHER DIBOSON BACKGROUNDS

1963 The  $WW$  and other diboson backgrounds have both their shape and normalization taken from MC  
 1964 simulation. They are validated in dedicated control regions and found to agree with data well.  
 1965 As  $WW$  is the largest of these backgrounds and is irreducible, validating the estimate is of particular  
 1966 importance. The validation region is constructed by requiring the pre-selection cuts on leptons and  $m_{\ell\ell}$ ,  
 1967  $n_b = 0$ , and  $m_T > 100$  GeV. The  $m_{T2}$  variable [?] is an additional discriminant that will isolate  
 1968 the  $WW$  background, and a requirement of  $m_{T2} > 160$  GeV is placed to define the  $WW$  validation  
 1969 region. This cut gives a 60% purity for the validation region. The derived normalization factor in the  
 1970 region is  $1.15 \pm 0.19$  and is thus consistent with unity. Figure 5.11 shows the  $m_{T2}$  distribution and how  
 1971 it distinguishes the  $WW$  background.

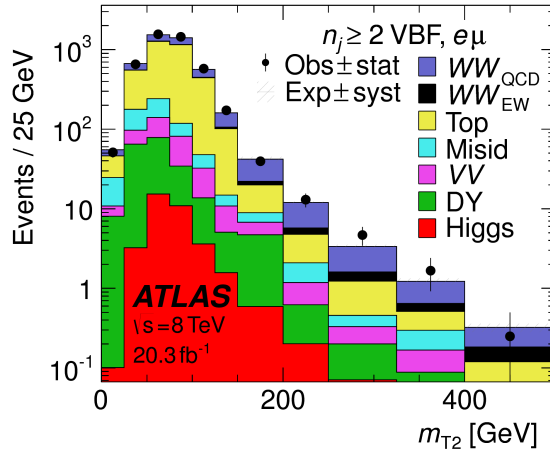


**Figure 5.11:** Distribution of  $m_{T2}$  in the  $WW$  validation region of the VBF analysis [61].

1972 5.5.6 HIGGS PRODUCTION VIA GLUON-GLUON FUSION

1973 Because this analysis is dedicated to measuring the VBF contribution to Higgs production, the com-  
1974 ponent of Higgs production from gluon-gluon fusion is treated as a background. The shape is taken  
1975 directly from simulation, using the generators described in table 5.4. In the final combined fit of all dif-  
1976 ferent signal regions, the normalization is controlled by either a combined signal strength parameter  $\mu$ ,  
1977 which controls the normalization of both ggF and VBF production, or a separate parameter  $\mu_{\text{ggF}}$  de-  
1978 pending on the interpretation being presented in the final results.

1979 5.5.7 BACKGROUNDS WITH MISIDENTIFIED LEPTONS

1980 As discussed previously, the  $W + \text{jets}$  and QCD multijet backgrounds are derived with fully data-driven  
1981 methods. These backgrounds do not make a large contribution to the final VBF signal region but their  
1982 estimation methods are discussed briefly here.

1983  $W + \text{jets}$  BACKGROUND

1984 The  $W + \text{jets}$  background enters the signal region by having one of the jets mis-reconstructed as a lep-  
1985 ton. The background is estimated by constructing a control sample with two leptons, where one lepton  
1986 passes the usual lepton quality cuts but the second lepton fails one of those cuts (also known as the “anti-  
1987 identified” lepton). This control region is rich in the  $W + \text{jets}$  contribution because if a second lepton is  
1988 reconstructed in a  $W + \text{jets}$  event it is likely to be poor quality. The purity of this  $W + \text{jets}$  control sample  
1989 is 85% to 90% depending on the exact configuration of leptons in the final state.

1990 The signal region estimate of  $W + \text{jets}$  is estimated by extrapolation from the control sample to the sig-  
1991 nal region using extrapolation factors derived in a  $Z + \text{jets}$  control sample in data. The extrapolation fac-  
1992 tor is the ratio of the number of lepton candidates satisfying all quality criteria to the number of lepton  
1993 candidates anti-identified. This ratio is measured in bins of  $p_T$  and  $\eta$ . Thus, the final signal region esti-  
1994 mate (binned as the extrapolation factor is binned) is simply the number of events in the anti-identified  
1995 lepton control sample multiplied by the extrapolation factor derived from the  $Z + \text{jets}$  control sample.

1996 Figure 5.12 shows the extrapolation factors derived for electrons and muons.

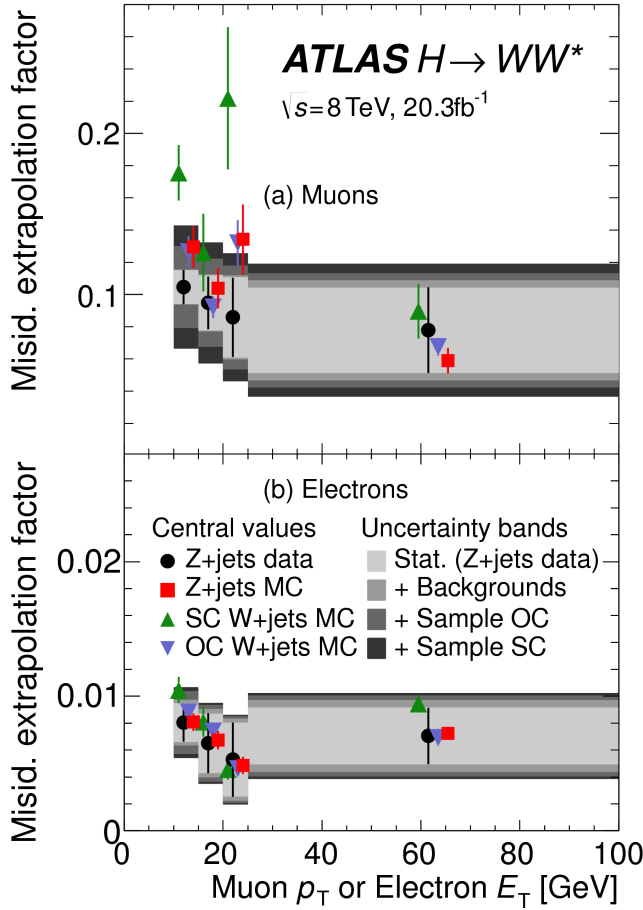


**Figure 5.12:** Extrapolation factors for the  $W$ +jets estimate derived for muons (a) and electrons (b) as a function of lepton  $p_T$  [61].

### 1997 QCD MULTIJET BACKGROUND

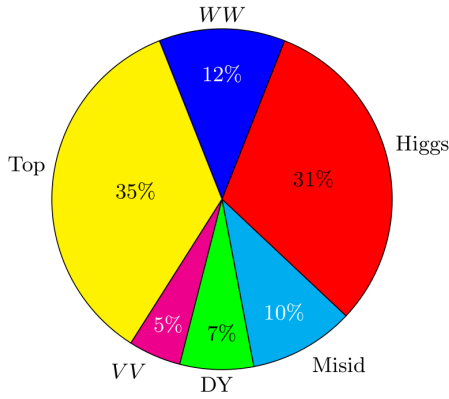
1998 The method for estimating the multijet background is very similar to the  $W$ +jets estimation method.  
 1999 The control sample in this case has two anti-identified leptons but otherwise satisfies all signal region  
 2000 requirements. The extrapolation factor is estimated from a multijet sample and applied twice to the  
 2001 control sample.

### 2002 5.5.8 BACKGROUND COMPOSITION IN FINAL SIGNAL REGION

2003 After all of these estimation procedures, the final signal region composition can be calculated. The esti-  
 2004 mated yields are all shown in table 5.7. Figure 5.13 shows the relative percentages of the different back-

ground for the different flavor and same flavor final states. In  $e\mu$ , the leading backgrounds are top backgrounds, ggF Higgs, and SM  $WW$  production. In  $ee/\mu\mu$ , the leading background is Drell-Yan, followed by top and ggF Higgs.

(a)  $n_j \geq 2$  VBF,  $e\mu$



(b)  $n_j \geq 2$  VBF,  $ee/\mu\mu$

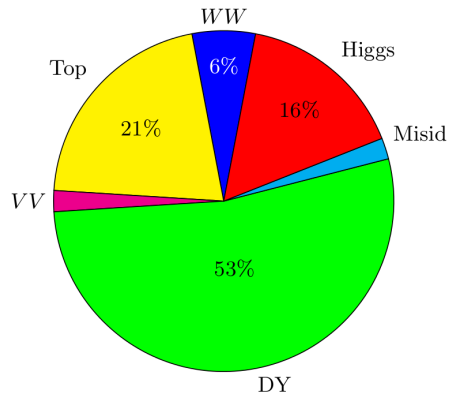


**Figure 5.13:** Background composition in final VBF signal region [61].

## 5.6 SYSTEMATIC UNCERTAINTIES

There are two main types of systematic uncertainties that are assessed for the analysis. First, theoretical uncertainties associated with the various signal and background yield estimates are discussed. Then, experimental uncertainties due to detector effects are shown. Normalization uncertainties refer to uncertainties that affect the cross section of the process in question in the signal region being probed. Shape uncertainties refer to systematic uncertainties that affect the shape of the final discriminating variable (either  $m_T$  or  $O_{\text{BDT}}$ ).

### 5.6.1 THEORETICAL UNCERTAINTIES

There are four main components to theoretical uncertainties assigned to signal and background processes taken from Monte Carlo. Each one is a different source of variation in the overall acceptance for that process. The first involves variation of the QCD renormalization and factorization scales used in the calculation. In this case, the two scales are varied independently and simultaneously by factors of two high or low and quantifying the resulting variation in normalization and shape for the process. This

approximates the correction to the cross section that would come from including the next order of the QCD calculation (referred to as scale uncertainty). Next, there is an uncertainty associated with the PDF set used in generating the events. The uncertainty eigenvectors for the given PDF set are studied, and the envelope of maximal variation is taken as an uncertainty. Finally, there are two uncertainties associated with the choice of MC software (referred to as PDF uncertainty). An uncertainty associated with the generator chosen for the hard scattering process is evaluated by keeping the parton showering software constant but varying the matrix element generator and taking the maximal variation as an uncertainty (referred to as the generator uncertainty). The converse variation can also be done, where the matrix element generator remains constant and the generator used for the underlying event/parton shower modeling is varied (referred to as the UE/PS uncertainty). In cases where the background is normalized in a control region, the systematic uncertainty arises from variations of the extrapolation factor  $\alpha$  between the CR and the SR, which can affect the normalization of the background in the SR.

There are two additional uncertainties that are applied to the Higgs processes as well. First, there are uncertainties assigned to the Higgs total production cross section. Then, there are uncertainties assigned based on the fact that the analysis is done in exclusive jet bins and it is possible for signal events to migrate from one bin to the next depending on the presence or absence of jets. These are assigned using the Jet Veto Efficiency (JVE) procedure [?] for ggF events and the Stewart-Tackmann (ST) method [80] for VBF production.

Table 5.12 shows the total theory uncertainties on the backgrounds in the cut-based analysis. These are the sum in quadrature of the uncertainties from each of the variations described above.

Process	Theory syst. (%)
ggF $H$	48
Top	26
QCD $WW$	37
$Z/\gamma^* \rightarrow \tau\tau$	6.1

**Table 5.12:** Systematic uncertainties for various processes in the cut-based VBF analysis, given in units of % change in yield.  
Values are given for the low  $m_{jj}$  signal region.

Figures 5.14 and 5.15 show the variations in the extrapolation factor from the PDF and QCD uncertainties on the top background estimate, binned in  $m_T$ , for the cut-based analysis. In both cases, there

2043 was no significant shape uncertainty but normalization uncertainties were assigned according to the  
 2044 maximal variation. These uncertainties enter into the 26% total uncertainty on top quoted in table 5.12.  
 2045 While the estimate for the same-flavor  $Z/\gamma^* \rightarrow \ell\ell$  background is data-driven, there is still a sys-  
 2046 tematic uncertainty taken for the non-closure of the method in Monte Carlo. This is taken as the max-  
 2047 imum of the deviation of the non-closure factor  $f_{\text{corr}}$  from unity and its uncertainty, or  $\max(|1 -$   
 2048  $f_{\text{corr}}|, \delta f_{\text{corr}})$ . For the cut-based analysis this non-closure uncertainty 23%, while for the BDT analy-  
 2049 sis it is 17%.

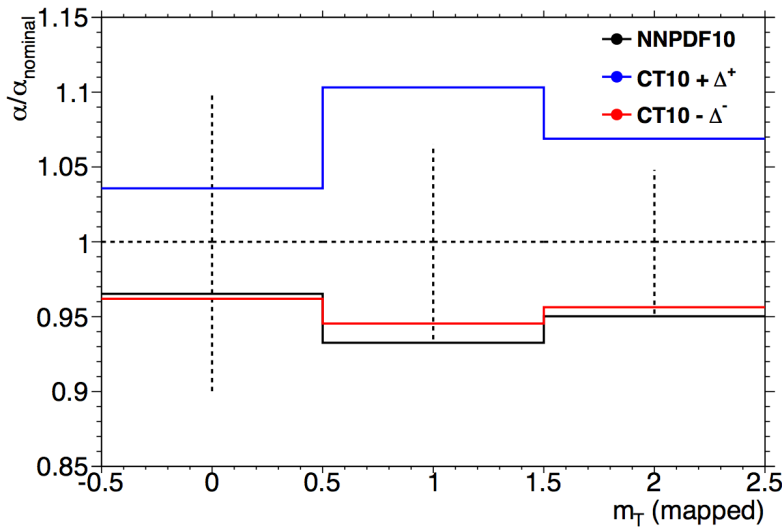
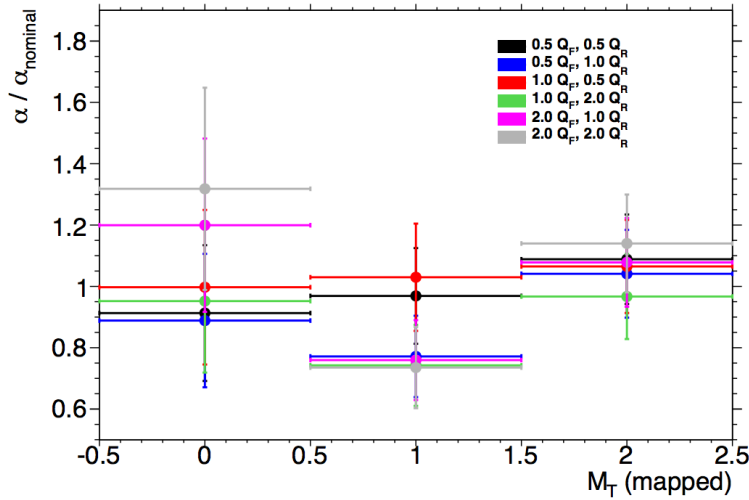


Figure 5.14: Variations in the top background extrapolation factor in the cut-based analysis due to PDF uncertainties, binned in  $m_T$ .

### 2050 5.6.2 EXPERIMENTAL UNCERTAINTIES

2051 In this analysis, the theoretical uncertainties end up being the most dominant, but there are some ex-  
 2052 perimental uncertainties that make a contribution as well. The first is the uncertainty on the measured  
 2053 integrated luminosity, which affects backgrounds whose normalization is taken from MC and is mea-  
 2054 sured to be 2.8% in the 8 TeV dataset [81]. The dominant sources of uncertainty overall are uncertainties  
 2055 on the jet energy scale and resolution and the  $b$ -tagging efficiency. Additional sources include lepton  
 2056 uncertainties on identification, resolution, and trigger efficiency, as well as uncertainties on the missing  
 2057 transverse momentum .



**Figure 5.15:** Variations in the top background extrapolation factor in the cut-based analysis due to QCD scale uncertainties, binned in  $m_T$ .

2058     The jet energy scale uncertainty is split into several independent components, including jet-flavor  
 2059     dependent calorimeter response uncertainties, uncertainties on modeling of pile-up interactions, uncer-  
 2060     tainties on extrapolation from the central to forward detector regions, and MC non-closure [82]. The  
 2061     uncertainty on energy scale for jets used in this analysis ranges from 1% to 7% depending on the jet  $p_T$   
 2062     and  $\eta$ . The jet energy resolution varies from 5% to 20%, with uncertainties ranging from 2% to 40%  
 2063     (the largest uncertainties occurring at the selection threshold).

2064     The b-tagging efficiency is independently measured in data samples enriched in dileptonic decays of  
 2065      $t\bar{t}$  events or in events where a muon is reconstructed in the vicinity of a jet [83, 84]. The efficiencies and  
 2066     their uncertainties are binned in  $p_T$  and decomposed into uncorrelated components using an eigenvec-  
 2067     tor method [? ]. Uncertainties on the efficiency range from 1% to 7.8%. The uncertainty on the rate  
 2068     of misidentification of  $c$ -jets as  $b$ -jets ranges from 6-14%, while the uncertainty on the rate of light jet  
 2069     mis-tagging ranges from 9-19% depending on  $p_T$  and  $\eta$ .

2070     The total experimental uncertainties on different signal and background components are summa-  
 2071     rized in table 5.13. They are compared to the level of other statistical and systematic uncertainties as well.  
 2072     Overall, the experimental uncertainties are sub-dominant compared to the statistical and theoretical  
 2073     uncertainties.

Sample	Total error	Stat. error	Expt. syst. err.	Theo. syst. err.
$n_j \geq 2$ VBF-enriched				
$N_{\text{sig}}$	13	-	6.8	12
$N_{\text{bkg}}$	9.2	4.7	6.4	4.5
$N_{WW}$	32	-	14	28
$N_{\text{top}}$	15	9.6	7.6	8.5
$N_{\text{misid}}$	22	-	12	19
$N_{VV}$	20	-	12	15
$N_{\tau\tau} (\text{DY})$	40	25	31	2.9
$N_{ee/\mu\mu} (\text{DY})$	19	11	15	-

**Table 5.13:** Composition of the post-fit uncertainties (in %) on the total signal ( $N_{\text{sig}}$ ), total background ( $N_{\text{bkg}}$ ), and individual background yields in the VBF analysis [61].

## 2074 5.7 RESULTS

2075 While the combined results of all the  $H \rightarrow WW^*$  sub-analyses will be discussed in the next chapter, this  
 2076 section presents the results of the VBF specific analysis and interpretations. As table 5.7 shows, the final  
 2077 cut-based signal region contains 20 events in data with  $m_T < 150$  GeV, 14 coming from the  $e\mu$  channel  
 2078 and 6 coming from the  $ee + \mu\mu$  channel. The BDT analysis has many more candidates due to its looser  
 2079 selection, and the yields in each bin of  $O_{\text{BDT}}$  are shown in table 5.14.

2080 Figure 5.16(a) shows the final distribution of data candidates compared to the expected  $m_T$  distri-  
 2081 bution for signal and background. The data are very consistent with a VBF Higgs hypothesis. Fig-  
 2082 ure 5.16(b) shows where the data candidates fall in the two-dimensional binning of  $m_T$  and  $m_{jj}$  used  
 2083 in the fit for the cut-based analysis.

2084 Figure 5.17 shows the distributions of  $O_{\text{BDT}}$  and  $m_T$  in the VBF BDT analysis. Again the data are  
 2085 quite consistent with a VBF Higgs hypothesis.

2086 Because the cut-based result is used as a validation for the BDT analysis and the two signal regions are  
 2087 not fully orthogonal, it is interesting to explore which events overlap between the two analyses. Of the  
 2088 twenty events in the cut-based signal region, only seven were not selected by the BDT analysis, while the  
 2089 other thirteen also enter the BDT signal region. Figure ?? shows where the different analysis candidates  
 2090 lie in the  $m_{jj}$ - $m_T$  plane. This shows clearly that the advantage of the BDT analysis is that it can extract

(a) Before the BDT classification

Selection	Summary						Composition of $N_{\text{bkg}}$											
	$N_{\text{obs}}/N_{\text{bkg}}$	$N_{\text{obs}}$	$N_{\text{bkg}}$	$N_{\text{signal}}$	$N_{\text{ggF}}$	$N_{\text{VBF}}$	$N_{\text{VH}}$	$N_{\text{WW}}$	$N_{\text{WW}}^{\text{NEW}}$	$N_{\text{WW}}^{\text{QCD}}$	$N_t$	$N_{\text{Wj}}$	$N_{\text{misid}}$	$N_{ij}$	$N_{VV}$	$N_{\text{Drell-Yan}}$	$N_{\tau\tau}^{\text{QCD}}$	$N_{\tau\tau}^{\text{NEW}}$
$e\mu$ sample	$1.04 \pm 0.04$	718	689	13	15	2.0	90	II	327	42	29	23	31	—	2.2	130	2	—
$ee/\mu\mu$ sample	$1.18 \pm 0.08$	469	397	6.0	7.7	0.9	37	3	132	17	5.2	1.2	10.1	168	23	1	—	—

(b) Bins in  $O_{\text{BDT}}$ 

$e\mu$ sample	Composition of $N_{\text{bkg}}$																	
	Bin 0 (not used)	1.02	$\pm 0.04$	661	650	8.8	3.0	1.9	83	9	313	40	26	21	28	2.2	126	1
Bin 1	0.99	$\pm 0.16$	37	37	3.0	4.2	0.1	5.0	1.0	17	3.1	3.3	1.8	2.6	—	4.0	0.2	—
Bin 2	2.26	$\pm 0.63$	14	6.2	1.2	4.2	—	1.5	0.5	1.8	0.3	0.4	0.3	0.8	—	0.3	0.3	—
Bin 3	5.41	$\pm 2.32$	6	1.1	0.4	3.1	—	0.3	0.2	0.3	0.1	—	—	0.1	—	0.1	0.1	—
$ee/\mu\mu$ sample	Composition of $N_{\text{bkg}}$																	
	Bin 0 (not used)	1.91	$\pm 0.08$	396	345	3.8	1.3	0.8	33	2	123	16	4.1	1.1	8.8	137	20.5	0.5
Bin 1	0.82	$\pm 0.14$	53	45	1.5	2.2	0.1	3.0	0.5	10.4	1.8	0.8	0.2	0.9	26	1.7	0.1	—
Bin 2	1.77	$\pm 0.49$	14	7.9	0.6	2.5	—	0.8	0.3	1.1	0.2	0.2	—	0.3	4.4	0.3	0.1	—
Bin 3	6.52	$\pm 2.87$	6	0.9	0.2	1.7	—	0.1	0.2	0.2	—	—	—	—	0.7	—	—	—

**Table 5.14:** Event selection for the VBF BDT analysis. The event yields in (a) are shown after the pre-selection and the additional requirements applied before the BDT classification (see text). The event yields in (b) are given in bins in  $O_{\text{BDT}}$  after the classification [61].

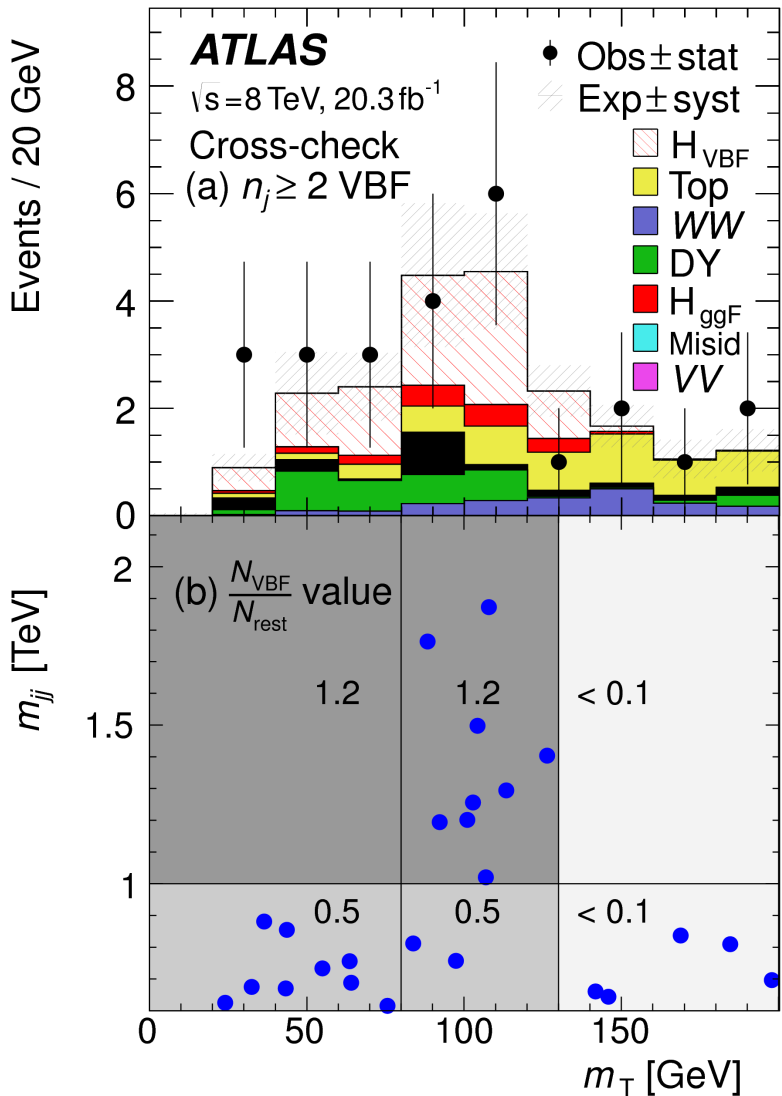


**Figure 5.16:** Post-fit distributions in the cut-based VBF analysis. Panel (a) shows the one-dimensional  $m_T$  distribution, while (b) shows the data candidates split into the bins of  $m_T$  and  $m_{jj}$  used in the final fit [61].

2091 signal candidates lower  $m_{jj}$  region due to its ability to recognize correlations with other variables.  
 2092 While the context of these results in the broader  $H \rightarrow WW^*$  statistical analysis will be presented  
 2093 in the next chapter, the significance of the VBF observation can be shown here. In the BDT analysis,  
 2094 the expected signal significance was  $2.7\sigma$ , while the observed significance was  $3.1\sigma$ . In the cut-based  
 2095 analysis, the expected significance was  $2.1\sigma$  and the observed significance was  $3.0\sigma$ . The compatibility  
 2096 between these two results can be evaluated by computing the probability of observing a larger difference

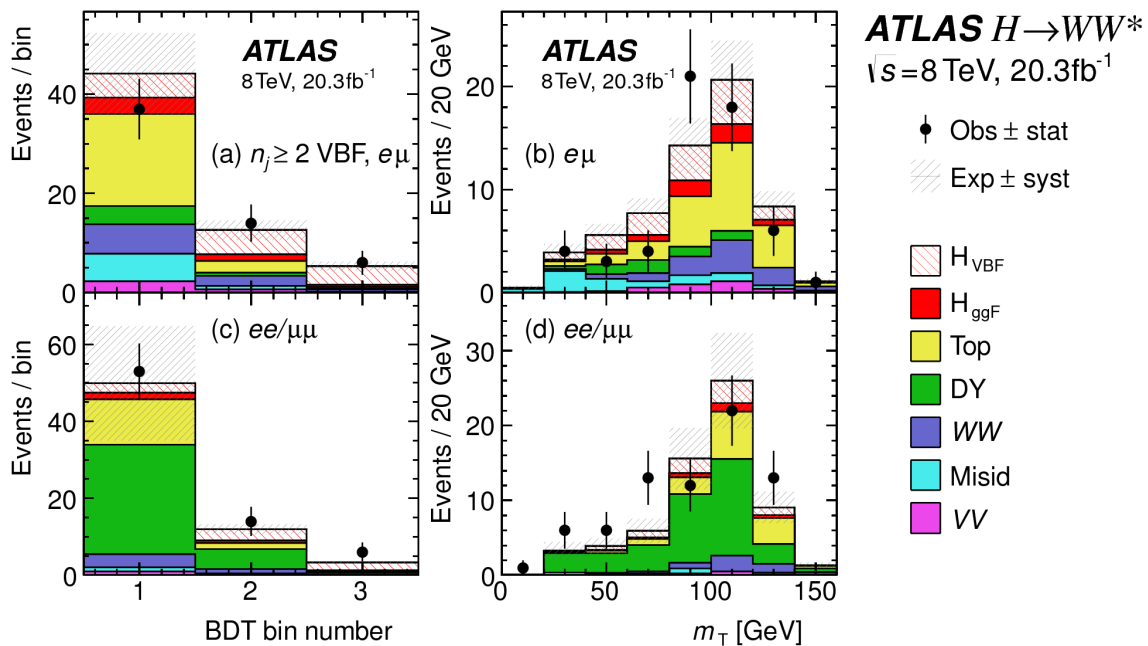


Figure 5.17: Postfit distributions in the BDT VBF analysis [61].

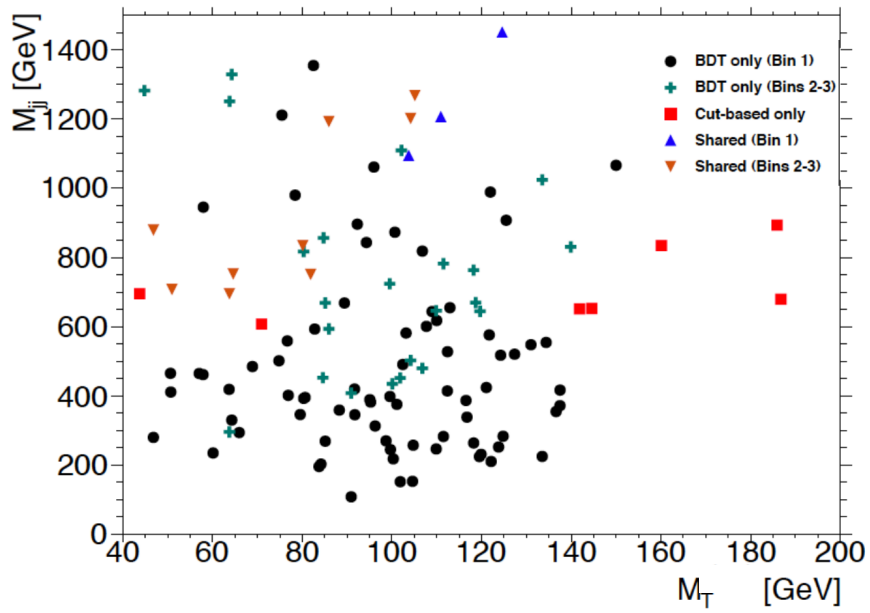


Figure 5.18: Overlap between cut-based and BDT VBF signal region candidates in the  $m_{jj}$ - $m_T$  plane.

2097 in  $Z_0$  values than the one measured. Using toy Monte Carlo with the ggF signal strength fixed to unity  
2098 and considering only statistical uncertainties, this probability is computed to be 79%, indicating good  
2099 agreement between the analyses. This result represents the first observation of the vector boson fusion  
2100 production of a Higgs boson.

*The feeling is less like an ending than just another  
starting point.*

Chuck Palahniuk

# 6

2101

2102

## Combined Run I $H \rightarrow WW^* \rightarrow \ell\nu\ell\nu$

2103

## results

2104

### 6.1 INTRODUCTION

2105

In the final statistical analysis of  $H \rightarrow WW^* \rightarrow \ell\nu\ell\nu$ , the dedicated gluon-gluon fusion and vector boson fusion sensitive signal regions are all combined into a single fit to determine the main parameters of interest, the Higgs signal strength  $\mu$  and mass  $m_H$ . Therefore, while the specific requirements applied for the VBF sensitive analysis are discussed in chapter 5, the final measurement of these parameters can only be discussed in combination with the results of the ggF dedicated analysis. For example, because ggF Higgs production is considered a background in the VBF analysis, the ggF dedicated signal regions can actually constrain the normalization of this background in the VBF dedicated region.

2110

This chapter presents the combined interpretation of results in the  $H \rightarrow WW^* \rightarrow \ell\nu\ell\nu$  analysis

SR category $i$			Fit var.
$n_j$ , flavor	$\otimes m_{\ell\ell}$	$\otimes p_T^{\ell 2}$	
$n_j = 0$	$e\mu$	$\otimes [10, 30, 55]$	$\otimes [10, 15, 20, \infty]$
	$ee/\mu\mu$	$\otimes [12, 55]$	$\otimes [e, \mu]$
			$m_T$
$n_j = 1$	$e\mu$	$\otimes [10, 30, 55]$	$\otimes [10, 15, 20, \infty]$
	$ee/\mu\mu$	$\otimes [12, 55]$	$\otimes [e, \mu]$
			$m_T$
$n_j \geq 2$ ggF	$e\mu$	$\otimes [10, 55]$	$\otimes [10, \infty]$
$n_j \geq 2$ VBF	$e\mu$	$\otimes [10, 50]$	$\otimes [10, \infty]$
	$ee/\mu\mu$	$\otimes [12, 50]$	$\otimes [10, \infty]$
			$O_{BDT}$
			$O_{BDT}$

Table 6.1: All signal regions definitions input into final statistical fit [61].

for gluon fusion and vector boson fusion Higgs production. First, the results of the dedicated gluon fusion search are presented. Then, a comparison of the individual production mode signal strengths ( $\mu_{ggF}$  and  $\mu_{VBF}$  and a measurement of the combined signal strength ( $\mu$ ) are shown. Subsequently, the measured values of the Higgs couplings to fermions and vector bosons is presented. Finally, the cross section measurement for ggF and VBF production are shown.

## 6.2 RESULTS OF DEDICATION GLUON FUSION $H \rightarrow WW^* \rightarrow \ell\nu\ell\nu$ SEARCH

The details of the dedicated gluon fusion  $H \rightarrow WW^* \rightarrow \ell\nu\ell\nu$  search are not discussed in this thesis and instead left to more comprehensive sources [61]. However, a brief summary of the results are essential for describing the results of the full analysis and interpreting the results of the dedicated VBF search in this broader context.

Table 6.1 shows the individual signal regions that were input into the final statistical fit. The ggF dedicated bins use  $m_T$  as their discriminating variable and are separated into bins of  $p_T$  of the subleading lepton as well. The VBF dedicated bin uses the  $O_{BDT}$  distribution as its final discriminant.

Table 6.2 shows the yields in the various signal regions in both data and expected signal and back-

<sup>2127</sup> grounds. The yields for signal and background are all scaled according to the final normalizations calcu-  
<sup>2128</sup> lated in the fit.

	$N_{\text{obs}}$	$N_{\text{bkg}}$	$N_{\text{ggF}}$	$N_{\text{VBF}}$
$n_j = 0$	3750	$3430 \pm 90$	$300 \pm 50$	$8 \pm 4$
$n_j = 1$	1596	$1470 \pm 40$	$102 \pm 26$	$17 \pm 5$
$n_j \geq 2, \text{ggF } e\mu$	1017	$960 \pm 40$	$37 \pm 11$	$13 \pm 1.4$
$n_j \geq 2, \text{VBF}$	130	$99 \pm 9$	$7.7 \pm 2.6$	$21 \pm 3$

**Table 6.2:** Post-fit yields in the different ggF and VBF dedicated signal regions [61].

<sup>2129</sup> Figure 6.1 shows the final post-fit  $m_T$  distribution in the  $n_j \leq 1$  regions. The data are very consistent with the hypothesis of ggF Higgs production. These yields are used as input, along with the VBF results

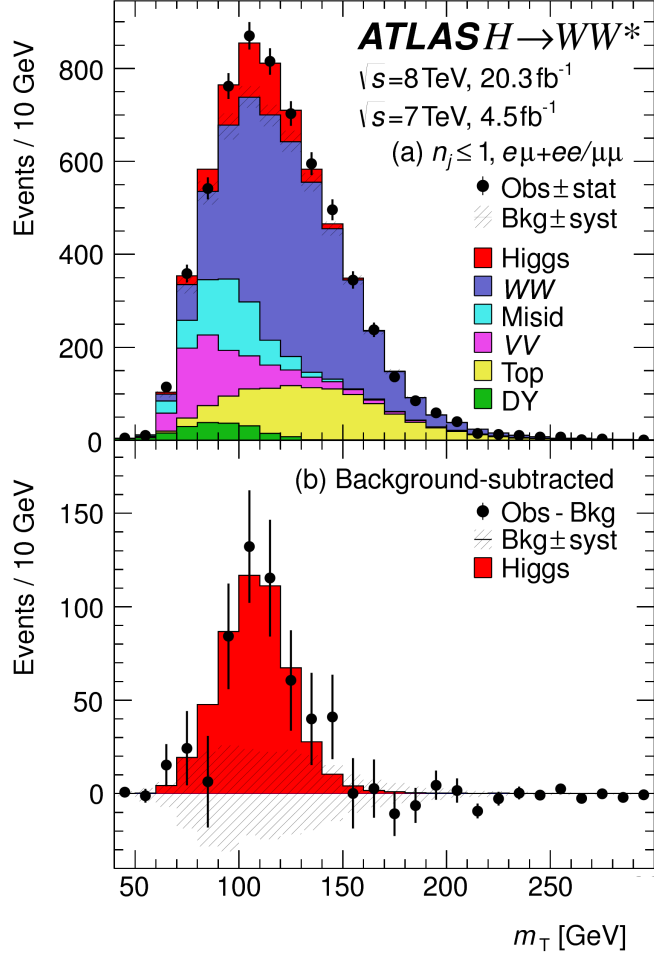


**Figure 6.1:** Post-fit  $m_T$  distribution in the  $n_j \leq 1$  regions [61].

2130

2131 in chapter 5, for the physical interpretation of results presented in subsequent sections.

2132 **6.3 SIGNAL STRENGTH MEASUREMENTS IN GGF AND VBF PRODUCTION**

2133 When all of the signal regions are combined in the fit, there can be a combined measurement of the sig-  
 2134 nal strength as well as the individual ggF and VBF signal strengths. The combined signal strength is the  
 2135 ratio of the sum of the gluon fusion and VBF cross sections to the theory prediction, or a signal strength  
 2136 for the total Higgs production cross section that this analysis is sensitive to. The final measured com-  
 2137 bined signal strength  $\mu$  is measured shown in equation 6.1.

$$\begin{aligned} \mu &= 1.09 \quad {}^{+0.16}_{-0.15} \text{ (stat.)} \quad {}^{+0.08}_{-0.07} \left( \frac{\text{expt}}{\text{syst}} \right) \quad {}^{+0.15}_{-0.12} \left( \frac{\text{theo}}{\text{syst}} \right) \quad \pm 0.03 \left( \frac{\text{lumi}}{\text{syst}} \right) \\ &= 1.09 \quad {}^{+0.16}_{-0.15} \text{ (stat)} \quad {}^{+0.17}_{-0.14} \text{ (syst)} \\ &= 1.09 \quad {}^{+0.23}_{-0.21}. \end{aligned} \tag{6.1}$$

2138 Figure 6.2 gives the best fit signal strength  $\hat{\mu}$  as a function of the hypothesized Higgs mass. The value  
 2139 at 125.36 GeV corresponds to the  $\mu$  quoted in equation 6.1. This value of the Higgs mass is used because  
 2140 it is the most precise mass measurement from ATLAS, a result of the combined  $\gamma\gamma$  and  $ZZ$  mass mea-  
 2141 surements [? ].

2142 As explained in chapter 3, a probability  $p_0$  can be computed using the test statistic  $q_0$  to quantify the  
 2143 probability that the background could fluctuate to produce an excess at least as large as the one observed  
 2144 in the data. The local  $p_0$  value is shown in figure 6.3 as a function of  $m_H$ . The minimum  $p_0$  value is  
 2145 at  $m_H = 130$  GeV and corresponds to a significance of  $6.1\sigma$ . The curve is relatively flat and the sig-  
 2146 nificance is the same at 125.36 GeV within the quoted precision. The expected significance for a signal  
 2147 with strength  $\mu = 1.0$  is  $5.8\sigma$ . This represents the first discovery level significance measurement in the  
 2148  $H \rightarrow WW^* \rightarrow \ell\nu\ell\nu$  analysis.

2149 All the results presented so far in this section have been for the combined gluon fusion and VBF pro-  
 2150 duction modes. However, each signal strength can be calculated separately in the likelihood as well.  
 2151 There are two ways to do this. First, the likelihood can be parameterized in terms of a single parameter,

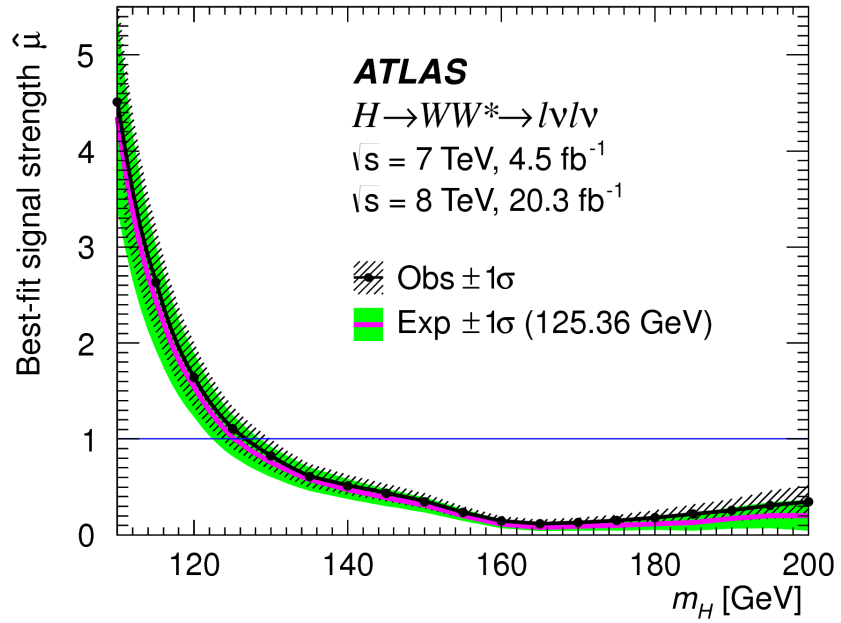


Figure 6.2: Best fit signal strength  $\hat{\mu}$  as a function of hypothesized  $m_H$  [61].

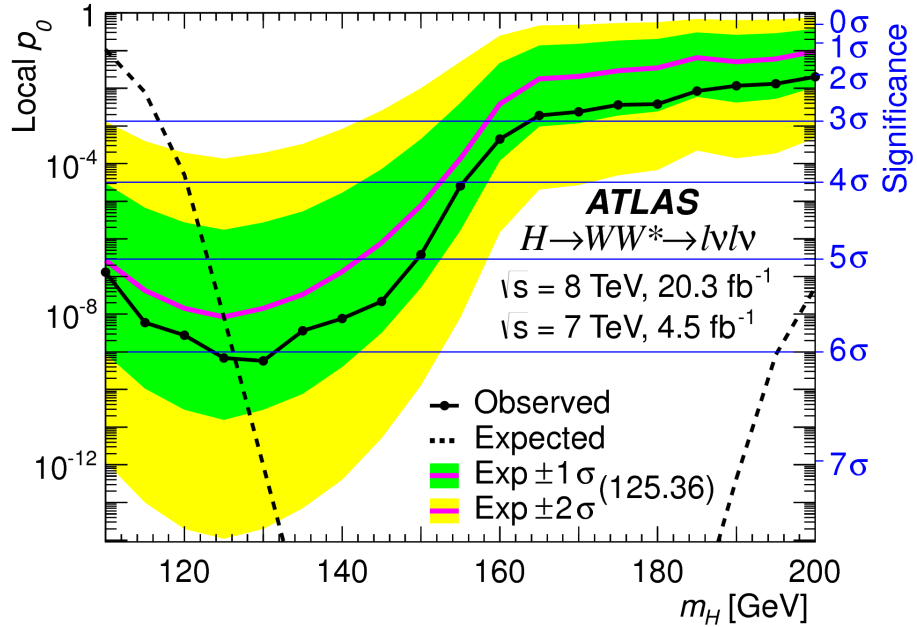
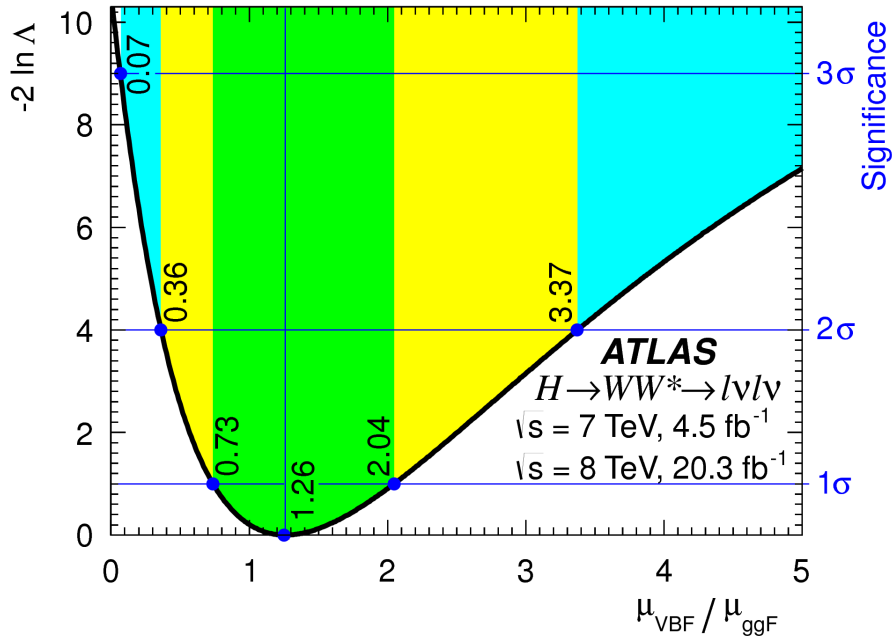


Figure 6.3: Local  $p_0$  as a function of  $m_H$  [61].

the ratio of the VBF and gluon fusion signal strengths. With this method, the significance of the VBF observation can be evaluated. Figure 6.4 shows the likelihood as a function of the ratio  $\mu_{\text{VBF}}/\mu_{\text{ggF}}$ .



**Figure 6.4:** Likelihood as a function of  $\mu_{\text{VBF}} / \mu_{\text{ggF}}$  [61].

2154     The best fit value of the ratio of signal strengths is shown in equation 6.2. Within the quoted uncer-  
 2155     tainties, it is consistent with a ratio of unity.

$$\frac{\mu_{\text{VBF}}}{\mu_{\text{ggF}}} = 1.26^{+0.61}_{-0.45} \text{ (stat.)}^{+0.50}_{-0.26} \text{ (syst.)} = 1.26^{+0.79}_{-0.53} \quad (6.2)$$

2156     The null hypothesis for VBF production corresponds to a ratio of  $\mu_{\text{VBF}} / \mu_{\text{ggF}} = 0$ . The likelihood in  
 2157     figure 6.4 gives a significance of  $3.2\sigma$  at  $\mu_{\text{VBF}} / \mu_{\text{ggF}} = 0$ , as quoted in chapter 5.

2158     In addition to the ratio of signal strengths, each signal strength can be varied independently in the  
 2159     likelihood as well. Figure 6.5 shows the two dimensional likelihood scan in the  $\mu_{\text{ggF}}-\mu_{\text{VBF}}$  plane. The  
 2160     best fit values of the two signal strengths are shown in equation 6.3. Both are consistent with unity  
 2161     within their uncertainties.

$$\begin{aligned} \mu_{\text{ggF}} &= 1.02 \pm 0.19^{+0.22}_{-0.18} = 1.02^{+0.29}_{-0.26} \\ \mu_{\text{VBF}} &= 1.27 \pm 0.44^{+0.44}_{-0.40} \pm 0.29^{+0.29}_{-0.21} = 1.27^{+0.53}_{-0.45}. \end{aligned} \quad (6.3)$$

(stat.) (syst.)

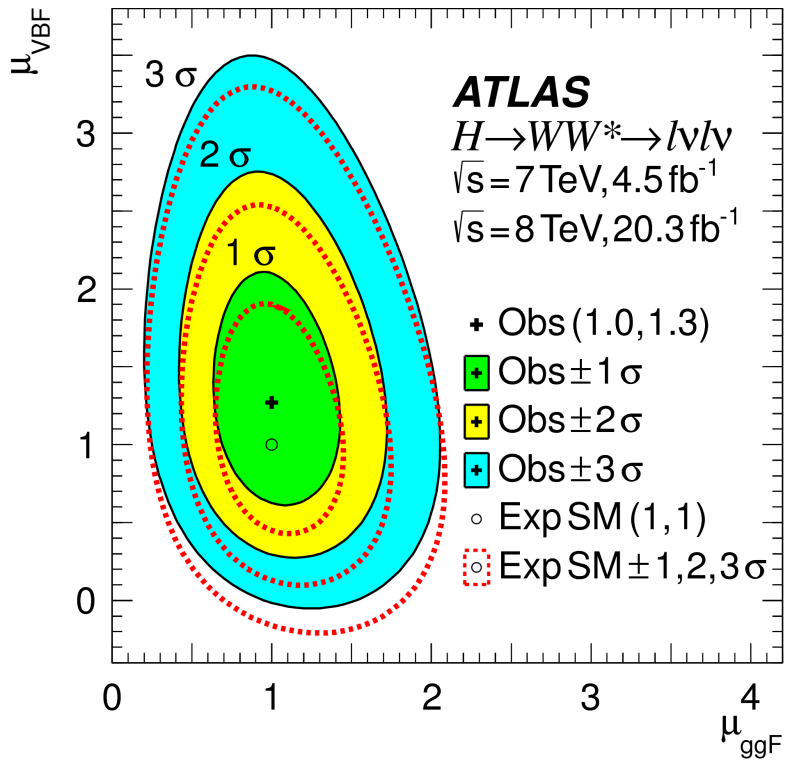


**Figure 6.5:** Likelihood scan as a function of  $\mu_{\text{VBF}}$  and  $\mu_{\text{ggF}}$  [61].

## 2162 6.4 MEASUREMENT OF HIGGS COUPLINGS TO VECTOR BOSONS AND FERMIONS

2163 Similar to the parameterization of signal strength, the couplings of the Higgs to fermions and bosons can  
 2164 also be parameterized. The parameter of interest in this case is  $\kappa$ , or the ratio of the measured coupling  
 2165 to the standard model expectation. Both the fermion and boson couplings have these so-called scale fac-  
 2166 tors,  $\kappa_F$  for fermions and  $\kappa_V$  for bosons. Gluon fusion production is sensitive to the fermion couplings  
 2167 through the top quark loops in its production, while VBF production is sensitive to the vector boson  
 2168 couplings in its production. Both modes are sensitive to the vector boson couplings in their decays. The  
 2169 signal strengths will have dependence on the coupling scale factors as described in equation 6.4 [18].

$$\begin{aligned} \mu_{\text{ggF}} &\propto \frac{\kappa_F^2 \cdot \kappa_V^2}{(\mathcal{B}_{H \rightarrow f\bar{f}} + \mathcal{B}_{H \rightarrow gg}) \kappa_F^2 + (\mathcal{B}_{H \rightarrow VV}) \kappa_V^2} \\ \mu_{\text{VBF}} &\propto \frac{\kappa_V^4}{(\mathcal{B}_{H \rightarrow f\bar{f}} + \mathcal{B}_{H \rightarrow gg}) \kappa_F^2 + (\mathcal{B}_{H \rightarrow VV}) \kappa_V^2}. \end{aligned} \quad (6.4)$$

2170 Figure 6.6 shows the two-dimensional likelihood scan of  $\kappa_F$  and  $\kappa_V$ . The best-fit values are given in  
2171 equation 6.5. The best-fit values are consistent with unity within their uncertainties.

$$\begin{aligned} \kappa_F &= 0.93 & +0.24 & +0.21 & = 0.93 & +0.32 \\ \kappa_V &= 1.04 & +0.07 & +0.07 & = 1.04 & \pm 0.11. \end{aligned} \quad (6.5)$$

(stat.) (syst.)

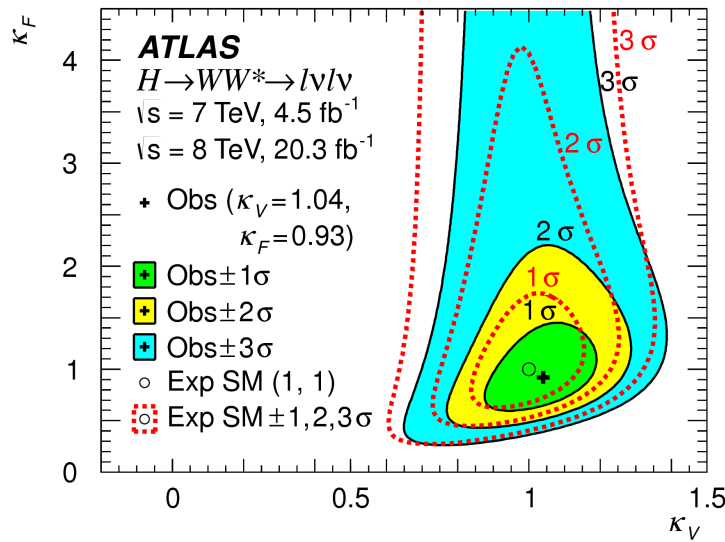


**Figure 6.6:** Likelihood scan as a function of  $\kappa_F$  and  $\kappa_V$  [61].

2172

## 2173 6.5 HIGGS PRODUCTION CROSS SECTION MEASUREMENT

2174 Another measurement that comes naturally from the signal strength numbers quoted earlier is the pro-  
2175 duction cross section and 7 and 8 TeV for both gluon fusion and VBF production. The general equa-  
2176 tion for calculating the cross section is given in equation 6.6.

$$\begin{aligned} (\sigma \cdot \mathcal{B}_{H \rightarrow WW^*})_{\text{obs}} &= \frac{(N_{\text{sig}})_{\text{obs}}}{\mathcal{A} \cdot \mathcal{C} \cdot \mathcal{B}_{WW \rightarrow \ell\nu\ell\nu}} \cdot \frac{1}{\int L dt} \\ &= \hat{\mu} \cdot (\sigma \cdot \mathcal{B}_{H \rightarrow WW^*})_{\text{exp}} \end{aligned} \quad (6.6)$$

2177  $(N_{\text{sig}})_{\text{obs}}$  is the number of events observed in data.  $\mathcal{A}$  is the geometric and kinematic acceptance of the  
 2178 detector, while  $\mathcal{C}$  is the efficiency of the signal region selection for events that are reconstructed in the  
 2179 detector. The branching ratio of a  $WW$  system to leptons must also be divided out. The production  
 2180 cross section depends on the center of mass energy and the production mode desired (gluon fusion or  
 2181 VBF), and so three separate cross section measurements are quoted in equation 6.7.

$$\begin{aligned}
 \sigma_{\text{ggf}}^{\text{7TeV}} \cdot \mathcal{B}_{H \rightarrow WW^*} &= 2.0 \pm 1.7 {}^{+1.2}_{-1.1} = 2.0 {}^{+2.1}_{-2.0} \text{ pb} \\
 \sigma_{\text{ggf}}^{\text{8TeV}} \cdot \mathcal{B}_{H \rightarrow WW^*} &= 4.6 \pm 0.9 {}^{+0.8}_{-0.7} = 4.6 {}^{+1.2}_{-1.1} \text{ pb} \\
 \sigma_{\text{VBF}}^{\text{8TeV}} \cdot \mathcal{B}_{H \rightarrow WW^*} &= 0.51 {}^{+0.17}_{-0.15} {}^{+0.13}_{-0.08} = 0.51 {}^{+0.22}_{-0.17} \text{ pb.}
 \end{aligned} \tag{6.7}$$

(stat.) (syst.)

2182 The predicted cross section values for gluon fusion are  $3.3 \pm 0.4$  pb at 7 TeV and  $4.2 \pm 0.5$  pb at 8 TeV,  
 2183 consistent with the measured values within their uncertainties. For vector boson fusion, the predicted  
 2184 cross section is  $0.35 \pm 0.02$  pb, again consistent with the measured value.

## 2185 6.6 CONCLUSION

2186 The combined analysis of the gluon fusion and vector boson fusion processes in  $H \rightarrow WW^* \rightarrow \ell\nu\ell\nu$   
 2187 in the 7 and 8 TeV datasets has yielded the first discovery level significance for Higgs production in this  
 2188 decay channel. Additionally, precise measurements of the couplings to vector bosons and fermions are  
 2189 given. Finally, signal strengths and cross sections for each production mode are measured. Figure 6.7  
 2190 shows the  $H \rightarrow WW^* \rightarrow \ell\nu\ell\nu$  measurements in comparison with other Higgs decay channels in  
 2191 ATLAS. The measurement of signal strength from this channel remains the most sensitive in both the  
 2192 gluon fusion and VBF production modes for the Run 1 dataset.

**ATLAS**

### Individual analysis

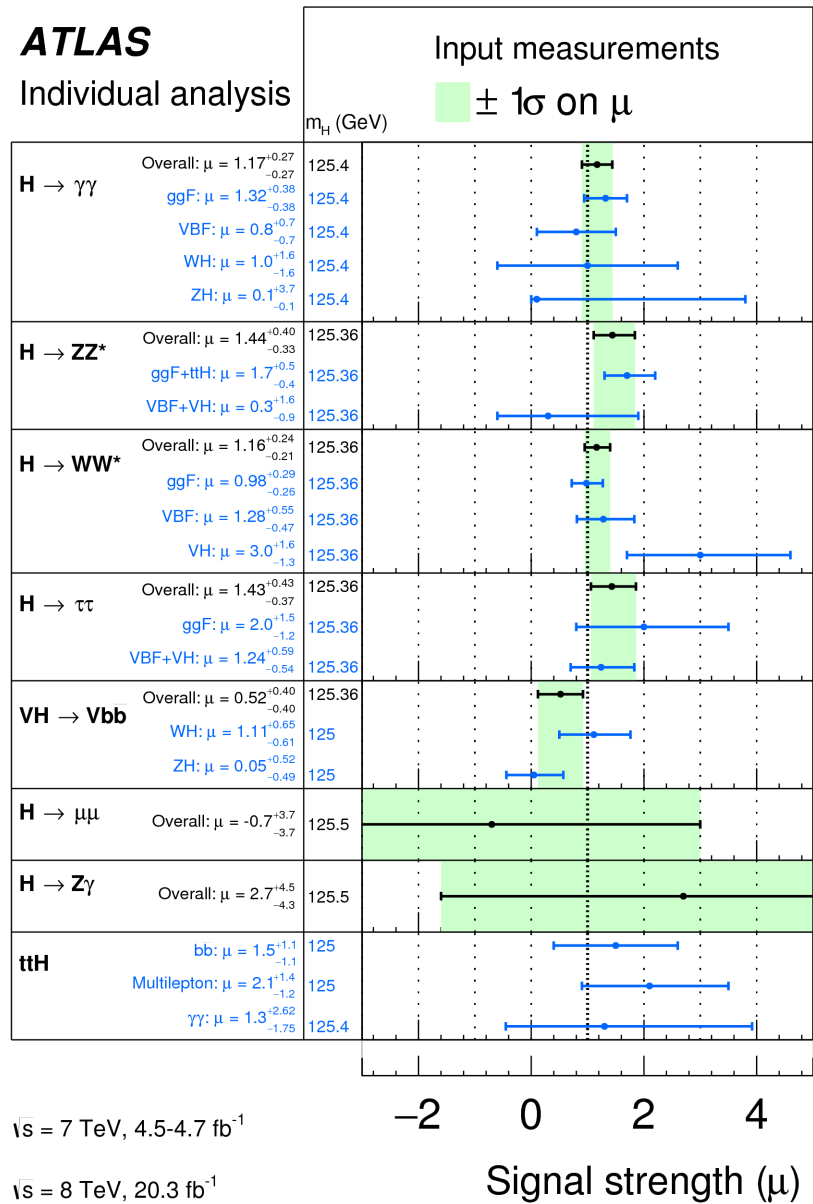


Figure 6.7: Comparison of signal strength measurements in different Higgs decay channels on ATLAS [85].

## Part III

2193

2194 Search for Higgs pair production in the

2195

$HH \rightarrow b\bar{b}b\bar{b}$  channel in LHC Run 2 at  $\sqrt{s} =$

2196

13 TeV

*Passion is in all great searches and is necessary to all  
creative endeavors.*

W. Eugene Smith

# 7

2197

## 2198 Search for Higgs pair production in boosted 2199 $b\bar{b}b\bar{b}$ final states

### 2200 7.1 INTRODUCTION

2201 After the discovery of the Higgs boson in the ATLAS Run 1 dataset and the subsequent measurements  
2202 of its properties, the Higgs transformed into a potential tool in searches for physics beyond the Stan-  
2203 dard Model. The pair production cross section of the Higgs can be enhanced through BSM physics.  
2204 Studying di-Higgs production also probes the Higgs self-coupling, shedding light on the structure  
2205 of the Higgs potential. This chapter presents a search for resonant production of a Higgs pair in the  
2206  $X \rightarrow HH \rightarrow b\bar{b}b\bar{b}$  final state in  $3.2 \text{ fb}^{-1}$  of data collected at  $\sqrt{s} = 13 \text{ TeV}$ . In particular, this  
2207 chapter focuses on a search for this final state in the regime where  $m_X$  is large ( $\gtrsim 1 \text{ TeV}$ ) and the Higgs  
2208 bosons in the decay are significantly boosted. A tailored selection for this boosted selection, using novel

2209 techniques in jet substructure and  $b$ -tagging, is discussed. Then, the data-driven background estimate is  
 2210 presented. Finally, the results of the search are shown. The signal models used as benchmarks are a spin-  
 2211 2 Randall Sundrum graviton (RSG) and a narrow width spin-0 resonance. These models are described  
 2212 in more detail in Chapter 1. Limits on signal models are reserved for the next chapter where the results of  
 2213 this chapter are combined with the results of a separate selection dedicated to the lower  $m_X$  regime.

## 2214 7.2 MOTIVATION

2215 With the center of mass energy increase from  $\sqrt{s} = 8$  TeV to  $\sqrt{s} = 13$  TeV, the LHC and ATLAS  
 2216 are able to probe new resonances at higher mass scales than previously accessible in Run 1. This is a  
 2217 powerful motivator for searching for a new resonance in the early 13 TeV data. Figure 7.1 shows the  
 2218 ratios of parton luminosities between 8 and 13 TeV for different resonance masses. For a resonance of  
 2219  $M_X = 2$  TeV, the cross section at  $\sqrt{s} = 13$  TeV is roughly a factor of 10 larger than at  $\sqrt{s} = 8$  TeV.

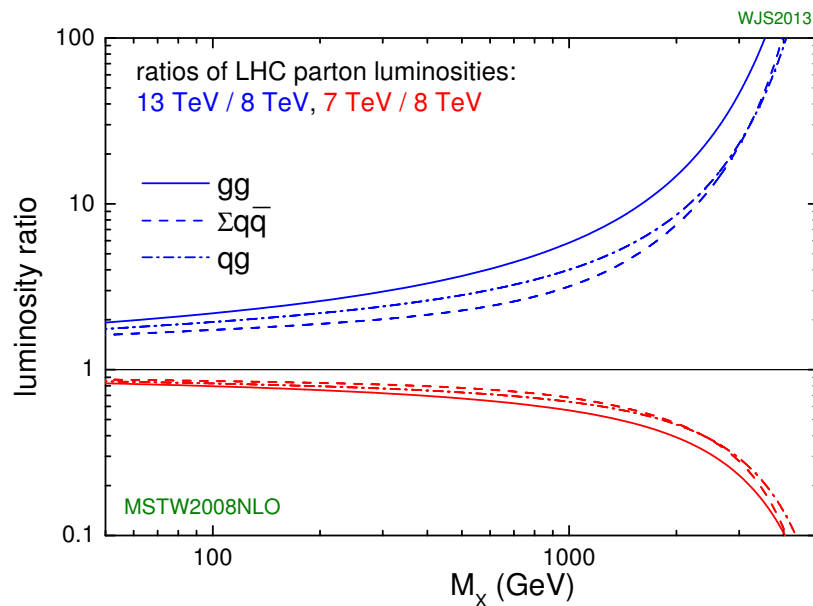


**Figure 7.1:** Parton luminosity ratios as a function of resonance mass  $M_X$  for 13/8 TeV and 7/8 TeV [86].

2220 Higgs pair production offers a vast array of unprobed regions of phase space where searches for BSM  
 2221 physics can be made. Chapter 1 discusses some possibilities for both resonant and non-resonant enhance-

ment of the di-Higgs production cross section. Given the increased mass reach of the LHC in Run 2, it is particularly important to focus on resonant searches at high  $m_X$ . One consideration when conducting a search in the  $HH$  final state is which decay modes of the Higgs to consider. Figure 7.2 shows the branching ratio of the  $HH$  final state for different combinations of decays of each individual Higgs. As the largest branching ratio for the 125 GeV Higgs is  $H \rightarrow b\bar{b}$ , the  $HH \rightarrow b\bar{b}b\bar{b}$  branching ratio is also the largest at 33%.

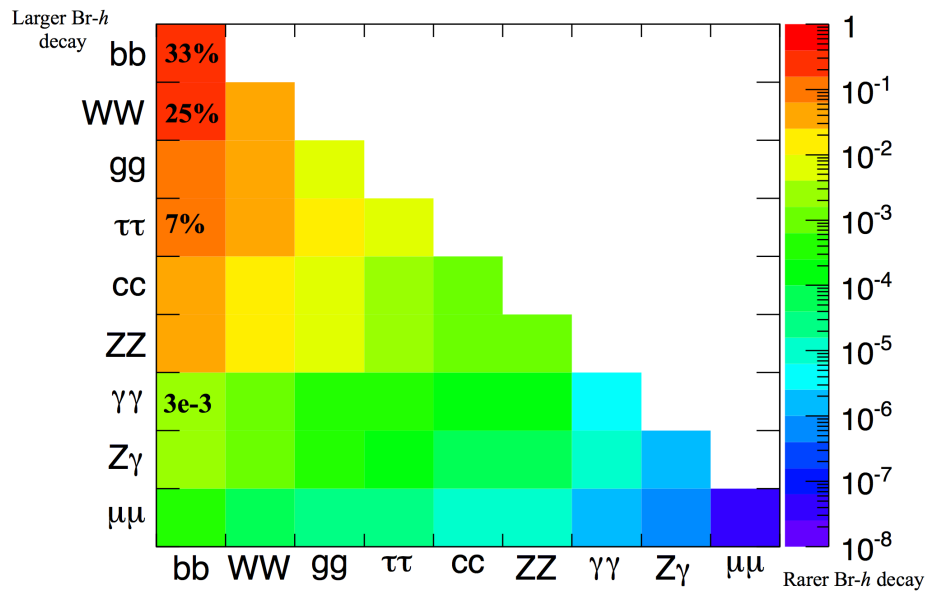


Figure 7.2: Summary of  $HH$  branching ratios [87].

At high  $m_X$ , the Higgs bosons resulting from the decay of a heavy resonance will have large  $p_T^*$ . The  $\Delta R$  between the decay products of the Higgs is inversely proportional to the Higgs  $p_T$ , as shown in equation ??.

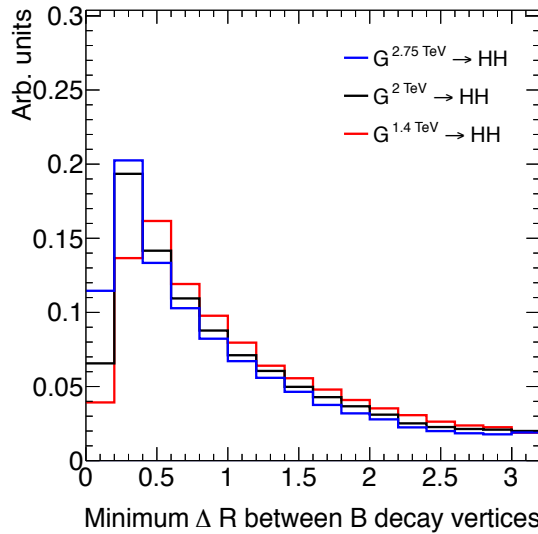
$$\Delta R \approx \frac{2m}{p_T} \quad (7.1)$$

Figure 7.3 shows the minimum  $\Delta R$  between truth level  $B$  decay vertices in simulation samples for Randall-Sundrum gravitons of different masses. The figure shows that as the mass of the graviton increases, the  $\Delta R$  distribution between the  $b$  quarks in the Higgs decay tends to shift to lower values. Be-

---

\*In the limit that  $m_H \ell \ell m_X$ , the Higgs  $p_T$  is roughly  $m_X/2$ .

cause of this effect, it is necessary to tailor a selection to target these merged  $b$ -jets.



**Figure 7.3:** Minimum  $\Delta R$  between  $B$  decay vertices for different RSG masses in a  $G_{\text{KK}}^* \rightarrow HH \rightarrow 4b$  sample with  $c = 1$

## 7.3 DATA AND SIMULATION SAMPLES

### 7.3.1 SIGNAL MODELS

While the resonance search is by its nature generic (as it is a simple search for a peak in the  $4b$  invariant mass spectrum), there are two signal models that the selection requirements have been optimized for. The first is Randall-Sundrum (RSG) model, where a tower of massive spin-2 Kaluza-Klein gravitons is predicted. The second is a heavy narrow spin-0 resonance, the so-called “heavy Higgs”. This type of resonance arises, for example, in the two Higgs doublet model (2HDM). More details about the physics of these models and their motivation is given in chapter 1.

Signal graviton ( $G_{\text{KK}}^*$ ) events are generated at leading order (LO) with **MADGRAPH5 v2.2.2** [88]. The PDF set used is the **NNPDF2.3 LO** set [89]. For modeling parton shower and hadronization in jets, **PYTHIA 8.186** is used with the A14 tune [73, 90]. The free parameters in the RSG model are the graviton mass and the coupling constant  $c \equiv k/\bar{M}_{\text{Pl}}$ <sup>†</sup>. Both the production cross section and width of the

<sup>†</sup> $k$  is the curvature constant for the warped extra dimension and  $\bar{M}_{\text{Pl}}$  is the Planck mass divided by  $8\pi$

2247 graviton are proportional to  $c^2$ . Samples are generated at both  $c = 1$  and  $c = 2$  for a variety of mass  
2248 points between 300 GeV and 3 TeV.

2249 The second signal sample is a heavy spin-0 resonance  $H$  with a fixed width of  $\Gamma_H = 1$  GeV. This  
2250 is generated with **MADGRAPH5** and uses the **CT10** PDF set [76]. The parton shower and hadronization  
2251 are handled by **HERWIG ++** with the **CTEQ6L1** PDF set and the **UEEE5** event tune [77, 91, 92]. Because  
2252 the width and branching ratios depend on 2HDM parameters, each mass point generated with this fixed  
2253 width corresponds to a different point in the 2HDM parameter phase space. Mass points are generated  
2254 between 300 GeV and 1 TeV as with the RSG signal samples.

### 2255 7.3.2 BACKGROUND SAMPLES

2256 While the dominant **QCD** multijet background is estimated with a fully data-driven method, the sub-  
2257 dominant backgrounds  $t\bar{t}$  and  $Z + \text{jets}$  are modeled with some input from simulation.

2258  $t\bar{t}$  events are simulated at next-to-leading order (NLO) with the **POWHEG-BOX** version 1 generator us-  
2259 ing the **CT10** PDF set [93]. The parton shower, hadronization, and underlying event are simulated with  
2260 **PYTHIA 6.428** with the **CTEQ6L1** PDF set [72]. The Perugia 2012 tune is used [94]. NNLO **QCD** cor-  
2261 rections to the cross sections are computed in **Top++ 2.0** [95]. The top quark mass is set to 172.5 GeV.  
2262 The shapes of distributions in  $t\bar{t}$  are taken from MC while the normalization is taken from data.

2263 Finally, the  $Z + \text{jets}$  background is simulated with **PYTHIA 8.186** and the **NNPDF2.3** LO PDF set. This  
2264 background is negligible compared to the others and is taken fully from MC.

### 2265 7.3.3 DATA SAMPLE AND TRIGGER

2266 This analysis is done on  $3.2 \text{ fb}^{-1}$  of data taken in 2015 at  $\sqrt{s} = 13$  TeV. The details of the machine  
2267 conditions during this time can be found in Chapter 2. Only data which was taken during stable beam  
2268 conditions with all detectors functioning is used. Events must pass a trigger which requires a single  
2269 360 GeV large radius ( $R = 1.0$ ) jet to be reconstructed in the HLT. Figure 7.4 shows the trigger effi-  
2270 ciency for various trigger options as a function of graviton mass. Above  $m_G > 1$  TeV, the single large  
2271 radius jet trigger is 99% efficient for events passing the signal selection.

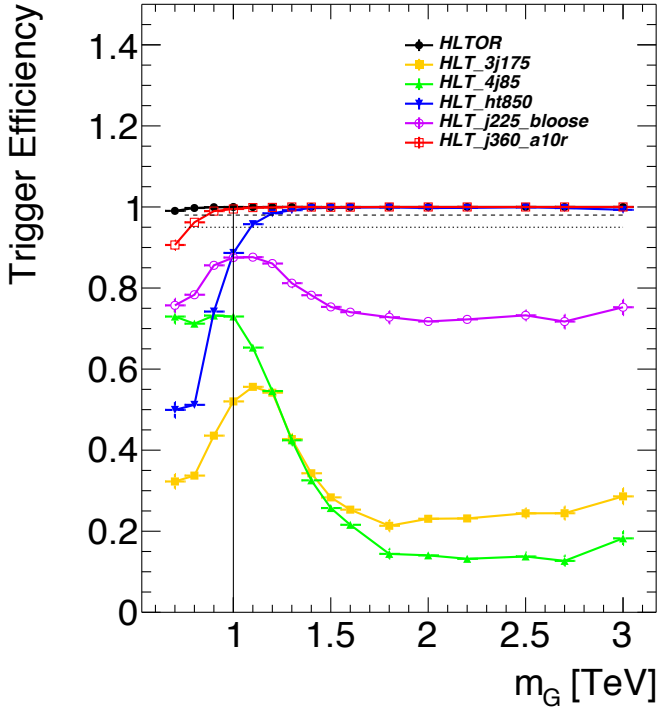


**Figure 7.4:** Trigger efficiency for events passing all signal region selections as a function of mass in  $G_{\text{KK}}^* \rightarrow HH \rightarrow 4b$  samples with  $c = 1$  [96]. In the trigger names, “j” refers to a jet or jets. “ht” refers to  $H_T$ , the scalar sum of transverse momenta in the event. “bloose” refers to a loose  $b$ -tagging requirement applied to the jet. “a10r” refers to anti- $k_T$  jets with  $R = 1.0$ . The numbers at the end are the thresholds on the given quantity in GeV.

## 2272 7.4 EVENT RECONSTRUCTION AND OBJECT SELECTION

2273 The boosted selection first begins by defining a unique set of objects that can be exploited to increase  
 2274 signal efficiency in the kinematic regime where the final state  $b$ -jets are very merged.

### 2275 7.4.1 LARGE RADIUS ( $R = 1.0$ ) JETS

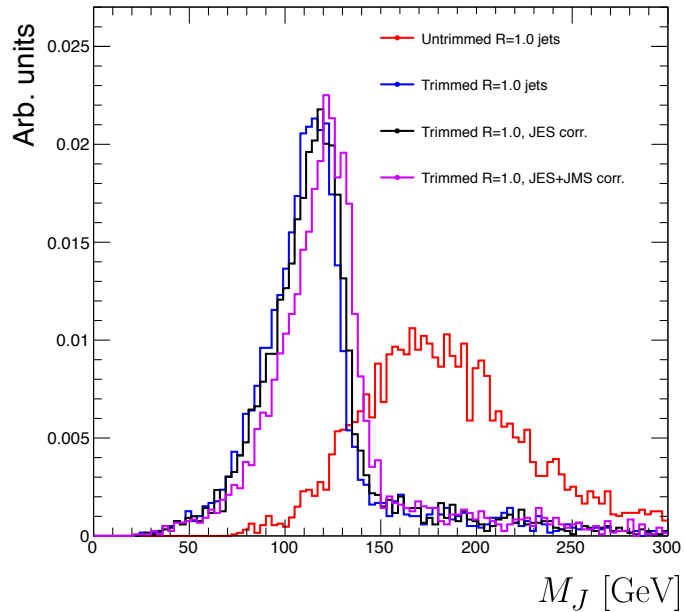
2276 The first step towards reconstructing the final state is to define objects that can be used to measure the  
 2277 kinematics of the Higgs bosons. In the boosted selection anti- $k_T$  jets with a radius parameter of 1.0  
 2278 are used. These jets are much larger in angular size than the typical  $R = 0.4$  jets and are intended to  
 2279 encompass both jets resulting from the Higgs decay<sup>‡</sup>. The jets are built from clusters in the calorimeter

---

<sup>‡</sup>This is in contrast to the resolved selection, which uses two  $R = 0.4$  anti- $k_T$  jets for each Higgs

2280 calibrated with local calibration weighting [56].

2281 Because of the large extent of these jets, great care must be taken to remove potential contributions  
2282 of calorimeter clusters from pile-up. This is done using a technique called jet trimming [97]. With trim-  
2283 ming, the constituents of the large radius jet are re-clustered with a smaller radius with the  $k_T$  algorithm.  
2284 Then, these so-called subjets are removed from the larger jet if  $p_T^{\text{subjet}}/p_T^{\text{jet}} < f_{\text{cut}}$ . In this analysis, the  
2285 subjet radius is  $R = 0.2$  and  $f_{\text{cut}} = 0.05$ . Trimming has been shown to improve the mass resolution  
2286 of large radius jets. Figure 7.5 shows the effect of trimming on the large radius jet mass ( $M_J$ ). Because  
2287 the large radius jet fully contains the higgs decay products, its invariant mass should correspond to the  
2288 125 GeV mass of the Higgs. The trimming algorithm brings the jet mass much closer to the expected  
2289 Higgs mass and improves the mass resolution.



2280 **Figure 7.5:** Comparison of untrimmed and trimmed jet masses for large radius jets in a RSG sample with  $m_{G_{\text{KK}}^*} = 1 \text{ TeV}$ .  
2281 JES (JMS) refers to the standard jet energy (mass) scale calibration for ATLAS [56].

2290 The large radius jets are required to satisfy  $250 < p_T < 1500 \text{ GeV}$ . They must also be within  
2291  $|\eta| < 2.0$  in order to ensure that the full jet is within the inner detector tracking volume. Finally, they  
2292 are required to have  $M_J > 50 \text{ GeV}$ . The upper  $p_T$  cut and lower threshold on mass are applied to  
2293 correspond to the kinematic range where uncertainties are available in ATLAS calibrations [98, 99].

2294 7.4.2 TRACK JETS AND  $b$ -TAGGING

2295 Because the  $b$ -jets from boosted Higgs decays are so close together (as illustrated in figure 7.3), narrow ra-  
2296 dius jets are required to fully resolve both  $b$ -jets. The minimum radius feasible for jets based on calorime-  
2297 ter deposits is determined by the calorimeter granularity. However, because  $b$ -tagging relies on informa-  
2298 tion from the inner detector, it is possible to define another type of jet that can have a smaller radius and  
2299 better  $b$ -tagging resolution. These jets are called “track jets” [99, 100].

2300 Track jets are formed by applying the usual anti- $k_T$  clustering algorithm to tracks that are required  
2301 to be consistent with the primary vertex. After the jet axis has been determined using these tracks, a sec-  
2302 ond step of track association is also performed to add tracks that can be useful for  $b$ -tagging [100]. In this  
2303 analysis, the tracks are clustered with a radius parameter of  $R = 0.2$ . This radius has been shown to  
2304 give good performance in boosted Higgs tagging [99, 100]. Figure 7.6 shows a comparison among dif-  
2305 ferent track jet radii of the efficiency for reconstructing two  $b$ -jets from each Higgs in a RSG sample as a  
function of mass. Track jets with radius of 0.2 give the best performance, especially at high mass. In this

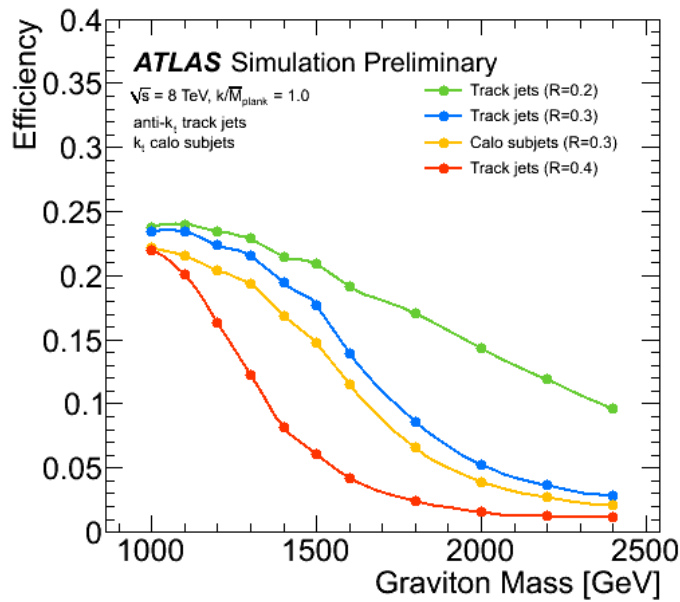


Figure 7.6: Efficiency of finding two  $b$ -jets from each Higgs in an RSG event using calorimeter jets with  $R = 0.3$  or different track jet radii [100]

2307 analysis, track jets are required to have  $p_T > 10 \text{ GeV}$  and  $|\eta| < 2.5$ . They must also have at least two  
2308 tracks.

### 2309 7.4.3 MUONS

2310 Muons are used in this study to correct the four-momenta of calorimeter jets by accounting for semi-  
2311 leptonic  $b$  decays. The muons used are combined ID and MS muons which must satisfy tight identifica-  
2312 tion requirements [52]. The muons must have  $p_T > 4 \text{ GeV}$  and  $|\eta| < 2.5$ . Table 7.1 summarizes the  
2313 object requirements described in this section.

	$R$	$p_T$	$ \eta $	$M$
Calorimeter jets	1.0	$250 < p_T < 1500 \text{ GeV}$	$< 2.0$	$> 50 \text{ GeV}$
Track jets	0.2	$> 10 \text{ GeV}$	$< 2.5$	-
Muons	-	$4 \text{ GeV}$	$< 2.5$	-

**Table 7.1:** Summary of requirements on objects used in the  $X \rightarrow HH \rightarrow b\bar{b}b\bar{b}$  search

## 2314 7.5 EVENT SELECTION

2315 The first requirement in the boosted selection is for  $\geq 2$  large radius jets satisfying the selections outlined  
2316 above. The two highest momentum large-R jets in the event are referred to as “Higgs candidates”. The  
2317 leading jet is required to have  $p_T > 350 \text{ GeV}$ .

2318 Track jets satisfying the object selections are matched to Higgs candidate jets via ghost association [101].  
2319 Each Higgs candidate must have at least 2 track jets associated with it. These basic requirements are illus-  
2320 trated in figure 7.7

2321 The QCD multijet background produces less central jets than high mass resonances, so there is an ad-  
2322 dditional requirement that the two Higgs candidates be close together in  $\eta$ . The large-R jets are required  
2323 to satisfy  $|\Delta\eta(JJ)| < 1.7$ .

2324 The final set of requirements ensures that the Higgs candidates are consistent with expected proper-  
2325 ties of the 125.0 GeV Higgs. First, a variable ( $X_{hh}$ ) is defined to measure the consistency of both of the

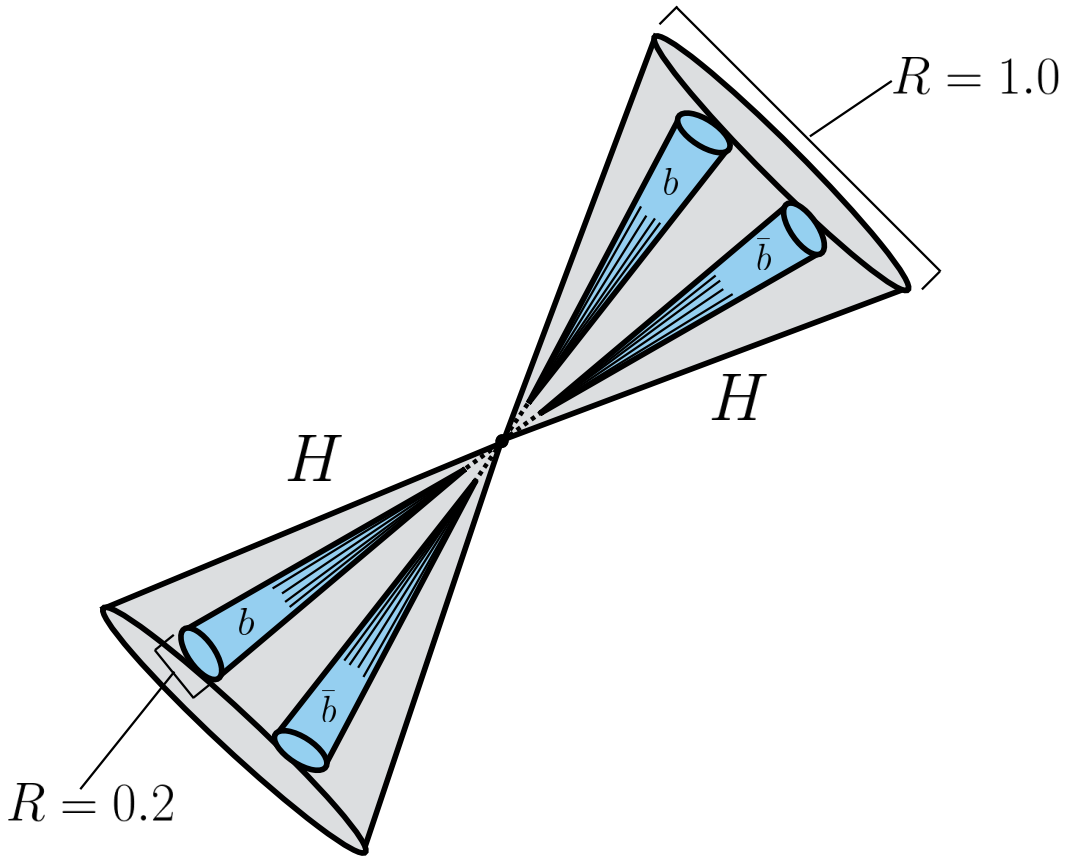


**Figure 7.7:** Illustration of the boosted selection requirements on Higgs candidates. Each large-radius calorimeter jet (Higgs candidate) must contain two track jets

2326 Higgs candidate jets with the SM Higgs mass. This is shown in equation 7.2.

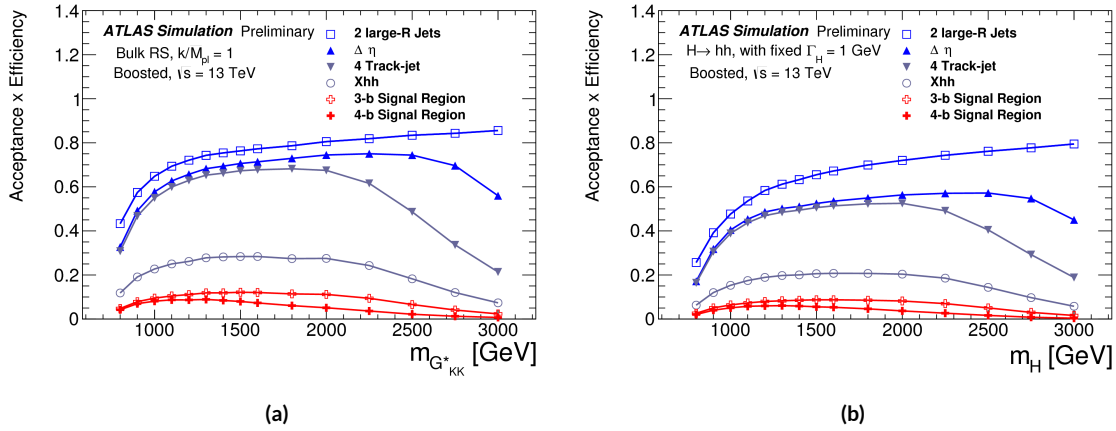
$$X_{hh} = \sqrt{\left(\frac{M_J^{\text{lead}} - 124 \text{ GeV}}{0.1 M_J^{\text{lead}}}\right)^2 + \left(\frac{M_J^{\text{sublead}} - 115 \text{ GeV}}{0.1 M_J^{\text{sublead}}}\right)^2} \quad (7.2)$$

2327 The mass values in the  $X_{hh}$  formula are optimized to maximize signal efficiency. The sub-leading jet  
2328 typically has a lower mass due to semi-leptonic  $b$  decays and final state radiation.  $X_{hh}$  effectively acts as  
2329 a  $\chi^2$  measurement of the consistency of the two Higgs candidate masses with the signal hypothesis. The  
2330 denominators of each term ( $0.1 M$ ) give the uncertainty on the mass measurement for the large radius  
2331 jets. Events are required to satisfy  $X_{hh} < 1.6$ .

2332 The last requirement applied is on the number of  $b$ -tagged track jets. There are two signal regions de-

fined. The first requires exactly four  $b$ -tagged track jets, two in each Higgs candidate (known as the 4 signal region). At high resonance masses, this requirement is inefficient, so an additional signal region requiring only three  $b$ -tagged track jets is also defined (known as the 3 $b$  signal region). While this has a larger background it is also more efficient for high resonance masses. For both signal regions, threshold on MV<sub>2</sub> score is chosen such that the algorithm is 77% efficiency in finding true  $b$ -jets<sup>§</sup>. Different working points were tested and this was found to be optimal. Appendix A has more details on this optimization.

Before making the requirement on  $X_{hh}$ , the masses of the Higgs candidates are corrected for semi-leptonic  $b$  decays using muons with the criteria outlined in the previous section. Any muons within a  $\Delta R < 0.2$  of a  $b$ -tagged track jet have their four-momenta added to the four-momentum of the Higgs candidate. This correction does not affect the pre-selection requirements but does affect the  $X_{hh}$  requirement and the final invariant mass distribution used.



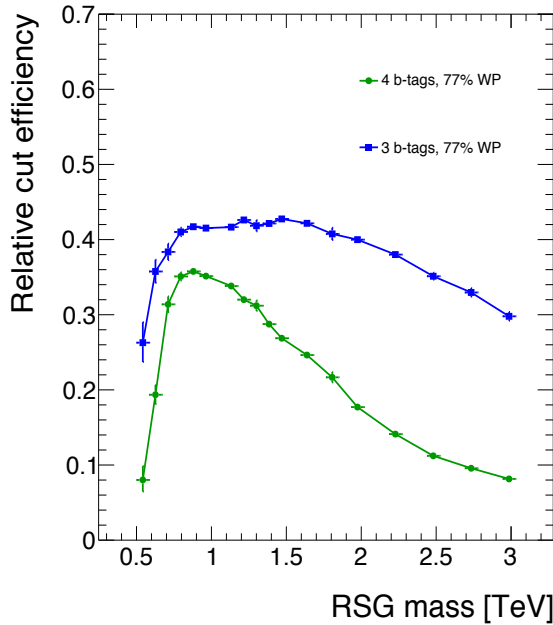
**Figure 7.8:** Acceptance  $\times$  efficiency as a function of mass for (a) RSG and (b) narrow heavy scalar signal models [102].

Figure 7.8 shows the product of acceptance and efficiency as a function of mass for both the RSG and narrow heavy scalar resonance signal models. After  $m_X > 1$  TeV, the efficiency of the 4 $b$  requirement begins to decline. After  $m_X > 2$  TeV, the efficiency of requiring two track jets in each Higgs candidate begins to decline as well. Both of these behaviors illustrate the difficulty of resolving the merged decay

<sup>§</sup>The specific MV<sub>2</sub> algorithm chosen is MV<sub>2c20</sub>, where the fraction of charm events used in the training is 20%

2349 products at high mass. More details on the degradation of the  $b$ -tagging efficiency at high masses are  
2350 shown in appendix B.

2351 Figure 7.9 shows a more detailed comparison of the signal efficiency in the  $3b$  vs  $4b$  signal regions for  
2352 the RSG model. The efficiencies shown here are relative to all prior selection requirements.



2353 **Figure 7.9:** Efficiency of requiring 3 or 4  $b$ -tagged track jets vs. RSG mass. The efficiency quoted is relative to the previous  
2354 selection requirements (rather than an absolute efficiency).

2355 The final discriminating variable used in the boosted analysis is  $M_{2J}$ , the invariant mass of the two  
2356 Higgs candidates. In order to improve the mass resolution, the four-momenta of each Higgs candidate  
2357 are scaled by  $m_h/M_J$ . The effect of this correction is small in the boosted analysis but is done for consistency  
2358 with the resolved selection.

2359 Table 7.2 shows the effect of the selection requirements on signal and background simulations as well  
2360 as data.

## 2361 7.6 DATA-DRIVEN BACKGROUND ESTIMATION

2362 The largest background to this final state is QCD multijet production, constituting 80-90% of the total  
2363 background. Because of the difficulties in modeling higher order QCD processes, this background is

Selection	Data	$m_{G_{KK}^*} = 1\text{TeV}$	$m_{G_{KK}^*} = 2\text{TeV}$	$t\bar{t}$	$Z+\text{jets}$
N(fiducial large-R jets) $\geq 2$	2202396	23.3	0.48	32345.2	4255.7
leading large-R jet $p_T > 350\text{ GeV}$	1873741	22.9	0.48	26511.7	3649.9
Both large-R jet $m > 50\text{ GeV}$	1854625	21.2	0.47	24369.8	3575.8
Both large-R jet $p_T < 1500\text{ GeV}$	1853601	21.2	0.46	24346.5	3572.9
$ \Delta\eta(JJ)  < 1.7$	1435273	20.8	0.44	20751.0	3265.8
$\geq 2$ track-jets per large-R jet	1224727	19.8	0.40	18234.5	2692.6
$3 b\text{-tags}, X_{hh} < 1.6$	316	3.4	0.067	46.7	2.0
$4 b\text{-tags}, X_{hh} < 1.6$	20	2.9	0.030	1.4	0.0

**Table 7.2:** Effect of boosted selection on data, RSG signal models,  $t\bar{t}$ , and  $Z+\text{jets}$ . The numbers from simulation are normalized with the MC generator cross section and do not take into account the data driven estimates described in section 7.6 [103].

estimated with a fully data-driven method. The only other non-negligible background is  $t\bar{t}$ , constituting the other 10-20%. Due to the presence of  $t\bar{t}$  in the sideband region where the QCD background will be estimated, the normalization of the QCD and  $t\bar{t}$  backgrounds are simultaneously estimated.

### 7.6.1 MASS REGION DEFINITIONS

The first step in the data-driven background estimate is to define a sideband mass region where the background normalization can be derived. Additionally, a control region is defined where the background estimate can be validated. The control (CR) and sideband (SB) regions are defined using a radial distance in the two-dimensional large-R jet mass plane,  $R_{hh}$ , which is defined in equation 7.3.

$$R_{hh} = \sqrt{(M_J^{\text{lead}} - 124\text{ GeV})^2 + (M_J^{\text{sublead}} - 115\text{ GeV})^2} \quad (7.3)$$

Events in the sideband region are required to fail the signal region  $X_{hh} < 1.6$  requirement and have  $R_{hh} > 35.8\text{ GeV}$ . The control region consists of those events which are not in the signal or sideband regions. Figure 7.10 shows the definition of the signal, control, and sideband mass regions. Table 7.3 summarizes the mass region selections for the three different regions used in the analysis.

---

\*The  $Z+\text{jets}$  background is a sub-percent level contribution

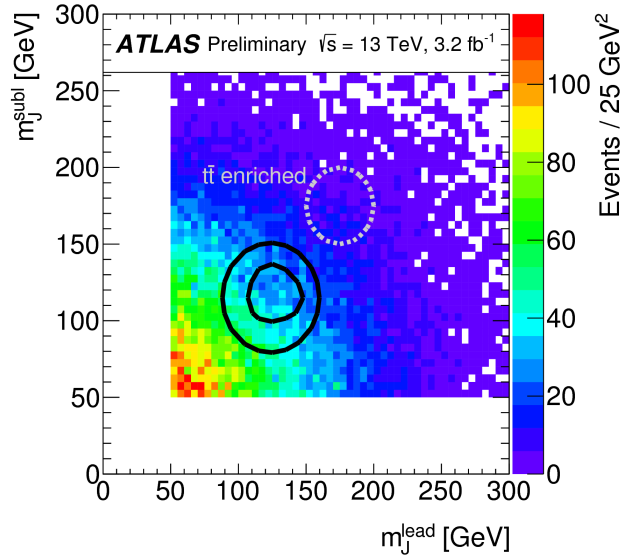


**Figure 7.10:**  $M_J^{\text{sublead}}$  vs.  $M_J^{\text{lead}}$  in a 2  $b$ -tag data sample. The signal region is defined by the inner black contour ( $X_{hh} < 1.6$ ) and the sideband region is defined by the outer contour ( $R_{hh} > 35.8 \text{ GeV}$ ). The region between the black contours is the control region. The mass region which is enriched in  $t\bar{t}$  background is also shown for illustration. [102]

Region	Requirement	Notes
Signal Region (SR)	$X_{hh} < 1.6$	-
Control Region (CR)	$R_{hh} < 35.8 \text{ GeV}$ and $X_{hh} > 1.6$	Used for validation of background estimates
Sideband Region (SB)	$R_{hh} > 35.8 \text{ GeV}$	Used to derive background normalization

**Table 7.3:** Mass region definitions used for background estimation

### 2374 7.6.2 BACKGROUND ESTIMATION

2375 The method for estimating the background in this analysis is similar to the ABCD method presented in  
 2376 Chapter 5. In this case, the two handles used to define different regions for the estimate are the number  
 2377 of  $b$ -tagged track jets and the mass regions. A region requiring exactly two  $b$ -tagged track jets in one large-  
 2378 R jet (referred to as the 2-tag or  $2b$  region) is defined for use in the background estimate. The number of  
 2379 expected background events in the  $3b$  and  $4b$  signal regions is then given by equation 7.4.

$$N_{\text{bkg}}^{3(4)-\text{tag},\text{SR}} = \mu_{\text{Multijet}} N_{\text{Multijet}}^{2-\text{tag},\text{SR}} + \beta_{t\bar{t}} N_{t\bar{t}}^{3(4)-\text{tag},\text{SR}} + N_{Z+\text{jets}}^{3(4)-\text{tag},\text{SR}} \quad (7.4)$$

2380 In this equation,  $N_{\text{bkg}}^{3(4)\text{-tag}}$  is the expected number of background events in the  $3b$  or  $4b$  signal regions.  
 2381  $N_{\text{Multijet}}^{2\text{-tag}}$  is the number of multijet events in the 2-tag region.  $N_{t\bar{t}}^{3(4)\text{-tag}}$  is the number of  $t\bar{t}$  events  
 2382 predicted in the MC for the  $3b$  or  $4b$  signal region, and the variable is similarly defined for the  $Z+jets$   
 2383 background. The  $\beta_{t\bar{t}}$  parameter is a scale factor used to correct the normalization of the  $t\bar{t}$  estimate in  
 2384 the signal region.  $\mu_{\text{Multijet}}$  is an extrapolation factor that is derived in the sideband region and used to  
 2385 estimate the ratio of 2-tag events to 3(4)-tag events in the signal region. It is defined in equation 7.5.

$$\mu_{\text{Multijet}} = \frac{N_{\text{Multijet}}^{3(4)\text{-tag,SB}}}{N_{\text{Multijet}}^{2\text{-tag,SB}}} = \frac{N_{\text{data}}^{3(4)\text{-tag,SB}} - \beta_{t\bar{t}} N_{t\bar{t}}^{3(4)\text{-tag,SB}} - N_{Z+jets}^{3(4)\text{-tag,SB}}}{N_{\text{data}}^{2\text{-tag,SB}} - \beta_{t\bar{t}} N_{t\bar{t}}^{2\text{-tag,SB}} - N_{Z+jets}^{2\text{-tag,SB}}} \quad (7.5)$$

2386 The  $t\bar{t}$  scale factor ( $\beta_{t\bar{t}}$ ) and the QCD multijet extrapolation factor ( $\mu_{\text{Multijet}}$ ) are estimated together in  
 2387 a simultaneous fit in the sideband region. Then, the number of events in the 2-tag signal region is used,  
 2388 along with the  $t\bar{t}$  estimate in the  $3b$  and  $4b$  signal regions and  $\mu_{\text{Multijet}}$ , to estimate the total number of  
 2389 background events in the two final signal regions. The shape of the final discriminant  $M_{2J}$  is also taken  
 2390 from the 2-tag signal region where there are more statistics. This method is illustrated graphically in  
 2391 figure 7.II.

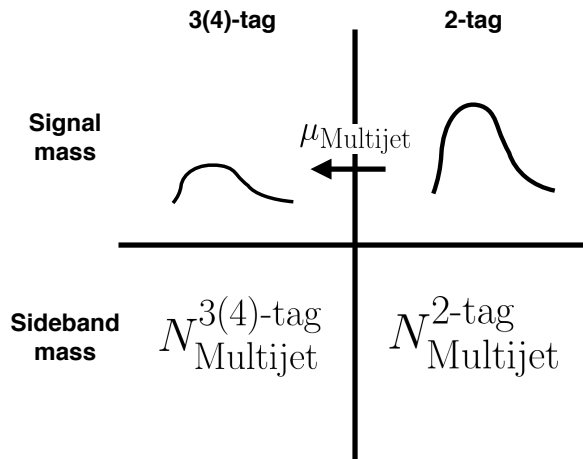
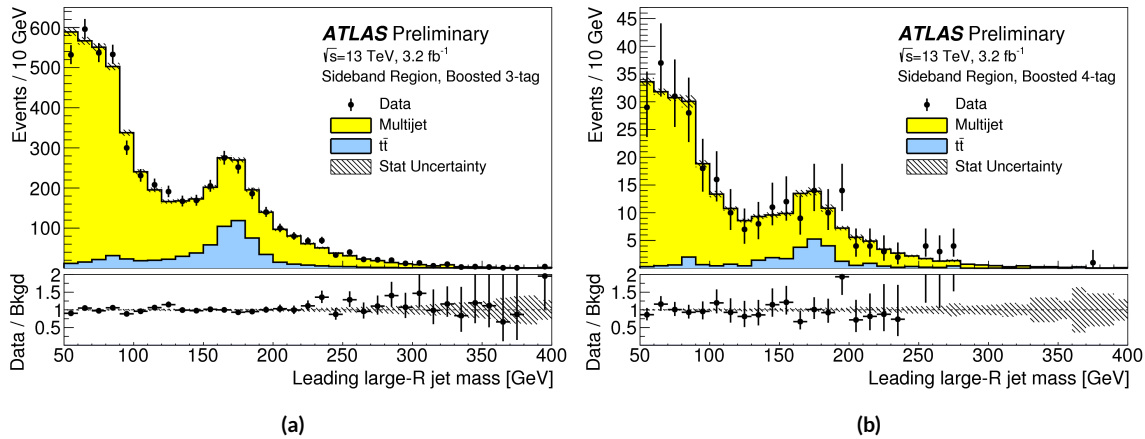


Figure 7.11: An illustration of the data-driven background estimation technique for the boosted analysis

2392 In the  $3b$  region, the fit yields values of  $\mu_{\text{Multijet}} = 0.160 \pm 0.03$  and  $\beta_{t\bar{t}} = 1.02 \pm 0.09$ . In the  $4b$   
 2393 region, the fit gives  $\mu_{\text{Multijet}} = 0.0091 \pm 0.0007$  and  $\beta_{t\bar{t}} = 0.82 \pm 0.39$ . The uncertainties quoted

2394 are statistical only. The larger uncertainties in the  $4b$  values indicate the lower statistics available in that  
 2395 region.

2396 Figure 7.12 shows the distributions of data and background estimates in the  $3b$  and  $4b$  sideband re-  
 2397 gions after the background fit has been done. The normalizations are constrained from the fit to match  
 2398 that of the data, but good modeling of the shape of the mass of the leading large-R jet is seen as well. The  
 2399 shapes of the kinematic distributions in the  $4b$  region are taken from the  $3b$  region due to the better MC  
 2400 statistics in that region.



2401 **Figure 7.12:** Leading large-R jet mass in the  $3b$  (a) and  $4b$  (b) sideband regions. The multijet and  $t\bar{t}$  backgrounds are  
 2402 estimated using the data-driven methods described above. Because their normalizations are derived in the sideband region,  
 2403 the total background normalization is constrained by default to match the normalization of the data [102].

### 2401 7.6.3 BACKGROUND SHAPE FIT

2402 As mentioned in the previous section, the background shape in the 3-tag and 4-tag signal regions is taken  
 2403 from the 2-tag signal mass region. Due to the limited statistics available, the background shapes are ad-  
 2404 ditionally smoothed after being extrapolated to the 3-tag and 4-tag signal regions. Only the data in the  
 2405 range  $900 < M_{2J} < 2000$  GeV is included in the fit due to the limited statistics available above 2 TeV.  
 2406 Both the  $t\bar{t}$  and QCD multijet background are independently fit with an exponential shape,  $y = e^{ax+b}$ .  
 2407 Other shapes are considered and used for the systematic uncertainties. Table 7.4 shows the fit values for  
 2408 the parameters. Because both the  $3b$  and  $4b$  QCD shapes come from the 2-tag region, the slopes derived  
 2409 are very similar.

	<i>a</i>	<i>b</i>
QCD (4b)	$0.00545 \pm 0.00021$	$5.44 \pm 0.24$
$t\bar{t}$ (4b)	$0.00746 \pm 0.00021$	$4.88 \pm 0.36$
QCD (3b)	$0.00545 \pm 0.00021$	$8.30 \pm 0.24$
$t\bar{t}$ (3b)	$0.00746 \pm 0.00021$	$8.58 \pm 0.36$

**Table 7.4:** Parameters derived for exponential fit to background  $M_{2J}$  shape in the  $3b$  and  $4b$  signal regions [103]

#### 2410 7.6.4 VALIDATION OF BACKGROUND ESTIMATE

2411 The background estimate can be validated by using the method to estimate the number of events in the  
 2412 control mass region rather than the signal mass region. Figure 7.13 shows the  $M_{2J}$  distribution in the  $3b$   
 2413 and  $4b$  control regions, comparing data and background estimates. In both cases, both the background  
 2414 shape and normalization are consistent with the data, indicating good agreement. The ratio of data to  
 2415 the background estimates is also fit to a line in the figure to test for any shape difference. The slope of the  
 2416 line is within  $1\sigma$  (from the fit uncertainties) of flat, further indicating that the data is consistent with the  
 2417 background estimate in the control region.

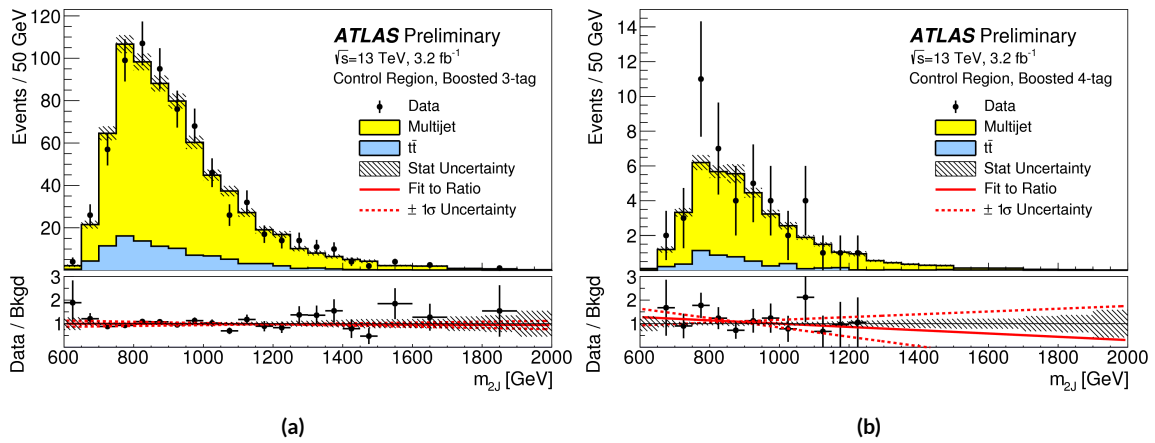


**Figure 7.13:** Di-jet invariant mass ( $M_{2J}$ ) in the  $3b$  (a) and  $4b$  (b) control regions. The multijet and  $t\bar{t}$  backgrounds are estimated using the data-driven methods described above [102].

2418 Table 7.5 shows the yields in data and background estimates in the 3-tag and 4-tag sideband and con-  
 2419 trol regions. Again, here, it can be seen that the total number of predicted background events from the  
 2420 data driven method is consistent with the number of data events in the region.

Sample (3-tag)	Sideband Region	Control Region
Multijet	$4328 \pm 27$	$607 \pm 10$
$t\bar{t}$	$683.5 \pm 8.1$	$99.6 \pm 3.1$
$Z+jets$	$31.8 \pm 3.7$	$7.7 \pm 1.8$
Total	$5043 \pm 28$	$715 \pm 11$
Data	5043	724
Sample (4-tag)	Sideband Region	Control Region
Multijet	$247.4 \pm 1.5$	$34.7 \pm 0.6$
$t\bar{t}$	$28.4 \pm 1.5$	$5.1 \pm 0.7$
$Z+jets$	$3.4 \pm 1.2$	$0.6 \pm 0.5$
Total	$279.2 \pm 2.5$	$40.3 \pm 1.0$
Data	279	45

**Table 7.5:** The number of events in data and predicted background events in the boosted 3-tag and 4-tag sideband and control regions. The uncertainties shown are statistical only. [102]

## 2421 7.7 SYSTEMATIC UNCERTAINTIES

2422 The systematic uncertainties in this analysis can be divided into two broad categories. The first type is  
 2423 uncertainties associated with the modeling of the signal processes. The second type of uncertainty is  
 2424 associated with both the shape and normalization of the background prediction.

### 2425 7.7.1 SIGNAL MODELING UNCERTAINTIES

2426 The signal modeling uncertainty has three main components: theoretical uncertainty on the acceptance,  
 2427 experimental uncertainties on the large-R jets, and experimental uncertainties on the track jets related to  
 2428  $b$ -tagging. In this analysis the experimental uncertainties are the most significant.

2429 The first uncertainty on signal modeling is the theoretical uncertainty on the acceptance. As explained  
 2430 in section 5.6.1, there are four components to this uncertainty. The first is related to missing higher order  
 2431 terms from the matrix element calculations which is estimated by varying the QCD renormalization and  
 2432 factorization scales. The second is uncertainty due to the PDF set used. The third is a generator uncer-  
 2433 tainty which is estimated by modifying the generator used to model the underlying event and hadroniza-

2434 tion. Finally, there is an uncertainty associated with the modeling of the initial state and final state radia-  
2435 tion (ISR/FSR). The total theoretical uncertainty on the signal yield is 3%, and this is dominated by the  
2436 ISR/FSR modeling.

2437 There are uncertainties on the large-R jets in both the jet energy scale (JES) and jet energy resolution  
2438 (JER) as well as the jet mass scale (JMS) and jet mass resolution (JMR). These are evaluated using  $\sqrt{s} =$   
2439 8 TeV data from Run 1 of ATLAS and extrapolated to the Run 2 beam and detector conditions using  
2440 MC<sup>¶</sup>. The details of these uncertainties can be found in reference [104].

2441 Uncertainties on the track jets are related to the  $b$ -tagging efficiency. The total uncertainty on the sig-  
2442 nal yield due to  $b$ -tagging is evaluated by propagating variations of the  $b$ -tagging efficiency through the  
2443 boosted selection requirements. The uncertainties are calculated jet-by-jet and parameterized as a func-  
2444 tion of  $b$ -jet  $p_T$  and  $\eta$  [105]. For high  $p_T$   $b$ -jets (with  $p_T > 300$  GeV), the uncertainties are extrapolated  
2445 using MC simulation from the lower  $p_T$   $b$ -jets [106].

2446 Table 7.6 shows the systematic uncertainties on the signal normalization for models with  $m_{G_{KK}^*} =$   
2447 1.5 TeV and both  $c = 1$  and  $c = 2$  as well as a narrow width heavy scalar. The dominant uncertainty  
2448 comes from  $b$ -tagging and this uncertainty is larger in the 4-tag region than the 3-tag region.

#### 2449 7.7.2 BACKGROUND UNCERTAINTIES

2450 Uncertainties on the QCD multijet background normalization and shape are estimated using the control  
2451 mass region. As shown previously, the background predictions in the control region match with the  
2452 data yields within the statistical uncertainty in both the 3-tag and 4-tag control regions. As an additional  
2453 protection, the statistical uncertainty on the background prediction in the control region is assigned as a  
2454 systematic uncertainty on the normalization of the QCD background.

2455 Additional robustness tests are done by varying the definition of the control mass region and the  $b$ -  
2456 tagging requirements used to define the 2-tag sample. In all cases, the effect of the variations is found to  
2457 be within the statistical uncertainties on the background normalization in the control region.

2458 Shape uncertainties on the background are evaluated using two techniques. First, as shown in fig-

---

<sup>¶</sup>The uncertainties are correspondingly larger due to the uncertainty of this extrapolation.

Source	Background	$G_{\text{KK}}^*$		$H$
		$c = 1$	$c = 2$	
Luminosity	-	5.0	5.0	5.0
3-tag				
JER	< 1	< 1	< 1	< 1
JES	2	< 1	< 1	< 1
JMR	1	12	12	11
JMS	5	14	13	17
$b$ -tagging	1	23	22	23
Theoretical	-	3	3	3
Multijet Normalization	3	-	-	-
Statistical	2	1	1	1
Total	7	31	30	33
4-tag				
JER	< 1	< 1	< 1	< 1
JES	< 1	< 1	< 1	< 1
JMR	4	12	13	13
JMS	5	13	13	14
$b$ -tagging	2	36	36	36
Theoretical	-	3	3	3
Multijet Normalization	14	-	-	-
Statistical	3	1	1	1
Total	15	42	42	43

**Table 7.6:** Summary of systematic uncertainties in the total background and signal event yields (expressed in %) in the boosted 3-tag and 4-tag signal regions. Systematic uncertainties on the signal normalization are shown for models with  $m_{G_{\text{KK}}^*} = 1.5$  TeV and both  $c = 1$  and  $c = 2$  as well as a narrow width heavy scalar.

ure 7.13, the ratio between the data and background prediction is fit with a linear function. The uncertainties on the slope of this fit are assigned as shape uncertainties. An additional uncertainty is assigned by using alternate power law fit functions for the smoothing of the background shape. Table 7.7 shows the alternate shapes used. The largest difference between the nominal fit function and the alternates, taking into account the  $1\sigma$  uncertainty band on each fit as well, is taken as a shape uncertainty.

The uncertainties on the  $t\bar{t}$  background are obtained by propagating the various experimental variations (JES, JER, JMS, JMR,  $b$ -tagging) through the analysis selection requirements. Table 7.6 summarizes

Functional Form
$f_1(x) = p_0(1-x)^{p_1}x^{p_2}$
$f_2(x) = p_0(1-x)^{p_1}e^{p_2 x^2}$
$f_3(x) = p_0(1-x)^{p_1}x^{p_2} x$
$f_4(x) = p_0(1-x)^{p_1}x^{p_2} \ln x$
$f_5(x) = p_0(1-x)^{p_1}(1+x)^{p_2} x$
$f_6(x) = p_0(1-x)^{p_1}(1+x)^{p_2} \ln x$
$f_7(x) = \frac{p_0}{x}(1-x)^{p_1-p_2} \ln x$
$f_8(x) = \frac{p_0}{x^2}(1-x)^{p_1-p_2} \ln x$

**Table 7.7:** Alternate fit functions used to model the  $M_{JJ}$  distribution in the QCD multijet background. In the equations,  $x = M_{JJ}/\sqrt{s}$ .

2466 the background uncertainties in the 3-tag and 4-tag regions.

## 2467 7.8 RESULTS

2468 Table 7.8 shows the observed yields in the 3-tag and 4-tag signal regions for the boosted analysis com-  
 2469 pared to the predicted number of background events. In the 3-tag region, 316 events are observed with  
 2470 a predicted background of  $285 \pm 19$ . In the 4-tag region, 20 events are observed with a predicted back-  
 2471 ground of  $14.6 \pm 2.4$ . Figure 7.14 shows the  $M_{JJ}$  distribution in the 3-tag and 4-tag regions. There are  
 2472 some small excesses in the data, in particular in the 3-tag region around  $M_{JJ} \approx 900$  GeV and in the  
 2473 region of  $1.6 < M_{JJ} < 2.0$  TeV. The significance of these excesses will be evaluated in the next chapter  
 2474 in the statistical combination with the resolved results.

Sample	Signal Region (3-tag)	Signal Region (4-tag)
Multijet	$235 \pm 14$	$13.5 \pm 2.4$
$t\bar{t}$	$48 \pm 22$	$1.2 \pm 1.0$
$Z+jets$	$2.0 \pm 2.2$	-
Total	$285 \pm 19$	$14.6 \pm 2.4$
Data	316	20
$G_{KK}^*(1000 \text{ GeV}), c = 1$	$3.4 \pm 0.9$	$2.9 \pm 1.1$

**Table 7.8:** Observed yields in the 3-tag and 4-tag signal regions for the boosted analysis compared to the predicted number of background events Errors correspond to the total uncertainties in the predicted event yields. The yields for a graviton with  $m_{G_{KK}^*} = 1 \text{ TeV}$  and  $c = 1$  are also shown. [102]

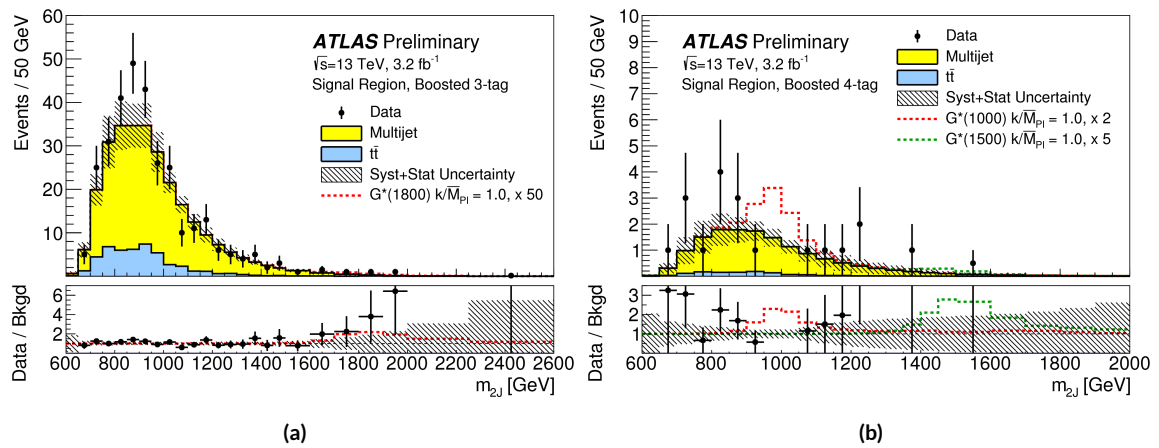


**Figure 7.14:** Di-jet invariant mass ( $M_{2J}$ ) in the  $3b$  (a) and  $4b$  (b) signal regions. The multijet and  $t\bar{t}$  backgrounds are estimated using the data-driven methods described above. In the  $3b$  region, a graviton signal with  $m_{G_{KK}^*} = 1.8 \text{ TeV}$  and  $c = 1$  is overlaid, with the cross section multiplied by a factor of 50 so that the signal is visible. In the  $4b$  region, signals with  $m_{G_{KK}^*} = 1.0 \text{ TeV}$  and  $m_{G_{KK}^*} = 1.5 \text{ TeV}$  are overlaid, both with  $c = 1$  and the yields multiplied by factors of 2 and 5 respectively [102].

*There is no real ending. It's just the place where you stop  
the story.*

Frank Herbert

# 8

2475

2476

## Combined limits from boosted and resolved searches

2477

2478 8.1 INTRODUCTION

2479 In order to cover the full mass range of possible resonances decaying to di-Higgs final states, two distinct  
2480 tailored selections were produced. The resolved selection is more sensitive in the mass range of  $400 < m_X < 1100$  GeV while the boosted selection is more sensitive to masses in the range  $1100 < m_X <$   
2481  $3000$  GeV. Chapter 7 presents the details of the boosted selection and results. In setting limits on spin-2  
2482 Randall-Sundrum graviton (RSG) and narrow width heavy scalar ( $H$ ) models, the results of the boosted  
2483 selection are combined with the results of the resolved selection to cover the full mass range.  
2484

2485 This chapter presents limits on signal models resulting from the  $X \rightarrow HH \rightarrow b\bar{b}b\bar{b}$  search in both  
2486 the resolved and boosted selections. It first presents a brief overview of the resolved results that go into

2487 the limit setting. Then, an overview of the statistical methods used for the search and limit setting is  
2488 given. Finally, limits on the RSG and heavy scalar models are presented.

2489 **8.2 RESOLVED RESULTS**

2490 The details of the resolved selection will not be presented here and can be found in reference [102]. In  
2491 basic terms, the selection searches for four  $R = 0.4$  b-tagged calorimeter jets (where each pair of jets is  
2492 one Higgs candidate). This is distinct from the boosted methodology which searches for merged decay  
2493 products. The backgrounds to the resolved selection are the same as those presented in Chapter 7 for the  
2494 boosted analysis.

2495 Table 8.1 shows the results for data yields and expected background in the resolved signal region. Fig-  
2496 ure 8.1 shows the  $M_{2J}$  distribution in the resolved signal region. The total number of events is consis-  
2497 tent with the prediction and no significant excess is seen. One event in the boosted 4-tag signal is shared  
2498 with the resolved signal region and has a mass of 852 GeV.

Sample	Signal Region Yield
Multijet	$43.3 \pm 2.3$
$t\bar{t}$	$4.3 \pm 3.0$
$Z + \text{jets}$	-
Total	$47.6 \pm 3.8$
Data	46
SM $hh$	$0.25 \pm 0.07$
$G_{\text{KK}}^*(800 \text{ GeV}), c = 1$	$5.7 \pm 1.5$

**Table 8.1:** Observed yields in the resolve selection 4-tag signal region compared to the predicted number of background events Errors correspond to the total uncertainties in the predicted event yields. The yields for a graviton with  $m_{G_{\text{KK}}^*} = 800 \text{ GeV}$  and  $c = 1$  are also shown. [102]

2499 **8.3 SEARCH TECHNIQUE AND RESULTS**

2500 The statistical technique used for the search in this analysis is the same as that used in the  $H \rightarrow WW^*$   
2501 analysis presented in section 3.6.2. The test statistic  $q_0$  is used to define the  $p$ -values which measure the

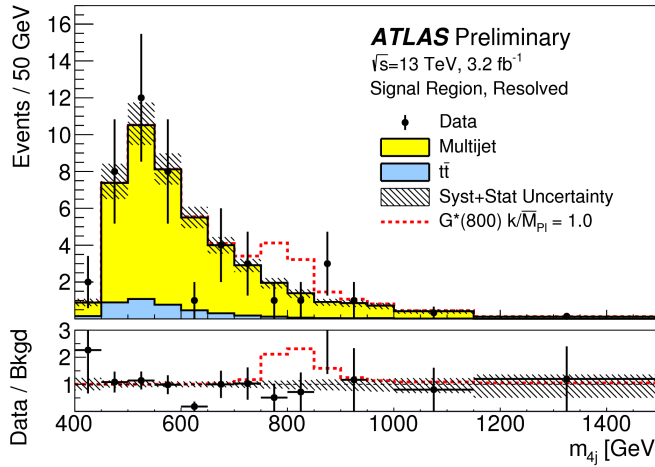


**Figure 8.1:** Di-jet invariant mass ( $M_{2J}$ ) in the resolved signal region. A graviton signal with  $m_{G^*_\text{KK}} = 800 \text{ GeV}$  and  $c = 1$  is overlaid. [102].

compatibility of the data with the background-only hypothesis corresponding to a signal strength  $\mu = 0$ .

Local  $p_0$  values are computed to quantify the probability that the background could produce a fluctuation greater than or equal to the one observed in the data. In the resolved analysis, no significant excesses are observed. The largest discrepancy with respect to the background only hypothesis occurs near a resonance mass of 900 GeV and is found to be less than  $2\sigma$  in significance.

In the boosted selection, the largest local excess is a broad excess in the  $3b$  signal region that begins near  $M_{2J} \approx 1.7 \text{ GeV}$ . Assuming a  $G^*_\text{KK}$  with this mass and  $c = 1.0$ , the local significance of this excess is  $2.0\sigma$ .

#### 8.4 LIMIT SETTING

In the absence of any significant excess observed in the data, limits on different signal models can be set. This section describes the limit setting procedure and presents combined results of the resolved and boosted analyses.

2515 8.4.1 LIMIT SETTING PROCEDURE

2516 The procedure used for setting exclusion limits in this analysis is the  $\text{CL}_s$  method [107]. The first step in  
 2517 setting the limits is to define a test statistic which will be used. For limit setting, the test statistic is shown  
 2518 in equation 8.1.

$$\tilde{q}_\mu = \begin{cases} -2 \ln \frac{L(\mu, \hat{\theta}(\mu))}{L(0, \hat{\theta}(0))} & \hat{\mu} < 0 \\ -2 \ln \frac{L(\mu, \hat{\theta}(\mu))}{L(\hat{\mu}, \hat{\theta})} & 0 \leq \hat{\mu} < \mu \\ 0 & \hat{\mu} > \mu \end{cases} \quad (8.1)$$

2519 In the above equation,  $\mu$  is the value of the signal strength under test,  $\hat{\mu}$  is the best fit  $\mu$ ,  $\hat{\theta}$  is the  
 2520 best fit value of the nuisance parameters,  $\hat{\theta}$  is the best fit value of the nuisance parameters under the fixed  
 2521  $\mu$  value, and  $L$  is the Poisson likelihood of the data (as described in section 3.6.2).

2522 The test statistic  $\tilde{q}_\mu$  is constructed to protect against two interesting corner cases when setting the  
 2523 upper limit on the cross section. First, it protects against negative signal strengths  $\mu$  which are unphys-  
 2524 ical. Second, it does not count excesses in the data larger than those expected by a signal strength  $\mu$  as  
 2525 evidence against the  $\mu$  hypothesis.

2526 The  $\text{CL}_s$  statistic is constructed by taking a ratio of two probabilities.  $\text{CL}_{s+b}$  is the probability that  
 2527 the signal+background hypothesis would produce a value of the test statistic that is less than or equal  
 2528 to the observed value\*.  $\text{CL}_b$  is the probability that the background only hypothesis will pro-  
 2529 duce a value of the test statistics less than or equal to the observed. The  $\text{CL}_s$  statistic is then the ratio  
 2530  $\text{CL}_{s+b}/\text{CL}_b$ . A 95% upper limit on the cross section is set at the value of  $\mu$  that makes the  $\text{CL}_s$  statistic  
 2531 less than 5%.

2532 In practice, the limits are computed numerically within an asymptotic approximation for the distri-  
 2533 bution of the test statistic  $\tilde{q}_\mu$ . The details of this approximation can be found in reference [63].

2534 The resolved and boosted analyses are combined using a very simple procedure rather than a full sta-  
 2535 tistical combination. For each mass point tested, the limit which gives the most stringent constraint is  
 2536 used. This means that for mass points below 1.1 TeV the resolved signal region is used, while at and

---

\*Lower values of  $\tilde{q}_\mu$  mean better compatibility

2537 above this point the combination of the orthogonal  $3b$  and  $4b$  boosted signal regions is used.

2538 **8.4.2 LIMIT SETTING RESULTS**

2539 Figure 8.2 shows the combined 95% upper bounds as a function of mass for three different models:

2540  $G_{\text{KK}}^*$  with  $c = 1$ ,  $G_{\text{KK}}^*$  with  $c = 2$ , and a narrow heavy scalar  $H$ .

2541 The cross section of  $\sigma(pp \rightarrow G_{\text{KK}}^* \rightarrow hh \rightarrow b\bar{b}b\bar{b})$  with  $c = 1$  is constrained to be less than 70 fb  
2542 for masses in the range  $600 < m_{G_{\text{KK}}^*} < 3000$  GeV. For the RSG model with  $c = 2$ , cross sections  
2543 limits between 40 fb and 200 fb are set for the mass range of  $500 < m_{G_{\text{KK}}^*} < 3000$  GeV. Masses in  
2544 the range of  $475 < m_{G_{\text{KK}}^*} < 785$  GeV are excluded with  $c = 1$  (with an exclusion of the range 465  
2545 to 745 GeV expected). Masses less than 980 GeV are excluded with  $c = 2$  (with an exclusion for masses  
2546 less than 1 TeV expected).

2547 In the heavy Higgs model, the cross section upper limits for  $\sigma(pp \rightarrow H \rightarrow hh \rightarrow b\bar{b}b\bar{b})$  ranges from  
2548 30 to 300 fb in the mass range of  $500 < m_H < 3000$  GeV. The resolved analysis can also set an upper  
2549 limit on the Standard Model di-Higgs production cross section discussed in chapter 3. The upper limit  
2550 on  $\sigma(pp \rightarrow hh \rightarrow b\bar{b}b\bar{b})$  in the Standard Model is constrained to be less than 1.22 pb.

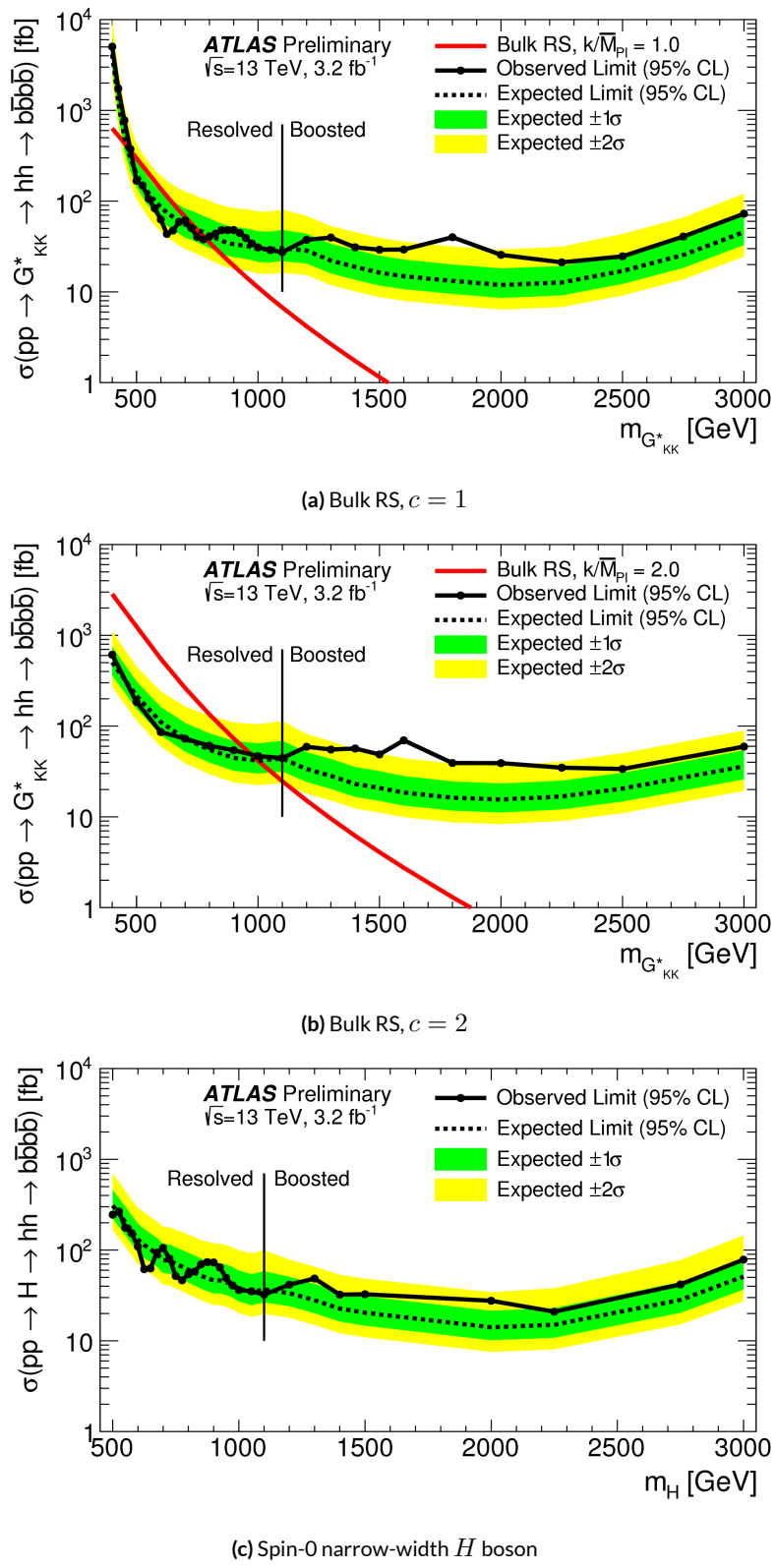


**Figure 8.2:** Expected and observed upper limit as a function of mass for  $G_{\text{KK}}^*$  in the RSG model with (a)  $c = 1$  and (b)  $c = 2$ , as well as (c)  $H$  with fixed  $\Gamma_H = 1$  GeV, at the 95% confidence level in the  $\text{CL}_s$  method. [102]

2551

## Part IV

2552

## Looking ahead

# 9

2553

2554

## Conclusion

2555 This dissertation presented two distinct studies: the observation and measurement of the Higgs boson  
2556 in the  $H \rightarrow WW^* \rightarrow \ell\nu\ell\nu$  channel at  $\sqrt{s} = 7$  TeV and  $\sqrt{s} = 8$  TeV and a search for Higgs pair  
2557 production in the  $HH \rightarrow b\bar{b}b\bar{b}$  channel at  $\sqrt{s} = 13$  TeV with the ATLAS detector in  $pp$  collisions at  
2558 the Large Hadron Collider.

2559 In the  $H \rightarrow WW^* \rightarrow \ell\nu\ell\nu$ , results from both the discovery of the Higgs boson and the full  
2560 ATLAS Run 1 dataset were presented. With the full  $20.3 \text{ fb}^{-1}$  at  $\sqrt{s} = 8$  TeV and  $4.2 \text{ fb}^{-1}$  at  $\sqrt{s} =$   
2561 7 TeV, ATLAS achieved discovery level significance in the  $H \rightarrow WW^*$  channel alone and obtained  
2562 the first observation of vector boson fusion production in that channel. The combined signal strength  
2563 is measured to be  $\mu = 1.09^{+0.23}_{-0.21}$ . The total observed significance of the  $H \rightarrow WW^*$  process is ob-  
2564 served to be  $6.1\sigma$  (with  $5.8\sigma$  expected). Advanced methods for background reduction and estimation,  
2565 particularly in same-flavor lepton final states, are shown. The VBF signal strength is measured to be  
2566  $\mu_{\text{VBF}} = 1.27^{+0.53}_{-0.45}$  with an observed significance of  $3.2\sigma$  (with  $2.7\sigma$  expected).

2567 These results required many novel innovations. The increase of pileup interactions in the higher in-  
2568 stantaneous luminosity LHC conditions of 2012 led to a degradation of missing transverse momentum  
2569 resolution. As a result, the prominent  $Z/\gamma^*$ +jets background of the same flavor  $H \rightarrow WW^* \rightarrow \ell\nu\ell\nu$   
2570 final states increased greatly. New variables, including a track-based missing transverse momentum and  
2571 a measurement of the balance between the dilepton system and recoiling jets, allowed for significant re-  
2572 duction of this background. In the VBF channel, selections were optimized to exploit the unique VBF  
2573 final state topology. Incorporating these variables into a boosted decision tree technique allowed the  
2574 analysis to exceed the  $3\sigma$  observation threshold.

2575 At  $\sqrt{s} = 13$  TeV, a search for Higgs pair production in the  $b\bar{b}b\bar{b}$  final state with  $3.2 \text{ fb}^{-1}$  was con-  
2576 ducted. A signal region optimized for the boosted final states arising from high mass resonances was  
2577 constructed. This signal region utilized large-radius calorimeter jets and  $b$ -tagging with small radius track  
2578 jets to maximize the signal acceptance. No significant excesses were observed, and upper limits on cross  
2579 sections are placed for spin-2 Randall Sundrum gravitons (RSG) and narrow spin-0 resonances. The  
2580 cross section of  $\sigma(pp \rightarrow G_{\text{KK}}^* \rightarrow hh \rightarrow b\bar{b}b\bar{b})$  with  $k/\bar{M}_{\text{Pl}} = 1$  is constrained to be less than  $70 \text{ fb}$  for  
2581 masses in the range  $600 < m_{G_{\text{KK}}^*} < 3000 \text{ GeV}$ . For the RSG model with  $k/\bar{M}_{\text{Pl}} = 2$ , cross sections  
2582 limits between  $40 \text{ fb}$  and  $200 \text{ fb}$  are set for the mass range of  $500 < m_{G_{\text{KK}}^*} < 3000 \text{ GeV}$ . The cross  
2583 section upper limits for  $\sigma(pp \rightarrow H \rightarrow hh \rightarrow b\bar{b}b\bar{b})$  ranges from  $30$  to  $300 \text{ fb}$  in the mass range of  
2584  $500 < m_H < 3000 \text{ GeV}$ .

# A

2585

2586

## Optimization of $b$ -tagging working point in

2587

$$X \rightarrow HH \rightarrow b\bar{b}b\bar{b} \text{ search}$$

2588 To the  $3b$  and  $4b$  signal regions in the boosted  $X \rightarrow HH \rightarrow b\bar{b}b\bar{b}$  search, the MV2 algorithm with a  
2589 20% fraction of charm events in training is used (MV2c2o). Once the algorithm is selected, an efficiency  
2590 working point must also be chosen. This working point defines the efficiency with which true  $b$ -jets  
2591 are tagged and also fixes the overall background rejection of the algorithm. Higher efficiency working  
2592 points accept more true  $b$ -jets but also allow for more background. Five different working points (70%,  
2593 77%, 80%, 85%, 90%) are tested. With each working point, the full data driven background estimation  
2594 method is run to quantify the amount of background that will be present in the final signal region. The  
2595 significance is quantified using the median discovery significance for signal and background with Poisson

2596 errors, given in equation A.1 [108].

$$Z = \sqrt{2 \left( (s + b) \ln \left( 1 + \frac{s}{b} \right) - s \right)} \quad (\text{A.1})$$

2597 Note that in the limit where  $s$  is much smaller than  $b$ , this equation reduces to the more well known

2598  $s/\sqrt{b}$ .

2599 Figure A.1 shows the estimated significance as a function of signal mass in RSG  $c = 1$  models for  
2600 the  $3b$  and  $4b$  signal regions. The 77% working point gives the best performance over a wide range of  
2601 masses in the  $4b$  signal region. As this is the region which contributes the most to the total discovery  
2602 significance, the 77% efficiency working point is chosen for the analysis.

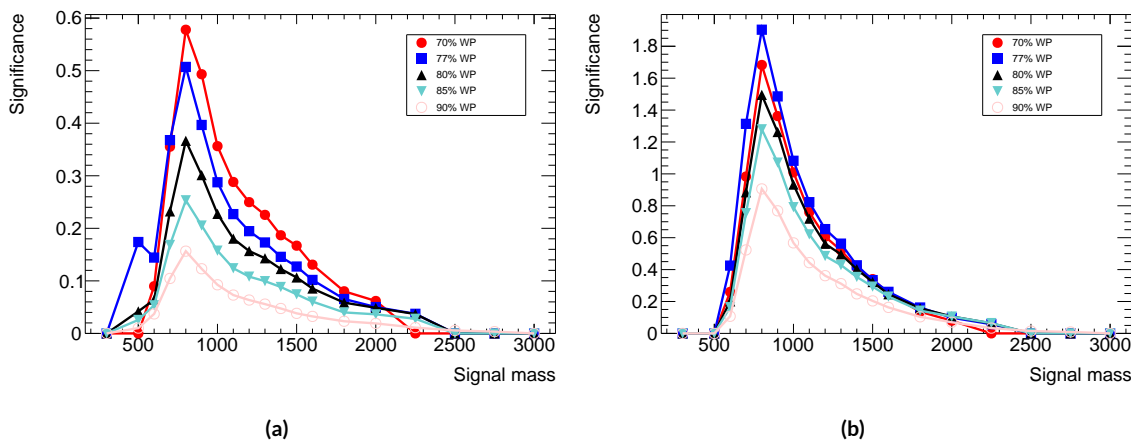


**Figure A.1:** Estimated significance as a function of signal mass for RSG  $c = 1$  models in the  $3b$  (a) and  $4b$  (b) regions for different  $b$ -tagging efficiency working points

# B

2603

2604

## *b*-tagging performance at high $p_T$

2605 One of the limiting factors of the signal acceptance in the *FourB full* search at high resonance masses is  
2606 the degradation of the *b*-tagging efficiency for high  $p_T$  jets. This appendix presents a study of the under-  
2607 lying causes of this degradation.

### 2608 B.I MV<sub>2</sub> ALGORITHM OVERVIEW

2609 The MV<sub>2</sub> algorithm is a boosted decision tree incorporating twenty-four input variables constructed  
2610 from three lower level input algorithms: IPxD, SV<sub>1</sub>, and JetFitter. IPxD uses the two and three dimen-  
2611 sional impact parameter information of tracks in the jet to construct templates for light, charm, and bot-  
2612 tom quarks and compute likelihood ratios. SV<sub>1</sub> is a secondary vertex reconstruction algorithm. JetFitter  
2613 attempts to fit to the full decay chain of the *B* hadron, looking for multiple decay vertices aligned along a  
2614 single axis. Figure B.I summarizes the inputs to MV<sub>2</sub>.

IP2D and IP3D (6 inputs)	SV1 (8 inputs)	JetFitter (8 inputs)
$\log(p_b/p_u)$	Mass	Mass
$\log(p_b/p_c)$	Energy fraction	Energy fraction
$\log(p_c/p_u)$	# tracks at vertex	# vertices
	# 2 track vertices	# tracks at vertex
	Lxy	# 1 track vertices
	L3d	# 2 track vertices
	3D significance	3D significance
	$\Delta R$	$\Delta R$
Kinematics (2 inputs)		
	$p_T$	
	$\eta$	

**Figure B.1:** Summary of the inputs to the MV2  $b$ -tagging algorithm

2615    **B.2 CHANGES IN MV2 SCORE AT HIGH  $p_T$**

2616    The degradation of  $b$ -tagging at high  $p_T$  was studied in particular in the context of RSG models at high  
 2617    mass. Figure B.2 shows the  $p_T$  of the leading track jet inside of the leading calorimeter jet in RSG events.  
 2618    At high  $m_{G_{KK}^*}$ , the  $p_T$  spectrum of track jets is much harder than at lower masses due to the increased  
 2619    Higgs  $p_T$ .

2620    Figure B.3 shows the MV2c20 algorithm score for the leading and subleading track jets inside of the  
 2621    leading calorimeter jet. In both cases, it can be seen that at higher RSG masses the MV2 score shifts to-  
 2622    wards more background like (negative) values. Additionally, this effect is more pronounced in the lead-  
 2623    ing track jet than the subleading.

2624    To understand what is causing this change in the MV2c20 score, the same comparisons can be made  
 2625    for the input variables of MV2c20. The focus in these comparisons will be on the leading track jet as  
 2626    this is the one seen to have the largest difference in MV2 score. Figure B.4 shows the log likelihood ratio  
 2627     $\log(p_b/p_u)$  from the IP3D (three dimensional impact parameter) algorithm. At higher masses, the IP3D  
 2628    likelihood ratio distribution does become more background-like.

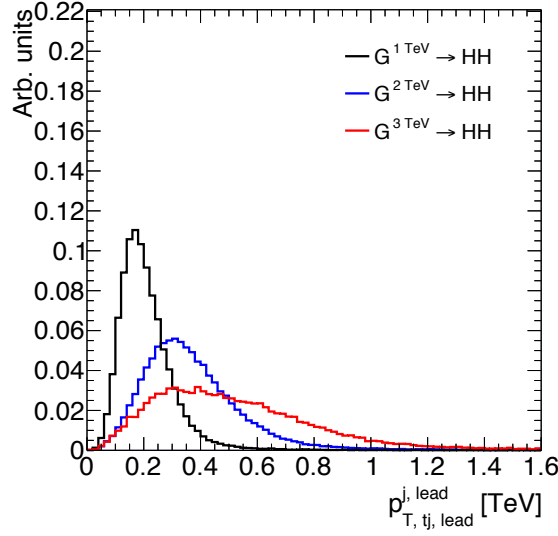


**Figure B.2:**  $p_T$  of the leading track jet in the leading calorimeter jet for different signal masses in RSG  $c = 1$  models

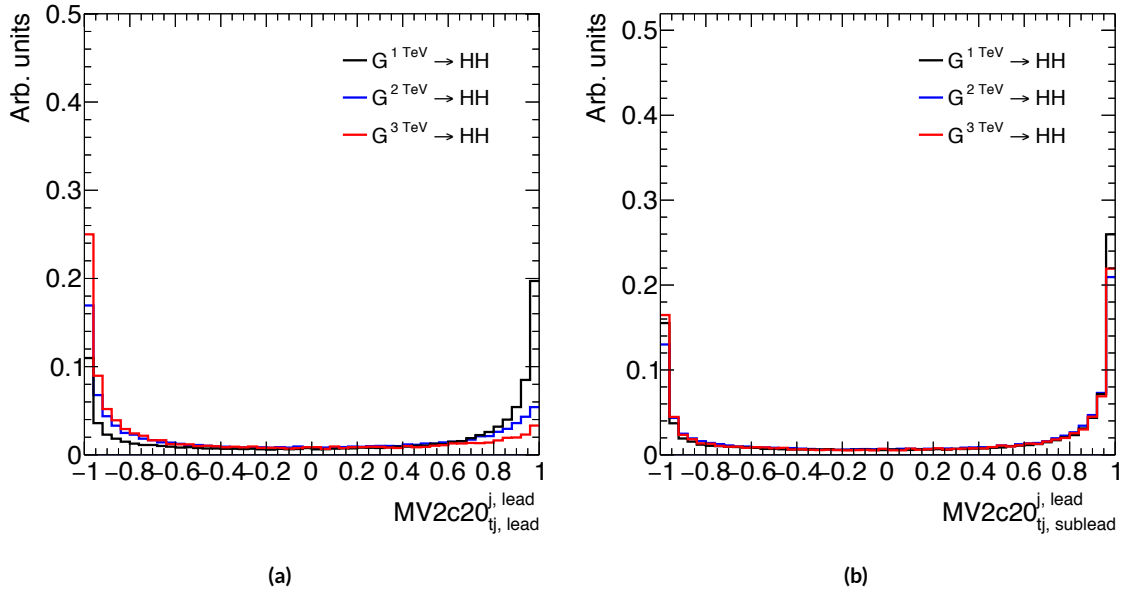


**Figure B.3:** MV2c20 score for the leading track jet (a) and subleading track jet (b) of the leading calorimeter jet for different signal masses in RSG  $c = 1$  models

2629     Figure B.5 shows the mass and number of tracks at the secondary vertex computed by the SVI algo-  
 2630     rithm. When there is no secondary vertex found, the algorithm assigns a default negative value for these  
 2631     quantities. Both of these distributions show that there is a significantly larger fraction of jets where no  
 2632     secondary vertex is found in the high mass samples compared to the  $m_{G_{KK}^*} = 1$  TeV sample. The SVI

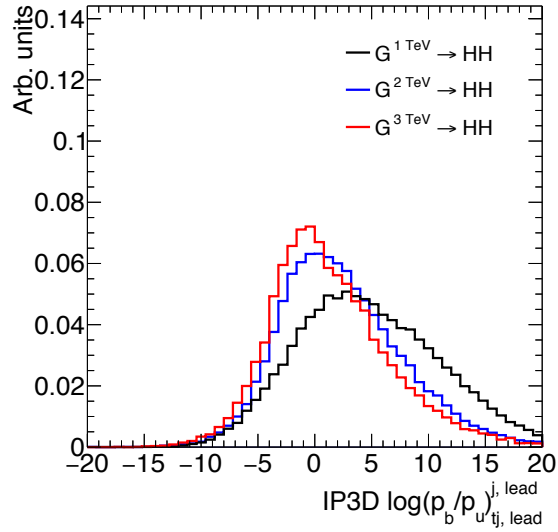


**Figure B.4:** IP3D log-likelihood ratio ( $\log(p_b/p_u)$ ) of the leading track jet in the leading calorimeter jet for different signal masses in RSG  $c = 1$  models

algorithm's inability to find a secondary vertex could be an important factor in the overall MV<sub>2</sub> score shift, as this eliminates eight of the input variables that would normally contribute information to the algorithm.

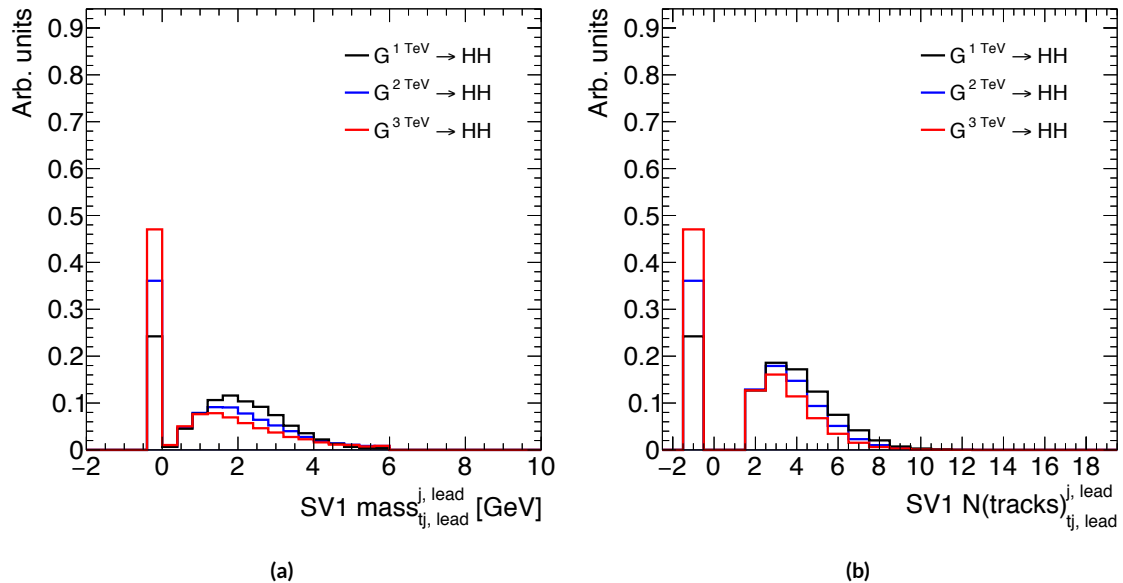


**Figure B.5:** Mass (a) and number of tracks (b) for the secondary vertices computed with the SV1 algorithm. When no secondary vertex is found, the quantities are assigned to default negative values.

2636      Figure B.6 shows the same quantities for the JetFitter algorithm. In this case, there is also a change in  
 2637      the fraction of jets which have their secondary vertices successfully reconstructed, but this change is not  
 2638      as drastic as that seen in SV1. There is also an increase in the number of jets which have high values of  
 2639      mass.

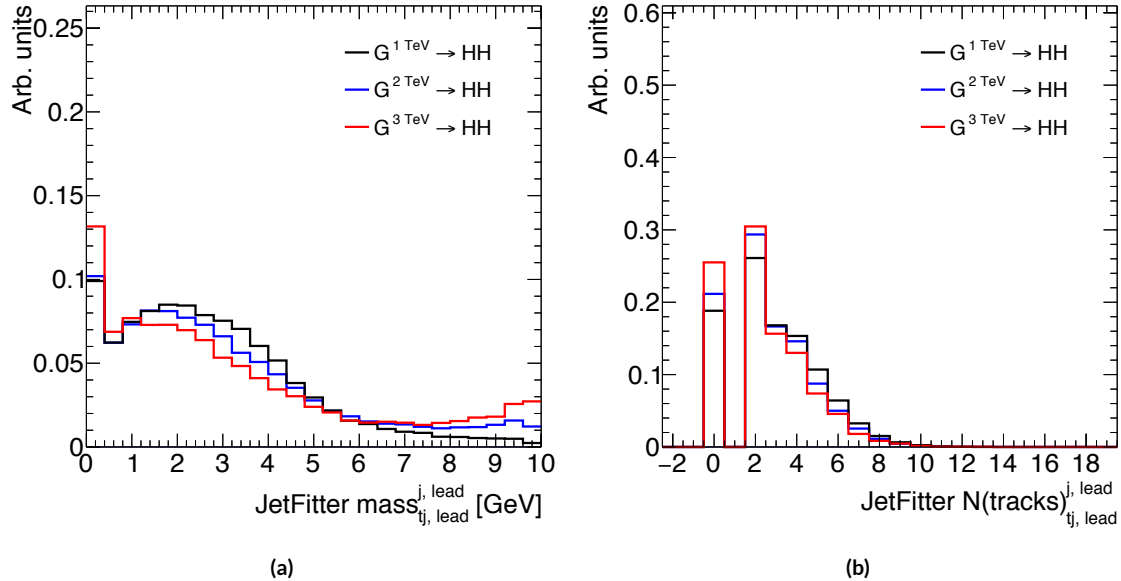


**Figure B.6:** Mass (a) and number of tracks (b) for vertices computed with the JetFitter algorithm. When no vertices are found, the quantities are assigned to default negative values.

### 2640    B.3    TAGGING EFFICIENCY BY INDIVIDUAL JET

2641    In the last section, the largest changes in MV2 score were seen for the leading track jet inside the leading  
 2642    calorimeter jet. To confirm that the overall 4*b* tagging efficiency is indeed degrading because of degra-  
 2643    dation of the leading track jet efficiency, the tagging efficiency for each individual jet as a function of mass  
 2644    can be compared. This is shown in figure B.7. The figure shows that the leading jet tagging efficiency  
 2645    in both calorimeter jets degrades heavily, while the sub-lead jet tagging efficiency remains relatively con-  
 2646    stant.

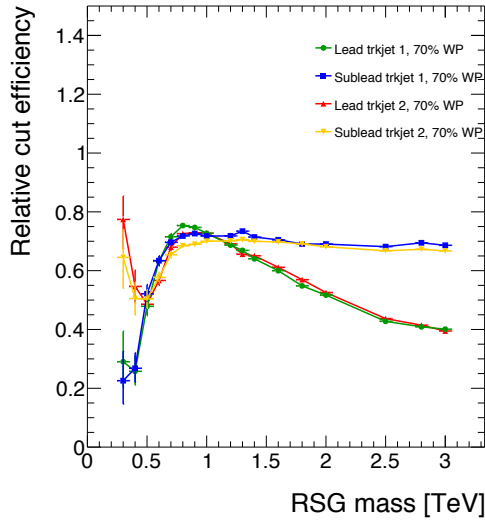


**Figure B.7:** MV2c20  $b$ -tagging efficiency for each of the four track jets in the boosted  $4b$  selection as a function of RSG mass for  $c = 1$  models.

#### B.4 EFFECT OF MULTIPLE $b$ -QUARKS INSIDE ONE JET

One hypothesis for why the efficiency of  $b$ -tagging the leading track jet degrades is that at high masses, the  $b$  quarks get close enough together that both of them are inside of the leading track jet. Because MV<sub>2</sub> is not tuned for tagging multiple  $b$  quarks inside one jet, the tagging efficiency could degrade. Figure B.8 shows MV<sub>2</sub> scores and SV<sub>1</sub> mass for cases where there are two  $b$  quarks at truth level within the radius of the leading track jet compared to cases where there is only one true  $b^*$ . This figure suggests that the presence of two  $b$ -quarks inside the leading jet is not the cause of the degradation in efficiency. There is a change in the shape of the MV<sub>2</sub> score distribution, but it is not nearly as pronounced as that seen in B.3 at higher masses. Additionally, the fraction of jets with no secondary vertex found is nearly identical in the track jets with two truth  $b$ -quarks.

---

\*When two truth  $b$  quarks are required in the leading jet, the subleading jet is required to have zero. When one is required for the leading, one is also required for the subleading.

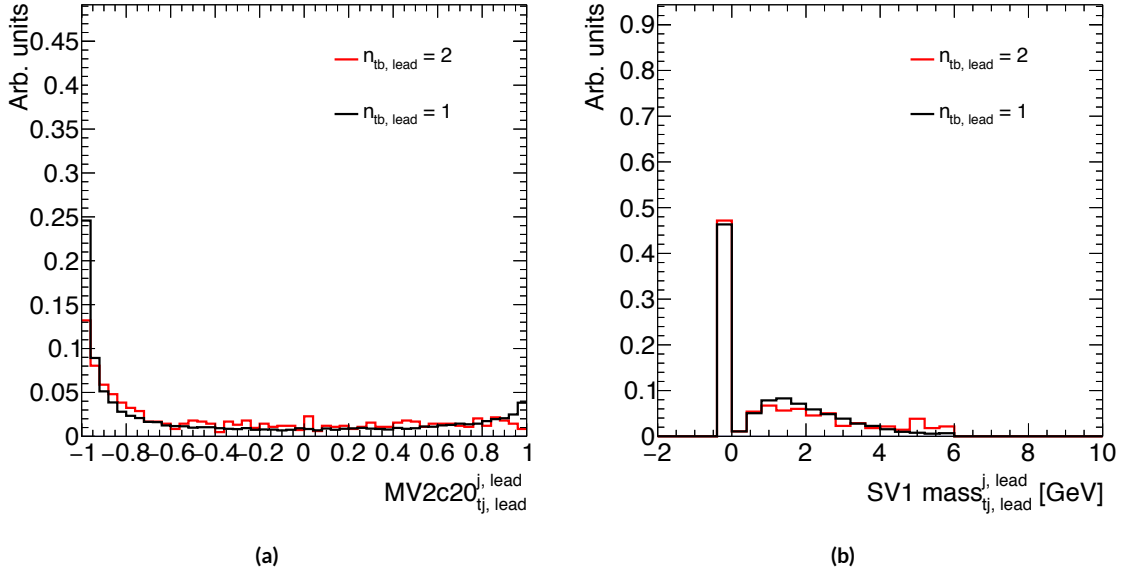


**Figure B.8:** MV2c20 score (a) and SV1 mass (b) for leading track jets with two truth  $b$  quarks ( $n_{tb, \text{lead}} = 2$ ) compared to those with only one truth  $b$  ( $n_{tb, \text{lead}} = 1$ ).

## 2657 B.5 CHANGES IN TRACK QUALITY AT HIGH $p_T$

2658 Another hypothesis for the degradation of the  $b$ -tagging efficiency is a decrease in track quality for high  
 2659  $p_T$   $b$  jets. One way to check the overall quality of the tracking inside the jet is to investigate quantities  
 2660 related to the leading track inside of the track jet. Figure B.9 shows the fit  $\chi^2/n_{\text{DOF}}$  and number of hits  
 2661 in the pixel detector for the leading track of the leading track jet. In both cases, the figure shows that in  
 2662 higher mass samples, the quality of the leading track inside of the track jet degrades substantially. The  
 2663 fit quality is lessened and the tracks have less hits in the pixel detector. This is likely due to the fact that  
 2664 at higher  $p_T$ , the  $B$ -hadron will sometimes live long enough to miss the IBL and first pixel layer, thus  
 2665 decreasing the number of hits on the track.

2666 To check whether this is the cause for the shift in the MV2 score and the higher difficulty in recon-  
 2667 structing secondary vertices, jets whose leading track have at least four pixel hits are compared with those  
 2668 whose tracks have less than four pixel hits. The results for the MV2 score and SV1 mass are shown in fig-  
 2669 ure B.10. Track jets where the leading track does not have at least four pixel hits are more likely to not  
 2670 have a secondary vertex reconstructed. Additionally, their MV2c20 score is shifted more significantly to

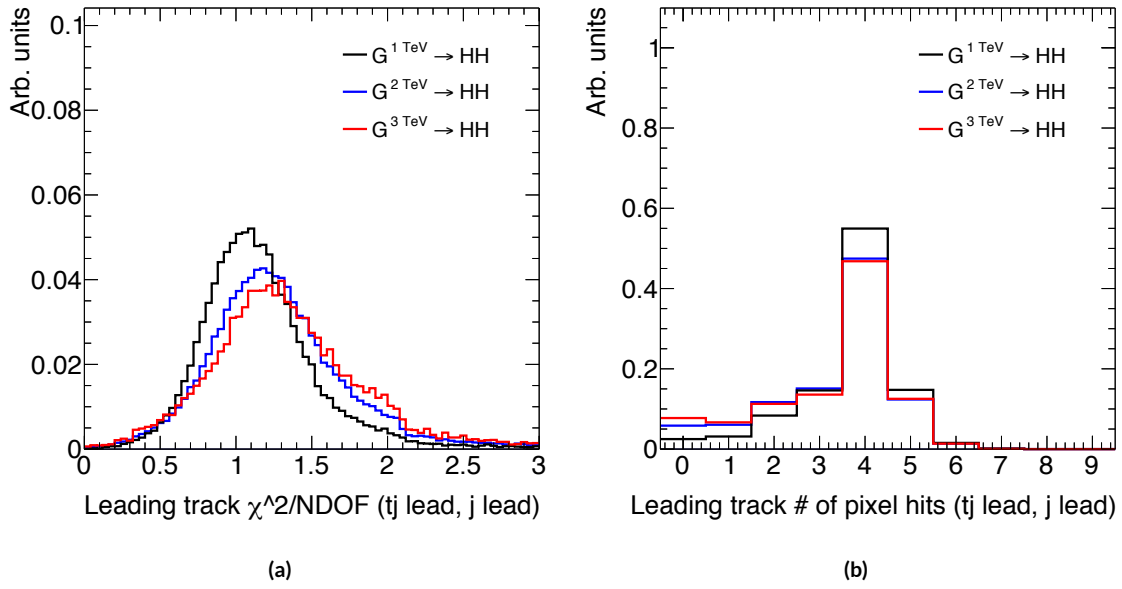


**Figure B.9:** Track fit  $\chi^2/\text{nDOF}$  (a) and number of pixel detector hits (b) for the leading track of the leading track jet in different mass RSG  $c = 1$  samples

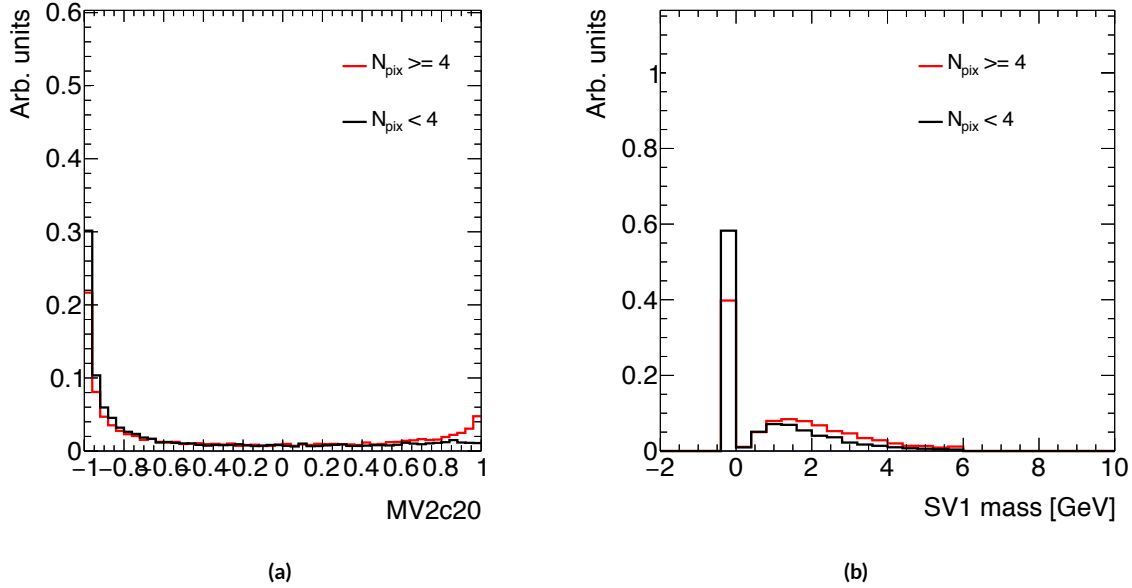


**Figure B.10:** MV2c20 score (a) and SV1 mass (b) for leading track jets whose leading track jet has at least four pixel hits ( $N_{\text{pix}} \geq 4$ ) compared to those which do not ( $N_{\text{pix}} < 4$ ).

background-like values. This seems to confirm the hypothesis that degrading track quality is responsible  
<sup>2671</sup> for the lowered  $b$ -tagging efficiency at high  $p_T$ .  
<sup>2672</sup>

# References

2673

- 2674 [1] Georges Aad et al. Observation of a new particle in the search for the Standard Model Higgs  
2675 boson with the ATLAS detector at the LHC. *Phys. Lett.*, B716:1–29, 2012. doi: 10.1016/j.physletb.  
2676 2012.08.020.
- 2677 [2] Serguei Chatrchyan et al. Observation of a new boson at a mass of 125 GeV with the CMS experi-  
2678 ment at the LHC. *Phys. Lett.*, B716:30–61, 2012. doi: 10.1016/j.physletb.2012.08.021.
- 2679 [3] David Griffiths. *Introduction to elementary particles*. 2008.
- 2680 [4] F. Halzen and Alan D. Martin. *QUARKS AND LEPTONS: AN INTRODUCTORY*  
2681 *COURSE IN MODERN PARTICLE PHYSICS*. 1984. ISBN 0471887412, 9780471887416.
- 2682 [5] Christopher G. Tully. *Elementary particle physics in a nutshell*. 2011.
- 2683 [6] K. A. Olive et al. Review of Particle Physics. *Chin. Phys.*, C38:090001, 2014. doi: 10.1088/  
2684 1674-1137/38/9/090001.
- 2685 [7] Matthew D. Schwartz. *Quantum Field Theory and the Standard Model*. Cambridge University  
2686 Press, 2014. ISBN 1107034736, 9781107034730. URL <http://www.cambridge.org/us/academic/subjects/physics/theoretical-physics-and-mathematical-physics/quantum-field-theory-and-standard-model>.
- 2689 [8] S. Dawson. Introduction to electroweak symmetry breaking. In *High energy physics and cos-  
2690 mology. Proceedings, Summer School, Trieste, Italy, June 29-July 17, 1998*, pages 1–83, 1998. URL  
2691 <http://alice.cern.ch/format/showfull?sysnb=0301862>.
- 2692 [9] S. L. Glashow. Partial Symmetries of Weak Interactions. *Nucl. Phys.*, 22:579–588, 1961. doi:  
2693 10.1016/0029-5582(61)90469-2.
- 2694 [10] Steven Weinberg. A Model of Leptons. *Phys. Rev. Lett.*, 19:1264–1266, 1967. doi: 10.1103/  
2695 PhysRevLett.19.1264.
- 2696 [11] A. Salam. *Elementary Particle Theory*. Almqvist and Wiksell, Stockholm, 1968.
- 2697 [12] J. Iliopoulos S.L. Glashow and L. Maiani. *D2:1285*, 1970.
- 2698 [13] R. Keith Ellis, W. James Stirling, and B. R. Webber. QCD and collider physics. *Camb. Monogr.  
2699 Part. Phys. Nucl. Phys. Cosmol.*, 8:1–435, 1996.

- 2700 [14] P. W. Higgs. Broken symmetries and the masses of gauge bosons. *13*:508, 1964.
- 2701 [15] P. W. Higgs. Spontaneous symmetry breakdown without massless bosons. *145*:1156, 1966.
- 2702 [16] F. Englert and R. Brout. Broken symmetry and the mass of gauge vector mesons. *13*:321, 1964.
- 2703 [17] G. S. Guralnik, C. R. Hagen, and T. W. .B. Kibble. Global conservation laws and massless parti-  
2704 cles. *Phys. Rev. Lett.*, *13*:585, 1964. doi: [10.1103/PhysRevLett.13.585](https://doi.org/10.1103/PhysRevLett.13.585).
- 2705 [18] LHC Higgs Cross Section Working Group, S. Heinemeyer, C. Mariotti, G. Passarino, and  
2706 R. Tanaka (Eds.). Handbook of LHC Higgs Cross Sections: 3. Higgs Properties. 2013.
- 2707 [19] J. Baglio, A. Djouadi, R. Gröber, M. M. Mühlleitner, J. Quevillon, and M. Spira. The mea-  
2708 surement of the Higgs self-coupling at the LHC: theoretical status. *JHEP*, *04*:151, 2013. doi:  
2709 [10.1007/JHEP04\(2013\)151](https://doi.org/10.1007/JHEP04(2013)151).
- 2710 [20] Matthew J. Dolan, Christoph Englert, and Michael Spannowsky. New Physics in LHC Higgs  
2711 boson pair production. *Phys. Rev.*, *D87*(5):055002, 2013. doi: [10.1103/PhysRevD.87.055002](https://doi.org/10.1103/PhysRevD.87.055002).
- 2712 [21] Roberto Contino, Margherita Ghezzi, Mauro Moretti, Giuliano Panico, Fulvio Piccinini, and  
2713 Andrea Wulzer. Anomalous Couplings in Double Higgs Production. *JHEP*, *08*:154, 2012. doi:  
2714 [10.1007/JHEP08\(2012\)154](https://doi.org/10.1007/JHEP08(2012)154).
- 2715 [22] R. Grober and M. Mühlleitner. Composite Higgs Boson Pair Production at the LHC. *JHEP*, *06*:  
2716 020, 2011. doi: [10.1007/JHEP06\(2011\)020](https://doi.org/10.1007/JHEP06(2011)020).
- 2717 [23] Lisa Randall and Raman Sundrum. A Large mass hierarchy from a small extra dimension. *Phys.*  
2718 *Rev. Lett.*, *83*:3370–3373, 1999. doi: [10.1103/PhysRevLett.83.3370](https://doi.org/10.1103/PhysRevLett.83.3370).
- 2719 [24] Kaustubh Agashe, Hooman Davoudiasl, Gilad Perez, and Amarjit Soni. Warped Gravitons at the  
2720 LHC and Beyond. *Phys. Rev.*, *D76*:036006, 2007. doi: [10.1103/PhysRevD.76.036006](https://doi.org/10.1103/PhysRevD.76.036006).
- 2721 [25] A. Liam Fitzpatrick, Jared Kaplan, Lisa Randall, and Lian-Tao Wang. Searching for the Kaluza-  
2722 Klein Graviton in Bulk RS Models. *JHEP*, *09*:013, 2007. doi: [10.1088/1126-6708/2007/09/013](https://doi.org/10.1088/1126-6708/2007/09/013).
- 2723 [26] Julien Baglio, Otto Eberhardt, Ulrich Nierste, and Martin Wiebusch. Benchmarks for Higgs Pair  
2724 Production and Heavy Higgs boson Searches in the Two-Higgs-Doublet Model of Type II. *Phys.*  
2725 *Rev.*, *D90*(1):015008, 2014. doi: [10.1103/PhysRevD.90.015008](https://doi.org/10.1103/PhysRevD.90.015008).
- 2726 [27] G. C. Branco, P. M. Ferreira, L. Lavoura, M. N. Rebelo, Marc Sher, and Joao P. Silva. Theory  
2727 and phenomenology of two-Higgs-doublet models. *Phys. Rept.*, *516*:1–102, 2012. doi: [10.1016/j.physrep.2012.02.002](https://doi.org/10.1016/j.physrep.2012.02.002).
- 2728 [28] Howard E. Haber and Oscar Stål. New LHC benchmarks for the  $\mathcal{CP}$ -conserving two-Higgs-  
2729 doublet model. *Eur. Phys. J.*, *C75*(10):491, 2015. doi: [10.1140/epjc/s10052-015-3697-x](https://doi.org/10.1140/epjc/s10052-015-3697-x).

- 2731 [29] Jose M. No and Michael Ramsey-Musolf. Probing the Higgs Portal at the LHC Through Reso-  
 2732 nant di-Higgs Production. *Phys. Rev.*, D89(9):095031, 2014. doi: 10.1103/PhysRevD.89.095031.
- 2733 [30] Johan Alwall, Michel Herquet, Fabio Maltoni, Olivier Mattelaer, and Tim Stelzer. MadGraph  
 2734 5:Going Beyond. *JHEP*, 1106:128, 2011. doi: 10.1007/JHEP06(2011)128.
- 2735 [31] Lyndon R Evans and Philip Bryant. LHC Machine. *J. Instrum.*, 3:S08001, 164 p, 2008. URL  
 2736 <https://cds.cern.ch/record/1129806>. This report is an abridged version of the LHC  
 2737 Design Report (CERN-2004-003).
- 2738 [32] ATLAS Collaboration. The ATLAS experiment at the CERN Large Hadron Collider. *JINST*, 3:  
 2739 S08003, 2008. doi: 10.1088/1748-0221/3/08/S08003.
- 2740 [33] CMS Collaboration. The cms experiment at the cern lhc. *Journal of Instrumentation*, 3(08):  
 2741 S08004, 2008. URL <http://stacks.iop.org/1748-0221/3/i=08/a=S08004>.
- 2742 [34] LHCb Collaoration. The LHCb Detector at the LHC. *JINST*, 3:S08005, 2008. doi: 10.1088/  
 2743 1748-0221/3/08/S08005.
- 2744 [35] ALICE Collaboration. The alice experiment at the cern lhc. *Journal of Instrumentation*, 3(08):  
 2745 S08002, 2008. URL <http://stacks.iop.org/1748-0221/3/i=08/a=S08002>.
- 2746 [36] Lyndon Evans. The Large Hadron Collider. In Holstein, BR and Haxton, WC and Jawahery,  
 2747 A, editor, *ANNUAL REVIEW OF NUCLEAR AND PARTICLE SCIENCE, VOL 61*,  
 2748 volume 61 of *Annual Review of Nuclear and Particle Science*, pages 435–466. 2011. doi: {10.1146/annurev-nucl-102010-130438}.
- 2750 [37] ATLAS Collaboration. Luminosity Determination in  $pp$  Collisions at  $\sqrt{s} = 7$  TeV Using the  
 2751 ATLAS Detector at the LHC. *Eur. Phys. J.*, C 71:1630, 2011. doi: 10.1140/epjc/s10052-011-1630-5.
- 2752 [38] Mike Lamont for the LHC team. The First Years of LHC Operation for Luminosity Production.  
 2753 International Particle Accelerator Conference, 2013. URL [https://accelconf.web.cern.ch/accelconf/IPAC2013/talks/moyab101\\_talk.pdf](https://accelconf.web.cern.ch/accelconf/IPAC2013/talks/moyab101_talk.pdf).
- 2755 [39] Paul Collier for the LHC team. LHC Machine Status. CERN Resource Review Board, 2015.  
 2756 URL <https://cds.cern.ch/record/2063924/files/CERN-RRB-2015-119.PDF>.
- 2757 [40] Track Reconstruction Performance of the ATLAS Inner Detector at  $\sqrt{s} = 13$  TeV. Technical  
 2758 Report ATL-PHYS-PUB-2015-018, CERN, Geneva, Jul 2015. URL <https://cds.cern.ch/record/2037683>.

- 2760 [41] M Capeans, G Darbo, K Einsweiller, M Elsing, T Flick, M Garcia-Sciveres, C Gemme, H Pernegger, O Rohne, and R Vuillermet. ATLAS Insertable B-Layer Technical Design Report. Technical Report CERN-LHCC-2010-013. ATLAS-TDR-19, CERN, Geneva, Sep 2010. URL <https://cds.cern.ch/record/1291633>.
- 2761  
2762  
2763
- 2764 [42] ATLAS Collaboration. ATLAS Trigger Operations Public Results. 2015. URL <https://twiki.cern.ch/twiki/bin/view/AtlasPublic/TriggerOperationPublicResults>.
- 2765  
2766  
2767
- 2768 [43] ATLAS Collaboration. ATLAS Luminosity Public Results, Run 1. 2012. URL <https://twiki.cern.ch/twiki/bin/view/AtlasPublic/LuminosityPublicResults>.
- 2769  
2770  
2771  
2772  
2773  
2774
- 2775 [44] ATLAS Collaboration. ATLAS Luminosity Public Results, Run 2. 2015. URL <https://twiki.cern.ch/twiki/bin/view/AtlasPublic/LuminosityPublicResultsRun2>.
- 2776  
2777  
2778  
2779  
2780
- 2781 [45] T Kawamoto, S Vlachos, L Pontecorvo, J Dubbert, G Mikenberg, P Iengo, C Dallapiccola, C Amelung, L Levinson, R Richter, and D Lellouch. New Small Wheel Technical Design Report. Technical Report CERN-LHCC-2013-006. ATLAS-TDR-020, CERN, Geneva, Jun 2013. URL <https://cds.cern.ch/record/1552862>. ATLAS New Small Wheel Technical Design Report.
- 2782  
2783  
2784  
2785  
2786
- 2787 [46] Y. Giomataris, Ph. Reboursard, J.P. Robert, and G. Charpak. Micromegas: a high-granularity position-sensitive gaseous detector for high particle-flux environments. *Nuclear Instruments and Methods in Physics Research Section A: Accelerators, Spectrometers, Detectors and Associated Equipment*, 376(1):29 – 35, 1996. ISSN 0168-9002. doi: [http://dx.doi.org/10.1016/0168-9002\(96\)00175-1](http://dx.doi.org/10.1016/0168-9002(96)00175-1). URL <http://www.sciencedirect.com/science/article/pii/0168900296001751>.
- 2788  
2789  
2790  
2791  
2792
- 2793 [47] T. Alexopoulos, J. Burnens, R. de Oliveira, G. Glonti, O. Pizzirusso, V. Polychronakos, G. Sekhniaidze, G. Tsipolitis, and J. Wotschack. A spark-resistant bulk-micromegas chamber for high-rate applications. *Nuclear Instruments and Methods in Physics Research Section A: Accelerators, Spectrometers, Detectors and Associated Equipment*, 640(1):110 – 118, 2011. ISSN 0168-9002. doi: <http://dx.doi.org/10.1016/j.nima.2011.03.025>. URL <http://www.sciencedirect.com/science/article/pii/S0168900211005869>.
- 2793  
2794  
2795  
2796  
2797
- 2798 [48] Joao Pequenao and Paul Schaffner. An computer generated image representing how ATLAS detects particles. Jan 2013. URL <https://cds.cern.ch/record/1505342>.
- 2799  
2800  
2801  
2802  
2803
- 2804 [49] Improved electron reconstruction in ATLAS using the Gaussian Sum Filter-based model for bremsstrahlung. Technical Report ATLAS-CONF-2012-047, CERN, Geneva, May 2012. URL <https://cds.cern.ch/record/1449796>.

- 2792 [50] Electron efficiency measurements with the ATLAS detector using the 2012 LHC proton-proton  
2793 collision data. Technical Report ATLAS-CONF-2014-032, CERN, Geneva, Jun 2014. URL  
2794 <https://cds.cern.ch/record/1706245>.
- 2795 [51] Georges Aad et al. Electron and photon energy calibration with the ATLAS detector using LHC  
2796 Run 1 data. *Eur. Phys. J.*, C74(10):3071, 2014. doi: 10.1140/epjc/s10052-014-3071-4.
- 2797 [52] Georges Aad et al. Measurement of the muon reconstruction performance of the ATLAS detec-  
2798 tor using 2011 and 2012 LHC proton–proton collision data. *Eur. Phys. J.*, C74(11):3130, 2014. doi:  
2799 10.1140/epjc/s10052-014-3130-x.
- 2800 [53] W Lampl, S Laplace, D Lelas, P Loch, H Ma, S Menke, S Rajagopalan, D Rousseau, S Snyder,  
2801 and G Unal. Calorimeter Clustering Algorithms: Description and Performance. Technical  
2802 Report ATL-LARG-PUB-2008-002, ATL-COM-LARG-2008-003, CERN, Geneva, Apr 2008.  
2803 URL <https://cds.cern.ch/record/1099735>.
- 2804 [54] Georges Aad et al. Topological cell clustering in the ATLAS calorimeters and its performance in  
2805 LHC Run 1. 2016.
- 2806 [55] Matteo Cacciari, Gavin P. Salam, and Gregory Soyez. The Anti- $k(t)$  jet clustering algorithm.  
2807 *JHEP*, 04:063, 2008. doi: 10.1088/1126-6708/2008/04/063.
- 2808 [56] Monte Carlo Calibration and Combination of In-situ Measurements of Jet Energy Scale, Jet En-  
2809 ergy Resolution and Jet Mass in ATLAS. Technical Report ATLAS-CONF-2015-037, CERN,  
2810 Geneva, Aug 2015. URL <http://cds.cern.ch/record/2044941>.
- 2811 [57] Georges Aad et al. Performance of  $b$ -Jet Identification in the ATLAS Experiment. 2015.
- 2812 [58] Expected performance of the ATLAS  $b$ -tagging algorithms in Run-2. Technical Report ATL-  
2813 PHYS-PUB-2015-022, CERN, Geneva, Jul 2015. URL <http://cds.cern.ch/record/2037697>.
- 2815 [59] Georges Aad et al. Performance of Missing Transverse Momentum Reconstruction in Proton-  
2816 Proton Collisions at 7 TeV with ATLAS. *Eur. Phys. J.*, C72:1844, 2012. doi: 10.1140/epjc/  
2817 s10052-012-1844-6.
- 2818 [60] Performance of Missing Transverse Momentum Reconstruction in ATLAS studied in Proton-  
2819 Proton Collisions recorded in 2012 at 8 TeV. Technical Report ATLAS-CONF-2013-082, CERN,  
2820 Geneva, Aug 2013. URL <http://cds.cern.ch/record/1570993>.
- 2821 [61] ATLAS Collaboration. Observation and measurement of Higgs boson decays to  $WW^*$  with the  
2822 ATLAS detector. *Phys. Rev. D*, 92(012006), 2015.

- 2823 [62] Aaron James Armbruster. Discovery of a Higgs Boson with the ATLAS detector. 2013. CERN-  
 2824 THESIS-2013-047.
- 2825 [63] G. Cowan, K. Cranmer, E. Gross, and O. Vitells. Asymptotic formulae for likelihood-based tests  
 2826 of new physics. *Eur. Phys. J., C* 71:1554, 2011. doi: 10.1140/epjc/s10052-011-1554-0.
- 2827 [64] ATLAS Collaboration. Limits on the production of the Standard Model Higgs Boson in  $pp$   
 2828 collisions at  $\sqrt{s} = 7$  TeV with the ATLAS detector. *Eur. Phys. J., C* 71:1728, 2011. doi: 10.1140/  
 2829 epjc/s10052-011-1728-9.
- 2830 [65] ATLAS Collaboration. Performance of the ATLAS muon trigger in  $pp$  collisions at  $\sqrt{s} = 8$   
 2831 TeV. *Eur. Phys. J. C*, (arXiv:1408.3179. CERN-PH-EP-2014-154):75. 19 p, Aug 2014. URL <https://cds.cern.ch/record/1749694>.
- 2833 [66] ATLAS collaboration. Electron trigger performance in 2012 ATLAS data, 2015. ATLAS-COM-  
 2834 DAQ-2015-091.
- 2835 [67] Paolo Nason. A new method for combining NLO QCD with shower Monte Carlo algorithms.  
 2836 *JHEP*, 11:040, 2004.
- 2837 [68] B. P. Kersevan and E. Richter-Was. The Monte Carlo event generator AcerMC version 2.0 with  
 2838 interfaces to PYTHIA 6.2 and HERWIG 6.5. 2004.
- 2839 [69] Nikolas Kauer and Giampiero Passarino. Inadequacy of zero-width approximation for a light  
 2840 Higgs boson signal. 2012.
- 2841 [70] T. Gleisberg, Stefan Hoeche, F. Krauss, M. Schonherr, S. Schumann, et al. Event generation with  
 2842 SHERPA 1.1. *JHEP*, 0902:007, 2009. doi: 10.1088/1126-6708/2009/02/007.
- 2843 [71] Michelangelo L. Mangano et al. ALPGEN, a generator for hard multiparton processes in  
 2844 hadronic collisions. *JHEP*, 0307:001, 2003. doi: 10.1088/1126-6708/2003/07/001.
- 2845 [72] Torbjorn Sjostrand, Stephen Mrenna, and Peter Z. Skands. PYTHIA 6.4 Physics and Manual.  
 2846 *JHEP*, 0605:026, 2006. doi: 10.1088/1126-6708/2006/05/026.
- 2847 [73] Torbjorn Sjostrand, Stephen Mrenna, and Peter Z. Skands. A Brief Introduction to PYTHIA 8.1.  
 2848 *Comput.Phys.Commun.*, 178:852–867, 2008. doi: 10.1016/j.cpc.2008.01.036.
- 2849 [74] G. Corcella et al. HERWIG 6: An event generator for hadron emission reactions with interfering  
 2850 gluons (including super-symmetric processes) . *JHEP*, 01:010, 2001. doi: 10.1088/1126-6708/2001/  
 2851 01/010.
- 2852 [75] J. M. Butterworth, Jeffrey R. Forshaw, and M. H. Seymour. Multiparton interactions in photo-  
 2853 production at HERA. *Z. Phys., C* 72:637, 1996. doi: 10.1007/s002880050286.

- 2854 [76] Jun Gao, Marco Guzzi, Joey Huston, Hung-Liang Lai, Zhao Li, et al. The CT10 NNLO Global  
 2855 Analysis of QCD. *Phys. Rev.*, D89:033009, 2014. doi: 10.1103/PhysRevD.89.033009.
- 2856 [77] P. M. Nadolsky. Implications of CTEQ global analysis for collider observables. *Phys. Rev.*, D 78:  
 2857 013004, 2008. doi: 10.1103/PhysRevD.78.013004.
- 2858 [78] A. Sherstnev and R. S. Thorne. Parton distributions for the LHC. *Eur. Phys. J.*, C 55:553, 2009.  
 2859 doi: 10.1140/epjc/s10052-008-0610-x.
- 2860 [79] S. Agostinelli et al. GEANT4, a simulation toolkit. *Nucl. Instrum. Meth.*, A 506:250, 2003. doi:  
 2861 10.1016/S0168-9002(03)01368-8.
- 2862 [80] I. Stewart and F. Tackmann. Theory uncertainties for Higgs mass and other searches using jet  
 2863 bins. *Phys. Rev.*, D 85:034011, 2012. doi: 10.1103/PhysRevD.85.034011.
- 2864 [81] ATLAS Collaboration. Luminosity Determination in  $pp$  Collisions at  $\sqrt{s} = 7$  TeV Using the  
 2865 ATLAS Detector at the LHC. *Eur. Phys. J.*, C 71:1630, 2011. doi: 10.1140/epjc/s10052-011-1630-5.
- 2866 [82] Jet energy scale and its systematic uncertainty in proton-proton collisions at  $\sqrt{s} = 7$  tev with  
 2867 atlas 2011 data. *ATLAS-CONF-2013-004*, 2013.
- 2868 [83] Calibrating the  $b$ -tag efficiency and mistag rate in  $35 \text{ pb}^{-1}$  of data with the atlas detector.  
 2869 *ATLAS-CONF-2011-089*, 2011.
- 2870 [84] ATLAS Collaboration. Measurement of the  $b$ -tag Efficiency in a Sample of Jets Containing  
 2871 Muons with  $5 \text{ fb}^{-1}$  of Data from the ATLAS Detector. *ATLAS-CONF-2012-043*, 2012. URL  
 2872 <http://cdsweb.cern.ch/record/1435197>.
- 2873 [85] Georges Aad et al. Measurements of the Higgs boson production and decay rates and coupling  
 2874 strengths using  $pp$  collision data at  $\sqrt{s} = 7$  and 8 TeV in the ATLAS experiment. *Eur. Phys. J.*,  
 2875 C76(1):6, 2016. doi: 10.1140/epjc/s10052-015-3769-y.
- 2876 [86] W.J. Stirling.  $7/8$  and  $13/8$  TeV LHC luminosity ratios. 2013. URL [http://www.hep.ph.ic.ac.uk/~wstirlin/plots/lhclumi7813\\_2013\\_v0.pdf](http://www.hep.ph.ic.ac.uk/~wstirlin/plots/lhclumi7813_2013_v0.pdf).
- 2877 [87] J Alison. Experimental Studies of hh. Oct 2014. URL <http://cds.cern.ch/record/1952581>.
- 2878 [88] J. Alwall et al. The automated computation of tree-level and next-to-leading order differential  
 2879 cross sections, and their matching to parton shower simulations. *JHEP*, 07:079, 2014.
- 2880 [89] Richard D. Ball et al. Parton distributions with LHC data. *Nucl. Phys. B*, 867:244, 2013.
- 2881 [90] ATLAS Collaboration. ATLAS Run 1 Pythia8 tunes. (ATL-PHYS-PUB-2014-021), Nov 2014.  
 2882 URL <https://cds.cern.ch/record/1966419>.

- 2885 [91] M. Bahr et al. Herwig++ Physics and Manual. *Eur. Phys. J. C*, 58:639–707, 2008. doi: 10.1140/epjc/s10052-008-0798-9.
- 2886
- 2887 [92] Stefan Gieseke, Christian Rohr, and Andrzej Siódmiak. Colour reconnections in Herwig++. *Eur. Phys. J. C*, 72:2225, 2012. doi: 10.1140/epjc/s10052-012-2225-5.
- 2888
- 2889 [93] Simone Alioli, Paolo Nason, Carlo Oleari, and Emanuele Re. A general framework for imple-  
2890 menting NLO calculations in shower Monte Carlo programs: the POWHEG BOX. *JHEP*, 06:  
2891 043, 2010.
- 2892 [94] Peter Zeiler Skands. Tuning Monte Carlo Generators: The Perugia Tunes. *Phys. Rev. D*, 82:  
2893 074018, 2010. doi: 10.1103/PhysRevD.82.074018.
- 2894 [95] Michał Czakon and Alexander Mitov. Top++: A Program for the Calculation of the Top-Pair  
2895 Cross-Section at Hadron Colliders. 2011.
- 2896 [96] Baojia (Tony) Tong. Private communication.
- 2897 [97] D. Krohn, J. Thaler, and L.-T. Wang. Jet Trimming. *JHEP*, 02:084, 2010. doi: 10.1007/  
2898 JHEP02(2010)084.
- 2899 [98] ATLAS Collaboration. Identification of Boosted, Hadronically Decaying W Bosons and Com-  
2900 parisons with ATLAS Data Taken at  $\sqrt{s} = 8$  TeV. 2015.
- 2901 [99] Expected Performance of Boosted Higgs ( $\rightarrow b\bar{b}$ ) Boson Identification with the ATLAS Detector  
2902 at  $\sqrt{s} = 13$  TeV. Technical Report ATL-PHYS-PUB-2015-035, CERN, Geneva, Aug 2015. URL  
2903 <https://cds.cern.ch/record/2042155>.
- 2904 [100] Flavor Tagging with Track Jets in Boosted Topologies with the ATLAS Detector. Technical  
2905 Report ATL-PHYS-PUB-2014-013, CERN, Geneva, Aug 2014. URL <https://cds.cern.ch/>  
2906 [record/1750681](https://cds.cern.ch/record/1750681).
- 2907 [101] Matteo Cacciari and Gavin P. Salam. Pileup subtraction using jet areas. *Phys. Lett. B*, 659:119,  
2908 2008. doi: 10.1016/j.physletb.2007.09.077.
- 2909 [102] Search for pair production of Higgs bosons in the  $b\bar{b}b\bar{b}$  final state using proton-proton collisions  
2910 at  $\sqrt{s} = 13$  TeV with the ATLAS detector. Technical Report ATLAS-CONF-2016-017, CERN,  
2911 Geneva, Mar 2016. URL <https://cds.cern.ch/record/2141006>.
- 2912 [103] Qi Zeng. Private communication.
- 2913 [104] ATLAS Collaboration. Identification of boosted, hadronically-decaying W and Z bosons in  
2914  $\sqrt{s} = 13$  TeV Monte Carlo Simulations for ATLAS. (ATL-PHYS-PUB-2015-033), Aug 2015.  
2915 URL <https://cds.cern.ch/record/2041461>.

- 2916 [105] ATLAS Collaboration. Calibration of  $b$ -tagging using dileptonic top pair events in a combinato-  
2917 rial likelihood approach with the ATLAS experiment. (ATLAS-CONF-2014-004), 2014. URL  
2918 <http://cds.cern.ch/record/1664335>.
- 2919 [106] ATLAS Collaboration. Performance of  $b$ -Jet Identification in the ATLAS Experiment. 2015.
- 2920 [107] Alexander L. Read. Presentation of search results: The CL(s) technique. *J. Phys. G*, 28:2693,  
2921 2002. doi: 10.1088/0954-3899/28/10/313.
- 2922 [108] Glen Cowan, Eilam Gross. Discovery significance with statistical uncertainty in the background  
2923 estimate. 2008. URL <http://www.pp.rhul.ac.uk/~cowan/stat/notes/SigCalcNote.pdf>.
- 2924



**T**HIS THESIS WAS TYPESET using L<sup>A</sup>T<sub>E</sub>X, originally developed by Leslie Lamport and based on Donald Knuth's T<sub>E</sub>X.

The body text is set in 11 point Egenolff-Berner Garamond, a revival of Claude Garamont's humanist typeface. The above illustration, *Science Experiment 02*, was created by Ben Schlitter and released under CC BY-NC-ND 3.0. A template that can be used to format a PhD dissertation with this look & feel has been released under the permissive AGPL license, and can be found online at [github.com/asm-products/Dissertate](https://github.com/asm-products/Dissertate) or from its lead author, Jordan Suchow, at [suchow@post.harvard.edu](mailto:suchow@post.harvard.edu).